Superhydrophobic Surfaces: from Fluid Mechanics to Optics

Promotiecommissie

Voorzitter:	Prof. Dr. K. J. Boller
Promotor:	Prof. Dr. F. Mugele
Overige Leden:	Dr. H. L. Offerhaus
	Dr. H. T. M. van den Ende
	Prof. D. Lohse
	Prof. M. Wessling
	Prof. Dr. F. Toschi (TU Eindhoven)
	Prof. Dr. E. Charlaix (Université Lyon 1, France)

The work described in this thesis
was carried out at the group for

Physics of Complex Fluids
Prof. Dr. F. Mugele
University of Twente
Postbus 217, 7500 AE Enschede
The Netherlands

Tel: +31 53 489 2106
Fax: +31 53 489 1096

This work was made possible by financial support from the joint Micro- and Nanofluidics programme of the Impact and MESA+ research institutes at Twente University and through the Deutsche Forschungsgemeinschaft (Grant No. MU 1472/4).

Superhydrophobic Surfaces: from Fluid Mechanics to Optics

PROEFSCHRIFT

ter verkrijging van
de graad van doctor aan de Universiteit Twente,
op gezag van de rector magnificus prof. dr. W. H. M. Zijm,
volgens besluit van het College voor Promoties
in het openbaar te verdedigen
op woensdag 3 december 2008 om 15.00 uur

door

Helmut Rathgen

geboren op 12 januari 1978
te Hamburg

Dit proefschrift is goedgekeurd door:

promotor: Prof. Dr. F. Mugele

Für Caroline

Contents

1 Introduction **1**
- 1.1 Superhydrophobic surfaces . . . 1
- 1.2 Optical diffraction gratings . . . 4

2 Theoretical background **7**
- 2.1 Capillary theory . . . 8
  - 2.1.1 Surface tension . . . 8
  - 2.1.2 Laplace's pressure . . . 9
  - 2.1.3 Young's angle . . . 10
  - 2.1.4 External forces . . . 12
- 2.2 Superhydrophobic surfaces . . . 15
  - 2.2.1 The lotus effect . . . 16
  - 2.2.2 Contact angle models on heterogeneous surfaces . . . 20
  - 2.2.3 Artificial superhydrophobic surfaces . . . 24
- 2.3 Stokesian dynamics of cavity-meniscus systems . . . 25
  - 2.3.1 A simple model for the resonance behavior . . . 26
  - 2.3.2 Stokes flow theory of an oscillating cavity-meniscus system . . . 28
  - 2.3.3 Hydrodynamic interaction . . . 30
- 2.4 Optical diffraction gratings . . . 33
  - 2.4.1 Grating diffraction . . . 33
  - 2.4.2 Rigorous Coupled Wave Analysis . . . 36

3 Microscopic properties of the superhydrophobic state **41**
- 3.1 Introduction . . . 42
- 3.2 Experiments . . . 43
- 3.3 Highly efficient, tunable transmission grating . . . 53
- 3.4 Tunable gold grating . . . 56
- 3.5 Summary and conclusions . . . 57

4 Gedankenexperiments with superhydrophobic surfaces **59**
- 4.1 Metastable states . . . 60
- 4.2 Qualitative picture of a drop on a superhydrophobic surface . . . 62

4.3 Connected surface patterns 67
4.4 Summary and Conclusions 69
4.5 Outlook 69

5 Large bandwidth, highly efficient optical gratings through high index materials 71
5.1 Introduction 72
5.2 Large bandwidth dielectric TIR grating 79
5.3 Intermezzo: 2^{nd} order TIR grating 82
5.4 Large bandwidth immersed grating 84
5.5 Classical transmission grating with large bandwidth and 100% peak efficiency 87
5.6 Summary and conclusions 89

6 Collective dynamics of ultrasound driven micromenisci 91
6.1 Introduction 92
6.2 Experiments 92
6.3 Deflection amplitude 94
6.4 Frequency response 95
6.5 Theory of a single cavity-meniscus system 95
6.6 Hydrodynamic interaction 97
6.7 Correct averaging 98
6.8 Summary and conclusions 99

7 Dynamics of a single cavity-meniscus system 101
7.1 Introduction 102
7.2 Experiments 102
7.3 Deflection amplitude 104
7.4 Frequency response 107
7.5 Pressure-to-displacement conversion 107
7.6 Summary and conclusions 109

8 Stokes flow theory of oscillating menisci 111
8.1 Single cavity-meniscus system 112
8.1.1 Inertia and damping 113
8.1.2 Potential 122
8.1.3 Relation between the deflection and driving pressure amplitudes 123
8.2 Hydrodynamic interaction 124

A Multilayer Rigorous Coupled Wave Analysis 127
A.1 Analytic formulation 127
A.1.1 Single layer grating 127
A.1.2 Multilayer grating 135
A.2 Numerical formulation 139
A.2.1 User level code 140
A.2.2 Numerical core routines 147

B On the effect of inhomogeneous meniscus displacement 151

C A setup for vapor deposition of self assembled silane monolayers 155
C.1 Traditional vapor deposition technique 155
C.2 Controlled vapor depostion 156

D Design of a chamber for diffraction measurements in pressure controlled liquid environment 159

E On the estimation of the error in χ^2 fitting 165

F Noise equivalent pressure for ultrasound detection using a meniscus on a fiber 169
F.1 Interference signal 169
F.2 Optical shot noise 169
F.3 Pressure to displacement conversion 170
F.4 Noise equivalent pressure 171
F.5 Detector performance 173

G Electric driving of micromenisci 175
G.1 Feasibility 175
G.2 Experiment 179
G.3 Conclusions 180

H Superhydrophobic photonic crystals 181
H.1 Experiment 181
H.2 Conclusions 186

I Confocal detection of meniscus oscillations 187
I.1 Experiment 187
I.2 Ultrasound induced oscillations 190
I.3 Frequency response 193
I.4 Conclusions 194

Summary and outlook 205

Samenvatting 209

List of publications 211

curriculum vitæ 213

Acknowledgments 215

Chapter 1

Introduction

1.1 Superhydrophobic surfaces

Many surfaces in nature, including various plant leafs [84, 44], bird feathers [14], troughs on the elytra of desert beetles [91], and legs of water strider [36], are *superhydrophobic*. A drop of water deposited on such a surface adopts the shape of a nearly perfect sphere that rolls off easily, leaving no trace of humidity behind. Thereby the plant prevents fouling, the bird keeps its feathering light –maintaining its ability to fly–, the beetle collects dew, and the water strider walks on the surface of a lake. Such

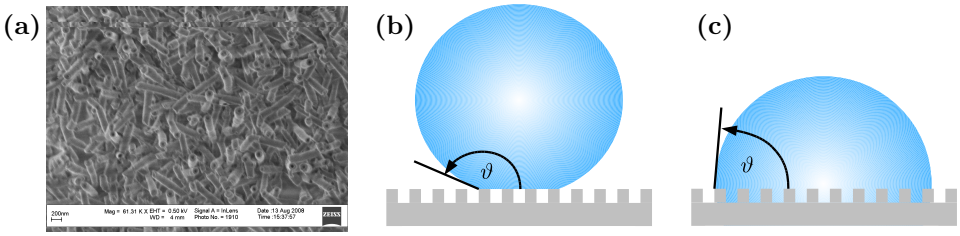

Figure 1.1: **Rough hydrophobic surfaces. (a)** Micro texture of a superhydrophobic surface (here *tropaeolum majus*). The figure shows a scanning electron micrograph of a leaf at 60,000x magnification. (Courtesy of Sissi de Beer) **(b-c)** Drop states on a superhydrophobic surface, **(b)** *superhydrophobic* state, **(c)** *impregnated* state.

superhydrophobicity is achieved by the combination of two parameters: an intrinsic *hydrophobicity* of the material (wax and plastics are examples of hydrophobic materials) and surface roughness, or *micro texture*. Figure 1.1(a) shows a scanning electron micrograph of a superhydrophobic plant leaf (here *tropaeolum majus*). The surface is covered with pillar-like objects with a characteristic size of about 500 nm. A water drop that is deposited on such a rough hydrophobic surface, rests on the crests of the texture, thereby entrapping air underneath, leading to a composite liquid-substrate interface that consists partially of solid-liquid interfaces and partially of liquid-gas

interfaces. This reduces the actual solid-liquid contact, promoting a spherical drop shape with a large contact angle (Fig. 1.1(b)).

Next to this superhydrophobic state, a drop on a superhydrophobic surface is known to exist also in an *impregnated* state, with liquid invading the texture as illustrated in Fig. 1.1(c). Both states result in a rather differnet behavior of the drop. While a drop in the superhydrophobic state will feature a high mobility, providing repellency and self-cleaning, a drop in the impregnated state will be in the so-called *sticky drop* state, characterized by a low mobility providing no liquid repellency and self-cleaning. It is therefore highly desirable to unveal the mechanisms that determine which state will be favored by a given liquid on a given surface.

Several models have been proposed to determine a critical condition for the transition between the two states, involving bending of the micromenisci [106], 'touch down' of the liquid-gas interfaces at the floor of the texture [9, 106, 56], partial penetration of the surface texture [80, 56], as well as dynamic mechanisms [109]. However, experiments that aimed at distinguishing between the competing models have not been conclusive. The problem poses the experimental challenge to observe *micron sized objects* that are *buried* at the interface between a bulk liquid and a bulk substrate with *nanometer resolution*. A clever idea was to scale up the system to larger dimensions and investigate the liquid-gas interfaces by optical microscopy [80]. However, at these larger dimensions, interfaces became more fragile and experiments were hampered by the limit of optical resolution. Atomic Force Microscopy provides sufficient spatial resolution and allows for an *in situ* measurement [52]. However, the measured surface forces require an interpretation, and the inherent tip-sample interaction influences the interfaces [118]. A third smart approach employs an *ex situ* measurement of a solidified and dissected drop [54]. A drop formed by a UV-curable polymer in the superhydrophobic state is solidified, dissected together with the adherent substrate, and studied by electron microscopy. This experiment unvealed details of the liquid-substrate interface with extraordinary resolution. However, it is limited to special liquids, and its destructive nature does not allow for an *in situ* measurement.

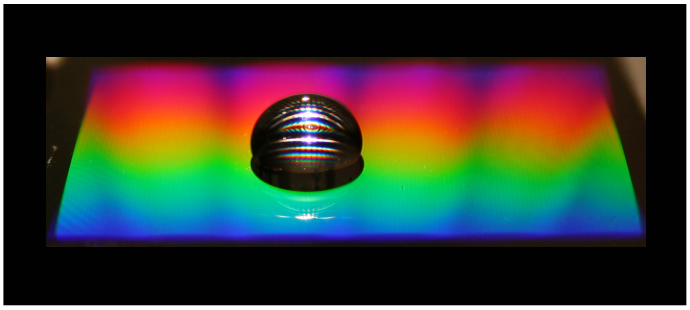

Figure 1.2: **Diffraction of light by an artificial superhydrophobic surface.**

Diffraction, on the other hand, is a phenomenon that is suitable to study *identical* objects that are arranged in a *periodic* manner. In a diffraction measurement, the wavelength of the radiation should be smaller but of the same order as the period

between the objects. For a superhydrophobic surface with a micro texture, visible light is suitable. Fig. 1.2 reproduces a photograph of a typical superhydrophobic surface, showing that the micron scale periodic texture (here a square grid of cylindrical pillars) diffracts white light into its beautiful colors.

In this thesis we employ diffraction from a superhydrophobic optical grating to study the properties of the liquid-gas interfaces at superhydrophobic surfaces on the microscopic scale (Chapter 3). By applying a hydrostatic pressure, we induce the transition from the superhydrophobic to the impreganted state in a controlled manner, and observe it *in situ*. We shall close the long standing debate on the transition mechanism. We shall also give design criteria for surface profiles that provide the largest stability of the superhydrophobic state. Furthermore, we shall evaluate the prospects of using superhydrophobic surfaces for tunable diffractive optical elements.

The use of light as a probe opens up the possibility to study also the *dynamic* behavior of the microscopic liquid gas interfaces. We shall study these aspects in Chapter 6. We shall observe that the dynamics are characterized by ultrasonic oscillations. We shall show that the oscillating interfaces are subject to strong hydrodynamic interaction that induces a collective resonance behavior. We shall describe those experiments through an unsteady Stokes flow model in Chapter 8.

The experiments call for the investigation of a single micromeniscus in the decoupled limit. Moreover, the sensitivity of the menisci to an applied ultrasound field suggests their use for low noise ultrasound detection. Both aspects stimulate experiments with a hydrophobic cavity fabricated on the end face of an optical fiber that serves as a combined meniscus and optical micro-cavity, allowing for a fiber-interferometric measurement of meniscus oscillations. We shall discuss those aspects in Chapter 7. We shall also investigate alternative approaches towards low noise ultrasound sensing, based on superhydrophobic photonic crystals (Appendix H) and confocal microscopy (Appendix I).

With regard to the measurement of the *static* shape of the microscopic liquid-gas interfaces through optical diffraction, 'solving' the inverse scattering problem requires a precise modeling of the diffraction process. This engages us in the study of optical grating diffraction and the development of a numerical code that is suitable to compute the diffraction from general grating profiles. We shall model the diffraction process by computing exact numerical solutions to the Maxwell equations. We shall use the so-called Rigorous Coupled Wave Analysis. These aspects shall be discussed in Appendix A (see also http://mrcwa.sourceforge.net/). We shall observe a total internal reflection (TIR) process that determines the intensity diffracted from a superhydrophobic optical grating. This observation shall guide us to investigate commercial dielectric TIR gratings through numerical simulations. We shall consider methods to increase the spectral bandwidth of dielectric optical gratings. In Chapter 5 we shall devise dielectric optical gratings with a spectral bandwidth that is larger than that of any grating known today. To give right to these purely optical aspects we shall now review the development of optical diffraction gratings.

1.2 Optical diffraction gratings

About a year after Newton had performed his prism experiments to support his corpuscular theory of light, the Scottish physicist James Gregory (1638–1675) studied bird feathers to find that a periodic object diffracts white light into its colors [124]. He had discovered the principles of optical grating diffraction, a phenomenon that could not be explained by Newtons 'light particle' theory. The phenomenon did not gain much attention, until in 1814 Fraunhofer invented the spectrograph, and used a grating to study the solar spectrum. He discovered dark lines in the solar spectrum (today called *Fraunhofer lines*), which were explained only in 1895 by Bunsen and Kirchhoff to be atomic absorption lines. The grating that he used consisted of fine equidistant wires that he had stretched between two threaded rods, similar to the first useful optical grating that was constructed before in 1785 by David Rittenhouse (see also [42, 41]).

Though a remarkable resolution could be achieved with wire gratings, the diffracted intensity –diffraction efficiency– was not always very high. The performance of optical gratings improved dramatically with the construction of ruling machines, (e.g. Rutherfurd (1816–1892) and Grayson (1856–1918)), that enabled around 500 lines per mm to be ruled into a metal or glass plate with a diamond point. While wire gratings were operated mainly in transmission (the diffracted light is collected on the transmission side of the grating), metallic ruled gratings could be operated in reflection and provided a greatly improved diffraction efficiency.

Today, diffraction gratings are an integral part of many modern optical systems, with applications in lasers, telescopes, spectroscopy and telecommunication. Still, about 150 years after their invention, metallic ruled (and holographic) gratings are unsurpassed in their spectral bandwidth, paired with a peak efficiency that exceeds 90%, reserving them a key role as a diffractive optical component and making them indispensable in spectroscopic applications. Fig. 1.3(a) shows schematically a modern blazed grating. The use of a rectangular ruling tip results in right angled triangular profile, characterized by a blaze angle α that determines the inclination of the long face of the grating teeth with respect to the horizontal surface. Waves are diffracted from the grating at angles

$$\sin\vartheta_m = \sin\vartheta_0 + \frac{m\lambda}{T}, \tag{1.1}$$

where m is the diffraction order, ϑ_0 is the angle of the 0^{th} diffraction order, λ is the wavelength of the light, and T is the period of the grating. Angles are measured with a positive sign in positive y-direction, and with a negative sign in negative y-direction. The grating is operated in -1^{st} order Littrow configuration, where the -1^{st} diffraction order is anti parallel to the incident beam. The blaze angle α is chosen such that the long face of the teeth is perpendicular to the incident beam, $\alpha = \vartheta_0$, suggesting that light is 'reflected' into the -1^{st} order. This scattering geometry is met at a specific wavelength λ_0, called the *design wavelength* or *blaze wavelength*. For all other wavelengths, the scattering angles deviate from the ideal geometry. It is a remarkable property of metallic ruled gratings that the diffraction efficiency remains high, even for large deviations from the ideal scattering geometry, resulting in an extraordinarily

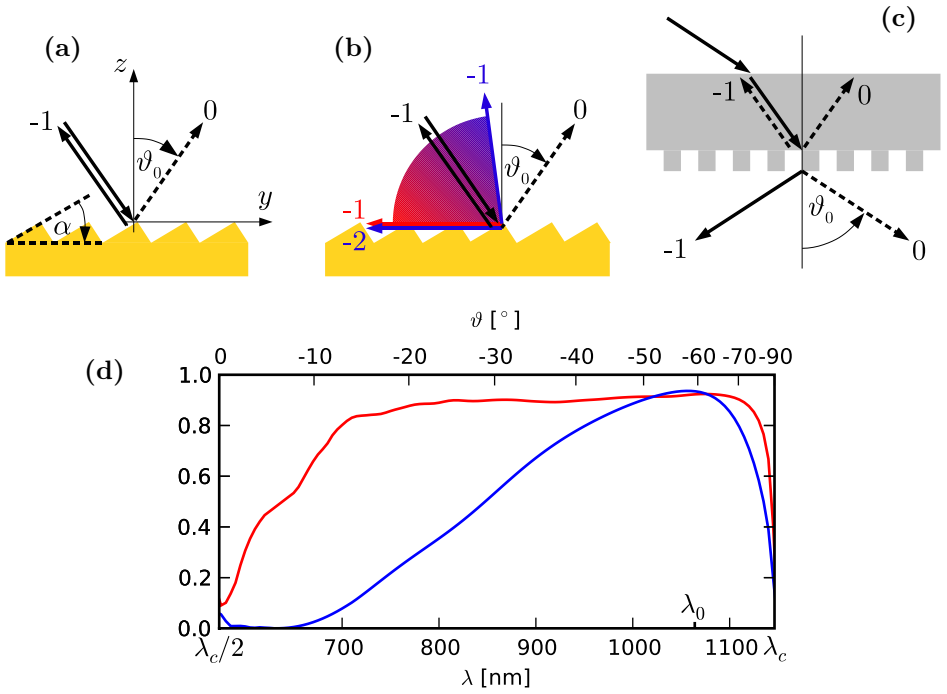

Figure 1.3: **Modern optical diffraction gratings. (a)** Blazed gold grating. **(b)** Usable spectral range of a diffraction grating. **(c)** Dielectric transmission grating. **(d)** Spectral characteristics of modern optical gratings (calculated). Red line: blazed gold grating. Blue line: fused silica transmission grating.

large spectral bandwidth. The Usable spectral range of an optical grating follows from the overlap of diffraction orders, as illustrated in Fig. 1.3(b). The longest wavelength – red most light– diffracted by the grating is $\lambda_c = T(1-\sin\vartheta_0)$. Blue light whose second order overlaps with the first order on the red edge shall be excluded from the incident light, requiring that light is restricted to an octave $\lambda_c/2 < \lambda < \lambda_c$. Figure 1.3(d) shows a calculated spectral range of an ideal blazed gold grating (blazed for $\vartheta_0 = 60°$ at $\lambda_0 = 1064$). The diffraction efficiency remains high over a large part of the octave.

Two deficiencies of metallic diffraction gratings are known, related to the absorbing nature of metals. The absorption of a metal is small (consider the absorption of a silver mirror which is typically $1-3\%$), but much larger than that of a dielectric (e.g. the absorption of a 1mm thick fused silica plate is typically $0.01-0.1\%$). (1) due to the inherent absorption, the maximal achievable diffraction efficiency is limited to about 90%. (2) generation of heat prohibits a large incident power.

The recent development of high power lasers has stimulated a demand for *dielectric* optical gratings that have a large resistance to high power. Figure 1.3(c) shows schematically a dielectric grating. It consists of rectangular grooves that are fabricated into the backside of a glass body. The grating is illuminated from the glass

side and the diffracted light is collected on the transmission side. In Fig. 1.3(d) the spectral characteristics of a dielectric grating is compared to the gold grating. Since the grating does not suffer from absorption losses, it reaches –at the design wavelength λ_0– a higher efficiency than the gold grating. Due to reflection losses, the diffraction efficiency remains below 100%. However, more importantly, as the wavelength deviates substantially from the design wavelength, the diffraction efficiency drops rapidly to nearly zero, resulting in a small spectral bandwidth.

In this thesis we shall devise dielectric optical gratings with a large spectral bandwidth –larger than that of a gold grating– and peak efficiency of 100% (Chapter 5).

Chapter 2

Theoretical background

In this chapter, our aim is to introduce established theoretical concepts as well as known experimental facts about liquids on small scales, superhydrophobic surfaces, dynamics of microscopic liquid-gas interfaces, and finally optical grating diffraction.

The chapter is organized as follows. In Sec. 2.1, we review relevant elements of *capillary theory* that deals with the description of liquid-gas interfaces on small scales (or generally, on scales where surface tension is important). In Sec. 2.2, we consider *superhydrophobic surfaces*, and discuss the origin of their extraordinary liquid repellency. In Sec. 2.3 we consider the fluid mechanics encountered at a superhydrophobic surface, more precisely we consider the (collective) hydrodynamics of one or more microscopic liquid-gas interfaces formed at the openings of hydrophobic cavities through unsteady Stokes flow theory. In Sec. 2.4 we outline the theory of optical grating diffraction.

2.1 Capillary theory

When I empty a glass of water, most of the fluid leaves the glass, however a small amount of liquid remains inside, forming small drops (typically about a millimeter in size) that stay attached to the wall, resisting all gravitational pull that drags on them. On small scales, surface tension dominates over the gravitational force, and determines the behavior of fluids and objects in contact with them. Surface tension determines the size of rain drops [117], makes a sand pile stable [112, 111], creates the foam on top of a beer [69], and allows plants to transport liquid to their leaves [13, 130]. Capillary forces typically become important on the millimeter scale, when they start to dominate over gravity. They remain a dominant force until molecular forces take over at scales below few tens of nanometers – in other words, the realm of surface tension extends nearly over six orders of magnitude. In this section we introduce basic theoretical concepts that are used to describe the behavior of liquid interfaces on these scales. We will first illustrate the origin of surface tension. We proceed in 2.1.2 with the introduction of Laplace's law that relates the effect of surface tension in a concise way to a pressure. Next, in 2.1.3 we consider a liquid-gas interface that is brought in contact with a solid. Finally, in subsection 2.1.4, we illustrate how external forces on liquid-gas interfaces can be incorporated through the concept of 'pressure paths'. We illustrate this concept using the problem of a meniscus at a vertical plate as an example.

2.1.1 Surface tension

Liquid is condensed matter. Though more fluctuating than a solid, every atom (or molecule) is in a bound state where it constantly experiences the attractive forces of its neighbors (in contrast to a gas, where molecules spend most of the time far away from each other, flying through empty space without experiencing attractive or repulsive forces, and meeting only occasionally to collide and continue their flight in another random direction). A molecule in the bulk liquid will experience forces equally distributed in all spatial directions (Fig. 2.1). In contrast, at the surface each molecule misses half of its neighbors, i.e. it misses half of its bonds. To bring a molecule to the surface and create an amount of surface area corresponding roughly to its cross section, we have to provide roughly the energy required to break half of its

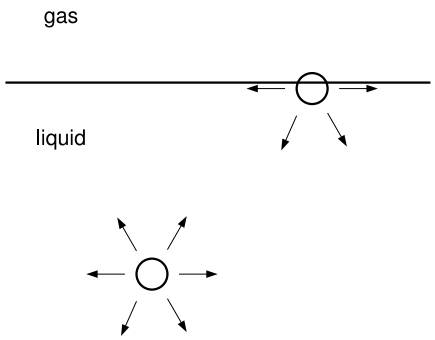

Figure 2.1: **Molecular origin of surface tension.** A molecule in the bulk liquid experiences forces equally distributed in all spatial directions. In contrast, a molecule at the surface misses half of its neighbors. To bring a molecule to the surface, an amount of energy approximately equal to half its binding energy is required.

bonds. This energy (per unit area) required to create new liquid surface is the surface energy or *surface tension*, typically denoted by σ. The liquid will seek to minimize its surface area. Any curved surface will tend to flatten. This results in an inwards oriented force. For the case of a spherical drop (with radius R) we can immediately write down the force: to enlarge the radius of the sphere by δr, we have to provide an amount of surface energy

$$\delta E = 8\pi R\sigma\, \delta R. \tag{2.1}$$

Since $\delta E = F\, \delta r$, the inward directed force at any point of the sphere is $8\pi R\sigma$. We can express the force in terms of a pressure as

$$P = \frac{F}{S} = \frac{8\pi R\sigma}{4\pi R^2} = \frac{2\sigma}{R} \tag{2.2}$$

Thus, the surface tension results in an additional pressure inside the liquid, or more precisely, if we cross the curved interface from outward to inwards, the pressure increases by $2\sigma/R$.

2.1.2 Laplace's pressure

In 1805 a french mathematician and astronomer who is probably most known for his contributions to potential theory and the development of the spherical harmonics, Laplace, noticed that above result can be cast into a simple form also for surfaces with an arbitrary shape [31]. He stated:

> *'Upon crossing a curved interface, the pressure changes by an amount equal to the product of the surface tension and the curvature.'* (2.3)

To define the curvature κ in a point p on a surface S, consider all curves C_α in S passing through p. Every such C_α has an associated curvature κ_α taken at p. Of those κ_α, at least one is characterized as maximal, κ_1, and one as minimal, κ_2, and these two curvatures κ_1 and κ_2 are known as the principal curvatures. The *curvature* at p in S is the sum of the principal curvatures

$$\kappa = \kappa_1 + \kappa_2. \tag{2.4}$$

One shows in differential geometry that the principle curvatures can be constructed by cutting two suitable planes through the surface that are perpendicular to each other, and the straight line that is formed by their intersection contains the surface normal vector. The intersection of each of the planes with the surface defines a curve and an associated curvature in point p. The sum of these two curvatures is the *curvature* of the surface, which is independent of the orientation of the planes, and for a specific orientation of the two planes the two individual curvatures are the two *principle curvatures*.

Specifically, in $\mathbb{R}^3$ the mean curvature is related to the unit normal vector n as

$$\kappa = \nabla n. \tag{2.5}$$

For the special case of a surface defined as a function of two coordinates $\hat{z} = S(x, y)$, above expression evaluates to

$$\begin{aligned}
\kappa &= \nabla \left(\frac{\nabla(S - z)}{|\nabla(S - z)|} \right) \\
&= \nabla \left(\frac{\nabla S}{\sqrt{1 + (\nabla S)^2}} \right) \\
&= \frac{\left(1 + \left(\frac{\partial S}{\partial x}\right)^2\right) \frac{\partial^2 S}{\partial y^2} - 2 \frac{\partial S}{\partial x} \frac{\partial S}{\partial y} \frac{\partial^2 S}{\partial x \partial y} + \left(1 + \left(\frac{\partial S}{\partial y}\right)^2\right) \frac{\partial^2 S}{\partial x^2}}{\left(1 + \left(\frac{\partial S}{\partial x}\right)^2 + \left(\frac{\partial S}{\partial y}\right)^2\right)^{3/2}}
\end{aligned} \tag{2.6}$$

All of the microscopic liquid systems considered in this work can –in principle– be described by evaluating suitable constant-mean-curvature surfaces (or as we shall see below, the curvature may also be a simple function of the height) under given constraints (e.g. that the volume be constant) and with suitable boundary conditions. In an unbounded medium, and with the absence of external forces, a given amount of liquid (constant volume) will always take the shape of a sphere. It is the boundary conditions that make things really interesting.

2.1.3 Young's angle

What happens if we bring a liquid-gas interface in contact with a rigid (undeformable) solid substrate (Fig. 2.2a)? In the vicinity of the line at which the liquid, gas, and solid phases meet, the *three-phase contact line*, we encounter three surfaces that all have

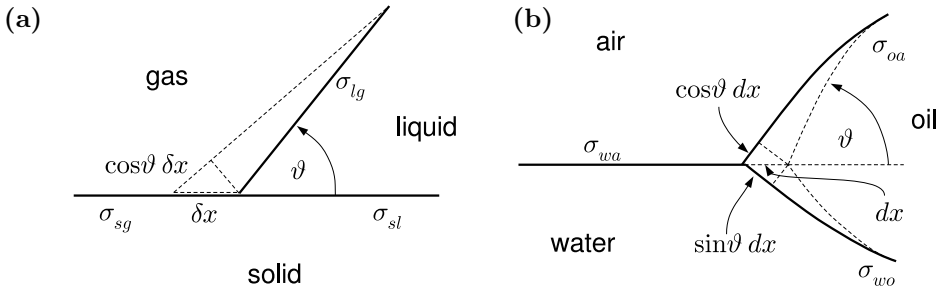

Figure 2.2: **Young's contact angle. (a)** For a liquid-gas interface in contact with a solid. An infinitesimal translation of the contact line between the solid, liquid, and gas phase results in the creation (and reduction) of liquid-gas, solid-liquid, and solid-gas interfacial area. The associated surface energies determine the angle between the interfaces. **(b)** For two immiscible liquids in contact with a gas phase, e.g. an oil drop floating on water.

their individual surface energy: in addition to the liquid-gas interface with surface energy σ_{lg}, there is the solid surface covered with liquid, with surface energy σ_{sl}, and the solid surface in contact with gas, with surface energy σ_{sg}. Let us denote the angle between the liquid-gas interface and the solid-liquid interface with ϑ. The system is in its potential minimum when $\delta E = 0$. Upon a translation δx of the contact line on the substrate, the surface energy changes by

$$\delta E = \sigma_{sl}\,\delta x - \sigma_{sg}\,\delta x + \sigma_{lg}\cos\vartheta\,\delta x. \tag{2.7}$$

Thus

$$\cos\vartheta = \frac{\sigma_{sg} - \sigma_{sl}}{\sigma_{lg}}. \tag{2.8}$$

Hence, the surface energies determine the *angle* that the liquid-gas interface takes with the substrate at its contact line. This angle, which is a material constant for a given solid-liquid-gas combination, is known as *Young's contact angle*, after the British physicist and physician Thomas Young (1773–1829), who discovered this phenomenon when studying the shape that a sessile drops adopts on a solid substrate [132]. Young's contact angle is frequently termed also *Young angle* or simply *contact angle*.

The concept can be extended to *deformable* substrates, as is the case e.g. with an oil drop floating on water (Fig. 2.2b), where the angles of the oil-water and oil-air interfaces can be expressed in a similar fashion, e.g. with respect to the water-air interface as

$$\sigma_{wa} = \sigma_{oa}\cos\vartheta + \sigma_{wo}\sin\vartheta. \tag{2.9}$$

Young's equation (Eq. (2.8)) can be evaluated as long as the right-hand-side takes a value in the range -1 to 1. However, one frequently encounters the case that the surface energy of the solid substrate, σ_{sg}, is rather high (e.g. with many metals), while the surface energy of the liquid, σ_{lg}, is comparably low (e.g. most organic liquids),

and on many occasions σ_{sg} is so dominant that still $\sigma_{sg} - \sigma_{sl}$ is larger than σ_{lg}, and the right-hand-side of Young's equation would be larger than 1. This case is known as *total wetting* (sometimes expressed as 'the contact angle is zero'), and corresponds to the case when the surface energy of a dry substrate is larger than the total surface energy of a substrate covered with liquid, which comprises both a solid-liquid and a liquid-gas interface. In this case the liquid spreads completely over the substrate, as is known e.g. with oil that 'wets' a steel plate (a drop deposited on a steel plate will flatten indefinitely, covering the plate with a thinner and thinner film governed by viscosity). This leads e.g. to the description of the dynamics of thin films (e.g. [116, 59]) and their instability and break up [121]. A spreading film will become thinner and thinner, and ultimately molecular forces will rule its behavior. This leads to concepts such as the *disjoining pressure* [32] and many types of short- and long-range molecular forces that govern the interactions in a liquid.

In this thesis, we are concerned with the other case that is characterized by a non-zero contact angle given by Young's equation. This case is known as *partial wetting*. It is encountered with a high energy liquid (e.g. water or mercury) and a low energy substrate (e.g. many polymers). In this case a drop deposited on the substrate will not spread indefinitely, rather it will halt and adopt the shape of a spherical cap with Young's angle at its contact line.

2.1.4 External forces

In many cases liquid-gas or liquid-liquid interfaces are subject to external forces. E.g. a sessile drop that is flattened due to gravity, a falling rain drop that is deformed by a surrounding air flow, and a bubble in a liquid that experiences lift forces, counterbalanced by viscous drag. To evaluate the effect of external forces on a liquid-gas interface, it is often useful to think in terms of 'pressure paths'. This concept is illustrated in this section using the meniscus formed by a liquid-gas interface at a vertical wall under the presence of gravity as an example. The system is illustrated in Fig.2.3(a). Let us start at a point in the gas phase. Everywhere in the gas phase the pressure is P_0. As we cross the liquid-gas interface far away from the wall, the pressure remains constant (there is no pressure change due to surface tension since the interface is flat). Thus, just below the liquid-gas interface, inside the liquid, the pressure is the ambient pressure P_0. As we move downwards, the pressure increases by the hydrostatic pressure $P_h = -\rho g z$ (note that the sign of the hydrostatic pressure is negative, since moving downwards corresponds to negative z). Let us stop moving downwards and instead move parallel to the meniscus. The pressure does not change. Thus, at depth z just underneath the curved liquid-gas interface of the meniscus, the pressure is $P = P_0 - \rho g z$. On the other hand, we may approach the same point through the gas phase. The pressure in the gas phase is constant, even if we start walking into the void space created by the meniscus. As we cross the curved liquid-gas interface, the pressure increases by $\sigma\kappa$ (in virtue of Laplace's law), thus $P = P_0 + \sigma\kappa$. Thus, we have found two ways in expressing the same pressure, and we may write

$$P_0 - \rho g z = P_0 + \sigma\kappa. \tag{2.10}$$

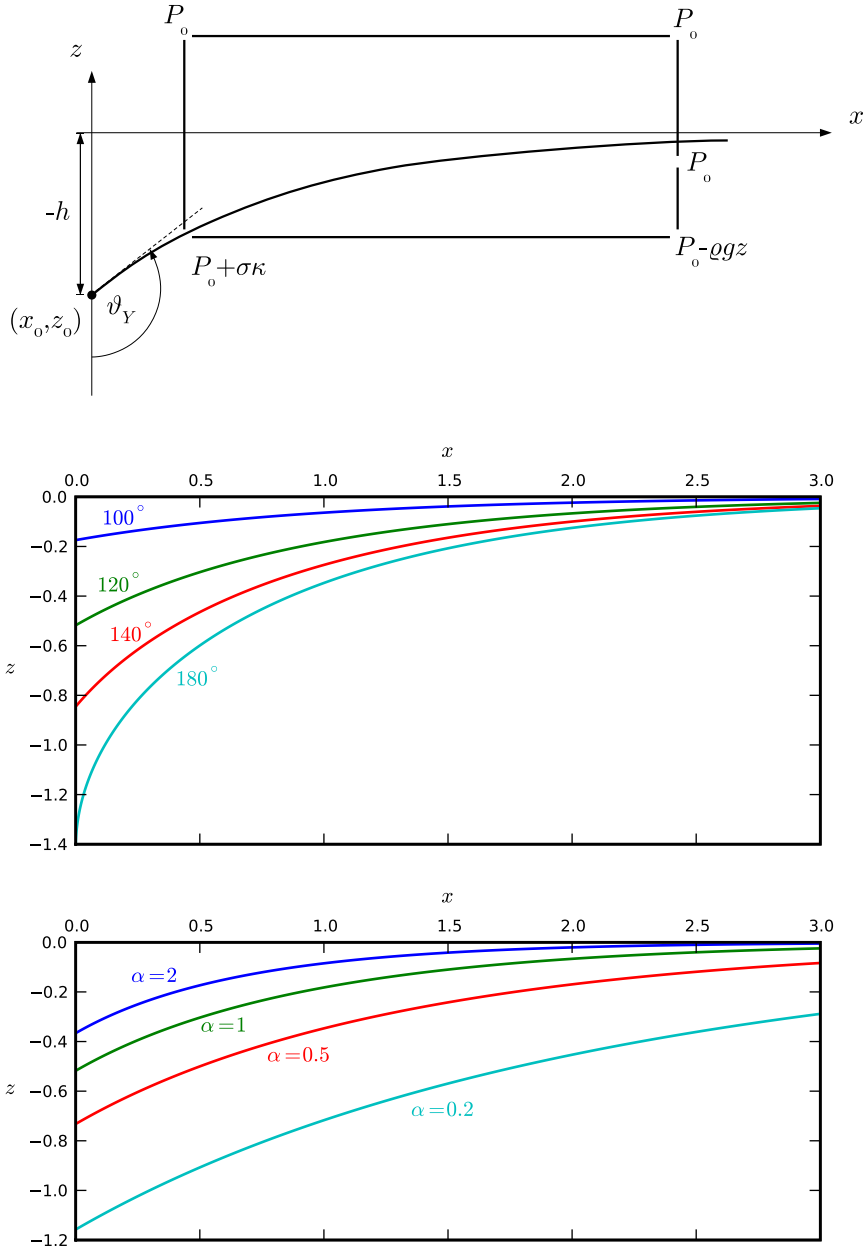

Figure 2.3: **Profile of a meniscus at a vertical plate. (a)** Schematic of the liquid-gas interface. Solutions to the meniscus profile (Eq. (2.19)) are plotted for several Young angles with $\alpha = 1$ **(b)**, and for several α with Young angle $\vartheta_Y = 120°$ **(c)**.

The P_0's cancel such that

$$-\rho g z = \sigma \kappa. \tag{2.11}$$

This 'pressure balance' governs the shape of the meniscus. Let us simplify it by merging all constants into one: $\alpha = \rho g/\sigma$, such that

$$-\alpha z = \kappa. \tag{2.12}$$

The constant α is closely related to the so-called *capillary length*

$$\lambda_c = \sqrt{\frac{\sigma}{\rho g}}, \tag{2.13}$$

which expresses the characteristic length scale below which surface tension dominates over gravity. We have to specify yet the boundary conditions. We can chose the coordinate system such that the liquid level approaches zero for $x \to \infty$, and we require that far away from the wall the interface is flat $\kappa \to 0$ for $x \to \infty$. In virtue of Young's law, we require that the angle between the liquid-gas interface at the vertical plate be the Young angle ϑ_Y. It remains to express κ in terms of the Cartesian coordinates to cast Eq. (2.12) into a differential equation. We find an expression for the curvature by replacing in Eq. (2.6) all derivatives to y by zero, and adding a minus sign to account for the particular parametrization with $z = z(x)$ as shown in the figure, such that

$$\kappa = -\frac{z''}{\left(1 + z'^2\right)^{3/2}}. \tag{2.14}$$

Combining with 2.12 yields

$$\alpha z = \frac{z''}{\left(1 + z'^2\right)^{3/2}}. \tag{2.15}$$

Multiplying by z' and integrating once yields

$$\frac{\alpha z^2}{2} + c = -\frac{1}{\left(1 + z'^2\right)^{1/2}}. \tag{2.16}$$

The integration constant c follows from the boundary condition $\kappa \to 0$ for $x \to \infty$, which implies that $z' \to 0$ and $z \to 0$ for $x \to 0$, such that $c = -1$, and thus

$$1 - \frac{\alpha z^2}{2} = \frac{1}{\left(1 + z'^2\right)^{1/2}}. \tag{2.17}$$

Using separation of variables we cast this into the form of an integral

$$\int_{z_0}^{z} \left(\frac{\sqrt{\alpha} z}{\sqrt{4 - \alpha z^2}} - \frac{2}{\sqrt{\alpha} z \sqrt{4 - \alpha z^2}} \right) dz = \int_{x_0}^{x} dx, \tag{2.18}$$

where we have settled the integration constant by letting the integration run from the point $(x_0, z_0) = (0, -h)$ onwards, corresponding to the point where the interface is attached to the wall. The integral yields [95, 7, 104, 40]

$$\sqrt{4-\alpha h^2} - \sqrt{4-\alpha z^2} + \ln\left(\frac{h\left(2+\sqrt{4-\alpha z^2}\right)}{z\left(2+\sqrt{4-\alpha h^2}\right)}\right) = \sqrt{\alpha}x. \tag{2.19}$$

The expression cannot be solved analytically for z. We therefore proceed with a description of the profile in terms of a parametrization $x(z)$. To express the boundary condition at the vertical plate we employ Young's condition. The Young condition determines the slope s_0 at the plate as $s_0 = \tan(\vartheta_Y - 90°)$. Since the solution $z(x)$ and its derivative $z'(x)$ are not known, the boundary condition cannot be evaluated directly. Thus, we evaluate Eq. (2.17) at $x = 0$ to relate $z'(0) = s_0$ to $z(0) = z_0 = -h$, to obtain

$$h^2 = \frac{2}{\alpha}\left(1 - \left(1+s_0^2\right)^{-1/2}\right). \tag{2.20}$$

Substituting this expression into the solution Eq. (2.19), yields the profile in terms of the known parameters s_0 and α. Figures 2.3(b-c) plot few such solutions for several Young angles with $\alpha = 1$ and for several α's with Young angle $\vartheta_Y = 120°$. This finishes our treatment of a meniscus at a vertical plate. The treatment illustrates how the concept of 'pressure paths' can be used to describe the influence of external forces on liquid-gas interfaces. It also illustrates some of the mathematical steps that may used to evaluate constant-mean-curvature surfaces.

2.2 Superhydrophobic surfaces

The largest Young angle of water on any known material is about 120° [30]. Such large intrinsic contact angle is achieved with the lowest energy surfaces known, such as fluoropolymers (Teflon) or wax. By contrast, many surfaces in nature, including various plant leafs [84, 44], legs of water strider [36], and geckos' feet [5, 37], are superhydrophobic, displaying apparent contact angles with water typically between 150° and 170° and low contact angle hysteresis. Such superhydrophobicity is achieved by the combination of two key parameters, low intrinsic surface energy and surface roughness [129, 20, 99]. Superhydrophobic surfaces display favorable properties that are interesting to applications. Amongst, an enhanced liquid repellency [88], the self cleaning effect [82] and drag reduction capabilities [28, 123]. This has recently stimulated extensive research on the development of artificial superhydrophobic [81, 99] and more generally superoleophobic [126] or superlyophobic [2] surfaces.

In the following sections the current understanding of superhydrophobic surfaces is reviewed. First, in Sec. 2.2.1 the phenomenology of superhydrophobic surfaces, the 'lotus effect' is discussed in greater detail. In Sec. 2.2.1 and 2.2.1 basic models that are frequently used to describe superhydrophobic surfaces, the Cassie-Baxter and the Wenzel model are introduced. Those are discussed critically in Sec. 2.2.2, and opposed to competing contact angle models. Finally in Sec. 2.2.3 practical aspects of artificial superhydrophobic surfaces are reviewed.

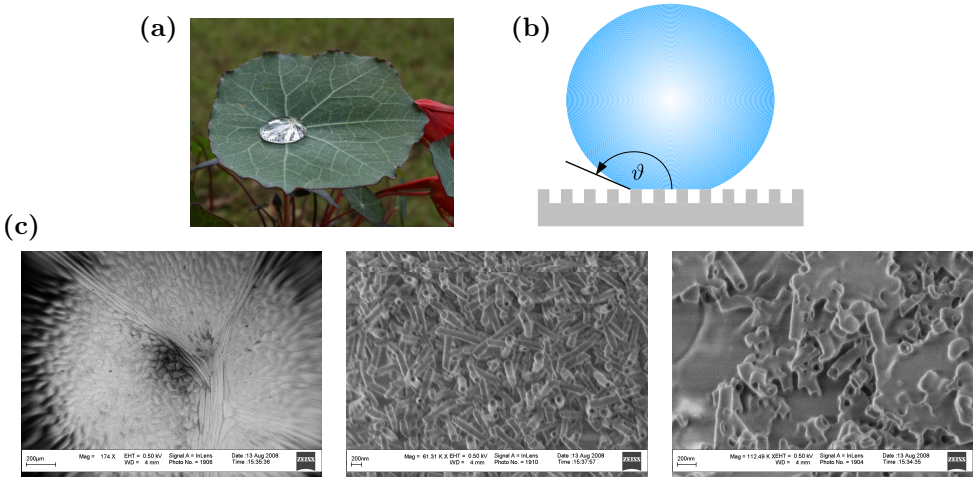

Figure 2.4: **The lotus effect (here with *tropaeolum majus*). (a)** Photograph of a drop on a *tropaeolum majus* leaf. The silvery appearance of the drops footprint is due to total internal reflection of light at microscopic liquid-gas interfaces, indicating that the drop is in the 'Cassie-Baxter state' (see text). **(b)** Schematic of a drop on a superhydrophobic surface. **(c)** Scanning electron micrographs of a *tropaeolum majus* leaf at increasing magnification (from left to right) 175x, 60,000x, 110,000x. The photographs were obtained 'as dissected' without the deposition of a conductive coating. (Courtesy of Sissi de Beer).

2.2.1 The lotus effect

The best-known example of a natural superhydrophobic surface is the surface of the lotus leaf. On a lotus leaf, a water drop adopts a contact angle typically larger than 160°. Fig. 2.4(a) shows a drop deposited on a superhydrophobic plant leaf (here *tropaeolum majus*). Numerous studies have suggested that the superhydrophobic character of the lotus leaf is due to a combination of surface chemistry –an intrinsically hydrophobic leaf ('waxy leaf')– and surface roughness on multiple scales. Fig. 2.4(c) shows scanning electron micrographs of a *tropaeolum majus* leaf at increasing magnification. At the smallest scale, the surface is covered with pillar-like objects with a characteristic size of about 500 nm. Two distinct models suggested independently by Cassie and Baxter [20] and Wenzel [129] are commonly used to explain the effect of surface roughness on the apparent macroscopic contact angle of liquid drops.

The Wenzel model

The Wenzel model recognizes that surface roughness increases the available surface area of the solid. The roughness r of a surface is defined as the ratio of the actual surface area A^* over the apparent macroscopic surface area A (Fig. 2.5) (implying $r \geq 1$). The apparent contact angle ϑ^* is defined by considering the energy variation

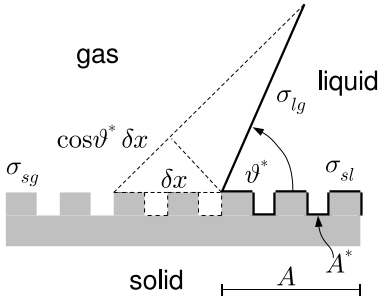

Figure 2.5: **The Wenzel model.** The surface energy of the solid-liquid interface is defined by considering the actual surface area A^*.

upon translation of the contact line on the rough surface as

$$\delta E = [r(\sigma_{sl} - \sigma_{sg}) + \sigma_{lg}\cos\vartheta^*]\,\delta x, \tag{2.21}$$

which modifies the surface contact angle according to

$$\cos\vartheta^* = r\cos\vartheta_Y, \tag{2.22}$$

where ϑ_Y is Young's angle. Wenzel's relation predicts two types of behavior. If the surface is *hydrophilic* ($\vartheta_Y < 90°$), the apparent contact angle is further *decreased*. In contrast, if the surface is *hydrophobic* ($\vartheta_Y > 90°$), the contact angle is *increased*. Generally, Wenzel's relation suggests that surface roughness enhances the intrinsic wetting behavior of the surface. Wenzel's relation also suggests the possibility of wetting and drying surfaces. E.g., for surfaces with $\vartheta_Y < 90°$, Wenzel's relation suggests the possibility of turning a partially wetting surface into a wetting surface with $\vartheta^* = 0$. For a contact angle of 60° such behavior is easily obtained with $r = 2$. In analogy, a hydrophobic surface with a contact angle of 120° would be turned into an ideal superhydrophobic surface with $\vartheta^* = 180°$ for $r = 2$. We will however see below that Wenzel's result is highly arguable.

The Cassie-Baxter model

The Cassie-Baxter model, on the other hand, postulates that the superhydrophobic nature of a rough surface is caused by microscopic pockets of air entrapped below the liquid droplet leading to a composite surface that consists partially of solid-liquid interfaces and partially of liquid-gas interfaces (Fig. 2.6). For flat liquid-gas interfaces, the energy variation δE associated with a variation δx of the contact line is considered as

$$\delta E = \left[\phi^S\sigma_{sl} + (1-\phi^S)\sigma_{lg} - \phi^S\sigma_{sg} + \sigma_{lg}\cos\vartheta^*\right]\delta x, \tag{2.23}$$

where ϕ^S is the solid-liquid surface fraction. The Cassie-Baxter result follows as

$$\cos\vartheta^* = -1 + \phi^s(1+\cos\vartheta). \tag{2.24}$$

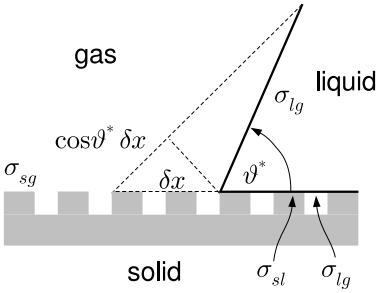

Figure 2.6: **The Cassie-Baxter model.** The liquid is assumed to 'float' on top of the texture forming microscopic air pockets, leading to a composite surface that consist partially of solid-liquid interfaces, and partially of gas-liquid interfaces.

Eq. (2.24) implies a behavior that is very different from the one predicted by the Wenzel equation. In contrast to the Wenzel relation, the Cassie-Baxter equation allows for the possibility of $\vartheta^* > 90°$ with $\vartheta_Y < 90°$. On the other hand it suggests that an ideal contact angle of 180° can be reached only in the limit $\phi^S \to 0$, but not with a finite ϕ^S, as suggested by the Wenzel model. However, as we shall see below, also the Cassie-Baxter model is highly arguable.

Competition between the Cassie-Baxter and Wenzel scenario

All the favorable properties of superhydrophobic surfaces, such as the self-cleaning effect [82] and drag reduction capabilities [28, 123], rely on the 'superhydrophobic state', where the drop rests on top of the texture. In this state a drop is highly mobile and can easily roll off from the surface, providing liquid-repellency as well as self-cleaning. In contrast, a drop in the 'impregnated' state is characterized by a low mobility ('sticky drop') providing no liquid-repellency and self-cleaning effect. It is therefore of great interest to understand the mechanisms that determine which of the two states will be adopt on a given surface with a given liquid.

Various thermodynamic arguments have been suggested to determine whether a drop on a superhydrophobic surface resides in the superhydrophobic or in the impregnated state [71, 86]. Frequently the total surface energies of both states are compared [57, 106], suggesting a critical Young angle

$$\cos\vartheta_c = -\frac{1-\phi^S}{r-\phi^S}. \tag{2.25}$$

The impregnated state is adopted if $\vartheta_Y < \vartheta_c$, whereas the superhydrophobic state is adopted if $\vartheta_Y > \vartheta_c$. Because $r > 1 > \phi^S$, the critical Young angle is necessarily greater than 90°. This prediction is in gross contrast to the recently discovered phenomenon of superoleophobicity [126], where the superhydrophobic state is observed with $\vartheta_Y < 90°$.

Figure 2.7: **Touchdown scenario.** The liquid-gas interfaces are assumed to collapses when they touch the floor of the texture.

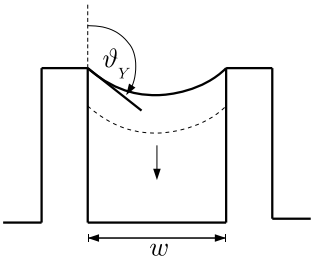

Figure 2.8: **Depinning scenario.** The interfaces are assumed to depin when their angle with respect to the vertical wall exceeds Young's angle.

Alternative arguments recognize the metastability [50, 119, 57, 106, 44, 92] of the superhydrophobic state. For an irreversible transition from the superhydrophobic state to the impregnated state due to a decrease of the drop size [106] or an increase of the pressure inside the drop [57, 105, 18], a 'touchdown' condition of the liquid-gas interfaces at the floor of the texture was suggested [9, 106], as well as a depinning condition at the ridge of the texture [106]. Both conditions recognize that the liquid-gas interfaces spanning between adjacent ridges of the texture are curved. For a drop that is smaller than the capillary length, the curvature of the liquid-gas interfaces is equal to the global curvature of the sessile drop, giving right to Laplace's law. For a drop under the influence of an additional applied pressure, the curvature κ of the liquid-gas interfaces is determined by evaluating Laplace's law locally.

The 'touchdown' scenario (Fig. 2.7) then suggests that liquid-gas interfaces collapse when they touch the floor of the texture. The touchdown condition depends on the particular geometry of the surface profile. For rectangular grooves of width w and depth h, touchdown is expected at a pressure drop ΔP over the interface expressed as

$$\Delta P = \frac{2\sigma h}{h^2 + (w/2)^2}. \tag{2.26}$$

Sufficiently deep grooves prevent touch down at the floor of the texture. In such a case, collapse of the superhydrophobic state due to depinning of the microscopic contact lines was suggested [106].

The 'depinning' scenario assumes that the contact angle at the sharp edges of the texture is limited by Young's angle (Fig. 2.8). It postulates that the liquid-gas interfaces can adopt any angle larger than the Young angle with respect to the horizontal surface and smaller than the Young angle with respect to the vertical

walls of the texture. A depinning condition is formulated by recognizing that the liquid-gas interfaces translate downwards on the walls of the texture if the angle of the interfaces with respect to the vertical walls exceeds Young's angle. In case of rectangular grooves, the collapse condition yields a critical pressure drop across the liquid-gas interface

$$\Delta P = \frac{\sigma \cos \vartheta}{w/2}. \tag{2.27}$$

The competing models highlight the difficulties in evaluating a condition for the transition between the superhydrophobic and the impregnated state, or more generally, in describing which state a drop will adopt on a given superhydrophobic surfaces. Besides, experimental studies of the microscopic features of superhydrophobic surfaces have remained elusive. Experiments have been limited by the resolution of optical microscopy [80]. They have been invasive [52] (Atomic Force Microscopy), or even destructive [54] (cross sections through solidified polymer drops measured with electron microscopy). Experimentally measured critical pressures and drop sizes fell short off the predicted ones [57] or did not provide enough resolution to distinguish between competing models [106].

We will present an experimental study of the transition from the superhydrophobic to the impregnated state in Chapter 3.

2.2.2 Contact angle models on heterogeneous surfaces

In recent articles published in major journals [126, 35, 2], several deficiencies of the Cassie-Baxter, Eq. (2.24), and the Wenzel model, Eq. (2.22), have been pointed out, that add to the one pointed out above. Amongst, it was shown that an extension of Cassie's and Baxter's approach to more complex surface patterns leads to a dependence of the contact angle on the particular geometry of the surface pattern, which was not observed in subsequent experiments [35]. Moreover –and maybe more importantly–, a gross contradiction between contact angles predicted by the Cassie-Baxter model and contact angles measured on superhydrophobic surfaces with low surface energy liquids [126] was observed. Furthermore, measured contact angles of water on superhydrophobic surfaces with a connected surface pattern fell behind the prediction of the Cassie-Baxter model [2] (see Chapter 4). Those results cast severe doubts on the Cassie-Baxter model.

In the present section we shall reconsider the Cassie-Baxter model, and point out what is so unphysical about it. We shall analyze it both for superhydrophobic (profiled) surfaces as well as for chemically heterogeneous surfaces, that is, for any surface for which it ought to be valid. We shall argue that instead models that appreciate a *local* contact angle should be used to describe the behavior of a liquid in contact with a superhydrophobic surface. Though local contact angle models of wetting on heterogeneous surfaces are well known in the context of superhydrophobic surfaces, and their fundamental concepts are well established [31, 132], a considerable fraction of the members of that community are still relatively conservative and slow to embrace those views. Many of them keep applying Cassie-Baxter's model, blissfully unaware of the advances of the theoretical understanding on wetting on heterogeneous surfaces.

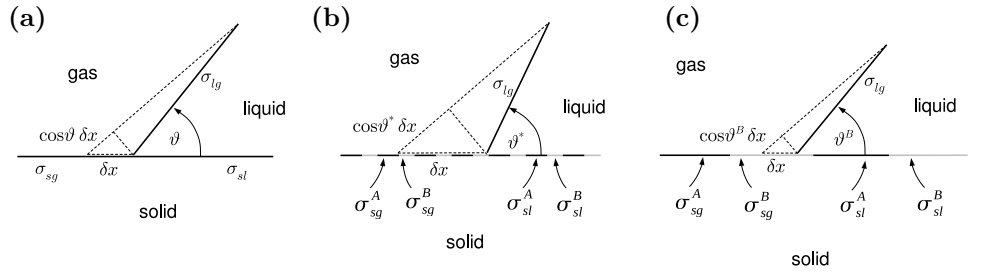

Figure 2.9: **Contact angle models on heterogeneous surfaces. (a)** Young's contact angle for a homogeneous surface. **(b)** Cassie-Baxter model favoring an average surface energy. **(c)** Model favoring a local contact angle.

It is my hope that this section persuades them to give these rigorous approaches at least some consideration. I will return to this subject matter in Chapter 4, where I will outline qualitatively several solutions to such type of models for a drop on a superhydrophobic surface.

It is important to stress that doubts are cast on the *model* of Cassie and Baxter, not a priori on the *equation*, meaning that in many cases –e.g. for water on a common superhydrophobic surface– a more realistic model may, and indeed should predict a contact angle similar to the one obtained from the Cassie-Baxter equation to capture numerous well established experimental results with high energy liquids on common superhydrophobic surfaces.

For an amount of liquid with surface energy σ_{lg} in contact with a flat, homogeneous solid substrate with solid-liquid surface energy σ_{sl} and solid-gas surface energy σ_{sg}, minimization of the potential energy determines the angle that the liquid-gas interface adapts with the solid substrate [132], as illustrated in Sec. 2.1.3. Fig. 2.9(a) illustrates again the energy minimization leading to $\cos\vartheta = (\sigma_{sg} - \sigma_{sl})/\sigma_{lg}$.

For a heterogeneous surface, the Cassie-Baxter model assumes that the liquid 'sees' an effective substrate-liquid and substrate-gas surface energy equal to the *averaged* surface energy of the respective composite surface. In case of a chemically heterogeneous surface that comprises areas of different surface energies σ_{sl}^A, σ_{sg}^A and σ_{sl}^B, σ_{sg}^B, with surface fraction ϕ^A, the mean surface energies of the liquid- and gas-covered substrate are

$$\langle\sigma_{sx}\rangle = \phi^A\sigma_{sx}^A + (1-\phi^A)\sigma_{sx}^B, \quad x = l, g. \tag{2.28}$$

In case of a superhydrophobic surface in the superhydrophobic state with flat liquid-gas interfaces, the mean surface energies are

$$\begin{aligned}\langle\sigma_{sl}\rangle &= \phi^S\sigma_{sl} + (1-\phi^S)\sigma_{lg},\\ \langle\sigma_{sg}\rangle &= \phi^S\sigma_{sg},\end{aligned} \tag{2.29}$$

where ϕ^S is the solid surface fraction. In terms of energy variations at the contact line, this assumes that the translation of the contact line δx is larger than the characteristic scale a of the heterogeneities, e.g., in case of a chemically heterogeneous surface

with a pattern that is periodic in two dimensions with a period a, this assumes that $\delta x > a$. Fig. 2.9(b) illustrates this requirement. In this case the energy variation upon translation of the contact line is approximately

$$\delta E = \left[\phi^A \sigma_{sl}^A + (1-\phi^A)\sigma_{sl}^B - (\phi^A \sigma_{sg}^A + (1-\phi^A)\sigma_{sg}^B) + \sigma_{lg}\cos\vartheta^*\right]\delta x, \tag{2.30}$$

such that the derivation of the contact angle is analogue to the derivation of the Young angle with effective surface energies as given by Eq. (2.28) or Eq. (2.29). In contrast, if $\delta x < a$ (Fig. 2.9(c)) the energy variation upon translation of the contact line is (in the present case, where the contact line is located on a patch with surface energy B)

$$\delta E = \left[\sigma_{sl}^B - \sigma_{sg}^B + \sigma_{lg}\cos\vartheta\right]\delta x. \tag{2.31}$$

Thus, the liquid-gas interface adopts the Young angle of surface B. The former corresponds to the Cassie-Baxter model (Fig. 2.9(b)), favoring an effective surface energy. The latter (Fig. 2.9(c)) corresponds to models as those suggested e.g. by Joanny, de Gennes, Shanahan, Schwartz and Swain and Lipowsky [50, 115, 113, 119], that appreciate a local Young angle.

In case of external perturbations, e.g., due to mechanical vibrations or a motion of the liquid volume due to gravity, the magnitude of δx follows from the detailed nature of the external forcing. We will return to such aspects in Chapter 4. In case of no external perturbations, the magnitude of δx is determined by thermal fluctuations. We consider first a typical microtextured surface and evaluate a lower boundary for the energy ΔE that corresponds to a variation of the contact line over one unit cell of the surface pattern. The energy required to cover one unit cell with liquid is of the order σa^2, where $\sigma = \sigma_{sl} - \sigma_{sg}$ in case of a chemically heterogeneous surface and $\sigma = \sigma_{lg}$ in case of a profiled surface. For a typical patterned surface the period a of the pattern is of the order 1μm. The liquid-gas and solid-liquid surface energies of water are larger than 0.01N/m. Thus $\Delta E > 10^{-14}$J. Energy variations due to thermal fluctuations are of the order $k_B T$. At room temperature $k_B T \approx 10^{-21}$J. Thus $\Delta E > 10^7 k_B T$, such that $\delta x \ll a$. Reverting above argument we estimate the order of magnitude of δx due to thermal fluctuations and find $\delta x = \sqrt{k_B T/\sigma} \approx 10^{-10}$m. The result corresponds to the typical scale of capillary waves or thermal wiggling of liquid molecules as expected, confirming $\delta x \ll a$. Therefore the second model according to Fig. 2.9 and Eq. (2.31) favoring a local contact angle applies to describe the behavior of liquid in contact with the heterogeneous surface.

The first model, the Cassie-Baxter model, favoring an average surface energy, was applicable if $a \ll 10^{-10}$m. Such a surface does not exist in nature since the typical size of atoms is larger than 10^{-10}m. Furthermore, the behavior of a liquid on such scales is governed by other phenomena and is described by microscopic models such as e.g. Lattice-Boltzmann or Molecular Dynamics approaches. It follows that the concept of an average surface energy, and thus the Cassie-Baxter model (and equivalently the Wenzel model), is not physical for *any* realistic heterogeneous surface.

Instead, a local contact angle model similar to the models suggested in [50, 115, 113, 119] should be applied. In such an approach boundary conditions on the substrate are formulated by requiring that the contact angle is *locally* the Young angle

corresponding to the local surface energy of the substrate, or equivalently by specifying areas of different solid-liquid surface energies, and requiring that δE is infinitesimally small (small enough such that corresponding variations δx of the position of the contact line are smaller than the characteristic scale of the heterogeneities).

Such a model has been formulated and addressed analytically for a drop without gravity on a chemically heterogeneous surface with areas with two different contact angles close to 90° and small perturbations of the contact line [50], as well as for general perturbations for chemically heterogeneous and rough surfaces in the Wenzel state [119]. The model has been treated analytically for liquid rise at a hydrophilic vertical plate featuring periodic patterns of hydrophobic areas [113]. Additionally, such a model has been addressed numerically for chemically heterogeneous surfaces with stripes that are of the same scale as the drop size [17] and similar geometries [114].

Swain and Lipowsky [119] offer a general result for the macroscopic apparent contact angle. Using the condition of a local contact angle (e.g. Eq. (4.5) in [119])

$$\sigma_{sg}(\boldsymbol{y}) = \sigma_{sl}(\boldsymbol{y}) + \sigma_{lg}\cos[\vartheta(\boldsymbol{y})], \tag{2.32}$$

the apparent contact angle is approximated as

$$\cos\vartheta^* = \int_{\partial\Gamma} \cos[\vartheta(\boldsymbol{y})]\, d\boldsymbol{y}, \tag{2.33}$$

where the integral extends over the contact line $\partial\Gamma$ that encloses the area Γ where the drop is in contact with the surface. Here σ_{sg} and σ_{sl} are the local surface tensions, ϑ is the local contact angle and $\boldsymbol{y}$ is the Cartesian coordinate on the surface. For a given contact line and surface pattern (expressed by the local contact angle $\vartheta(\boldsymbol{y})$, the result allows to evaluate an approximate value for a macroscopic apparent contact angle. However, the authors stress that the contact line $\partial\Gamma$ is not *a priori* known and is generally *not* described by a global energy minimization. They highlight the role of metastable drop conformations for the macroscopic apparent contact angle. For the case of chemically heterogeneous surfaces as well as for rough surfaces in the Wenzel state, Swain and Lipowsky offer several possible alternatives for a choice of the contact line. Amongst, they suppose to consider the evolution of the contact line during the motion of a drop on a surface, as well as 'placing' a drop on different positions of the surface and evaluating a corresponding local minimum of the free energy that will yield the contact line. They suggest to assign to each such contact line equal a priori probability. However, the authors judge the latter approaches 'prohibitively difficult'. A first approximation is provided by assuming that the contact line adopts all possible orientations on the surface, and those orientations occur with equal probability. In this case the macroscopic apparent contact angle is expressed as

$$\cos\vartheta^* = \sum_n L_n \cos\vartheta_n, \tag{2.34}$$

where L_n is the fraction of the total perimeter of the drop in contact with the surface composed of material n with contact angle ϑ_n. However, this assumptions cannot

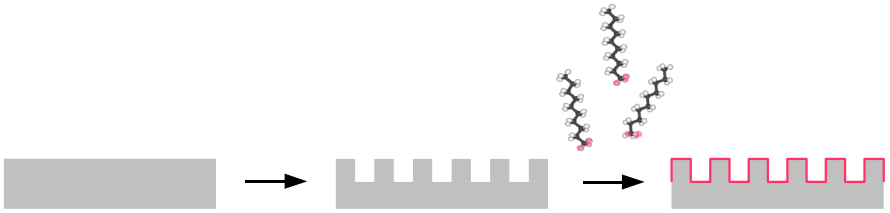

Figure 2.10: **Fabrication method for artificial superhydrophobic surfaces.** A silicon wafer is structured using micro lithography and deep reactive ion etching. Subsequently the structured surface is hydrophobized by vapor deposition of a self assembled monolayer of an alkylsilane.

be justified. In principle one of the first two alternatives suggested by the authors should be used to determine the actual position of the contact line. Those approaches correspond to a more realistic averaging over drop configurations observed in practice. Eq. (2.34) is mainly criticized because it does not account for metastable drop states and pinning of the contact line, which is relevant on profiled surfaces. Those aspects underline the difficulties in developing a realistic and physical contact angle model for heterogeneous surfaces.

Chapter 4 is devoted to discussing qualitatively the main features of several possible drop conformations on different types of superhydrophobic surfaces. In that chapter we will also pay more attention to the role of metastable drop states and possible choices of drop states that could be suitable for an evaluation of an apparent contact angle.

2.2.3 Artificial superhydrophobic surfaces

Since the first demonstration of an artificial superhydrophobic surface in the mid 90's [88], research groups around the globe have joined the quest for a cheap, durable, transparent, and possibly flexible superhydrophobic surface that competes with the remarkably successful superhydrophobic surfaces exemplified by nature.

Though artificial superhydrophobic surfaces arguable still lack behind the natural ones, in particular with regard to durability –or more generally 'regenerability'– today, superhydrophobic surface are routinely fabricated in research laboratories, and a large variety of fabrication processes has been successfully implemented [99, 65]. Typically one starts off by creating a structured surface, frequently through micro lithography, laser milling [49], deposition of nano-particles such as carbon nano tubes [52], micro-molding [96], etc.. Subsequently the structured surface is hydrophobized, typically by grafting a self assembled monolayer of an alkylsilane (possibly fluorinated) that binds covalently to the surface [72] (see also appendix C). Other commonly used hydrophobization methods include thiol-on-gold monolayers [6] and dip coating with amorphous Teflon. Alternative fabrication methods include the direct molding of the texture into a polymer such as PDMS or photo resist. Another very successful method has been to create 'fractal' [88] or simply disordered [126] 'fiber-mat-like'

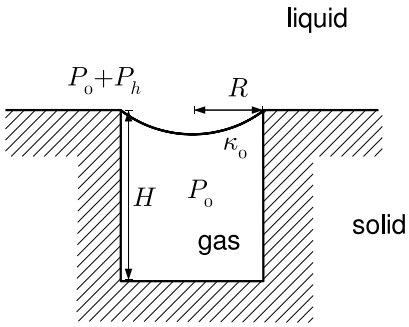

Figure 2.11: **Schematic of a single meniscus at the opening of a superhydrophobic cavity.** The cavity has a cylindrical shape with radius R and depth H. The gas pressure inside the cavity and above the liquid is the ambient pressure, such that –in virtue of Laplace's law– the rest curvature of the liquid-gas interface is given by $\kappa_0 = P_h/\sigma$.

surfaces from a suitable intrinsically hydrophobic material.

Throughout this work, silicon type superhydrophobic surfaces are used, that were layed out with 365 nm (I-line) lithography and etched through different variants of deep reactive ion etching (DRI), and hydrophobized by deposition of a self assembled fluorinated alkylsilane from the vapor phase (Fig. 2.10) (see also appendix C). The latter results in a molecular layer that is typically 1.5-1.6 nm thin (as determined by ellipsometry assuming the bulk refractive index of the alkylsilane) and results in advancing and receeding contact angles on the flat substrate in the range 110 to 120° respectively 100 to 106°, depending on the level of cleanliness of the initial sample.

2.3 Stokesian dynamics of cavity-meniscus systems

We shall now consider the dynamics of a liquid-gas interface that is pinned at the opening of a cylindrical gas-filled cavity. The system that we consider is shown schematically in Fig. 2.11. It consists of a circular cavity of radius R and depth H at the boundary between an unbounded flat solid and an unbounded liquid. The cavity is filled with gas, and a liquid-gas interface spans across its opening. The gas pressure inside the cavity and above the liquid is P_0, such that, in virtue of Laplace's law Eq. (2.3), at rest the interface is curved downwards with a curvature $\kappa_0 = P_h/\sigma$, where P_h is the hydrostatic pressure and σ is the surface tension. Under the influence of an applied ultrasound field the liquid-gas interface undergoes oscillations around it rest position. We aim for determining the frequency response of the system. First we evaluate in the following subsection a simple estimate for the resonance frequency of the system. Subsequently, in subsection 2.3.2, we outline a description of the system through unsteady Stokes flow theory.

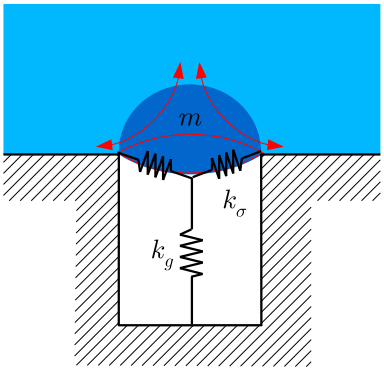

Figure 2.12: **Qualitative model of a cavity-meniscus system.** The vibrating meniscus is considered as a harmonic oscillator with a mass of the order ρR^3 and a spring constant $k = P_0 R^2/H + \sigma$ due to the isothermal compression of gas and the restoring force of surface tension.

2.3.1 A simple model for the resonance behavior

Fig. 2.12 illustrates a simple model. We assume the interface performs small amplitude oscillations around a rest position which we take as the flat interface $z = 0$. Considering Laplace's law, we assume that the curvature of the deflected interface is constant, such that it takes the shape of a spherical cap. Hence, the deflection z and the radius of curvature are related as

$$\kappa = \frac{4z}{z^2 + R^2} \approx 4z/R^2 \quad \text{for} \quad z \ll R. \tag{2.35}$$

We consider the potential energy and mass of the system. Considering isothermal compression of the gas, we write the pressure change due to gas compression as

$$\Delta P_G \approx \frac{P_0 z}{2H}. \tag{2.36}$$

In virtue of Laplace's law (Eq. (2.3)), we express the pressure change due to surface tension as

$$\Delta P_L = \sigma\kappa \approx \frac{4\sigma z}{R^2}. \tag{2.37}$$

Considering the force on the interface in the form of a harmonic force with spring constant K

$$F = Kz, \tag{2.38}$$

and the relation between force and pressure $F \approx P/R^2$, we evaluate the spring constant as

$$K = \frac{P_0}{2H} + 4\sigma. \tag{2.39}$$

Appreciating that flow fields are decayed on a scale R, we estimate the effective mass of the system as

$$M = \rho R^3. \tag{2.40}$$

The resonance frequency of the system follows as

$$f = \frac{1}{2\pi}\sqrt{\frac{K}{M}} = \frac{1}{2\pi}\sqrt{\frac{1}{\rho R^3}\left(\frac{P_0 z}{H} + 4\sigma\right)}. \tag{2.41}$$

This model is suitable to determine the order of magnitude of the resonance frequency. Several aspects about the model can be refined.

(1) The effect of inertia can be described in a quantitative manner. To this end, the hydrodynamic equations can be solved on different levels of approximation. We will discuss this in detail in the next section. In the simplest approximation, potential flow equations are considered, where one recognizes that the vorticity in the flow field $\boldsymbol{\nabla} \times \boldsymbol{v}$ vanishes everywhere except in a thin *boundary layer* around the moving body. Stressing $\boldsymbol{\nabla} \times \boldsymbol{v} = 0$, one expresses the velocity field in as the gradient of a scalar called *velocity potential* $\boldsymbol{v} = \boldsymbol{\nabla}\phi$. We shall demonstrate experimentally in Chapter 6 and 7 that potential flow theory is sufficient to capture inertial effects in the oscillating cavity-meniscus system.

(2) One may consider *dissipation* in the system. Dissipation is absent in above simple model. In potential flow theory, which considers *ideal* non-viscous fluids, dissipation may be incorporated in terms of *dissipation integrals* [51] that evaluate the bulk dissipation in an approximate manner from the flow fields calculated in the non-viscous approximation. This approximation has been applied to describe e.g. the viscous dissipation of oscillating bubbles. We will show experimentally in Chapter 7, that for the oscillating cavity-meniscus system, dissipation is *not* captured by potential flow in conjunction with dissipation integrals. The theoretical analysis presented in Chapter 8 shows that dissipation is dominated by vorticity generation in the boundary layer. Thus, to capture viscous dissipation in the fluid, the hydrodynamic equations must be approximated on the level of the unsteady Stokes flow equations that account for the viscosity of the fluid. Such a description is outlined in the subsequent section and described in detail in Chapter 8.

It is shown experimentally in Chapter 6 and 7 that the oscillating cavity-meniscus system is described accurately within the approximation of this unsteady Stokes flow model. The following possible refinements of the model are beyond experimental accuracy. We note them to provide a complete discussion.

(3) one may consider *thermal dissipation* inside the gas, which was shown to be significant for bubbles in a certain parameter range in [21]. Here one may follow the linear analysis suggested in [22].

(4) one may refine the description of the *potential force*. At high frequencies one may consider an alternative compression behavior of the gas, such as *adiabatic* compression.

(5) one may account for deviations of the liquid-gas interface from the spherical cap shape and account for Laplace's law locally. Such a model would account for higher order deformation modes of the liquid-gas interface.

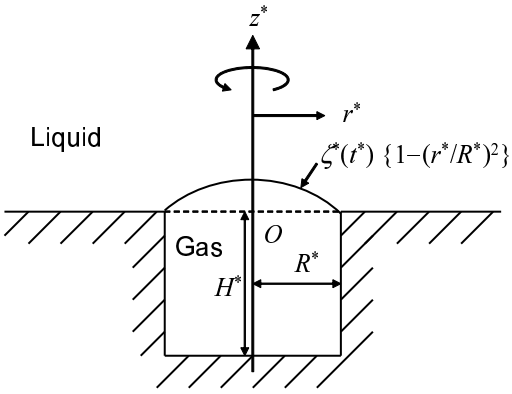

Figure 2.13: **Schematic of the theoretical model for a single cavity-meniscus system** Dimensional quantities such as the radius R^* and depth H^* of the cavity are denoted with a $*$. The interface is pinned at the edge of the cavity, and undergoes small amplitude parabolic deformations.

2.3.2 Stokes flow theory of an oscillating cavity-meniscus system

We shall now outline an unsteady Stokes flow model for a cavity-meniscus system (a detailed derivation is given in Chapter 8). Fig. 2.13 shows a schematic of the theoretical model. Dimensional quantities such as the radius R^* and depth H^* of the cavity are denoted with a $*$. The following approximations are introduced.

(1) we assume the meniscus is flat in equilibrium. This condition is satisfied when the deflection at rest is much smaller than the deflection amplitude and the radius of the cavity, $|\zeta_0^*| \ll R^*, \Delta\zeta^*$.

(2) we assume that the acoustic field is a function of time alone, expressed as $P^* = P_0^* + \Delta P^* \exp(\omega^* t^*)$, corresponding to a global pressure change. This requires that the ultrasound wavelength Λ^* is much larger than the system size $R^* \ll \Lambda^*$.

(3) We assume that the interface is pinned at the edge of the cavity, and undergoes small amplitude parabolic deformations

$$\zeta^*(t^*)(1 - r^{*2}/R^{*2}), \tag{2.42}$$

where $\zeta^*(t^*)$ is the deflection of the interface on the axis $r^* = 0$ and r^* is the radial coordinate. This assumption has been employed in [73]. In an experiment it requires that $|\zeta^*| \ll R^*$ and $|\zeta^*| \ll H^*$. As shown below, the parabolic shape implies that the curvature of the interface is approximately uniform, as far as $|\zeta^*| \ll R^*$, giving right to Laplace's law. It should be noted that the 'imposed shape' cannot be strictly verified. In a more realistic case, the local deformation of the interface should be taken into account, and Laplace's law should be applied locally at every point of the interface. Instead, we impose the shape of the interface. The parabolic shape implies that the interface oscillates with its fundamental oscillation mode. This approximation

should describe the behavior of the system for small ultrasound frequencies and up to the fundamental resonance frequency. At much higher frequencies, the interface may deform following other shapes, corresponding to higher order oscillation modes, as known e.g. from oscillation modes of a circular plate. Such oscillations are not included in the present model.

(4) We assume that far away from the meniscus the flow vanishes. We consider three cases for the boundary conditions. (i) no-slip on both the liquid-gas interface and the solid wall, (ii) free-slip on both the liquid-gas interface and the solid wall, (iii) free-slip on the liquid-gas interface and no-slip on the solid wall

(5) Considering discussions in [60] we assume the system is described by the unsteady Stokes flow equation

$$\begin{aligned} \nabla \boldsymbol{u} &= 0, \\ \partial_t \boldsymbol{u} &= -\frac{1}{\rho_L}\nabla p + \nu \nabla^2 \boldsymbol{u} \end{aligned} \tag{2.43}$$

For this approximation we consider the *Navier–Stokes* equation

$$\partial_t \boldsymbol{u} + (\boldsymbol{u}\cdot\boldsymbol{\nabla})\boldsymbol{u} = -\frac{1}{\rho}\boldsymbol{\nabla} p + \nu\Delta\boldsymbol{u} + (\zeta/\rho + \nu/3)\boldsymbol{\nabla}(\boldsymbol{\nabla}\cdot\boldsymbol{u}), \tag{2.44}$$

where $\boldsymbol{u}$ is the velocity field, ρ is the liquid density, p is the pressure, $\nu = \eta/\rho$ is the kinematic viscosity and ζ is the second viscosity. Assuming incompressible flow, we have $\boldsymbol{\nabla}\cdot\boldsymbol{u} = 0$, such that

$$\partial_t \boldsymbol{u} + (\boldsymbol{u}\cdot\boldsymbol{\nabla})\boldsymbol{u} = -\frac{1}{\rho}\boldsymbol{\nabla} p + \nu\Delta\boldsymbol{u}. \tag{2.45}$$

We appreciate that the oscillating motion of a solid body in a liquid generates vorticity in a layer of a characteristic thickness $\delta = \sqrt{2\nu/\omega}$, while at larger distances the flow decays to potential flow. Here ν is the kinematic viscosity and ω is the oscillation frequency. Let l be the size of the body and a be the amplitude of the oscillations. If $l \gg \delta$ and $a \ll \delta$, the time derivative and $(\boldsymbol{u}\cdot\boldsymbol{\nabla})\boldsymbol{u}$ term in the Navier-Stokes equation are of the order $|\partial_t \boldsymbol{u}| \approx u\omega \approx a\omega^2$ and $|(\boldsymbol{u}\cdot\boldsymbol{\nabla})\boldsymbol{u}| \approx u^2/l \approx a^2\omega^2/l$, such that the $(\boldsymbol{u}\cdot\boldsymbol{\nabla})\boldsymbol{u}$ term can be neglected.

We non-dimensionalize all quantities using the radius of the groove R^*, the liquid density ρ_L^*, and the kinematic viscosity ν^*, i.e.,

$$\begin{aligned} H = \frac{H^*}{R^*}, \quad r = \frac{r^*}{R^*}, \quad z = \frac{z^*}{R^*}, \quad \zeta = \frac{\zeta^*}{R^*}, \\ \omega = \frac{\omega^* R^{*2}}{\nu^*}, \quad p = \frac{p^* R^{*2}}{\rho_L^* \nu^*}, \quad \Delta = \frac{\Delta^* R^{*2}}{\rho_L^* \nu^*}, \quad \boldsymbol{u} = \frac{\boldsymbol{u}^* R^*}{\nu^*}, \\ \sigma = \frac{\sigma^* R^*}{\rho_L^* \nu^{*2}}, \quad \kappa = \kappa^* R^*, \end{aligned} \tag{2.46}$$

Stressing the axial symmetry of the system, separation of variables and suitable stream functions are used to cast the system into the form of a Helmholtz and Laplace

equation (see Chapter 8 for details). Those equations are solved. The solutions allow to determine the surface averaged normal stress on the liquid gas interface in terms of transfer functions Φ, Ψ as

$$\langle -p + 2\partial_z u_z \rangle = (\Phi(\omega) + i\Psi(\omega))\zeta, \tag{2.47}$$

allowing to express the total normal stress of liquid on the interface as

$$P_L = P_0 + \Delta \exp(i\omega t) - \langle -p + 2\partial_z u_z \rangle_S \exp(i\omega t). \tag{2.48}$$

An evaluation of the transfer functions Φ and Ψ for the different combinations of boundary conditions for the solid wall and the liquid-gas interface is given in Chapter 8.

Assuming isothermal compression of the gas inside the cavity, the gas pressure is written as

$$P_G = P_0 - \frac{P_0}{2H}\zeta \exp(i\omega t) + O((\zeta/H)^2). \tag{2.49}$$

Both pressures are linked through Laplace's law (Eq. (2.3)) as

$$P_G - P_L = \sigma\kappa. \tag{2.50}$$

The imposed shape of the interface determines the curvature as (using Eq. (2.6))

$$\kappa = \nabla \cdot \left(\frac{\nabla(z - \zeta(1 - r^2))}{|\nabla(z - \zeta(1 - r^2))|} \right) = 4\zeta + O(\zeta^3). \tag{2.51}$$

Here it is shown that the curvature of the assumed parabolic shape is uniform as long as ζ is small. Combining Eq. (2.48), (2.49), (2.50), and (2.51) we arrive at a relation between the displacement and the driving amplitude

$$(-\Phi(\omega) - i\Psi(\omega) + K)\zeta = -\Delta, \tag{2.52}$$

that describes the frequency response of the system. Here K represents the rigidity given by

$$K = \frac{P_0}{2H} + 4\sigma, \tag{2.53}$$

which is equivalent to the spring constant of a spring-mass system as evaluated in the preceding section (Eq. (2.39)). Eq. (2.52) is considered as the equation of motion of a cavity-meniscus system.

2.3.3 Hydrodynamic interaction

A technique that is suitable to study experimentally the dynamics of a cavity-meniscus system is optical diffraction (Chapter 6). In this case a large number of cavities (typically > 1000) are fabricated on a periodic grid with a lattice spacing a that is larger but not much larger than the cavity radius. Fig. 2.14(a) shows schematically such a system. The sample is then illuminated with a laser beam under a grazing

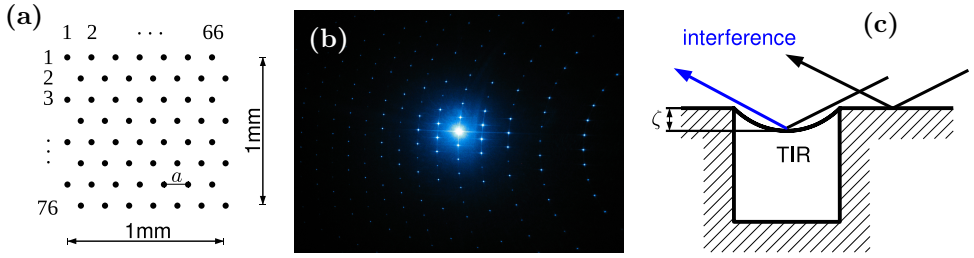

Figure 2.14: **Observation of meniscus oscillations through optical diffraction.** **(a)** Schematic of a typical experimental sample consisting of cylindrical cavities ($R = 3\mu$m) arranged on a 1×1mm hexagonal grid with lattice constant $a = 15\mu$m. **(b)** Diffraction pattern of the sample obtained by illumination with laser light (wavelength 488 nm) under grazing angle ($\vartheta \approx 70°$). **(c)** Interference phenomenon providing a relation between meniscus deflection and diffraction intensity.

incident angle and the intensity of one diffraction order is measured. The intensity is determined by the interference of waves scattered from the plain surface and waves scattered from the menisci and depends sensitively on the meniscus deflection, as illustrated in Fig. 2.14(c) (see Chapter 6 for details).

This measurement technique has several implications. First, since diffraction requires *identical* objects, all menisci must be deflected *collectively* with the same amplitude (see also appendix B), implying that the ultrasound wavelength Λ must be larger than the size l of the entire grid. Second, to obtain a good diffraction signal, the distance between the cavities should not be much larger than their diameter. This implies that the oscillating cavity-meniscus systems are no longer described as isolated systems that are surrounded by an infinite solid surface, rather they interact. Both conditions amplify each other: if the distance between the cavities is increased, the resonance frequency of the system shifts to higher frequencies, implying a shorter wavelength of the driving ultrasound. At the same time, the total system size is increased. In this way $\Lambda < l$ is quickly reached. In practice, the weak $1/r$-decay of the hydrodynamic interaction (see below) prohibits a measurement in the uncoupled limit with typical arrays consisting of ≈ 1000 micron sized cavities.

It is shown experimentally in Chapter 6 that the hydrodynamic interaction has a strong influence on the resonance behavior of the system. Fig. 2.15 illustrates the mechanism. It is at first sight counter intuitive. Following the simple model for the resonance behavior derived in Sec. 2.3.1, one may expect that the spring constant of a corresponding collective harmonic oscillator is about Nk and its mass is Nm, where k and m are the spring constant, respectively mass of an individual oscillator. This holds true for the spring constant, which is indeed determined by the local forces on each meniscus. However, the effective mass of the coupled system is not additive. In terms of scaling arguments for the decay of the flow fields, we recognize that a global flow field arises that extends over the entire meniscus system. The total mass M is estimated as $\rho N R^3 < M < \rho l^3$, suggesting that the effective mass of an individual

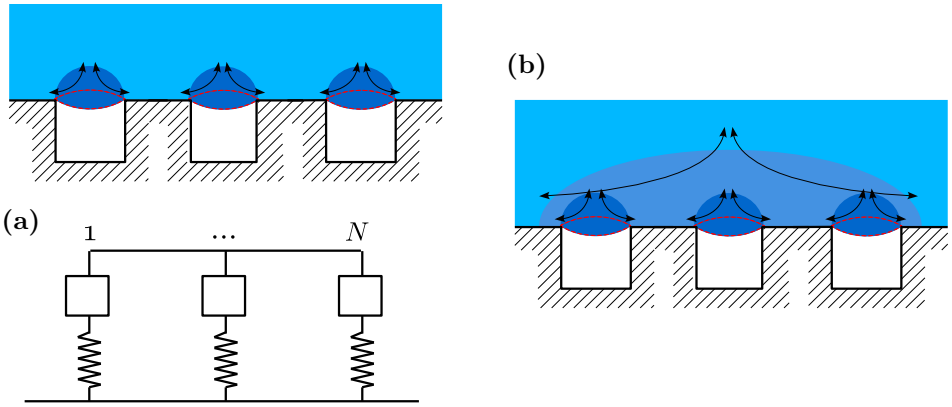

Figure 2.15: **Collective oscillations of multiple cavity-meniscus systems. (a)** A model that describes the system as N oscillators with a total spring constant $K = Nk$ and mass $M = Nm$ fails to capture the collective dynamics of the system. **(b)** A collective oscillation gives rise to a global flow field that results in an increased effective mass.

cavity meniscus system is increased, such that the resonance frequency is decreased. Therefore, it becomes necessary to account for hydrodynamic interaction.

We shall now derive the interactive force among multiple menisci. We consider two menisci labeled i and j and separated by a distance d_{ij}. Assuming $d_{ij} \gg R$, the surface averaged normal stress on the j-th interface due to the i-th interfacial motion is approximated as (see Chapter 8 for details)

$$\langle -p_i + 2\partial_z u_{zi} \rangle_{S_j} = \frac{\zeta_i \omega^2}{4 d_{ij}} + o(d_{ij}^{-1}). \tag{2.54}$$

We thus extend the equation of motion of a single cavity-meniscus system, Eq. (2.52), as

$$(-\Phi(\omega) - i\Psi(\omega) + K)\zeta_i = -\Delta + \sum_{i \neq j} \frac{\omega^2 \zeta_j}{4 d_{ij}}, \tag{2.55}$$

of which the second term on the right hand side accounts for the effect from the other menisci. The interaction is monopole, which is similar to that for the spherical bubbles suspended in liquid. Note that since this term contains ω^2, it leads to the increase of the virtual mass. For the multiple body problem, we write the simultaneous equations Eq. (2.55) in a matrix form with complex numbers, and numerically solve them to determine the deflections ζ_i. If the number of menisci is N, the size of the matrix to be inverted is $N \times N$.

It is shown experimentally in Chapter 6 that Eq. (2.55) accurately describes the resonance frequency of arrays of menisci. In some of the experiments the nearest neighbor distance between the cavities is of the same order as the cavity diameter. Those experiments correspond to a limiting case of the monopole approximation,

where the validity of $d_{ij} \gg R$ is not strict. Within the measurement accuracy, also these systems are well described by the model.

Finally, it should be pointed out that for the multi-meniscus system, the experimentally observed dissipation is *not* captured by the model (see peak heights in Fig. 6.4). By contrast, Fig. 7.4 shows that the Stokes flow theory for a single cavity captures dissipation correctly. Considering that above model for the hydrodynamic interaction does not describe explicitly the global flow field, we suggest that it misses a viscous dissipation in the global flow.

2.4 Optical diffraction gratings

Diffraction experiments are suitable to study *identical* objects that are arranged in a *periodic* manner. The most well known example is the determination of crystallographic structures through x-ray diffraction. In this work we employ optical diffraction from a superhydrophobic optical grating (see also Fig. 1.2) to study the microscopic properties of superhydrophobic surfaces (Chapters 3 and 6). To extract accurate real space information from the measured diffraction intensities, a precise modeling of the diffraction process becomes necessary. In this section we introduce the required theory of optical grating diffraction and formulate the numerical tools that are suitable to model such gratings.

Later we use these numerical tools to devise optical gratings with a large spectral bandwidth (Chapter 5). We will therefore also pay attention on the principles of optical grating design.

The section is organized as follows. In the following subsection we introduce elements of optical grating diffraction, and derive basic quantities that characterize a diffraction process, such as the directions of the diffracted waves and the dispersion. Subsequently, in subsection 2.4.2 we outline how the *intensity* of the diffracted waves can be calculated through an exact numerical treatment of Maxwell's equations.

2.4.1 Grating diffraction

Fig. 2.16 shows schematically an optical grating. It consist of a grating region G characterized by a periodically varying refractive index $n^G(y,z) = n^G(y+T,z)$ that is located at the boundary between two infinite halfspaces, the reflection region R and a transmission region T, that are characterized each by their refractive index n^R, respectively n^T. Generally, all refractive indices may be complex, with the exception of the reflection region, which must necessarily be transparent and characterized by a real refractive index.

As the grating is illuminated with a plane wave, a number of plain waves are scattered from the grating. Waves are scattered into the reflection region, and into the transmission region. Associated with every scattered wave is an amplitude and a wavevector. The wavevector expresses the direction of the wave, or, in case the wavevector is complex, the penetration depth of the evanescent wave. The components of the wavevectors in the periodic direction (here the y-components) are determined

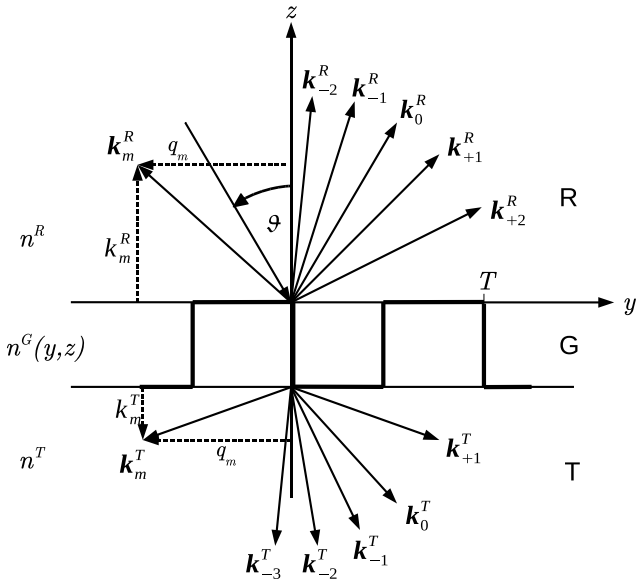

Figure 2.16: **Diffraction of a plane wave by an optical grating.** A number of diffracted waves with wavevectors k_m^S, $S = R, T$ are scattered into the reflection and transmission region, characterized each by their refractive index n^R and n^T, respectively.

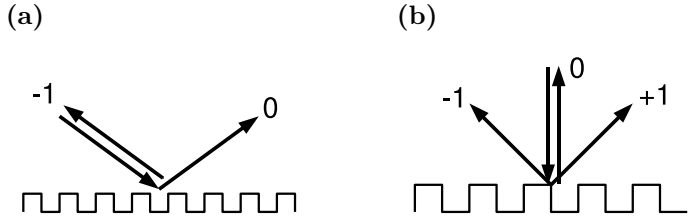

Figure 2.17: **Illustration of the Littrow configuration. (a)** -1^{st} order Littrow configuration. The grating period and the incident angle are chosen such that the -1^{st} diffraction order is anti-parallel to the incident beam. The groove width and depth are optimized such that nearly all of the diffracted intensity is scattered into the -1^{st} order. **(b)** Beam splitter configuration. The grating is illuminated perpendicular to the surface. Due to symmetry equal intensity is scattered into the $+1^{st}$ and -1^{st} diffraction order.

by Floquet's theorem as

$$q_m = q_0 + mQ, \tag{2.56}$$

where $m = -\infty, \ldots, +\infty$ is the diffraction order, $Q = \lambda/T$, and $q_0 = n^R \sin\vartheta_0$. Here ϑ_0 is the angle of the 0^{th} diffraction order. Angles are measured with a positive sign in positive y-direction, and with a negative sign in negative y-direction. We have non-dimensionalized the spatial coordinate through $r \mapsto 2\pi r/\lambda$. The z-components of the wavevectors are determined through the wave equation as

$$k_m^S = ({n^S}^2 - {q_m^S}^2)^{1/2}, \tag{2.57}$$

where $S = R, T$ denotes the reflection and transmission region, respectively. A real k represents a propagating diffraction order, a complex k represents an evanescent wave. The latter relations imply the grating equation

$$\sin\vartheta_m^S = \sin\vartheta_0^S + \frac{m\lambda}{n^S T}, \tag{2.58}$$

which expresses the angles of the scattered waves. The angular dispersion D follows by differentiating the latter equation with respect to λ,

$$D = \frac{\partial\vartheta_m^R}{\partial\lambda} = -\frac{m}{Tn^R\cos\vartheta_m^R}. \tag{2.59}$$

Generally, the highest diffraction efficiency is achieved if the grating is mounted in -1^{st} order Littrow configuration, where the -1^{st} diffraction order is anti parallel to the incident wave, that is $-q_{-1} = q_0$ (Fig. 2.17(a)). To see the benefit of this consider the opposite case: Suppose a reflection type grating with rectangular profile is illuminated at zero incident angle, that is, perpendicular to the surface. And suppose the period is small enough, such that only the $+1^{st}$ and the -1^{st} diffraction order are present (Fig. 2.17(b)). It is possible to choose a suitable width and depth of the grating grooves, such that the largest part of the diffracted intensity is scattered into the 0^{th} order, or, by choosing a different width and depth, most of the diffracted intensity is scattered into the first order (see e.g. [23] and 5). However, due to symmetry, the intensity of the $+1^{st}$ and the -1^{st} diffraction order must be equal, such that, at maximum 50% of the diffracted intensity is scattered into a single diffraction order [1]. In contrast, if the incident angle is chosen such that the -1^{st} diffraction order is anti parallel to the 0^{th} order, only the 0^{th} and the -1^{st} order are present, and the scattered intensity can be distributed at will among those two orders (by choosing a suitable groove width and depth), thus (nearly) 100% diffraction efficiency can be achieved. It should be noted that above argument holds rigorously only when the grating profile is symmetric. In Chapter 5 we give an example of a non-symmetric grating profile for which the Littrow configuration is indeed no longer the optimum scattering geometry. For a grating with a symmetric profile, the Littrow configuration

[1] This configuration is of interest for special applications, and is also known as the 'beam splitter configuration'.

is however the configuration that provides the largest diffraction efficiency in a single diffraction order, and this shall be the focus in this thesis.

The Littrow configuration settles the period of the grating as

$$T = m\lambda/(2n^R \sin \vartheta_0^R). \tag{2.60}$$

This settles as well the relation between the angular dispersion and the incident angle, since the Littrow condition substituted in Eq. (2.59) yields

$$D = 2/\lambda \tan \vartheta_0. \tag{2.61}$$

The dispersion is minimal at zero angle (perpendicular to the surface), and diverges at grazing angles.

Above identities determine the period, dispersion and scattering geometry of the grating. They are the starting point e.g. when aiming at the design of an optical grating that provides a given dispersion in a given wavelength range. However, the intensities of the diffracted waves must follow from a more elaborate treatment.

2.4.2 Rigorous Coupled Wave Analysis

Numerous methods have been developed over the past decades that solve Maxwell's equations in their time-dependent (e.g. Finite Difference Time Domain Method [120]), integral (e.g. the Generalized Source Method [122]) or differential form (e.g. Fourier Modal Method [64, 125]). One method that is well suited to compute the diffraction from an optical grating, as in the present case, is the Rigorous Coupled Wave Analysis (RCWA) [74, 75, 76, 39, 77, 93].

The RCWA was originally developed to characterize classical blazed gratings [77], and has been employed successfully to design highest quality optical gratings, as diverse as UV gratings in space telescopes [27], and highly efficient dielectric transmission gratings for chirped pulse amplification [26]. Besides, more recently its usefulness for solving the inverse diffraction problem of optical gratings has been demonstrated [83]. The demand for novel wafer inspection technologies for fast in-line process control in semiconductor fabrication, has triggered extensive research that aims at using the RCWA for the inversion of diffraction patterns in single shot, sub wavelength resolution, optical wafer inspection [107]. In this thesis, we apply the RCWA in both ways. In Chapter 3, we use it to solve an inverse diffraction type problem, and in Chapter 5, we apply it to devise a new class of large bandwidth highly efficient optical gratings.

The RCWA allows for calculating an exact solution to the Maxwell equations, for the diffraction of a plane wave from an optical grating whose unit cell contains arbitrary shapes and materials. In the following we will sketch the fundamentals of the method. A complete treatment (for the case of isotropic media and non-conical mount) and a sketch of the numerical implementation used in this work is given in appendix A. To describe an arbitrary surface profile, a grating is sliced into layers parallel to the surface. Fig.2.18 illustrates this process for a grating that features curved liquid-gas interfaces on top of its groove as encountered in Chapter 3. The

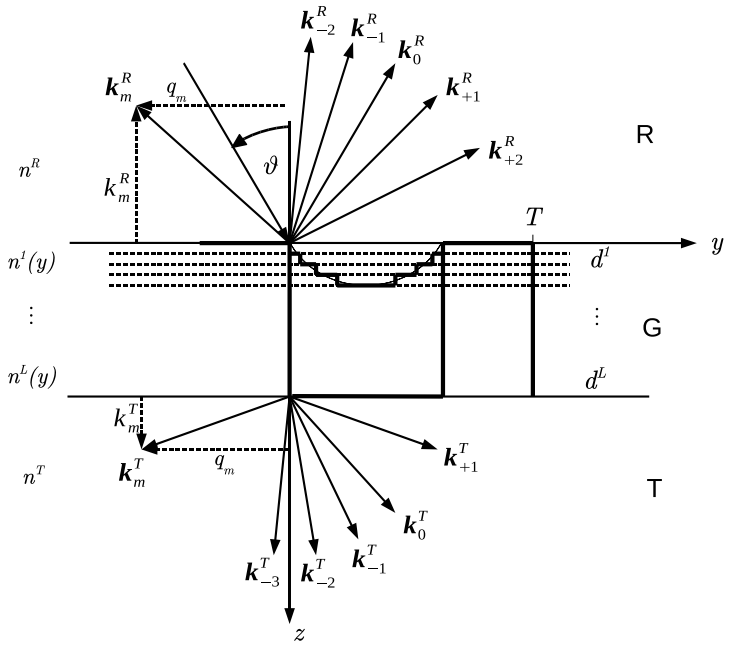

Figure 2.18: **Multilayer Rigorous Coupled Wave Analysis.** Space is divided into three regions. The reflection side with refractive index n^R, the transmission side with refractive index n^T, and the grating region. The grating itself is sliced into N layers parallel to the surface. The curved interface is approximated by layers with a thickness much smaller than the wavelength, such that in each layer, the refractive index $n^i(y) = n^i(y + T)$ is a function of y alone.

curved interface is approximated by layers with a thickness much smaller than the wavelength, such that in each layer, the refractive index is a function of y alone. The grating is thus represented by a stack of layers with periodic, generally complex refractive index $n^i(y) = n^i(y+T)$, $i = 1, \ldots, N$. The reflection and transmission region are characterized by their refractive indices n^R and n^T in the same manner as introduced above.

For the purpose of this outline, let us assume the incident light is s-polarized, and all media are isotropic. Then only the x-component of the electric field vector needs to be considered and the wave equation reduces to a scalar equation (the case of p-polarization is considered in appendix A). In each region, the electric field is expressed as a series of plane waves. In the reflection and transmission region, these are the diffraction orders as introduced above. We proceed by evaluating the wavevectors in all regions in space. We use the same normalization of the spatial coordinates as introduced above. The y-components of the wavevectors are the same in all regions in space, as determined above by Floquet's theorem. They are given by Eq. (2.56). The z-components of the wavevectors require an individual treatment in each region. They generally follow from Maxwell's equations through a suitable secular equation. In the reflection and transmission region, this is the kernel of the wave equation in free space, and the z-components of the wavevectors are those given by Eq. (2.57). To accept only waves that travel in a physically meaningful direction, and evanescent orders that do not diverge towards infinity, it is required that $k_m > 0$, respectively $\mathrm{Im}(\mathrm{k_m}) > 0$. Then, the electric fields in the reflection and transmission region are

$$\begin{aligned} E^R &= e^{i(q_0 y + k_0 z)} + \sum_m R_m e^{i(q_m y - k_m^R z)} \\ E^T &= \sum_m T_m e^{i(q_m y - k_m^T z)}. \end{aligned} \tag{2.62}$$

R_m and T_m are – so far unknown – reflection, respectively transmission coefficients. They determine the intensities of the transmitted and reflected diffraction orders, through the magnitude of the Poynting vector, as

$$\begin{aligned} I_m^R &= |R_m|^2 k_m^R / k_0^R \\ I_m^T &= |T_m|^2 k_m^T / k_0^R. \end{aligned} \tag{2.63}$$

In case no absorbing material is present, conservation of energy requires that

$$\sum_m I_m^R + I_m^T = 1, \tag{2.64}$$

which can serve as a test for the numerical accuracy of the calculation.

In the grating region, the determination of the propagation constants in z-direction requires a more elaborate treatment. Each layer is now treated separately to arrive at a secular equation. The dielectric constant $\epsilon^i = {n^i}^2$ is expanded into a Fourier series,

$$\epsilon^i = \sum_m \epsilon_m^i e^{imQy}, \tag{2.65}$$

and the electric field E^i is expanded into plane waves traveling in the y-direction, while the z-dependence of the waves is – for the moment – kept in unknown expansion coefficients, expressed as

$$E^i = \sum_m S^i_m(z) e^{iq_m y}. \tag{2.66}$$

This ansatz is substituted in the Maxwell equations, together with the Fourier expansion of the dielectric constant Eq. (2.65), yielding an (infinite) set of second order ODE's (with constant coefficients). This requires that the $S^i_m(z)$ are themselves series of plane waves in z-direction, and associated with the ODE is a secular matrix, that determines their propagation constants. This infinite matrix is truncated and its eigenvalues are found numerically, e.g. by Schur decomposition or singular value decomposition [97, 3].

With the knowledge of the propagation constants, the expansion of the electric field into plane waves can be formulated in every grating slice. It remains to determine their expansion coefficients, from which the diffraction intensities are eventually calculated through Eq. (2.63). The expansion coefficients are found by matching the field at all boundaries, and solving the resulting linear system.

This solution to the Maxwell equations is exact in the limit of an infinite number of plain waves retained in the expansion in every layer. In practice the expansion converges quickly, and typically less than $10 \cdot T/\lambda$ orders are required to obtain accurate results. A second numerical parameter is the thickness of the slices that are used to approximate an arbitrary profile. Typically, the discretization is accurate if the thickness is smaller than about $1/10 \cdot \lambda/n$. In practice the numerical accuracy can be verified by increasing the number of diffraction orders and decreasing the slice thickness until the variation of the computed diffraction intensity is much smaller then the desired numerical accuracy. In a typical computational project, one may begin with selecting a reference computation that represents one parameter choice of a grating geometry that is to be analyzed, and performs an accuracy test with this computation to determine suitable numerical parameters.

To make use of the Rigorous Coupled Wave Analysis, above scheme has to be cast into an efficient computer code. These aspects are often overlooked, though of paramount importance, if we are aiming for modeling tools that provide a high numerical performance, paired with a flexible user interface that is easily maintained and extended. For the purpose of this work, a coding philosophy was adopted that aims at combining the unsurpassed numerical power of Fortran 90 with the flexibility and abstraction provided by an object oriented programming approach. The computer code developed in this work is made freely available [101] under the GPLv3 [1] (open source). Its most important numerical schemes and principles of its user interface are discussed in appendix A.

Chapter 3

Microscopic properties of the superhydrophobic state

In this chapter we study the properties of the microscopic liquid-gas interfaces that span between adjacent ridges of a superhydrophobic texture, by analyzing the light diffracted from a superhydrophobic optical grating. By applying a hydrostatic pressure, we induce the transition from the superhydrophobic to the impreganted state in a controlled manner, and observe it in situ. *We determine the mechanism that governs the transition and give design rules for superhydrophobic surfaces that provide the largest resistance to impregnation. Prospects of superhydrophobic surfaces for tunable diffractive optical elements are evaluated.*

3.1 Introduction

Surfaces with artificial periodic micorpatterns have been studied extensively in recent years for their superhydrophobic - or more generally: superoleophobic - behavior [99, 57, 82, 118, 28, 126, 92, 106, 56, 80, 110], which is of interest to various applications such as self-cleaning surfaces [82] and drag reduction in microfluidic devices [118, 28]. All favorable properties of the superhydrophobic state rely on the presence of liquid-gas interfaces, which span the gaps between adjacent ridges of the surface patterns and thereby dramatically reduce the interaction between the liquid and the solid [99]. The exact shape of these micromenisci is crucial for our understanding of both the stability of the superhydrophobic state [92, 106, 56, 80, 110] as well as its function, e.g. drag reduction [118, 28]. Despite their central role, micromenisci have so far eluded a quantitative characterization and thereby compromised our detailed understanding of the superhydrophobic state. Here, we report nanometer-resolved measurements of the deflection of micromenisci under the influence of an applied hydrostatic pressure using optical diffraction. Below a threshold pressure, meniscus deformations are reversible, above it, the superhydrophobic state is destroyed irreversibly. We show that the macroscopic collapse is triggered by depinning of the microscopic contact lines at a threshold angle that is in close agreement with Young's macroscopic contact angle. It is therefore essential to employ the classical laws of Young [132] and Laplace [31] on the microscopic scale to derive stability criteria for the design of optimal superhydrophobic (and superoleophobic) surfaces. Furthermore, our results point towards novel applications of such surfaces as tunable optical gratings [25, 98, 78].

Despite great efforts, a fundamental understanding of the stability of the superhydrophobic state remains elusive. It was suggested to explain the transition from the superhydrophobic to the impregnated state under the influence of pressure through a minimization of the global energy [57], giving right to the two different wetting scenarios, known as the Cassie-Baxter and the Wenzel state (see also Sec. 2.2.1). In contrast, recently it was pointed out that the Cassie-Baxter and Wenzel models are unable to describe even the static contact angle of more complex surface patterns [35]. This suggested, that the *local* energy balance at the contact line determines the wetting state. Moulinet and Bartolo pointed out, that the impregnation of an evaporating drop on a superhydrophobic surface is accompanied by intermediate states characterized by a partial impregnation of the texture [80]. This suggested that it must ultimately be the *microscopic* force balance at the multifold of contact lines, that determines the wetting scenario. This idea is supported by recent works of the groups at MIT and Bell Labs, reporting about surfaces, that exhibit superhydrophobicity even with liquids that feature a Young angle much smaller than 90° [126, 2]. The authors point out, that the common macroscopic wetting models cannot explain the observed superoleophobicity. An experimental characterization of the microscopic properties of the superhydrophobic state is thus of great interest. This poses a great challenge. Previous approaches have been limited by the resolution of optical microscopy [80]. They have been invasive [52], or even destructive [54].

Here, we report on an optical diffraction experiment that allows to determine the shape of the liquid-gas interfaces *in situ* with nanometer resolution by measuring the

intensity of coherent light diffracted from a superhydrophobic optical grating. We determine the deflection ζ of the liquid-gas interfaces (see Fig.3.1c) for variable applied pressures by fitting the measured intensity of several diffraction orders to an optical model based on numerical solutions to Maxwell's equations. Upon increasing the hydrostatic pressure, we find the liquid-gas interfaces to bend downwards, until a critical pressure, that marks the transition from the superhydrophobic to the impregnated state. We explain our results by assuming that at every moment, the curvature is determined by a balance between the pressure drop across the interface and the Laplace pressure. We find that the wetting transition occurs at the very moment, when the angle of the microscopic interface with the cavity wall reaches the Young angle. Our results suggest, that the *microscopic* properties of the superhydrophobic state can be explained in detail through two fundamental assumptions that are known from *macroscopic* experience. (1) The pressure drop across the interface is the product of the surface tension σ and the mean curvature κ (this represents Laplace's law in its most general form, as expressed by Eq. 2.3). (2) The contact angle at the microscopic three-phase contact lines of the liquid-gas interfaces is the Young angle, as described by Eq. 2.8. Though widely known, both laws are not frequently applied to explain the microscopic properties of the superhydrophobic state, rather, in the common approach suggested originally by Cassie and Baxter [20], microscopic details are *smeared out* by evaluating a mean ('effective') surface energy (see also Chapter 1). These aspects are discussed in detail in Chapter 4. In the present chapter, we verify experimentally that the laws of Young and Laplace are applicable in their most basic form to describe the *microscopic* nature of superhydrophobic surfaces. Thereby, we shall close a long standing debate on the mechanism that governs the stability of the superhydrophobic state.

3.2 Experiments

The experimental setup is described in Fig.3.1. A sample (a,b) consists of four different gratings with rectangular grooves with a depth $d = 6\mu$m and different periods T and groove widths w on the micrometer scale (see Figure caption). Unless indicated otherwise, the data presented refer to the grating with $T = 8\mu$m and $w = 5\mu$m. The samples were fabricated by 365nm lithography and reactive ion etching of a silicon wafer, and subsequently hydrophobized with a monolayer of a perfluoroalkylsilane yielding advancing and receding contact angles on the flat substrate of 120° and 105°, respectively as described in Appendix C. The sample is mounted on the axis of a cylindrical glass container that is filled with demineralized water (d). The design of the measurement cell is detailed in Appendix D. The hydrostatic pressure above the sample is adjusted between -10kPa and +25kPa by controlling the liquid level in a flexible tube. The sample is illuminated with the 488nm beam of an Ar-ion laser under s-polarization (results obtained with p-polarization are qualitatively the same). Diffraction orders are observed at angles ϑ_m determined by the real solutions to the grating equation $\sin\vartheta_m = \sin\vartheta + \frac{m\lambda}{nT}$, where m is the diffraction order, ϑ is the angle of the 0^{th} diffraction order with respect to the surface normal, λ is the vacuum

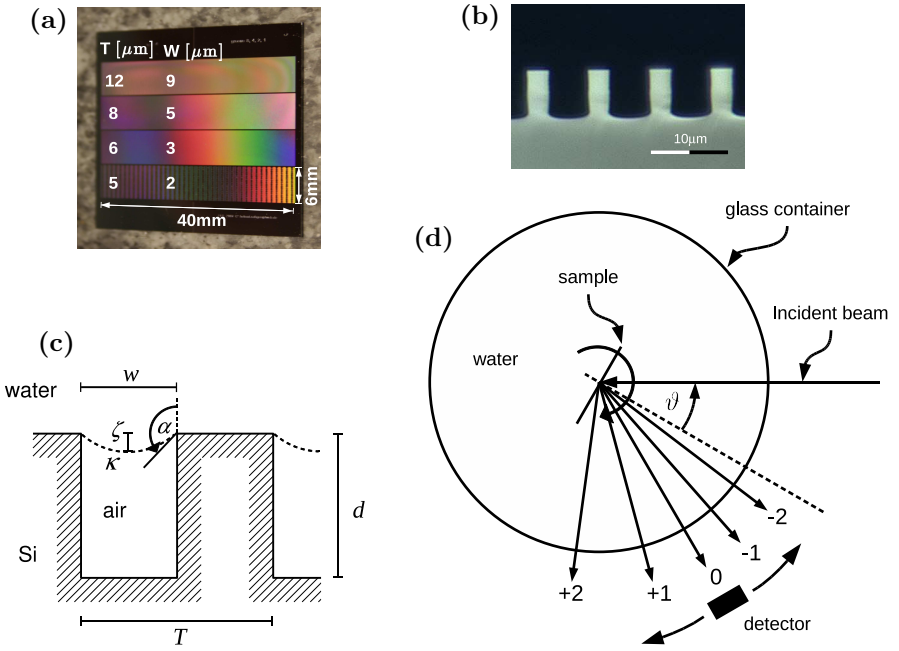

Figure 3.1: **Optical diffraction experiment with a superhydrophobic optical grating. a** Photograph of a sample consisting of four gratings each with a total size of 40x6 mm, and with periods (from top to bottom) 12, 8, 6, and 5μm, respectively groove widths 9, 5, 3, and 2μm. **b** Bright field microscope cross section through the grating with period 8μm. The silicon appears bright. **c** Schematic of a liquid-gas interface on a groove. The deflection ζ in the apex of the liquid-gas interface is linked to its curvature through geometry as $\zeta = 1/\kappa(1 - \sqrt{1 - R^2\kappa})$, where $R = w/2$ is half the groove width. A downward bent interface corresponds to a positive deflection and curvature. The angle α between the interface and the groove wall follows as $\kappa R = \cos\alpha$. **d** Experimental setup

wavelength of the light, and n is the refractive index of the adjacent medium water, $n = 1.33$ in this case. The sample (including the glass container) and the photodiode are mounted on separate rotation stages to allow for measuring independently the diffracted intensities as a function of the incident angle. To characterize the diffraction, we measure the intensity of a number of bright diffraction orders including the specular reflection, using a photodiode. To capture all diffracted intensity, the active area of the photodiode is large compared to the beam diameter. Measured intensities are normalized through the incident intensity. To take into account the reflection loss of the glass container, the incident intensity before and after the container was measured with no sample mounted. The glass container and the photodiode are mounted on independent rotation stages, such that the intensity of the diffracted beams can be measured independently, and as a function of the incident angle.

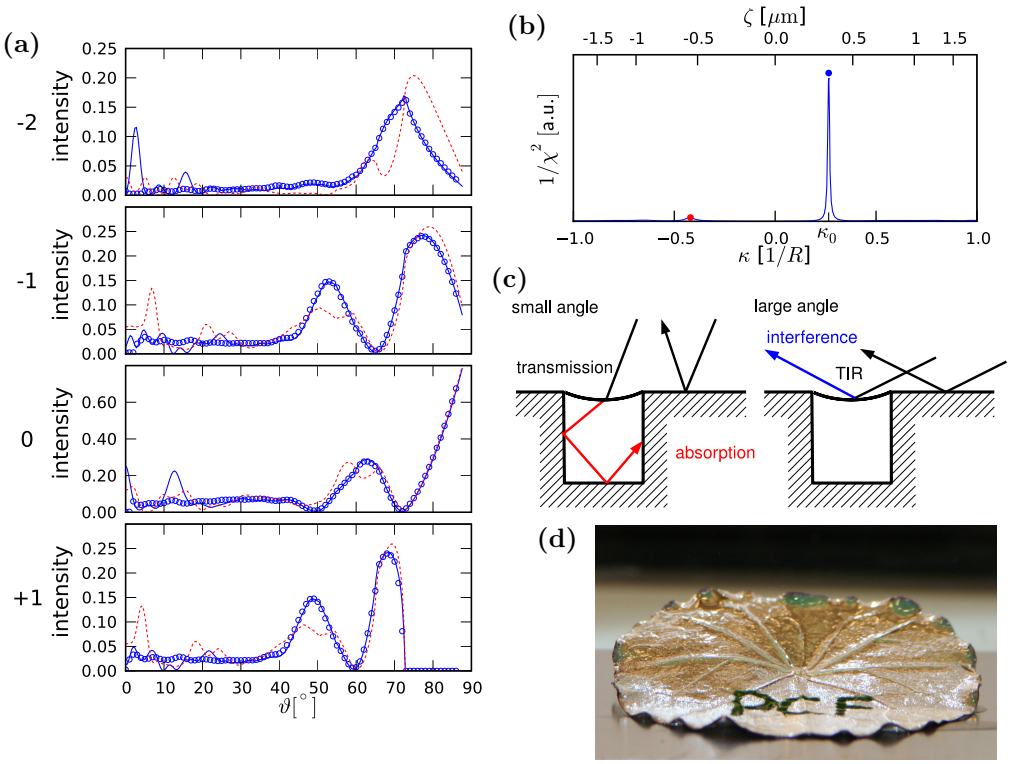

Figure 3.2: **Analysis of the angle resolved diffraction data. (a)** Intensity of the -2^{nd} to $+1^{st}$ diffraction order as a function of the incident angle. The intensity is normalized by the incident intensity. Experimental data (open symbols) are compared to theory (solid lines). The blue lines show the best fit corresponding to a downward bent meniscus with curvature $\kappa_0 = 0.265\,R^{-1}$ (or equivalently a deflection $\zeta_0 = 338 \pm 7$nm). The red line shows the theoretical data corresponding to an upward bent meniscus (red dot in (b)) which fails to fit the experimental data, showing that the fit is unique. **(b)** Inverse of the mean square deviation χ^2 versus ζ and κ (determined over the range $30° < \vartheta < 90°$). The blue and red dot mark the primary and secondary maximum corresponding to the curves in panel (a). **(c)** Illustration of the dominant scattering mechanisms. At small angles the incident light is mainly transmitted through the liquid-gas interfaces and undergoes absorption inside the groove. At large angles, total internal reflection occurs at the liquid gas interface, and the diffracted intensity is governed by the interference with light scattered from the silicon surface, resulting in a versatile diffractive interference phenomenon. **(d)** Photograph of a *tropaeolum majus* leaf immersed under water and viewed under a grazing angle. Total internal reflection at the leaf's superhydrophobic texture is at the origin of the beautiful silvery appearance. At patches, the outermost skin of the leaf has been dissected, thereby destroying its superhydrophobicity such that the area appears dark. In this way the logo of the Physics of Complex Fluids group was written into the leaf (courtesy of Sissi de Beer).

Figure 3.2 shows typical measured diffraction intensities (obtained at an initial hydrostatic pressure P_h = 7,500Pa). The curves show two regimes. For small angles (near perpendicular incidence) the intensity is small and nearly constant. In contrast, for large angles (towards grazing incidence) pronounced minima and maxima are observed, emerging approximately at the angle of total internal reflection between water and air, $\vartheta_T = 48.6°$. The data can be understood qualitatively through the theory of Fraunhofer diffraction.

In the Fraunhofer limit, the diffracted intensity is governed by the interference of the elementary waves scattered from the cell volume [15]. Here, two contributions are important, the light that is scattered by the water-silicon interface, and the light that is scattered by the water-air interface. At small angles, the light that impinges on the water-air interface is mainly transmitted, it undergoes several reflections inside the groove, and is mostly absorbed by the silicon. The diffracted intensity is thus comparably low. Fig.3.2a) illustrates this scenario. In contrast, at large angles, the light that impinges on the water-air interface, undergoes total internal reflection, and the diffracted intensity is governed by the interference with the light scattered by the water-silicon interface (Fig.3.2(b)). This total internal reflection is indeed at the origin of the beautiful silvery shining appearance of drops on top of a superhydrophobic plant leaf, as is seen in Fig.3.2(d). The interference condition depends on the incident angle, and a pronounced feature arises in the angular scan. Qualitatively, as the meniscus is deflected – consider the position ζ of the apex of the meniscus – the intensity of a diffraction order (with diffraction angle $\approx$ incident angle), changes sinusoidally with an angular period $\Delta\vartheta = \lambda/(2n\zeta\sin(\vartheta))$. This simplified model describes the data qualitatively, and indeed, an angular period of $\Delta\vartheta \approx 25°$ is observed in Fig.3.2. Substituted in the latter expression, it suggests $\zeta \approx 200$nm. This rough estimate can serve as a rapid qualitative analysis of the experimental data, and allows us to estimate the order of magnitude of the deflection. However, it does not allow for a quantitative measurement of the shape of the liquid surface. Even worse, it does not even allow to distinguish between upward and downward bent menisci. We thus calculate the diffracted intensity numerically by means of Rigorous Coupled Wave Analysis (RCWA) [77] (see also Appendix A). The obtained solution to the Maxwell equations is exact in the limit of an infinite number of diffraction orders retained in the underlying expansion into plain waves, and in the limit of sufficiently thin slices used to approximate an arbitrary grating profile, the curved liquid-gas interface in our case (see Sec.A.2.1 for a detailed discussion of the slicing procedure). Typically less than $10 \cdot T/\lambda$ orders are required to obtain accurate results, and the discretization is accurate if the thickness of the slices is smaller than $1/10 \cdot \lambda/n$. We carefully checked the free numerical parameters. In particular, we increased the accuracy, until the variation of the theoretical results was smaller than the error between theory and experiment. It turned out that exquisite parameters are required. A final number of $-128 \cdots +128$ diffraction orders was retained. To achieve the highest resolution, the curved liqud-gas interface was approximated with layers with a thickness of only 2 nm. Physical constants that enter the calculation, are the refractive indices of water, $n = 1.33$ and Si $n + ik = 4.367 + i0.079$ [66]. All calculations presented in this chapter were performed on a grid equipped with 2GHz Dual Core AMD Opteron$^{\text{TM}}$ processors, and took a

total of about 2400 cpu hours. To determine the curvature of the liquid-gas interface, we perform a least-square fit of the measured diffraction intensities against the theoretical optical model. In particular, we evaluate $\chi^2 = \sum \left(I_m^{exp}(\vartheta_i) - I_m^{theo}(\vartheta_i, \kappa)\right)^2$, on a dense mesh of possible curvatures in the range $\kappa \in [-R^{-1}, R^{-1}]$. The sum extends over the measured diffraction orders, $m = -2, \cdots + 2$, and the measured angles, ϑ_i. Fig.3.2(b) shows the inverse of the obtained χ^2. The position and full width at half maximum of the Lorentzian peak determine the curvature and its error (see appendix E) as $\kappa_0 = 0.265R^{-1}$ respectively $\delta\kappa = 0.0055R^{-1}$, corresponding to a deflection $\zeta = 338 \pm 7$nm. The corresponding theoretical intensity is shown with blue lines in Fig.3.2a). At large angles, the agreement between theory and experiment is truely remarkable, in particular, taking into account, that the experimental intensities are *not* rescaled to fit theory, rather, experimental and theoretical data are each normalized individually by their incident intensity. At small angles the theory overestimates the amplitude of the rapid angular oscillations, that are indeed also seen in experiment. These rapid oscillations are only present at small angles, before the onset of total internal reflection, when light transmits through the liquid-gas interface. They correspond to an interference between waves scattered from the top grating surface and waves scattered from the bottom of the grooves. This interference is weakened in experiment, since (a) the groove wall possesses a finite roughness, as opposed to theory, where a perfectly flat wall is assumed, and (b) more importantly, the depth of the grooves varies by more than $\lambda/2$ over the hole sample –the etch rate decreases towards the edge of the wafer–, such that an interference involving the bottoms of the grooves, is averaged out. In contrast, at large angles, the incident light interacts almost exclusively with the top grating surface and the liquid-gas interfaces. Both of these surfaces are very well defined and homogeneous over the hole sample. The *nm* smoothness, and nearly perfectly identical shape of the liquid-gas interfaces is at the origin of the high optical quality of the sample, resulting in the excellent agreement between experiment and theory in the total internal reflection regime. To give right to this highly sensitive diffraction measurement, in the following only the data with incident angle $> 30°$ is used for the fit. A small secondary peak is observed in the $1/\chi^2$-landscape at $\kappa = -0.42R^{-1}$. This upward bent liquid-gas interface is identified with an equivalent interference condition corresponding to a positive deflection, with a similar magnitude, and correspondingly a similar angular oscillation period $\Delta\vartheta$. The corresponding theoretical diffraction intensities are shown with a dashed red line in Fig.3.2. It can be seen that this equivalent interference condition fits the experimental data much worse, showing that the fit is unique – it reveals whether the liquid-gas interfaces are bent upwards or downwards.

To explain the measured curvature we assume that the pressure drop P_L across the interface is the product of the curvature and the surface tension σ, following Laplace's law. The gas pressure in the groove is the ambient pressure, such that the pressure drop across the interface is the hydrostatic pressure P_h. Pressure balance requires that $P_L = P_h$, resulting in a prediction for the curvature $\kappa = P_h/\sigma$. Inserting the surface tension of water $\sigma = 73$mN/m, and the experimental value of $P_h = 7500$Pa for the data shown in Fig. 3.2, we obtain $\kappa = 0.256\, R^{-1}$, in good agreement with the measured value.

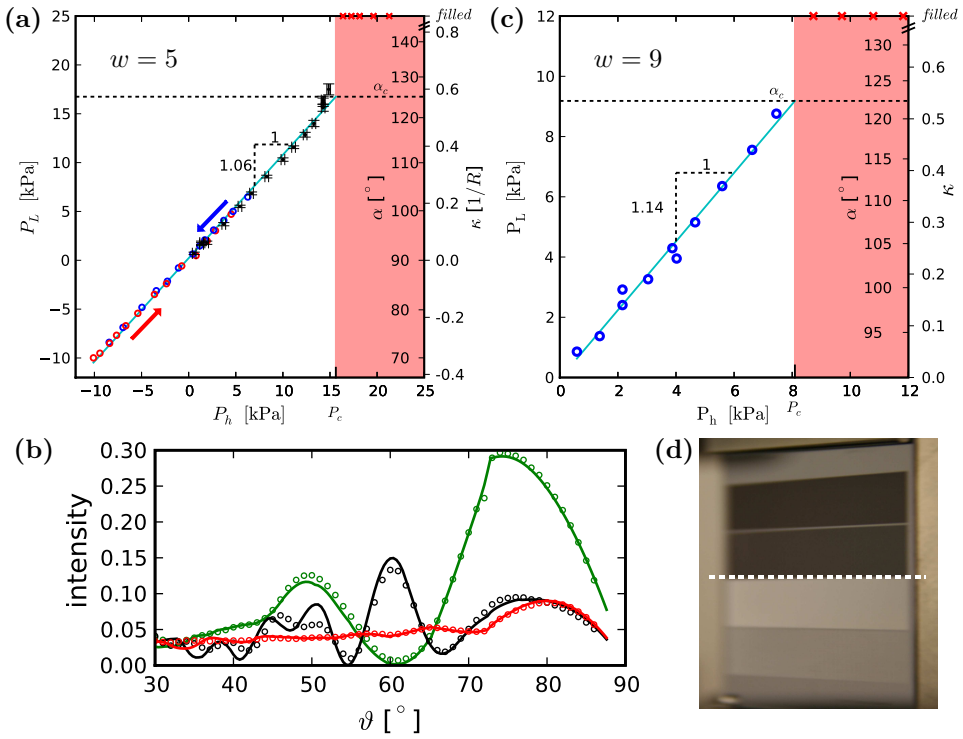

Figure 3.3: **Reversible bending of the liquid-gas interfaces under an applied hydrostatic pressure and wetting transition. (a)** The curvature of the liquid-gas interfaces is plotted in terms of the Laplace pressure $P_L = \sigma\kappa$ against the applied hydrostatic pressure. The pressure is first increased (red circles), subsequently decreased to negative pressures (blue circles), and returned to zero. The slope is determined as unity. As the pressure is further increased (black symbols), the interfaces bend increasingly downwards. At a threshold pressure P_{hc}, the sample switches irreversibly from the superhydrophobic to the impregnated state (red crosses). The transition is characterized by a critical angle α_c of the liquid-gas interface with the groove wall of $125 \pm 2°$, in close agreement with the Young angle (horizontal dashed line). **(b)** Diffraction intensity of the -1^{st} order for selected pressures. Fits to the optical model (lines) are shown along with the experimental data (symbols). Green represent a moderate pressure (uppermost red circle in (a)). Black corresponds to the last stable state (outermost black data point in (a)), characterized by a strongly curved interface. Red corresponds to the filled state (red crosse in panel (a)). **(c)** Same as in (a) for a sample with groove width 8μm. The critical angle $\alpha_c = 122 \pm 2$, observed at a correspondingly lower critical pressure is consistent with the one observed in (a). **(d)** Photograph of the sample after inducing the wetting transition for the two upper gratings (groove widths 8 and 4μm). The two upper gratings are in the filled state, and appear dark, while the two lower gratings remain in the superhydrophobic state and appear silvery.

To establish this further, we vary the hydrostatic pressure step-wise, and determine at each pressure the curvature of the liquid-gas interfaces through an angular diffraction measurement. Fig.3.3(b) shows how the characteristic minima and maxima in the angular scan change as the interfaces bend under the applied hydrostatic pressure. The red and blue symbols in Fig.3.3(a) show the test of the pressure balance for a sequence of applied pressures. The curvature of the interfaces (outer right axis) increases and decreases reversibly as the hydrostatic pressure is varied from zero to 15kPa, to -10kPa, and finally back to zero. The corresponding Laplace pressure is equal to the hydrostatic pressure, indicated by a slope of unity, confirming above pressure balance.

We proceeded by increasing the hydrostatic pressure to larger and larger values (black symbols with error bars in Fig.3.3a). Above a threshold, the distinct maxima and minima in the diffraction curves disappear (red symbols in Fig.3.3b), accompanied by a change of the visual appearance of the sample from silvery to dark (Fig.3.3c), suggesting that the liquid-gas interfaces have vanished, and the sample has undergone a transition from the superhydrophobic to the impregnated state. A fit to the optical model shows that indeed, all diffraction curves for pressures above the critical pressure are best described by diffraction data corresponding to grooves that are filled (red line in Fig.3.3b). While the critical pressure to induce the transition is well-defined, the transition itself typically takes a few minutes, which we attribute to the dissolution of the previously entrapped air. Once the transition is complete, it is irreversible. Increasing or decreasing the applied hydrostatic pressure below the critical pressure (down to a minimum of -10kPa), does not recover the superhydrophobic state.

To infer the microscopic condition of the wetting transition, we examine the last stable shape of the liquid-gas interfaces measured before the transition. The black symbols in Fig.3.3(b) show the diffraction intensity corresponding to the last stable state. The optics theory (black line) determines the curvature as $\kappa_c = -0.57 \pm 0.02R^{-1}$. Through geometry, this translates into an angle α_c between the meniscus and the groove wall of $\alpha_c = 125 \pm 2^\circ$, in close agreement with the macroscopic Young angle of the substrate. The inner right axis in Fig.3.3 denotes the angle α for all data. It is seen, that indeed, the transition occurs at the Young angle. To probe this further, we move on to a sample with larger groove width ($w = 8\mu$m). We expect that the wetting transition occurs at the same angle α, but the latter being reached at a higher pressure. Fig.3.3(c) shows the result, confirming the previous observations.

The present results show that the microscopic behavior of a generic superhydrophobic surface (including its wetting transition) can be described quantitatively by invoking only two fundamental assumptions. (1) Laplace's law (the pressure drop across a curved interface is $\sigma\kappa$), and (2) the Young condition (the angle at the three-phase contact line is the Young angle). Following Gibbs [128], at a sharp edge, the latter is expressed by requiring that the liquid-gas interface may adopt any angle larger than the Young angle with respect to the adjacent horizontal surface, and smaller than the Young angle with respect to the adjacent vertical surface (Fig.3.4a) [1]. At small hydrostatic pressure the interface is flat. The contact angle is well within the range

[1] Gibbs' condition is equivalent to assuming that the sharp edge is curved on a scale much smaller than the entire liquid-gas interface and the contact angle is always the Young angle (see also [87]).

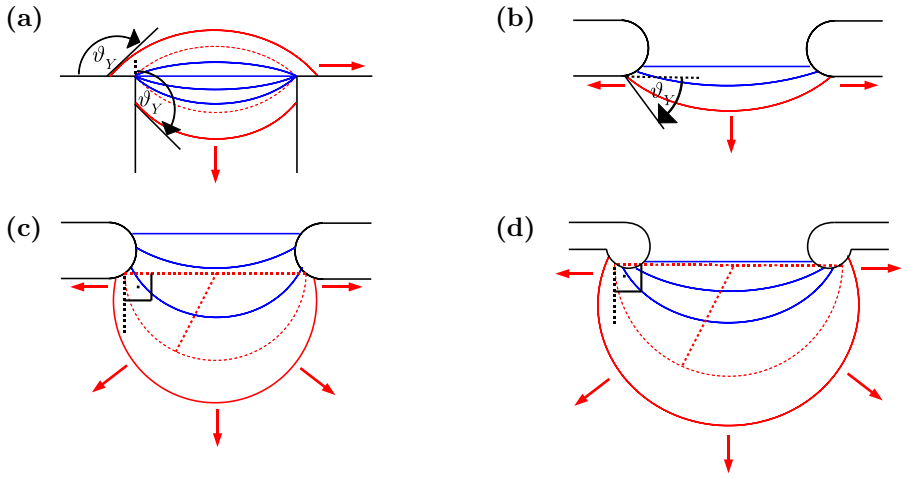

Figure 3.4: **Microscopic model of the wetting transition. (a)** For the present surface profile with perpendicular walls. **(b)** For a reentrant surface profile. For a drop on a superhydrophobic surface, Laplace's law requires that liquid-gas interfaces are bent downwards (corresponding to a pressure decrease upon crossing the interface from the liquid to the gas phase). With a reentrant surface profile Young's condition is satisfied with downward bent interfaces even for liquids with a Young angle smaller than 90°.**(c-d)** Illustration of the ultimate stability limit, **(c)** for liquids with a Young angle *larger* than 90°. **(d)** for liquids with a Young angle *smaller* than 90°.

of Gibbs' condition. As the pressure is increased, the interface bends downwards, thereby increasing its angle with respect to the groove wall. At larger and larger bending, the angle exceeds Young's angle and the interface must translate inwards, with liquid invading the groove. Our results verify quantitatively that the wetting transition is induced when the microscopic contact angle exceeds Young's angle on the vertical wall, demonstrating that the Gibbs condition provides the ultimate stability limit of superhydrophobic surfaces. In analogy with the critical pressure for filling, there is a critical *negative* pressure, at which the liquid-gas interface with the horizontal surface reaches the Young angle, and the contact line must translate outwards (top red line in Fig.3.4a). For large negative pressures, we find indeed that macroscopic bubbles grow out of the sample and merge to a continuous cushion, as expected for depinning of the contact lines on the horizontal surface [2]. The usefulness of this microscopic mechanical model lies in the ease of describing general complex surface profiles without the need of an involved energy minimization [119]. E.g. 'reentrant' surfaces that provide liquid repellency for substances with a contact angle smaller than 90° ('superoleophobicity') [126, 2] can be described in analogy (Fig.3.4b).

An ultimate stability limit and corresponding optimal surface profile follows in a

[2] a quantitative confirmation of the critical condition was impeded by early bubble nucleation at defect sites of the sample that interfered with the optical measurement.

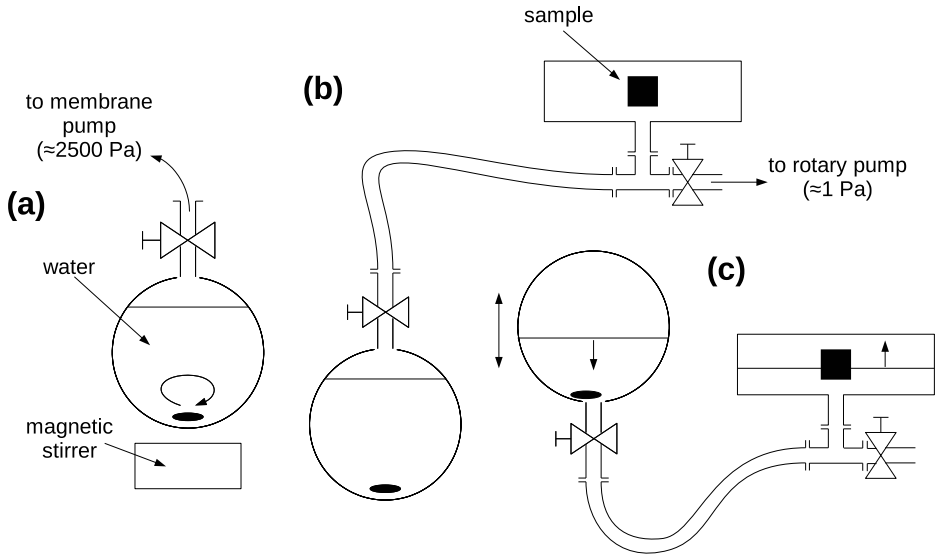

Figure 3.5: **Setup for experiments under vapor condition. (a)** Degassing of the water. **(b)** Evacuation and flushing of the chamber. **(c)** Flooding of the chamber and experiments with variable hydrostatic pressure.

similar fashion. In this case, the microscopic mechanism for the wetting transition is slightly different. Let us consider first a liquid with a contact angle *larger* than 90°, say 120°, and a reentrant surface profile (Fig. 3.4c). At large applied pressure, the liquid-gas interface is suspended from below on the reentrant texture. Upon increasing the hydrostatic pressure, the interface bends increasingly downwards (accompanied by a small translation of the contact line in case the edge is curved), until the interface forms a perfect half circle (dashed red line). From this moment on, a further growth of the interface results in a *decrease* of the curvature, and thus in a decrease of the pressure that the interface can sustain. Thus, upon a further increase of the hydrostatic pressure, the interface expands vigorously, and the angle between the interface and the ceiling immediately reaches the Young angle (outermost dashed line), and the interface translates and collapses. Thus, for a liquid with a contact angle larger than 90° reentrant type profiles represent already optimal profiles that provides the largest possible resistance to impregnation, expressed by a critical angle with respect to the vertical $\alpha_c = 180°$. The corresponding critical pressure follows from the particular geometry of the surface pattern in the lateral direction. A rather high critical pressure could be achieved with cylindrical holes of radius R, that result in $P_c = 2\sigma/R$. In analogy, for a liquid with a contact angle *smaller* than 90°, say 30°, an inward circled edge (Fig. 3.4d) could further increase the stability limit, however not above the same ultimate limit $\alpha_c = 180°$.

To address the irreversibility [57, 9, 105, 18] of the wetting transition, we repeat

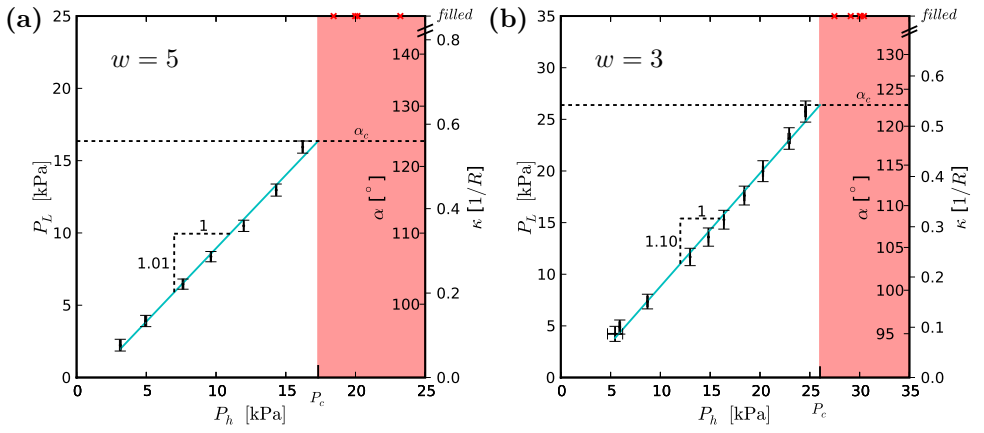

Figure 3.6: **Bending and wetting transition for a single constituent water-vapor system. (a)** For a sample with groove width 5μm. **(b)** For a sample with groove width 3μm.

our experiments near the coexistence line of the water-vapor phase transition, that is, we evacuate the chamber, thereby degassing the water, and admitting only vapor inside the sample grooves. Fig.3.5 shows a schematic of an experimental setup that allows to do so. Water is degassed overnight using a glass balloon, a magnetic stirrer, and a membrane pump (a). The valve of the glass balloon is closed and the membrane pump detached. The sample is mounted in the empty measurement cell, and the glass balloon connected to the cell and a rotary pump through suitable mid range vacuum stainless steel bellows and valves (b). The valve of the glass balloon remains closed. The rotary pump is turned on. The valve to the rotary pump is opened, and the chamber including the steel bellow is evacuated to the end pressure of the rotary pump ($\approx$ 1Pa). For several times, the chamber is flushed with water vapor, by opening the valve of the glass balloon for few seconds and closing it again. At last, the chamber is again evacuated to the end pressure of the rotary pump, the valve to the pump is closed, and the pump disconnected from the system. The valve of the glass balloon is opened, and the balloon is turned upside down and lifted to a level higher than the measurement chamber. Water flows from the balloon to the measurement chamber, entering the chamber through a flange in its bottom (c). Thereby the vapor volume in the chamber condenses. The grooves of the sample are filled with vapor, and the liquid level slowly rises above them, enclosing their vapor volume. Subsequently, the level of the balloon is increased in steps. The hydrostatic pressure is determined by measuring the height of the liquid level with a measuring tape. At each step, a full diffraction measurement is recorded. The pressure inside the grooves and above the water level is now the vapor pressure P_v = 2300Pa of water at the given temperature ($\approx 20°$). The pressure drop across the interface is thus exactly the hydrostatic pressure. As in the case of the water-air system, upon increasing the hydrostatic pressure, the interfaces bend downwards, and collapse as the angle between the liquid-gas interface

and the groove wall reaches the Young angle. Fig.3.6 shows the result. While in case of the water-air system, the translation of the liquid-gas interfaces into the groove required few minutes time, determined by the dissolution of the air into the water, here the transition is immediate, characterized by the instantaneous condensation of all vapor inside the groove, and limited only by a viscous drag, that the liquid experiences as it invades the groove. Remarkably, also for the water-vapor system, the wetting transition is still irreversible. That is, upon decreasing the hydrostatic pressure below the critical pressure that marks the transition, the system does not return back into the superhydrophobic state, even though the pressure inside the grooves is the smallest possible (the pressure inside the grooves is the vapor pressure plus an inevitable, small, hydrostatic pressure). This result suggests that the quest to superhydrophobic surfaces exhibiting a *reversible* wetting transition, may be most successful by pursuing mechanisms of external forcing such as electric heating [55] or photo chemistry [48].

Until here, the diffraction from a superhydrophobic surface served 'merely' as a tool to gain a detailed insight into the microscopic properties of the superhydrophobic state. However, superhydrophobic surfaces could also be used to provide new optical functionality. In the following section we demonstrate, that a superhydrophobic surface fabricated from glass (and immersed in water) could readily serve as an easy and cost effective immersed dielectric grating [85, 24, 79, 25] that provides effectively 100% diffraction efficiency and is (through the mechanism of bending the interfaces) additionally *in situ* tunable, at high switching speed [103].

3.3 Highly efficient, tunable transmission grating

The expected high smoothness and homogeneity of the liquid-gas interfaces of the presented optical grating, intrigues the question, whether the concept of a superhydrophobic optical grating could serve as a simple and effective way of implementing an immersed, or 'buried', dielectric grating. Fig.3.7(a) shows a schematic of a buried transmission grating. Rectangular grooves are fabricated into the backside of a glass body. The grating is illuminated from the glass side. The transmission region is provided by a dielectric material, that is index matched with the material on the incident side – in contrast to an ordinary transmission grating, where the transmission region is air. Thereby the effective reflectivities for the fundamental mode traveling in the grating region, on the top and bottom grating surface are equalized, and a scattering loss into the ordinary reflected order is suppressed. This mechanism of reducing reflection losses was the topic of a recent paper [24], where the authors showed, that, indeed, if the refractive index in the incident and transmission medium are exactly equal, e.g., if the transmission medium is provided by a second glass body, 100% diffraction efficiency can be achieved. In our case, the refractive indices of the glass and the water are not exactly identical, nevertheless, given the expected high smoothness of the liquid-gas interfaces, paired with a potentially easy fabrication, it is worth evaluating the diffraction characteristics of such a device. Though, a word of prudence is in place. One important application of dielectric gratings, that has gained

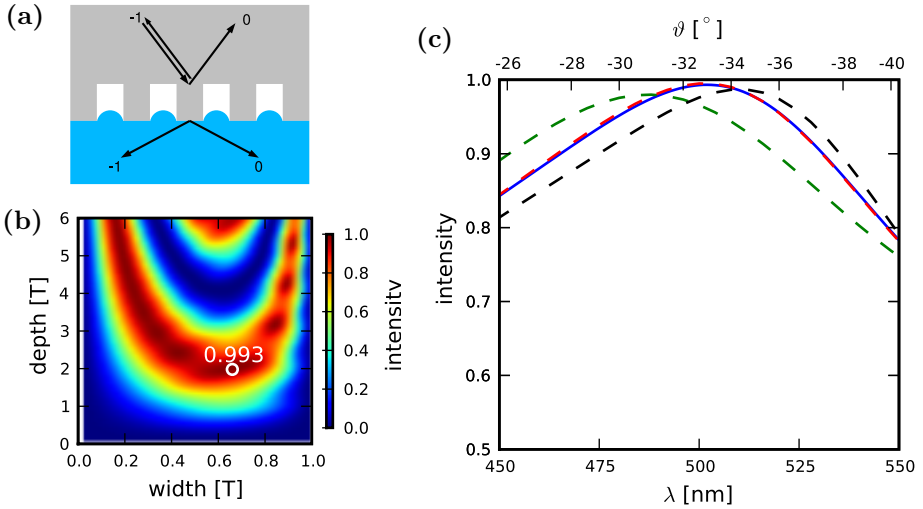

Figure 3.7: (a) Schematic of a superhydrophobic tunable transmission grating. (b) Diffraction efficiency of the transmitted -1^{st} diffraction order as a function of groove width and depth, assuming a flat liquid-gas interface. The groove width and depth are measured in units of the period $T = 345$nm. The white circle marks the choice of the groove width and depth, that yields the highest diffraction efficiency ($w = 0.66T$ and $d = 1.98T$, respectively) (c) Spectral characteristics of the grating. The solid blue line show the result obtained with optimum groove width and depth for a flat meniscus. The dashed lines show the result obtained with optimum width ($w = 0.66T$) but too large depth ($d = 0.21T$), for increasing meniscus deflection. The black dashed line represents a slightly bent meniscus ($\zeta = -0.1R$). The green dashed line represents a maximally bent meniscus ($\zeta = -R$). The red dashed line represents a medium bent meniscus ($\zeta = -0.5R$), that allows to recover the excellent diffraction characteristics obtained with optimum groove width and depth.

much attention recently, is chirped pulse compression. Often chirped pulses have a wavelength in the near infrared. The immersed grating based on a superhydrophobic surface, that we introduce below, utilizes water on the transmission side. Water shows a notable absorption in the infrared (the penetration depth, or attenuation to the $1/e$ part, is of the order 2 cm at 1μm [43]). Therefore, we believe, that the device, cannot be used in this form for infrared high power laser applications. It should however be possible to find a sufficiently transparent liquid with the required large surface tension to realize a superhydrophobic grating also for infrared wavelengths. However, more importantly, water is truely transparent over the visible spectrum, and down to the near UV. A large number of modern optical applications uses this spectral range. We shall thus select 500nm as the design wavelength λ_0 of the optical grating.

Generally, a high diffraction efficiency is achieved when the grating is arranged in -1^{st} order Littrow configuration, where the reflected -1^{st} order is anti parallel to the

incident beam, characterized by $-q_{-1} = q_0$ (see Fig.3.7(a)). This also means, that the diffraction orders on the transmission side are symmetric. In virtue of Eq. (2.58), the Littrow configuration settles the period of the grating to

$$T = \lambda/(2n^R \sin \vartheta_0), \tag{3.1}$$

where ϑ_0 is the angle of the 0^{th} diffraction order. Here, we assume $\vartheta_0 = 30°$, which determines the period as $T = 345$nm. This determines also the angular dispersion

$$D = 2/\lambda \tan \vartheta_0, \tag{3.2}$$

as found by differentiating Eq. (2.58) with respect to λ, and applying the Littrow condition.

Generally, a binary (rectangular profile) optical grating, has a high diffraction efficiency only for certain choices of the groove width and depth, determined by the phase shift that the fundamental and the first mode in the grating region accumulate as they travel in normal direction [23]. Therefore, to design a buried superhydrophobic grating, we first calculate the diffraction efficiency as a function of groove width and depth, assuming – for the moment – a flat liquid-gas interface. Fig.3.7(b) shows the plot. The grating provides $> 99\%$ diffraction efficiency for a broad range of widths and depths. Indeed, the regions of high efficiency are considerably broader as compared to a classical transmission grating, and more importantly, the theoretical peak efficiency reaches 99.3% as compared to 93% for a classical transmission grating (e.g. [23]). Thus, an immersed superhydrophobic transmission grating represents indeed a highly efficient buried grating, and can provide peak diffraction efficiencies that are superior to classical transmission gratings. Moreover, the predicted high efficiency is only slightly lower than the predicted 100% of an ideal buried grating featuring glass on the transmission side. In practice, the efficiency is limited by imperfections of the periodic profile, that inevitably result in scattering losses, and by the finite extent of the illuminated area – or the finite number of grooves involved in the scattering process – that results in a loss into a homogeneous background. It is thus well possible that the predicted high efficiency already exceeds the maximum efficiency achievable in practice, even with an ideal buried grating. Moreover, the superhydrophobic optical grating allows to tune the geometry of the unit cell in situ. In particular, by controlling the bending of the liquid-gas interface (through a suitable hydrostatic pressure), the optical path inside the groove, and consequently the phase shift between the two modes in the grating region, can be adjusted. In this way, the grating can be tuned to maximum efficiency, and thereby a fabrication tolerance – e.g. the etch depth – can be compensated, or the peak efficiency can be shifted to another wavelength. Fig.3.7(c) shows the spectral characteristics of the immersed superhydrophobic grating. The solid line reflects an optimal grating, with ideal groove width and depth $W = 0.66T$, respectively $D = 1.98T$, as marked by the white circle in (b). The dashed lines represent an imperfect grating, with the same groove width, but slightly too large depth $D = 0.21T$. For a nearly flat liquid-gas interface ($\zeta = -0.1R$, black line), the peak diffraction efficiency is shifted towards larger wavelength by about 10nm, and the diffraction efficiency at the design wavelength is decreased to

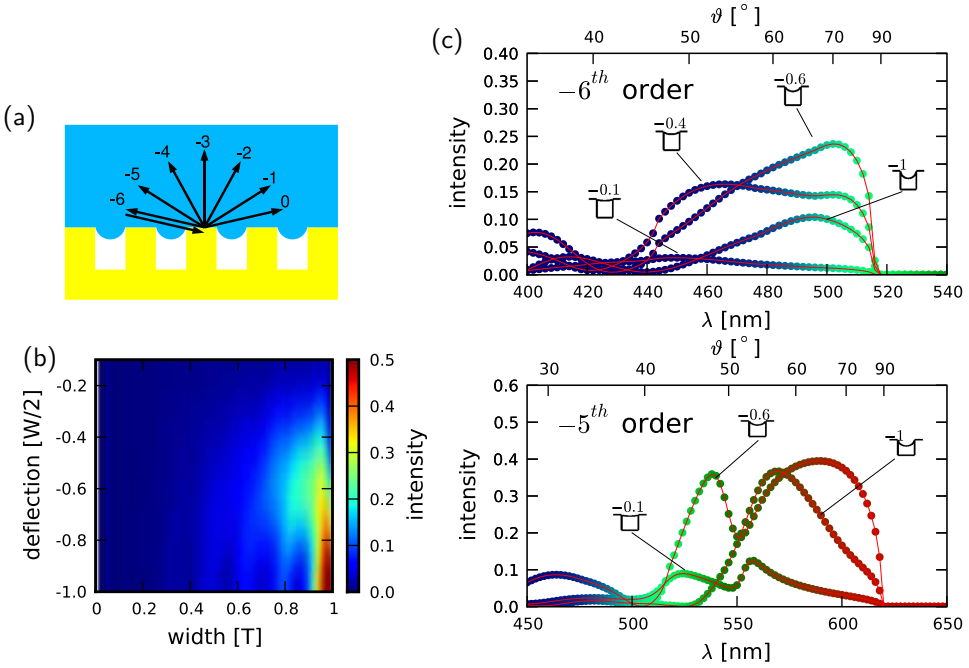

Figure 3.8: (a) Schematic of a superhydrophobic tunable gold grating. The grating is arranged in -6^{th} order Littrow configuration. (b) Diffraction efficiency of the -6^{th} diffraction order as a function of groove width and meniscus deflection, for a grating with groove depth $D = T = 1.2\mu$m. The groove width is measured in units of the period, the deflection is measured in units of half the groove width. (c) Spectral characteristics of a superhydrophobic gold grating for increasing meniscus deflection. The upper and lower panel shows the -6^{th}, respectively -5^{th} diffration order.

about 96%. Likewise, for a strongly deflected meniscus ($\zeta = -R$, blue line), the peak efficiency is shifted towards shorter wavelength. However, by tuning the deflection to $\zeta = -0.5R$ (red dashed line), the ideal diffraction characteristics featuring ¿99% peak efficiency can be restored. This makes the superhydrophobic grating an interesting component for applications were a high peak efficiency is required.

3.4 Tunable gold grating

The presented highly efficient, superhydrophobic transmission grating promises excellent diffraction characteristics, and its tunability should allow in practice to tweak the peak efficiency towards the theoretical optimum. However, its tuning range is rather limited. This stems from the maximum possible deflection of the liquid-gas interfaces, that is limited through fundamental capillary theory to half the groove

width [30]. And since the groove width is considerably smaller than the wavelength, a substantial change of the interference conditions of the modes in the grating region cannot be achieved. In contrast, what one would like to achieve, is indeed a phase shift as large as 2π, e.g., to be able to effectively switch on and off a part of the spectrum, or to shift the peak efficiency to a desired wavelength, or – if the target is a diffractive optical element offering a functionality comparable to a liquid crystal cell – to gain full control of the optical phase.

To achieve this, we increase the period, and the width of the grooves, and to this end, we turn back to a reflection type of grating, as studied initially. To allow for a high reflectivity, we replace the silicon by gold. Such a grating could be made hydrophobic in practice, by depositing a self assembled monolayer of an alkanethiol [6]. Fig.3.8(a) shows a schematic of the superhydrophobic gold grating. To allow for a large period, the grating is illuminated in a high order Littrow configuration. Throughout this section, we assume the grating is arranged in -6^{th} order Littorw configuration, and the incident angle is $70°$ – larger than the angle of total reflection between water and air, to allow for an interference phenomenon as observed before with the silicon grating – which determines the period of the grating as $T = 1.2\mu$m. For the refractive index of gold, we use the values tabulated in [90]. Fig3.8(b) shows the diffraction efficiency of the -6^{th} diffraction order as a function of groove width and meniscus deflection, assuming a groove depth $D = T$. A large diffraction efficiency is achieved at groove widths close to T. This large groove width allows for a comparably large deflection of the liquid-gas interfaces. From now on we assume the groove width is $W = 0.9T$. Fig3.8(b) shows the corresponding spectral characteristics of the -6^{th} and -5^{th} diffraction order for increasing meniscus deflection. Analog to the angular dependence of the diffracted intensity of the silicon grating, pronounced minima and maxima appear, and as the menisci are deflected, the minima and maxima shift. In particular, the peak diffraction efficiency of the -6^{th} diffraction order can be shifted by around 40nm, from about 460nm to 500nm. Thereby the diffraction intensity at 500nm and slightly above 460nm can be effectively turned on and off. Likewise, in the -5^{th} order, the diffraction intensity at around 530nm can be effectively turned on and off, and spectra with rather different spectral distributions can be produced. Whether or not such a spectral switching may find its way into an optics application – be it just a fast spectral filter (the grating is switchable at Mhz speed [103]), or a more sophistic grating application – is hard to foresee. Nevertheless, this demonstrates the feasibility of modulating an optical spectrum, by actively controlling the shape of the unit cell of a diffraction grating.

3.5 Summary and conclusions

We have introduced an optical diffraction measurement that allowed us to study the microscopic properties of the liquid-gas interfaces that span between adjacent ridges of the texture of a superhydrophobic surface, and we have observed the transition from the superhydrophobic to the impregnated state *in situ* on the microscopic level. We have shown that the macroscopic collapse is triggered by depinning of the microscopic

contact lines at a threshold angle that is in close agreement with Young's macroscopic contact angle. Our results provide essentially a contact angle measurement on a sub 10μm scale, whereby the measurement accuracy is $\approx 2^\circ$, comparable to the accuracy of macroscopic contact angle measurements. The results confirm that the assumption of a *local contact angle* that forms the basis of several models for contact angles on heterogeneous surfaces [50, 115, 113, 119], is satisfied well below the micrometer scale. The results are explained through a simple model that is based on the macroscopic laws of Laplace [31] and Young [132]. It is therefore essential to employ the classical laws of Laplace and Young on microscopic scales to formulate stability criteria for the design of optimal superhydrophobic (and superoleophobic) surfaces.

A good agreement between experimental and theoretical diffraction intensities was observed, suggesting that the liquid-gas interfaces are of high optical quality, both in terms of smoothness and equality. This suggested that a transparent superhydrophobic optical grating could provide an excellent buried dielectric grating, that is additionally cheap (easy to fabricate), and in situ tunable to its optimum diffraction efficiency. Finally, a higher order superhydrophobic gold grating was considered, that, in virtue of its large period and groove width, could provide a tuning range, that is large enough to effectively switch on and off parts of the spectrum. The device opens up perspectives for a superhydrophobic surface based optical phase array.

Chapter 4

Gedankenexperiments with superhydrophobic surfaces

In this chapter we consider the role of metastable drop conformations for the contact angle on superhydrophobic surfaces. We outline qualitatively several drop states and consider the effect of 'open' and 'connected' surface patterns.

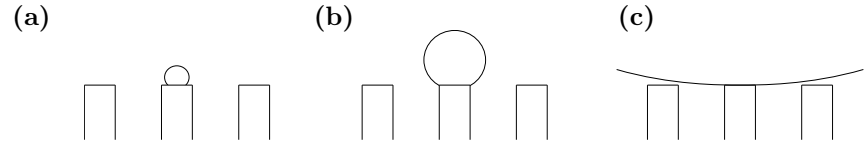

Figure 4.1: **Drop on a superhydrophobic surface in the absence of gravity.** Starting from an initially microscopic drop on one pillar **(a)**, the drop volume is increased **(b-c)**. In the absence of external perturbations, the liquid-gas interface remains attached to the initial pillar and grows to a near perfect sphere **(c)**.

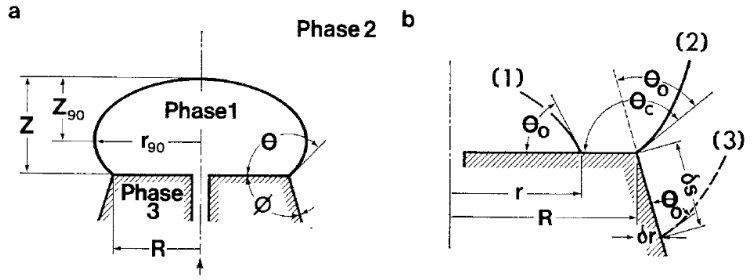

Figure 4.2: **A 'drop expansion' experiment on one pillar on macroscopic scales.** The denoted angle θ_0 is the Young angle, which is in this case smaller than 90°. θ_c measures the critical angle with respect to the flat surface. The critical condition for downward translation on the wall is illustrated by the dashed line. (From "Resistance to spreading of liquids by sharp edges" by J. F.'Oliver, C. Huh, and S. G. Mason. In *Journal of Colloid and Interface Science* **59**, p.568 (1977) ©2008 Elsevier. Reprinted by permission.)

The chapter is organized as follows. We first illustrate in Sec. 4.1 the role of metastable drop states. Subsequently we discuss in Sec. 4.2 the main features of drop conformations encountered in typical laboratory experiments with superhydrophobic surfaces. In Sec. 4.3 we review recent experimental data obtained with drops on 'connected' surface patterns, and sketch the main features of corresponding drop conformations. The chapter is concluded in Sec. 4.4. An outlook is given in Sec. 4.5.

4.1 Metastable states

Let us consider a superhydrophobic surface that is made up of cylindrical pillars. At first, let us neglect gravity. If we place a microscopic drop on one of the pillars (the drop shall be smaller than the width of the pillar), the drop adapts the usual spherical cap shape with the Young angle at the contact line Fig.4.1(a). Let us increase the liquid volume. The drop grows. To continuously satisfy the local Young condition, the contact line translates on the horizontal surface, until it reaches the edge of the pillar (Fig.4.1(b)). Upon further increase of the volume, the angle between

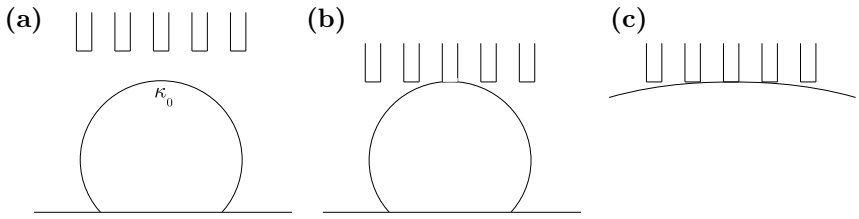

Figure 4.3: **A superhydrophobic surface under gravity turned up-side-down. (a)** The surface is approached from below with a sessile drop that has initially a curvature $\kappa_0 > 0$ in its tip. **(b)** Subsequently the volume of the drop is increased (and the height of the support of the drop is lowered accordingly). **(c)** The drop grows without the liquid-gas interface ever touching an adjacent pillar.

the horizontal surface and the liquid-gas interface increases. However, if the contact angle on the wall of the pillar is larger than 90°, the contact line does not slide downwards on the vertical wall of the pillar. Furthermore, the energy corresponding to a 'jump' of the contact line to an adjacent pillar is larger than the energy provided by thermal fluctuations (see also Sec. 2.2.2). Thus, the liquid-gas interface remains pinned at the edge of the initial pillar. The latter experiment can be realized in practice on the macroscopic scale. Fig.4.2 reprints a figure from [87], where the authors illustrate a similar experiment that they perform on macroscopic scales. In this case the experiment is performed under the influence of gravity (flattened drop), and with a liquid that has a contact angle smaller than 90°, and with an inclined side wall such that the contact line will translate downwards when the liquid volume is large enough. However, the crucial point concerning 'jumps' of the contact line is well understood. Under macroscopic conditions it is evident that the contact line will not 'jump' spontaneously (i.e. thermally driven) to the adjacent pillar. This comparison to the macroscopic scale can be helpful to understand the behavior of a liquid on small scales. The behavior of liquid on a superhydrophobic surface is understood easily by realizing that the microscopic liquid-gas interfaces behave essentially like an equivalent macroscopic system. Let us return to our gedankenexperiment under zero gravity conditions. We realize that however large we make the volume of the drop, its surface will not touch the adjacent pillar. One stable conformation for a drop on a superhydrophobic surface (under zero-gravity conditions) is thus a nearly perfect sphere that is attached to a single pillar (Fig.4.1(c)). In this case the apparent macroscopic contact angle is 180°.

One may argue that, however intelligible above gedankenexperiment may be, the zero-gravity condition represents nothing but an artificial, unrealistic case that has little to do with a drop placed on a real superhydrophobic surface under laboratory conditions. However, above gedankenexperiment is closer to a laboratory experiment than it may seem. To allow for gravity, let us turn the system up-side down (we imagine that we settle the drop on a suitable flat surface, e.g. on an ordinary hydrophobic

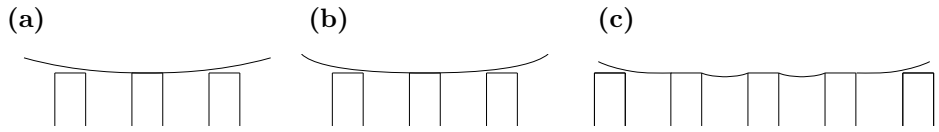

Figure 4.4: **Drop on a superhydrophobic surface under gravity.** Upon slowly turning on gravity the drop sags **(a)** and covers an increasing number of pillars **(b)**, however, at any time the liquid-gas interface remains in a condition just before touching the next pillar, such that the macroscopic contact angle remains 180° **(c)**.

surface). Let us also skip the procedure of 'pumping up' an initially microscopic drop (such a procedure may indeed be difficult in practice due to evaporation), and instead start right away with a macroscopic sessile drop (Fig.4.3a). In virtue of the Laplace law, the curvature of the drop increases from some value κ_0 in its apex to $\kappa_0 + P_h/\sigma$ at its foot. If we don't place a really large puddle, initially $\kappa_0 > 0$. Rather than increasing the volume of the drop, we now approach the drop with a superhydrophobic surface from the top, until one pillar gets in contact with the apex (Fig.4.3b). Now we can increase the volume and perform the same experiment as before. The resulting conformation of the drop is similar to the previous conformation, with one pillar attached to the surface and an apparent macroscopic contact angle of 180° (Fig.4.3c).

When gravity is admitted to the spherical drop resting on a single pillar (Fig.4.1), the drop will sag and its surface will get in contact with other pillars. One could speculate that such a conformation could be characterized by an apparent contact angle smaller than 180°, and maybe agree with contact angles observed experimentally on superhydrophobic surfaces with pillar patterns, which are typically between 150° and 170°. Let us therefore consider this case. The drop will sag as illustrated in Fig.4.4(b), and its surface will get in contact with adjacent pillars. Such a conformation is illustrated in Fig.4.4(c). As we increase the sagging of the drop (by further increasing gravity), this process repeats, and the drop gets in contact with an increasing number of pillars. However, at any time the drop surface is in a state 'just before touching the next pillar'. Thus, the apparent macroscopic contact angle is again 180°. This illustrates that gravity alone is not enough to 'break' a metastable drop conformation in such a way that the apparent contact angle becomes smaller than 180°. One mechanism that could provide a drop conformation with a contact angle smaller than 180° is external forcing. This is considered in the subsequent section.

4.2 Qualitative picture of a drop on a superhydrophobic surface

Above gedankenexperiments illustrate that the shape of a liquid drop on a superhydrophobic surface is not simply described by a minimal energy problem. Since thermal excitations are not large enough to perturb the contact line over heterogeneities, the system does not seek a global energy minimum by itself, rather every state that agrees

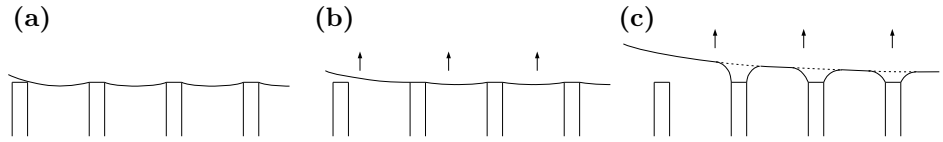

Figure 4.5: **Detachment of a sagged drop.** Gravity is slowly turned off. To satisfy the global shape change, the surface lifts upwards at any but the central pillar **(a-b)**. To satisfy the curvature $\kappa = \kappa_0 + P_h/\sigma$ imposed by Laplace's law, the surface forms catenoid like protuberances at the pillars **(c)**.

with the boundary conditions (local contact angle and volume constraint) is a stable state. The 'sphere-on-a-pillar' and the 'sagged-sphere' state encountered above are only two special cases. The question is then: which is the state that a drop adopts in a typical laboratory experiment? This is discussed in the following. We analyze qualitatively the main features of the three-dimensional shape of a sessile drop on a superhydropdrophobic surface.

Under realistic conditions of a contact angle measurement (e.g. using the sessile drop method), it is certainly impossible to maintain the fragile states described in above gedankenexperiment. Through external perturbations such as thermal drift, air flow, mechanical vibrations, or an uncompensated inclination of the substrate with respect to the gravitational force, one will sooner or later –possibly in an unwanted fashion– force the drop downwards or sidewards on the surface. This scenario suggests to evaluate a receding contact angle.

To this end, let us return to the drop under gravity that is sagged and in contact with many pillars. Let us consider the case where surface tension dominates over gravity, such that anywhere on the drop the curvature is close to the curvature κ_0 at the top of the drop. Let us now slowly turn *off* gravity. Due to the global change of the shape from a sag back towards a sphere, the surface will lift upwards at any but the central pillar. Fig.4.5a-b) illustrates this process at the edge of the foot region of the drop. Since $\kappa \approx \kappa_0$, the curvature of the liquid-gas interface changes only by a small amount (both the radius of curvature and the distance by which the surface is lifted are large compared to the pillar radius). To satisfy the condition of approximately constant curvature, while maintaining contact to the pillars, the surface must form catenoid-like protuberances (Fig.4.5c)). If the radius of a pillar is much smaller than the distance between two adjacent pillars, the protuberance are approximately independent. Since the characteristic scale of a protuberance is much smaller than the global radius of curvature, the protuberance must effectively provide zero curvature. Thus the surface is approximately a catenoid 'glued' to a flat. Let us evaluate how long a pillar stays attached to the surface.

The condition for the detachment is given by Young's condition. The liquid-gas interface detaches when the angle at the ridge of the pillar reaches the Young angle with respect to the flat surface (Fig.4.6a)) (indeed, it is the same condition as the critical condition for bubble expansion with an immersed superhydrophobic surface demonstrated experimentally in the preceding chapter). An intuitive guess for the

Figure 4.6: **Schematic of the detachment process at a single pillar. (a)** critical condition for detachment. **(b-c)** Model for the detachment of a single pillar. A pillar of radius R is retracted from a flat surface until, at a distance d, the liquid-gas interface reaches Young's angle with respect to the horizontal surface and detaches.

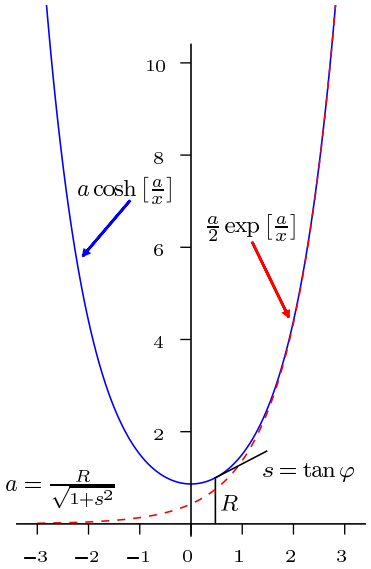

Figure 4.7: **Characteristic scale of a catenary.** The radius R of the pillar and the critical condition for detachment with the Young angle $\vartheta_Y = \varphi + 90°$ at the pillar's edge determine the scale a of the catenary.

critical distance at which the pillar detaches would be the radius of the pillar. Let us check this. Let us make a simple model with a flat surface, and one cylindrical pillar that touches it, and let us retract the pillar until it detaches (while maintaining the zero curvature of the initially flat surface) (Fig.4.6b-c)). The problem is somewhat counter intuitive. In fact, an interface as sketched in the figure does not exist (or has not been found to date). The only known surface with zero mean curvature in $\mathbb{R}^3$ without discontinuities –with exception of the plane and the rather special case of a helicoid– is the catenoid. It is obtained by revoluting a catenary (Fig.4.7), given by

$$y = \frac{a}{2}\left(e^{x/a} + e^{-x/a}\right) = a\cosh(x/a). \tag{4.1}$$

It is seen that the catenary grows indefinitely: though a catenoid has zero mean curvature at any x, it never approaches a flat surface. Therefore, a catenoid cannot be stitched seamlessly to a plane to yield another zero mean curvature surface. Indeed no known surface describes our problem, or in other words, our problem is strictly speaking ill posed. In nature, a small amount of gravity or the global curvature of the drop that is actually not exactly zero, fixes the problem. Here, we fix the problem by asking not for an x_0, where the catenary approaches infinity (a pole), rather we ask for the *characteristic scale* of the catenary above which it starts its rapid growth, i.e., we ask for the scale of the leading exponential term. Thus, we seek to determine a, for a given Young angle ϑ and given radius R of the pillar. Let us denote the slope corresponding to the Young angle with $s = \tan\varphi = \tan(\vartheta - 90°)$. We wish to solve

$$y'(x(R)) = s \tag{4.2}$$

for a, where $x(R)$ is the solution of the catenary equation to x. The latter is found through an inverse identity for the cosh

$$\cosh^{-1}(z) = \ln\left(z + \sqrt{z^2 - 1}\right). \tag{4.3}$$

Inserting above expressions in the derivative of the catenary equation yields

$$2s = \frac{R}{a} + \sqrt{\frac{R^2}{a^2} - 1} - \left(\frac{R}{a} + \sqrt{\frac{R^2}{a^2} - 1}\right)^{-1}, \tag{4.4}$$

which has an explicit solution to a, resulting in

$$a = \frac{R}{\sqrt{1 + s^2}}. \tag{4.5}$$

Thus, indeed, for moderate Young angles (as long as the Young angle is not close to 180°), the distance between the base surface and the pillar at which the protuberance detaches, is of the order R. One observation is worth noticing: the analogue result for a contact angle *smaller* than 90° (as is encountered e.g. with a superoleophobic surface) is not qualitatively different: we can imagine the pillar attached instead on the left branch of the catenary at negative x. Finally, it is worth considering

the detachment process itself: is the translation of the contact line on the face of the pillar a reversible process that we can stop half way (by reducing the distance between the pillar and the surface again), or is it an irreversible process, limited only by viscosity, that kicks in as soon as the Young angle at the ridge of the pillar is reached? Yes, it is irreversible. As the radius of the circular contact line on the face of the pillar decreases, the distance to the flat surface that was required to allow for a stable protuberance is only smaller (in virtue of Eq. (4.5)), such that the pulling force gets only stronger, amplifying the detachment process. For our gedankenexperiment with decreasing gravity or 'lifting' a sagged drop, this implies that the drop will easily detach from individual pillars. This agrees with the high mobility and low contact angle hysteresis observed with drops on superhydrophobic surfaces.

We now draw the connection between above gedankenexperiment of 'turning off gravity' to the real-life deposition of a drop on a superhydrophobic surface. Suppose we manage to place a drop on a superhydrophobic surface in the ideal 'sphere-on-a-pillar' or 'sagged-sphere' state (Fig.4.1(c),Fig.4.4(c)). However, during the experiment we introduce a perturbation, e.g., we apply for a short time a downward force on the tip of the drop (e.g. by an air flow, or by inertia arising after the macroscopic detachment of a syringe that we used to deposit the drop). In such a case, the drop will touch down on the surface, getting attached to many pillars, and relax back upwards, possibly detaching again from some of the pillars. Inertial effects aside, such a process is arguably similar to the one encountered in above gedankenexperiment of 'slowly turning on and off gravity'. Alternatively, we may slightly incline the surface, and roll the deposited drop back and forth. Arguably this results as well in a similar state.

The metastability of possible drop states leaves it open to us to decide what is our concept of a 'macroscopic apparent contact angle'. Evidently, whatever choice we make, the contact angle will be a function of not only the *size* of the drop, it will also depend on its *history*. Several possible choices are discussed in [119]. One possibility is to 'deposit' a drop on different locations of the surface and to evaluate for each position the corresponding local minimum of the free energy. Subsequently equal a priori probabilities are assigned to all such drop conformations and the apparent contact angle is evaluated from the corresponding ensemble average. Alternatively, an ensemble of drop conformations could be obtained by 'moving' a drop over the surface. Such ensemble averages are arguable because they cannot be rigorously justified and moreover they are not necessarily physical. In any case, those suggestions seem prohibitively difficult [119] and have remained ideas.

In contrast the 'marble-with-protuberances' obtained after slowly turning on and off gravity represents a drop conformation that is both well defined and conceptually simple. And –most importantly– possibly resembles closely the drop conformations encountered in a typical contact angle measurement. Thus, it could provide a feasible and realistic drop conformation for the evaluation of a macroscopic apparent contact angle. We are currently preparing corresponding numerical calculations.

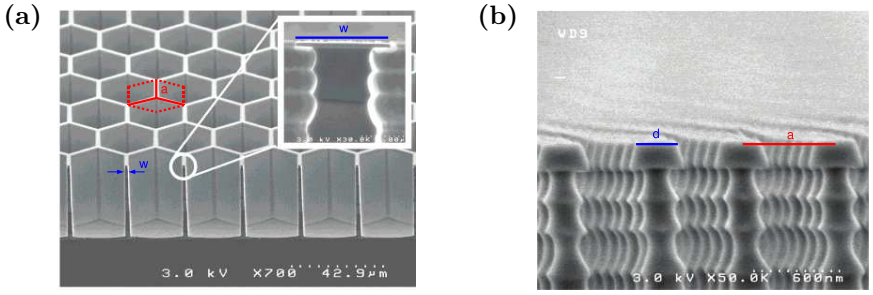

Figure 4.8: **Open and connected surface patterns. (a)** honeycomb **(b)** nanonails structure. Blue and red lines and annotations overlayed on the original figure denote the width w, respectively head diameter d and period a of the structure. (From "Nanonails: A simple geometrical approach to electrically tunable superlyophobic surfaces" by A. Ahuja, J. A. Taylor, V. Lifton, A. A. Sidorenko, T. R. Salamon, E. J. Lobaton, p. Kolodner, and T. N. Krupenkin. In *Langmuir* **22**, p.9 (2008) ©2008 ACS publications. Reprinted by permission.)

4.3 Connected surface patterns

Most common superhydrophobic surfaces feature an 'open' surface pattern with unconnected ridges. Periodic arrays of circular or square pillars and most natural superhydrophobic surfaces are good examples. Recently, superhydrophobic surfaces with a 'connected' surface pattern where studied experimentally [2]. In this case the ridges of the surface pattern form a connected grid. Fig.4.8 reprints a SEM image from [2]. It shows the type of honeycomb structures that were investigated in that work.

On such a structure water adopts an apparent macroscopic contact angle $\vartheta^* = 137.3°$ with a contact angle on a planar substrate $\vartheta_Y = 113.9°$ [2]. In this particular case, the solid surface fraction is

$$\phi_s = \frac{2}{\sqrt{3}\frac{d}{a}} \approx 0.077, \tag{4.6}$$

where $a = 30\mu$m and $d = 2.1\mu$m are the period of the surface pattern, respectively the width of the ridges. For this case, the Cassie-Baxter equation predicts an apparent macroscopic contact angle

$$\vartheta^* = 162.6°, \tag{4.7}$$

which is in contrast to the apparent contact angle found experimentally.

The relevance of the experimental data is underpinned by the simultaneous observation of a large apparent contact angle on an analogue superhydrophobic surface with an 'open' surface pattern. Fig. 4.8 shows the type of 'nanonail' structure studied in [2], providing an 'open' surface pattern. It is important to stress that the 'nanonail' and the 'honeycomb' samples were fabricated with the same protocol (including a silanization step by vapor deposition providing hydrophobicity) suggesting that the

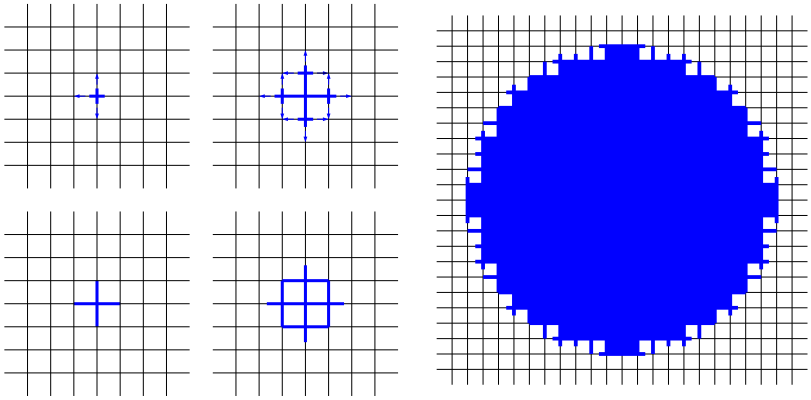

Figure 4.9: Gedankenexperiment with a superhydrophobic surface featuring a connected surface pattern. Blue lines mark the footprint of an initially microscopic drop whose volume is slowly increased (viewed from the top). As the drop grows, unit cells of the surface pattern are repeatedly embraced, thereby forming horizontal liquid-gas interfaces (blue region in (d)).

Young angle on both samples is the same. For the nanonails with head diameter $d = 380\text{nm}$ and pitch $a = 0.9\mu\text{m}$, the solid surface fraction is

$$\phi_s = \frac{\pi(d/2)^2}{a^2} \approx 0.14. \tag{4.8}$$

On this surface, water adopts a contact angle of 155.1°. This measured value is in fair agreement with the Cassie-Baxter equation, which predicts $\vartheta^* = 156.5°$.

It is important to stress that the honeycomb sample features a solid surface fraction that is almost a factor of two smaller than that of the nanonail pattern. Thus, from the point of view of a surface average, one would expect that the honeycomb pattern provides the larger contact angle. Yet, the opposite is the case. This suggests that a contact angle model that is based on an area weighted average cannot capture both results simultaneously.

We now describe qualitatively the conformation of a drop on a connected surface pattern. As an example we consider a square grid as shown in (Fig.4.9a)). Let us repeat the very first gedankenexperiment of increasing an initially microscopic drop with this surface. We can start by depositing a drop on the crossing of two ridges. As we increase the volume of the drop, the its contact line translates smoothly on the surface. Soon the contact line starts translating along the ridges in all four directions. At an early stage, the contact area between the drop and the surface takes the shape of a cross (Fig.4.9a)). The corresponding three-dimensional shape is a complex constant-mean-curvature surface (beautiful examples of such surfaces can be found in [17]). However, here let us merely look at the footprint of the drop. Let us further increase the volume. Soon, at each of the four ridges, the contact line approaches an adjacent crossing (Fig.4.9b)). How does the contact line translate further as the

drop volume is further increased? If it translated only outwards, the resulting finger would have a strong positive curvature that would be incompatible with the constant mean curvature of the the drop. In contrast, if the contact line translates along the perpendicular ridge, the global shape of the drop can relax more and more towards a spherical cap shape. Thus, the contact line translates mainly along the perpendicular ridge (Fig.4.9c)). This results in two contact lines approaching simultaneously the corner of a unit cell. As they meet, they merge, thereby embracing the unit cell, and forming a horizontal liquid-gas interface across its opening. Fig.4.9d) shows the corresponding footprint of the drop. As the drop volume is further increased, this process repeats. Fig.4.9e) shows the footprint of the drop at a later stage. Enclosed unit cells are painted blue. The corresponding global shape of the drop differs from a spherical cap shape only by small deformations in the vicinity of the macroscopic contact line. In this case advancing and receding macroscopic contact angles are well defined. The advancing contact angle is necessarily smaller than 180°, in contrast to the gedankenexperiment with an equivalent open surface pattern. An intuitive guess for the receding contact angle could be that it is close to the Young angle. As for the advancing contact angle, one may speculate that it is possibly considerably smaller than the contact angle of an equivalent surface with an open surface pattern.

4.4 Summary and Conclusions

Several stable conformations of a drop on a superhydrophobic surface were discussed qualitatively for 'open' as well as for 'connected' surface patterns. The effect of gravity and external forcing was considered, and its role in 'breaking' the metastability of high energy drop conformations analyzed. Experimental data for contact angles on connected surface patterns was reviewed, and a local contact angle model was outlined that may explain the 'lesser hydrophobicity' of such surfaces.

The considerations highlight the challenges in developing a complete model of superhydrophobic surfaces that describes experimentally observed contact angles on both open and connected surface patterns [2], and captures at the same time the behavior of low surface tension liquids on reentrant surface profiles [126]. A promising approach could be a local contact angle model similar to models suggested e.g. in [50, 115, 113, 119].

4.5 Outlook

The need for a detailed explanation of recent contact angle measurements on connected surface patterns as well as reentrant profiles [2, 126] may stimulate renewed theoretical efforts in describing superhydrophobic surfaces by means of local contact angle models. It is the hope that this may eventually lead to a detailed understanding of the complex shapes adopted by liquid drops on superhydrophobic surfaces.

From the point of view of experiments, a detailed characterization of contact angles on connected surface patterns promises further insight. It is of interest to investigate systematically the dependence of the apparent contact angle on the surface fraction

and pattern geometry. A similar systematic study with low surface energy liquids on reentrant surfaces is desired. Finally, it could be interesting to directly demonstrate the macroscopic nature of the superhydrophobic state, and actually show the local deformations at the contact line. To this end, it could be interesting to study a 'drop' formed with two density matched immiscible liquids on a superhydrophobic surface with a 'macroscopic' surface texture. Such a system could allow to study directly metastable conformations of a drop. E.g. it could allow to actually prepare a 'sphere-on-a-pillar' state in the laboratory.

Chapter 5

Large bandwidth, highly efficient optical gratings through high index materials

In this chapter we consider methods to increase the spectral bandwidth of dielectric optical gratings. Grating geometries are considered (i) in transmission, (ii) 'buried' grating between two glass bodies, (iii) TIR grating geometry. The effect of a high refractive index grating layer as well as slanted grating lamella is analyzed through numerical simulations. It is shown that a suitable high refractive index grating layer can improve the spectral bandwidth. Dielectric optical gratings with octave spanning -1dB bandwidth are devised, providing a spectral bandwidth that is larger than that of a gold grating.

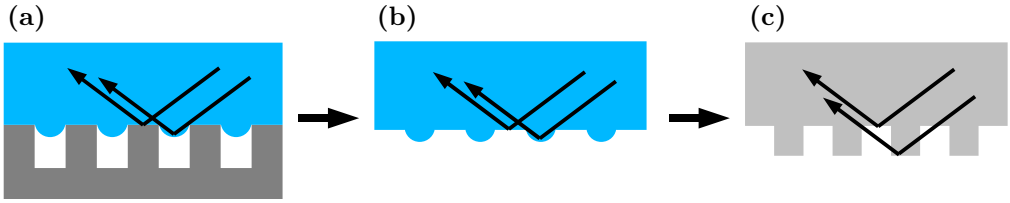

Figure 5.1: **Transformation of a superhydrophobic surface into a TIR grating.** **(a)** Superhydrophobic silicon grating. **(b)** Fictive TIR grating consisting of water. **(c)** Dielectric TIR grating.

5.1 Introduction

The interference phenomenon that arises when illuminating a superhydrophobic optical grating under a grazing incident angle (3.2), and that was understood as a 'total internal reflection' like process, poses the intriguing question, whether this phenomenon could be used to devise a highly efficient optical grating. To address this question we 'transform' the superhydrophobic grating as illustrated in Fig. 5.1. We are guided by the idea that we want to provide interference between *two* totally reflected waves – rather than a TIR and an ordinary reflected wave as is the case with the silicon superhydrophobic surface. We therefore replace the silicon entirely by air (b). The resulting 'water structure' is a rather fictive object. We thus replace the water by glass, and end up with the structure as shown in (c). To provide total internal reflection, we chose an incident angle larger than the angle of total reflection between glass and air. Considering general design rules for efficient optical gratings, we require the period to be small enough such that only one diffraction order is present, and we chose the scattering geometry according to the -1^{st} order Littrow configuration (see also Sec. 2.4.1), resulting in a scattering geometry as shown schematically in Fig. 5.2(a). We leave the Fraunhofer picture and instead consider coupled waves. Considering Eq. (2.56) and Eq. (2.57), it follows that all wavevectors in the transmission region are complex, suggesting that no transmitted wave is present. Thus, the only modes that are present are the 0^{th} and -1^{st} mode on the reflection side. This grating is called dielectric TIR grating.

It is indeed remarkable, given the more than 350 year long history of diffraction gratings [124] (see also 1), that this type of grating was discovered only recently [70, 67, 68]. The TIR grating geometry offers great benefits. Most importantly, a *reflection* type scattering geometry is achieved without the need of a metallic coating. The low absorption loss of the dielectric material results generally in a large diffraction efficiency, paired with a large resistance against laser induced damage [70, 67, 68]. Moreover, the grating does not suffer from the typical reflection losses of dielectric *transmission* gratings (see also Chapter 1). However, as is the case with all dielectric gratings, TIR gratings suffer from a small spectral bandwidth. As we shall show below, in case of the TIR grating the spectral bandwidth is particularly small. This renders the TIR grating unuseful for many applications, such as spectroscopy and

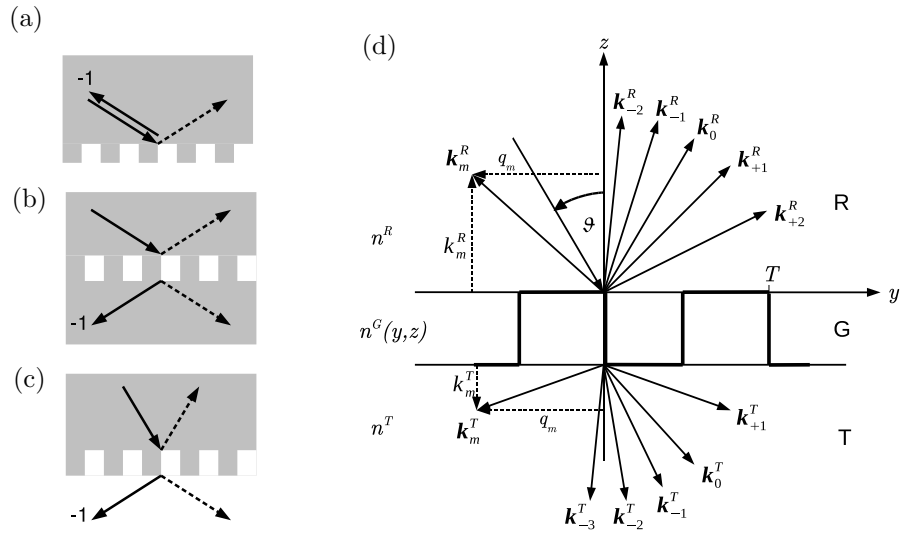

Figure 5.2: (a)–(c) Schematics of the investigated types of dielectric gratings, (a) TIR grating, (b) immersed grating, (c) classical transmission grating. (d) Scattering geometry of an optical grating.

astronomic application.

It is thus the question whether TIR gratings can be improved to provide a much larger spectral bandwidth. In this chapter we shall consider methods to increase the spectral bandwidth of a TIR grating. We will show that a suitable high refractive index grating layer can improve the spectral bandwidth. Allowing additionally for slanted grating lamella, we shall devise dielectric optical gratings with octave spanning -1dB bandwidth, providing a spectral bandwidth that is larger than that of a gold grating. Subsequently we will apply the concept of a high refractive index layer to increase also the spectral bandwidth of 'buried' dielectric gratings, as well as classical dielectric transmission gratings.

The chapter is organized as follows. In the remainder of this introduction, we shall walk through the principles of optical gratings, and optical grating design, using the fused silica dielectric TIR grating as an example. In Sec.5.2, we introduce the use of high index materials to dielectric TIR gratings, and present our numerical results for the diffraction characteristics of the devised designs of dielectric TIR gratings. In Sec.5.4, we extend the use of high index materials to immersed dielectric gratings. We start by analyzing qualitatively the challenge of designing an immersed grating with high dispersion, and subsequently present our numerical results on immersed gratings featuring a high index material. Finally, in Sec.5.5, the use of high index materials is extended to classical dielectric transmission gratings. The chapter is concluded in Sec.5.6.

Fig. 5.2(a) shows the schematic of a dielectric TIR grating. Similar to an ordinary transmission grating, rectangular grooves are fabricated into the backside of a glass

body, and the grating is illuminated from the glass side. However, in contrast to an ordinary transmission grating, the grating is illuminated under an incident angle that is larger than the angle of total internal reflection between glass and air ($\vartheta_T \approx 43.6°$), such that the zero-order transmitted beam is evanescent. Furthermore, the period T of the grating is chosen sufficiently small, such that all other diffraction orders on the transmission side are evanescent as well. This is achieved by stressing the scattering geometry of the grating.

Fig.5.2(d) illustrates the scattering geometry. Generally, as an optical grating is illuminated with a plane wave, a number of plain waves are scattered from the grating. Waves are scattered into the reflection region R , and into the transmission region T, that are characterized each by their refractive index n^R, respectively n^T. Associated with every scattered wave is an amplitude and a wavevector. The wavevector expresses the direction of the wave – or, in case the wavevector is complex, the penetration depth of the evanescent wave. The components of the wavevectors in the periodic direction (here the y-components, see Fig.5.2) are determined by the Bloch condition as $q_m = q_0 + mQ$, where $m = -\infty, \ldots, +\infty$ is the diffraction order, $Q = \lambda/T$, and $q_0 = n^R \sin\vartheta_0$. Here ϑ_0 is the incident angle. We have non-dimensionalized the spatial coordinate through $r \mapsto 2\pi r/\lambda$. The z-components of the wavevectors are determined through the wave equation as $k_m^S = (n^{S\,2} - q_m^{S\,2})^{1/2}$. $S = R, T$ denotes the reflection and transmission region, respectively. A real k represents a propagating diffraction order, a complex k represents an evanescent wave. The latter relations imply the grating equation

$$\sin\vartheta_m^S = \sin\vartheta_0^S + \frac{m\lambda}{n^S T}, \tag{5.1}$$

which expresses the angles of the scattered waves. Angles are measured with a positive sign in positive y-direction, and with a negative sign in negative y-direction. The angular dispersion D follows by differentiating the latter equation with respect to λ,

$$D = \frac{\partial\vartheta_m^R}{\partial\lambda} = -\frac{m}{T n^R \cos\vartheta_m^R}. \tag{5.2}$$

The TIR grating is then arrived at, by requiring

$$|q_m| > n^T. \tag{5.3}$$

This determines a range, where the period of the grating is sufficiently small.

Generally, the highest diffraction efficiency is achieved if the grating is mounted in -1^{st} order Littrow configuration, where the -1^{st} diffraction order is anti parallel to the incident wave, that is $-q_{-1} = q_0$. To see the benefit of this, consider the opposite case: Suppose a binary (rectangular profile) reflection grating is illuminated at zero incident angle, that is, perpendicular to the surface. And suppose the period is small enough, such that only the $+1^{st}$ and the -1^{st} diffraction order are present. It is possible to choose a suitable width and depth of the grating grooves, such that the largest part of the diffracted intensity is scattered into the 0^{th} order, or, by choosing a different width and depth, all of the diffracted intensity is scattered into the first order.

However, due to symmetry, the intensity of the $+1^{st}$ and the -1^{st} diffraction order must be equal, such that, at maximum 50% of the diffracted intensity is scattered into a single diffraction order. In contrast, if the incident angle is chosen such that the -1^{st} diffraction order is anti parallel to the 0^{th} order, only the 0^{th} and the -1^{st} order are present, and the scattered intensity can be distributed at will among those two orders (by choosing a suitable groove width and depth), thus (nearly) 100% diffraction efficiency can be achieved. Remarkably, near 100% diffraction efficiency can be achieved also with higher order Littrow configurations, characterized by $-q_m = q_0$, and even more surprising, this holds true even for higher order TIR gratings, where no longer all transmitted orders are forbidden. We will discuss this in detail in Sec. 5.3. This implies indeed, that the TIR grating condition can be relaxed. Rather than requiring that *all* diffraction orders on the transmission side be evanescent (as suggested originally in Ref.[70], and represented by Eq. (5.3)), it is sufficient to require that the 0^{th} transmitted order is evanescent, i.e., the ordinary condition for total internal reflection is satisfied, expressed as $|q_0| > n^T$. Independent of that, in most cases, one will design a grating for -1^{st} order Littrow configuration, because here, the overlap between higher diffraction orders is minimal – the angular range per diffraction order is largest – such that the largest spectral bandwidth can be achieved.

The Littrow configuration settles the period of the grating as

$$T = m\lambda/(2n^R \sin \vartheta_0^R). \tag{5.4}$$

From now on, we assume the wavelength is 1064nm, the refractive index of the glass is 1.45, and the incident angle is 60°. Thus, the period of the grating is $T = 423.66$nm in our case. This settles also the angular dispersion, since the Littrow condition substituted in Eq. (5.2) yields

$$D = 2/\lambda \tan \vartheta_0. \tag{5.5}$$

The dispersion is minimal at zero angle (perpendicular to the surface), and diverges at grazing angles. With the above parameters, the dispersion is $D = 0.187°/\text{nm}$. A comparably large dispersion is inherent to TIR gratings, because of the necessarily large incident angle.

To arrive at a highly efficient TIR grating, one varies the width w and depth d of the grating grooves, and evaluates the resulting intensity of the -1^{st} diffraction order with a suitable numerical method. A number of efficient numerical methods have been developed over the past decades, that allow to do so. Here, we use the multilayer rigorous coupled wave analysis, as devised in Ref.[77]. The numerical code used in this work [101], is written in FORTRAN 90 and Python [34], and is made freely available under the GPLv3. In this work, all calculations were performed on a grid equipped with 2GHz Dual Core AMD Opteron$^{\text{TM}}$ processors, and took only few hundred cpu hours.

The upper panel of Fig.5.3(a) shows the calculated diffraction intensity of the -1^{st} diffraction order as a function of groove width and depth, for s-polarized light (results for p-polarization and averaged s and p are included in the supplemental material). Broad regions appear, where the diffracted intensity is close to unity. This behavior

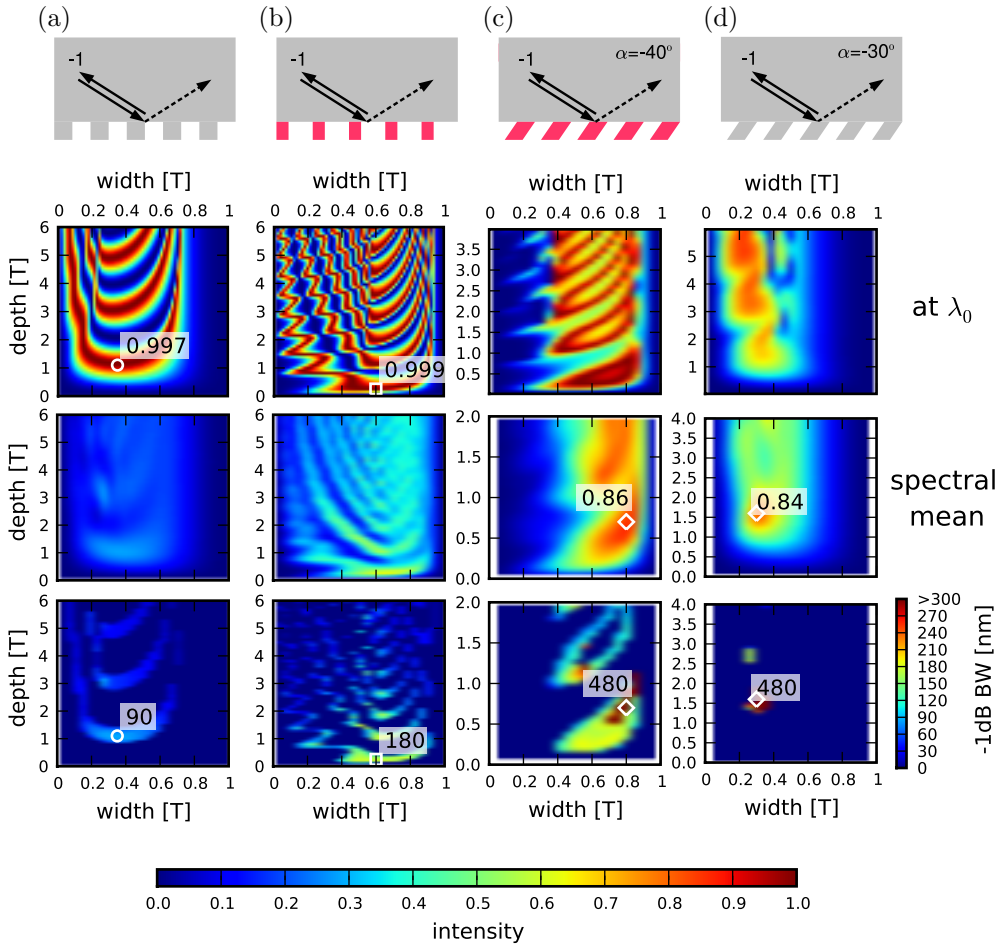

Figure 5.3: Diffraction efficiency of dielectric TIR gratings as a function of the groove width and depth. (a) silica TIR grating. (b) TIR grating based on a high index material (n=2.4). (c) TIR grating based on a high index material featuring slanted lamella ($\alpha = 40°$). (d) silica TIR grating featuring slanted lamella ($\alpha = 30°$). The upper panels show the diffraction efficiency at the design wavelength $\lambda_0 = 1064$nm. The middle panels show the mean diffraction efficiency, averaged over the theoretically accessible spectral band, as determined by the condition of non-overlapping diffraction orders, $\lambda_{cut}/2 < \lambda < \lambda_{cut}$, where $\lambda_{cut} = n^R T(1 + \sin\vartheta_0)$. The lower panel shows the $-1dB$ spectral bandwidth. The open white symbols mark optimal choices of the parameters w and d for each type of grating, and represent those values, for which the spectral characteristics is plotted in Fig.5.4. All results shown correspond to s-polarized light.

can be understood by considering the propagation constants in normal direction, of the modes that are excited inside the grating region [23]. As the grating is arranged in -1^{st} order Littrow configuration, only the fundamental and the first mode in the grating region carry a notable amount of energy. They propagate at different velocities, determined by their propagation constants. Thus, as they propagate, they accumulate a phase shift. The phase shift that the waves have accumulated as they couple out of the grating region, determines whether they are scattered into the ordinary reflected beam or into the -1^{st} order. In this way, by choosing the depth of the grooves, the intensity can be distributed at will among the 0^{th} and the -1^{st} order. The propagation constants of the modes are determined by their effective refractive indices. Those depend on the filling fraction of the grating, that is, the groove width. Consequently, depending on the groove width, a different depth is required to achieve the desired phase difference. The fringes in Fig.5.3(a) correspond to integer multiples of the interference condition. It should be noted, that, along a line in the center of each fringe, the intensity is truly unity. This is in contrast to classical transmission gratings, where the maximum theoretical intensity is limited by the effective reflectivity of the grating, which inevitably results in a scattering loss into the 0^{th} order, such that 100% diffraction efficiency cannot be reached (e.g. [24], and the discussion in Sec.5.4, and Fig.5.8(a)). The latter elevates the TIR grating as a unique component for applications where highest diffraction efficiencies are required. The width-depth-map suggests a number of possible choices for the width and depth, that result in a highly efficient TIR grating. To devise a TIR grating that is easily fabricated in practice, one may chose an intermediate width and a small depth, corresponding to a small aspect ratio. The white circle in the upper panel of Fig.5.3(a) represents one possible choice, with $w = 0.35T$ and $d = 1.1T$. To find the spectral characteristics of the corresponding grating, one varies the wavelength of the incident light, and evaluates the resulting diffraction efficiency. The latter may be done in two ways. (1) The incident angle is held fixed, while the wavelength is varied – this case is encountered, e.g., with gratings that are used for dispersion control in femtosecond laser applications, or with spectrometers that are equipped with a line CCD and operate without movable parts. (2) As the wavelength is varied, the incident angle is adapted, such that the grating continues to satisfy the Littrow condition for every wavelength – this case is encountered, e.g., in a classical scanning monochromator. Here, we consider the first case, motivated by the application of the dielectric TIR grating for pulse compression, and furthermore, because the range of possible incident angles for the TIR grating is not particularly large.

The blue line in Fig.5.4 shows the spectral characteristics of the dielectric TIR grating, with width $0.35T$ and depth $1.1T$, in comparison to a best blazed gold grating (in air), with period $T = 614$nm, that has the same dispersion and incident angle as the TIR grating. The blaze angle of the gold grating was optimized to yield the largest possible bandwidth and peak efficiency in the given wavelength range, found as 33°. The dielectric TIR grating shows excellent properties in a 50-100nm band around its design wavelength. In particular, it reaches 100% diffraction efficiency at its design wavelength, and provides scattering losses smaller than -1dB (95% diffraction efficiency) over a bandwidth of 84nm. Here, it provides unsurpassed diffraction

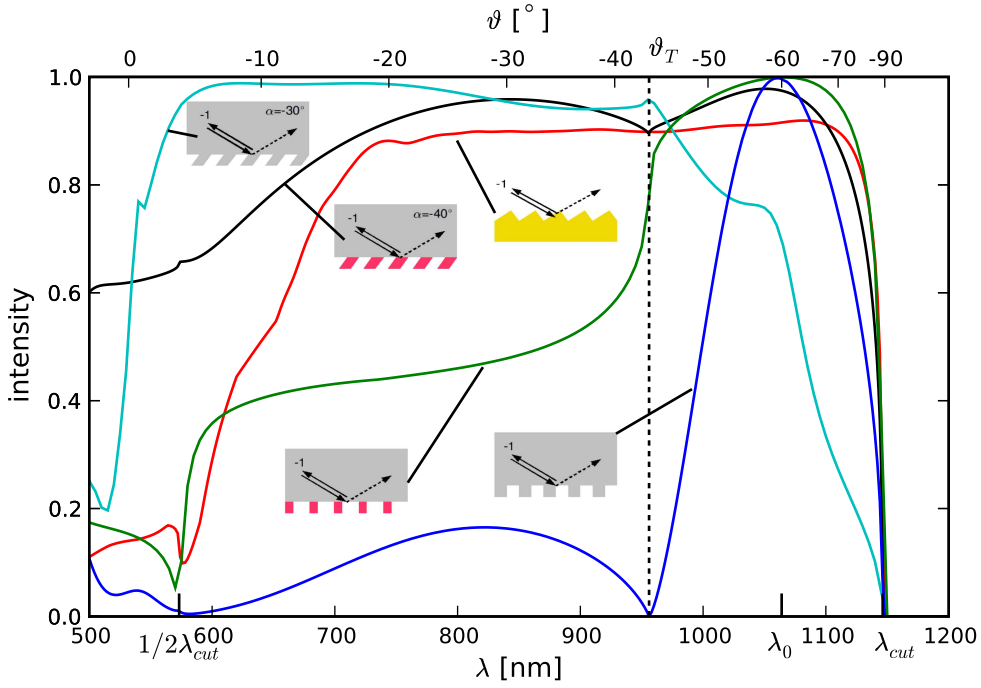

Figure 5.4: Spectral characteristics of dielectric TIR gratings (s-polarized light), as compared to a best blazed gold grating with blaze angle 33° (p-polarized light). The blue line shows the result for a silica TIR grating with groove width $0.35T$ and depth $1.1T$, corresponding to maximum peak efficiency and spectral bandwidth (white circle in Fig.5.3(a)). The green line shows the spectral characteristics of a dielectric TIR grating featuring a high index material ($n = 2.4$) in the grating region ($w = 0.6T$, $d = 0.25T$, as marked by the white square in Fig.5.3(b)). The black line shows the spectral characteristics of a dielectric TIR grating with a high index material and slanted lamella ($\alpha = 40°$), groove width $0.7T$, depth $0.5T$, corresponding to an optimal choice for large mean diffraction efficiency and simultaneously a comparably smooth spectrum, (white diamond in Fig.5.3(c)). The cyan line shows the result for a silica TIR grating with slanted lamella ($\alpha = 30°$), groove width $0.3T$, depth $1.6T$, optimized for high short wavelengths efficiency.

efficiency. Indeed, these high diffraction efficiencies cannot be reached with metallic gratings, whose inherent absorption inevitably results in losses [94]. However, as the wavelength is altered substantially from the design wavelength, the diffraction efficiency quickly drops to zero. In particular, as the angle of the -1^{st} diffraction order reaches the angle of total internal reflection between glass and air, the diffraction intensity drops to a sharp minimum, and for shorter wavelengths – corresponding to angles smaller than the angle of total internal reflection – the diffraction intensity does not recover its initially large value. These diffraction angles correspond to the case, when the -1^{st} diffraction order on the transmission side is no longer evanescent. However, a large diffraction intensity of the reflected -1^{st} order is not strictly forbidden at these scattering angles, as can be seen by the small but nonzero intensity value. This low diffraction efficiency over the largest part of the spectrum renders the TIR grating unusable for a large number of applications, including broadband pulse compression and most spectroscopic applications.

It is desirable, to resolve this issue, and to increase the spectral bandwidth of the TIR grating towards values that are comparable with metallic reflection gratings and dielectric transmission gratings, while maintaining the extraordinarily large peak diffraction efficiency, and the high resistance to laser induced damage. This is the first objective of this paper.

5.2 Large bandwidth dielectric TIR grating

The described phenomenon of a suppressed diffraction intensity at smaller angles, is remarkably robust. A first approach to increase the spectral bandwidth would be, to explore the landscape of possible combinations of the width and the depth, and to evaluate how this effects the spectral characteristics. However, the spectral bandwidth is only decreased. The lower panel of Fig.5.3(a) shows the $-1dB$ spectral bandwidth as a function of the grove width and depth. It is seen, that the previous choice (with $w = 0.35T$ and $d = 1.1T$) corresponds already to the largest possible bandwidth, and for larger depths, the reflectivity and the bandwidth decrease in an oscillatory fashion. This behavior is understood qualitatively by referring to the theory of Kogelnik, who gave an estimate for the bandwidth $\Delta\lambda$ (full width at half maximum) of dielectric transmission gratings in the limit of deep grooves as

$$\frac{\Delta\lambda}{\lambda} = \frac{T}{d}\cot\vartheta_0. \tag{5.6}$$

It is seen, that indeed, the bandwidth is largest at small d.

This qualitative insight suggests already a way to improve the spectral characteristics of the grating. As an increase of the groove depth reduces the spectral bandwidth of the grating, one should try the opposite, one should decrease the groove depth. To do so, the difference of the propagation constants of the two modes in the grating region has to be enlarged, that is, the refractive index contrast has to be increased. Thus, in the grating region, we replace the glass by a material that has a larger refractive index. Suitable high index optical materials that are routinely available in

the form of high quality thin films – through optical coating applications – are, e.g., Sapphire, diamond, TiO_2, etc.. The latter two materials offer the largest refractive index, around 2.4, in the wavelength range considered here [90]. From now on, we assume the refractive index of the high index material is 2.4. It should be noted, that the glass in the reflection region is kept. This is indeed important. If the material in the reflection region was changed together with the groove material, the grating period needed to be decreased accordingly. As a result, the entire computational problem was rescaled, such that no improvement was achieved.

The upper panel of Fig.5.3(b) shows the diffraction efficiency as a function of groove width and depth for the high index TIR grating. It is seen, that indeed, the first fringe is shifted towards shallower grooves. The smallest possible depth is achieved at around $w = 0.6T$ and $d = 0.25T$ (white square in Fig.5.3(b)). And indeed, here, the spectral bandwidth reaches its maximum (lower panel of Fig.5.3(b)). The green line in Fig.5.4 shows the corresponding spectral characteristics. The diffraction efficiency is increased over the entire spectrum as compared to the TIR grating based on glass. In particular, the $-1dB$ bandwidth around the design wavelength, is increased to 180nm, and is more than doubled as compared to the all-in-glass equivalent. Additionally, towards smaller wavelengths, in the range where the diffraction angle is larger than the angle of total internal reflection between glass and air, the diffraction efficiency is greater than 40%. This is a useful value for many spectroscopic applications. In addition, the moderate aspect ratio of the grating grooves (≈ 0.5), suggests that such a grating could be fabricated rather easily. Furthermore, the different nature of the grating and substrate material will probably help to fabricate structures with a very well defined depth, determined only by the thickness of the layer that is deposited prior to the etching process. The thickness of deposited layers can typically be controlled very accurately. Nevertheless, the natural question arises, whether this grating design can be further improved.

We have so far considered only the most simple of all grating profiles – rectangular grooves. It is well known that the diffraction efficiency of a gold grating – in particular its spectral characteristics – can be greatly improved, by choosing an appropriate blaze angle [94]. The blaze angle is chosen such that the incident beam and the diffracted beam are nearly perpendicular to the long face of the grating tooth (over the range of incident angles determined by the desired spectral range). Could the spectral characteristics of the TIR grating be further improved by using an equivalent geometry? As we will show below, the answer is yes, however, it is not sufficient to introduce a blaze, which becomes clear by considering the depth of the grooves necessary to accumulate the required phase shift in the grating region. As the geometry is more complex, the propagation constants of the waves vary in z-direction over the grating region, nevertheless, the mechanism for achieving maximum diffraction efficiency through the constructive interference of the fundamental and the first mode, is still qualitatively the same. And indeed, near 100% diffraction efficiency can be achieved with a large variety of groove geometries, such as symmetric triangles, asymmetric triangles, bow-ties, etc., by choosing a suitable width and depth. However, as is the case with rectangular grooves, generally a relatively large total depth is required, since the difference of the effective index of the propagation constants

is never very large. E.g, in the case of symmetric triangles, a height of several T is required to achieve near 100% diffraction efficiency. In contrast, the blazed geometry is characterized by a small aspect ratio. In particular, the aspect ratio is smaller than $T/2$ (the blazed geometry is characterized by a triangle that features a right angle in its tip, related to the original ruling process that uses an inclined rectangular cutter). Because of this small aspect ratio, the blazed geometry cannot provide a high diffraction efficiency, for the type of dielectric gratings discussed here. However, a geometry that provides inclined faces, without sacrificing the possibility of a large groove depth, is the slanted geometry, characterized by rectangular lamella that are sheared along the periodic direction with a slant angle α. The slant angle is defined as the angle by which the groove wall is rotated as compared to the normal direction. Clockwise rotation corresponds to positive angles. Indeed, the slanted geometry has much in common with the geometry of volume phase holographic gratings, where, in the general case, the crests of the holographically imprinted refractive index modulation are allowed to be slanted with respect to the grating normal (e.g. [8]).

To evaluate the diffraction characteristics of a slanted TIR grating, we compute the diffraction efficiency as a function of groove width, depth and wavelength for all slant angles $-90° < \alpha < 90°$, and for each slant angle, we evaluate the spectral bandwidth. The optimum slant angle is found as $\alpha = 40°$. Fig.5.3(c) shows the plot (a movie sequence showing the plots for all α, is included in the supplemental material). The $-1dB$ bandwidth exceeds 300nm in a region around $w = 0.8T$, $d = 0.7T$. The black line in Fig.5.4 shows the corresponding spectral characteristics. This grating has a diffraction efficiency larger than 90% over nearly the full octave, and outperforms the best blazed gold grating over the largest part of the spectrum. In particular, two broad peaks of high diffraction efficiency appear, at around 30°, and at the design angle, 60°. These broad peaks overlap, and provide very high diffraction efficiency over the hole spectrum. Around each of the peaks, the spectrum is smooth. A shallow kink remains at the wavelength that corresponds to a diffraction angle equal to the angle of total internal reflection. This kink is at the origin of the jump that is observed in the width-depth map of the bandwidth, at the boundary of the region of large bandwidth. As the kink reaches above the $-1dB$ limit, the bandwidth jumps from a value characterized by the width of the right peak, to a value characterized by the width of both peaks together. It should be noted, that a combination of width and depth can be chosen, such that the kink between the two peaks at the angle of total internal reflection, disappears, and the spectrum becomes completely smooth over the full spectral range. However, in this case the spectral bandwidth is slightly smaller. Similarly, a width and depth can be chosen such that the right peak maintains 100% diffraction efficiency at the design wavelength, while the left peak is still higher than 80%. However, in this case, the kink becomes more pronounced. The result plotted here, represents a compromise between largest possible bandwidth and smoothness of the kink. Independent of that, it may also be interesting to operate this grating only with scattering angles smaller than the angle of total internal reflection, that is, the incident light enters the grating under a large angle, and the scattered light returns under angles smaller than the angle of total internal reflection. Thereby, only the left part of the spectrum was used. The design could then be optimized to yield highest

efficiency specifically across the left peak.

The great improvement of the spectral characteristics provided by slanted lamella raises the question whether slanted lamella would also improve a single component TIR grating fabricated entirely from glass. As we will show now, the answer is yes, and it turns out that this is only achieved by optimizing the design in the way just described above, that is, by utilizing the left peak of the spectrum, while the right peak, at the design wavelength, remains small. This is indeed peculiar, because it means, that the grating does *not* feature high efficiency when the wavelength satisfies the Littrow condition, but at another wavelength, which also means, that one overlooks a highly efficient design, if one optimizes the grating parameters in the usual way at the design wavelength (because there the intensity is small). This is indeed remarkable. Recall the intuitive arguments that we put forward to explain why the Littrow configuration leads to a high efficiency. We considered the opposite case, when the incident wave is perpendicular to the surface, and the $+1^{st}$ and the -1^{st} diffraction order are aligned symmetrically around the surface normal. We argued, that, in this case, due to symmetry, the intensity of the orders must be equal, such that at maximum 50% diffraction efficiency can be achieved, and in contrast, if the grating is arranged in Littrow configuration, (near) 100% diffraction efficiency can be achieved. However, with the slanted geometry, the mirror symmetry of the grating around the surface normal is broken, and these arguments are no longer rigorously valid. It turns out that, for the slanted TIR grating in silica, this is indeed strongly violated, and the Littrow configuration is no longer the universal optimum scattering geometry, rather, the optimum is achieved when the white light enters under a large angle, and the arc of diffracted beams leaves under small angles. To the best of our knowledge, an efficient grating with this type of scattering geometry has not been reported before.

Fig.5.3(d) shows the diffraction efficiency as a function of groove width and depth for the slanted silica TIR grating. As with the slanted high index TIR grating, we have evaluated the dependence of the diffraction characteristics on the slant angle (see second movie in the supplemental material), and present here the optimum, found with $\alpha = 30°$. The largest bandwidth is found with width $w = 0.3T$ and depth $d = 1.6T$. The corresponding spectral characteristics are shown with a cyan line in Fig.5.4. The grating has excellent spectral characteristics for wavelength corresponding to diffraction angles below the angle of total internal reflection. For larger angles, the intensity falls off quickly, and at the design wavelength, it has already dropped below the $-1dB$ limit. This remarkable scattering geometry provides an unsurpassed diffraction efficiency over an almost 500nm band towards the short wavelength side of the spectrum. To the best of our knowledge, this represents again, the largest bandwidth highest efficiency reflection type optical grating devised so far.

5.3 Intermezzo: 2^{nd} order TIR grating

It may under certain circumstances be interesting to design a TIR grating in *higher* order Littrow configuration, for instance when high dispersion is required, however,

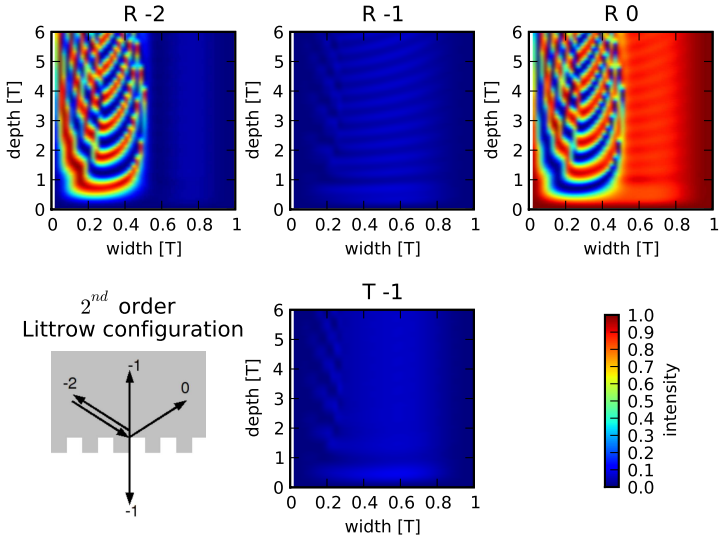

Figure 5.5: 2^{nd} **order TIR grating.** The intensities of the propagating diffraction orders of a silica dielectric TIR grating in 2^{nd} order Littrow configuration (incident angle 60°), s-polarized light, as a function of groove width and depth is shown. The upper panels show the reflected orders from -2 to $+1$ (left to right), the lower panel shows the -1^{st} transmitted order. It is seen, that near 100% diffraction efficiency in the Littrow order is achieved, despite the fact that a real (non-evanescent) transmitted order is present.

technologies to fabricate the corresponding small periods are not available. In virtue of Eq. (5.4), when we double the order m (say from -1 to -2), we should double the period, while the dispersion (Eq. (5.5)) remains the same. This has usually two effects. (1) diffraction orders overlap such that the usable spectral bandwidth is smaller. (2) part of the diffracted intensity is lost into the other orders, such that the diffraction efficiency is somewhat lower. Nevertheless, for metallic reflection gratings or dielectric transmission gratings, typically reasonable diffraction efficiencies can still be achieved at moderately large Littrow orders. However, how about dielectric TIR gratings? Here the situation is different. When we increase the grating period (while maintaining the Littrow condition), with reflection or transmission gratings 'new' diffraction orders appear 'next' to the littrow order, in contrast with the TIR grating, if we increase the Littrow order from -1 to -2, a new diffraction order appears on the transmission side (see Fig. 5.5), where there had previously been no order at all, and one may expect that now the diffracted intensity ends up in this order, just as with an ordinary transmission grating where none of the reflected orders carries a notable share of the diffracted intensity (rather, nearly all intensity ends up on the transmission side) and thus the reflecting character of the TIR grating is lost. And indeed, this is what was suggested originally in Ref. [70], where the TIR grating geometry was introduced

requiring that *all* orders on the transmission side are evanescent. However, as we will now show, this is not the case. The TIR grating geometry works very well also in higher order Littrow configuration, when transmitted orders are present. Probably because of some momentum conservation, or symmetry condition, the intensity of the transmitted orders reduces effectively to zero.

Fig.5.5 shows the diffracted intensity (as a function of groove width and depth) for a -2^{nd} order TIR grating. It is seen, that the diffracted intensity is distributed predominantly between the -2^{nd} and 0^{th} reflected order. For many choices of the groove width and depth, the intensity of the Littrow order reaches near 100%. The intensity of the -1^{st} transmitted order 'magically' reduces to zero. We can therefore relax the TIR grating condition to requiring solely that the ordinary transmitted wave is evanescent, that is, to requiring just the ordinary condition of total internal reflection.

5.4 Large bandwidth immersed grating

The described dramatic improvement of the spectral bandwidth of a dielectric TIR grating through a high index material, is more general. In particular, the introduction of a high index material improves dramatically also the performance of immersed dielectric gratings [85] at large incident angles. This is important, since, by virtue of Eq. (5.5), large angles correspond to large dispersion. In addition, the immersed dielectric grating has been suggested previously, for providing a device that is easily cleaned, and usable in a rough (dirty) environment. Fig.5.2(b) shows the schematic of an immersed dielectric grating. The system is identical to the TIR grating, except that the air on the transmission side is replaced by a glass body. Besides the practical advantages related to cleaning, immersed dielectric gratings have another particular advantage over ordinary transmission gratings. In contrast to the latter, they can provide theoretically 100% diffraction efficiency. The latter is the topic of a recent paper [24], where the authors show, that 100% diffraction efficiency is linked to equal effective reflectivity of the top and bottom boundary of the grating region. If the incident and transmission halfspaces have a different refractive index – as is the case for an ordinary transmission grating, where the transmission region is air – the reflectivities of the top and bottom grating boundary are different, such that, even if a suitable interference condition is met for the two modes that travel in the grating region, a finite intensity remains, that results in an inevitable reflection loss into the ordinary reflected order. Thus, the diffraction efficiency is at best one minus an effective reflectivity of the optical grating. The latter can be substantial, especially when highest efficiencies are required, as is the case in many laser applications, and especially with large angles, where the grating provides its largest dispersion. In contrast, the immersed dielectric grating does not suffer this deficiency, and it can theoretically provide 100% diffraction efficiency – analog to the TIR grating.

However, as was the case with the TIR grating, the spectral bandwidth is limited, and, more importantly, if operated with large incident angles – corresponding to large dispersion –, the immersed grating starts to loose its extraordinarily good character-

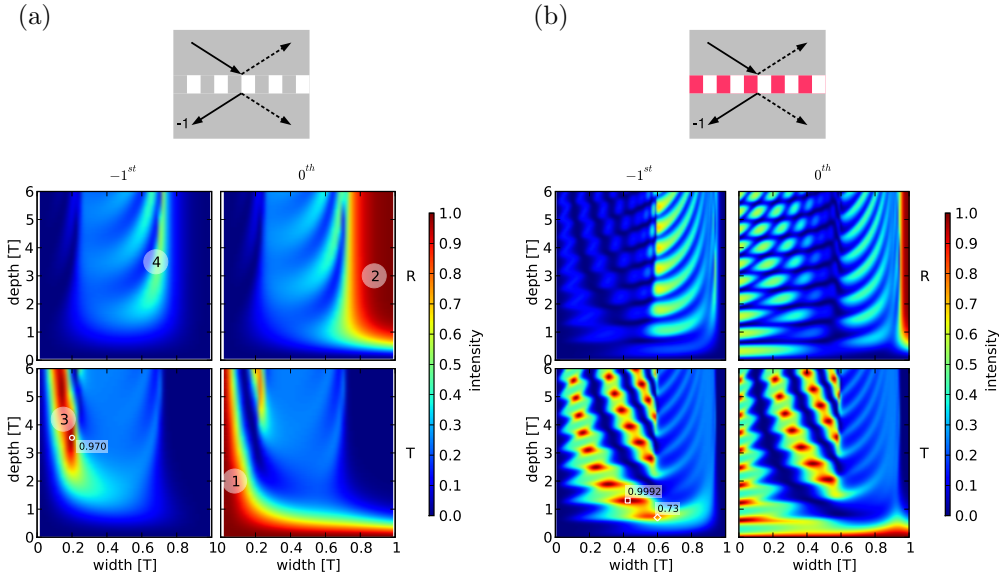

Figure 5.6: (a) diffraction efficiency for an immersed dielectric grating, illuminated under a large incident angle ($\vartheta_0 = 60°$). The upper panels show the reflected orders, the lower panels show the transmitted orders. The left and right panels show the -1^{st} and 0^{th} order, respectively. (b) same as in (a), for a grating featuring a high index material ($n = 2.4$) in the grating region.

istics. The four left panels of Fig.5.6 show the diffraction efficiency (s-polarization) as a function of groove width and depth, for an immersed dielectric grating, illuminated under a large incident angle (throughout this section, we consider the same incident angle, $\vartheta_0 = 60°$, and period, $T = 423.66$nm, as before, linked to the -1^{st} order Littrow condition, and providing the same dispersion). Four regimes appear. (1) At small groove depth, the ordinary transmitted intensity is large – the grating is negligible. (2) At large groove depth and large groove width, the ordinary reflected intensity is large – the grating region is increasingly similar to a large air gap, and total internal reflection occurs at the top grating surface. (3) Towards smaller groove widths, a region exists, where nearly all of the scattered intensity is scattered into the transmitted -1^{st} order – the grating resembles an efficient transmission grating. (4) Towards larger groove widths, a region exists, where a large part of the scattered intensity is scattered into the reflected -1^{st} order – the grating resembles a TIR grating. Thus, when illuminated with a large incident angle, depending on the groove width and depth, the immersed dielectric grating can be either more akin to a TIR grating or more akin to a transmission grating or somewhere in between. As a consequence of that, the regions of optimal choice of width and depth shrink to narrow domains, and, generally, a high diffraction efficiency is achieved only at rather large depths, corresponding to aspect ratios that are not easily fabricated in practice. Qualitatively, the four regimes described above, are a consequence, of the effective

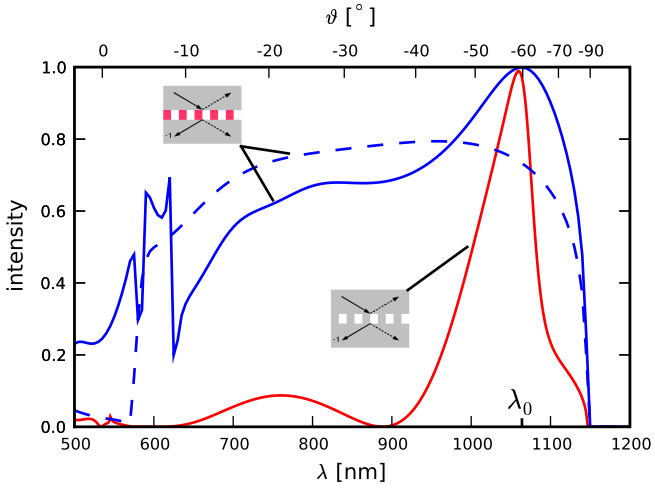

Figure 5.7: Spectral characteristics for an immersed dielectric grating featuring a high index material in the grating region (blue lines), as compared to its all-in-glass equivalent (red line). The solid blue line represents a design that is optimized for highest peak efficiency, corresponding to $w = 0.43T$ and $d = 1.3T$, as shown by the white square in Fig.5.6(b)). The dashed blue line represents a design that is optimized for maximum bandwidth, corresponding to $w = 0.6T$ and $d = 0.7T$, as shown by the white diamond in Fig.5.6(b).

refractive index experienced by the fundamental mode in the grating region, and the resulting reflectivities at the top and bottom interface. The effective refractive index of the fundamental mode is determined by the mean refractive index. For large groove width, the effective index is near to unity. Thus, as the incident angle is large, the fundamental mode in the grating region becomes evanescent. Therefore, a notable amount of light can traverse the grating region only if the thickness of the grating is of the same order as the penetration depth of the evanescent wave. This small thickness conflicts with the interference condition for the two modes in the grating region, that requires a sufficiently large thickness to accumulate the necessary phase difference between the fundamental and the first mode. Thus, for those groove widths, for which the fundamental grating mode is evanescent, a high diffraction efficiency cannot be achieved. As the incident angle is large, most of the reasonable choices for the width and depth fall into this regime. This makes the design of a high dispersion immersed grating a hard task. It is remarkable, that also here, the introduction of a high index material provides a solution, though, through a rather different mechanism then observed previously with the TIR grating. While, in case of the TIR grating, the high index material paved the way to a grating with shallow grooves, by providing a high refractive index contrast, here the high index material serves to increase the average refractive index in the grating region – potentially above the refractive index

of glass – to render the grating truly transparent for any incident angle (for most of the possible filling factors).

The four right panels of Fig.5.6 shows the diffraction efficiency of an immersed transmission grating using a high index material in the grating region (as before, we assume the refractive index of the high index material is $n = 2.4$). A region is opened up in the range $w < 0.6T$, where the grating becomes transparent. Near 100% diffraction efficiency is achieved with a number of possible choices of the width and depth. Fig.5.7 shows the corresponding spectral characteristics for two possible choices of the groove width and depth, as compared to the equivalent immersed grating fabricated entirely from glass. The solid blue line corresponds to $w = 0.43T$ and $d = 1.3T$, as shown by the white square in Fig.5.6(b), and represents a design that is optimized for highest peak efficiency in a narrow band around the design wavelength. The dashed blue line corresponds to $w = 0.6T$ and $d = 0.7T$, as shown by the white diamond in Fig.5.6(b), and represents a design that is optimized for maximum bandwidth (around 80% diffraction efficiency over nearly the full octave). To the best of our knowledge, the latter represents the largest bandwidth transmission grating (with the large dispersion considered here), devised so far.

5.5 Classical transmission grating with large bandwidth and 100% peak efficiency

The successful improvement of the spectral and dispersive characteristics of a dielectric TIR, as well as dielectric immersed gratings, described in the preceding sections, intrigues the question, whether a high index material can also contribute to improve transmission gratings of the classical design.

Fig.5.2(c) shows the schematics of a classical transmission grating. As in the case of the dielectric TIR grating, light is diffracted at the back side of a glass body. However, here the incident angle is smaller than the angle of total internal reflection, such that the light is mainly scattered into transmitted diffraction orders. This grating geometry has a number of great advantages. (1) Due to refraction, the transmitted orders leave the grating under a large angle, which, in virtue of Eq. (5.5) corresponds to large dispersion. Because of this, dielectric transmission gratings are usually superior over classical reflection gratings in the large dispersion regime (2) This is achieved without the need of a particularly small period, since, in virtue of Eq. (5.4), the period is determined by the incident angle, and the latter is – again, due to the refraction – comparably small. This facilitates fabrication in practice (though, the period is not smaller than that of a gold grating with equal dispersion – it is the same). (3) The diffracted wave lives in air, saving the necessity to couple out the arc of diffracted rays through a flat or suitably curved glass-air interface (in certain applications, such as e.g. grism applications, the coupling out through the glass-air interface, as faced e.g. in case of the TIR grating, may however also be used to a benefit, e.g., its dispersive nature may be specifically used to compensate for higher order dispersion [38]).

Because of these great advantages, the backside diffraction geometry is to date the primary choice for most dielectric grating applications.

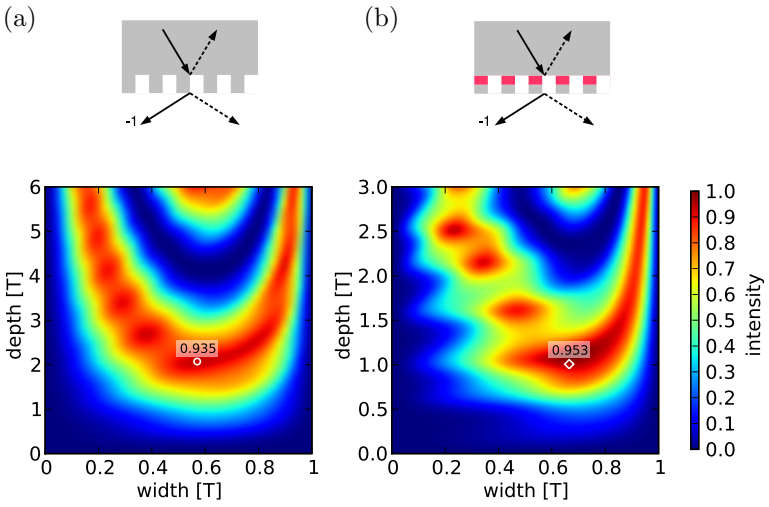

Figure 5.8: (a) diffraction efficiency of a classical dielectric transmission grating. (b) diffraction efficiency of a two-layer grating featuring a buried high index layer, with thickness ratio $r = 0.5$. White diamonds mark those values of the groove width and depth, for which the spectral characteristics are plotted in Fig.5.9.

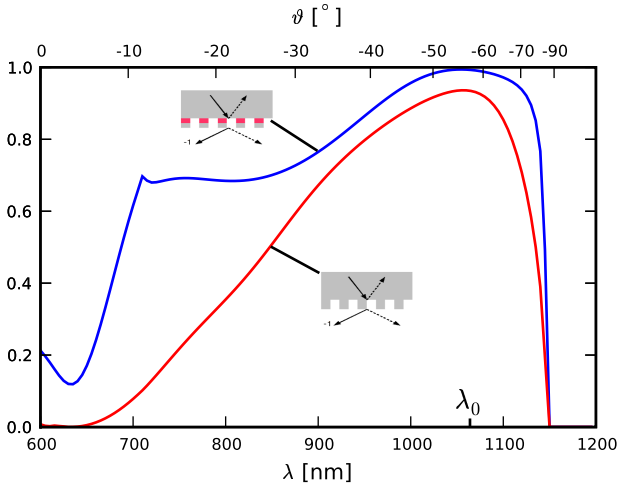

Figure 5.9: Spectral characteristics of a dielectric transmission grating featuring a buried high index layer (blue line), as compared to a classical transmission grating (red line). The groove width an depth are $w = 0.7T$, $d = 1.1T$, respectively $w = 0.57T$, $d = 2.07T$, as shown by the diamond and circle in Fig.5.8.

Fig.5.8(a) shows the diffraction efficiency as a function of groove width and depth, for a classical dielectric transmission grating. The grating period is $T = 423.66$nm, as before, and the incident angle is chosen such that the diffraction angle of the transmitted -1^{st} order is $60°$, such that both the diffraction angle and the angular dispersion are the same as before. Maximum diffraction efficiency is achieved for width $w = 0.57T$ and depth $d = 2.07T$, corresponding to the center of the first fringe (white circle). The effective reflectivity of the top and bottom surface of the grating region are not equal, such that a reflection loss into the ordinary reflected order is encountered, and the diffraction efficiency remains smaller than 100%. The maximum diffraction efficiency is found as 93.5% with $w = 0.57T$ and $d = 2.07T$. The red line in Fig.5.9 shows the corresponding spectral characteristics.

The qualitative understanding of the reflection loss suggests that a low loss into the fundamental reflected order could be achievable, if the effective refractive index in the grating region for the fundamental mode is close to $\sqrt{n^R}$, and the thickness of the grating region is close to an integer multiple of $\lambda/(4n^R)$, as is the principle of single layer anti-reflection coatings. In contrast, a large reflection loss into the fundamental order was expected, if the effective refractive index of the fundamental mode in the grating region is high. A substitution of the glass in the grating region by a high index material is therefore not promising. However it turns out, that a simple two-layer grating is already enough. To ensure a low reflectivity at the bottom grating surface, the high index grating layer is buried underneath the glass layer, as shown in Fig.5.8(b). To find the optimum thickness of both grating layers, we evaluated the diffraction efficiency as a function of width, depth and ratio $r = d_h/d_g$ of the thickness d_h and d_g of the high index layer, respectively the glass layer (third supplemental movie). Fig.5.8(b) shows the optimum choice corresponding to $r = 0.5$. The optimum width and depth is found as $w = 0.7T$ and $d = 1.1T$. Remarkably, the grating reaches effectively 100% diffraction efficiency. Thus, the TIR grating featuring a buried high index layer is indeed a complementary approach to a transmission grating featuring 100% diffraction efficiency, and an alternative to the immersed dielectric grating devised in [24]. Additionally, the spectral characteristics are greatly improved. The blue line in Fig.5.9 shows the spectral characteristics. The grating surpasses a classical transmission grating over the entire spectrum. To the best of our knowledge, this represents the largest bandwidth, high efficiency transmission grating devised to date.

5.6 Summary and conclusions

We have analyzed the diffraction characteristics of dielectric gratings that feature a high index grating layer, and shown parameter choices that are superior in terms of bandwidth and efficiency. A qualitative understanding is supplied in combination with rigorous calculations. The common grating types were considered, including reflection gratings, immersed transmission gratings and classical transmission gratings. Several profile types were explored, including novel structures, that comprise a combination of enhanced material and enhanced geometry. The suggested devices are within current

manufacturing capabilities. The gratings are compared to existing technology and applications are pointed out. We expect these types of gratings to become a useful addition to the existing range of grating geometries.

Chapter 6

Collective dynamics of ultrasound driven micromenisci

We study the dynamics of periodic arrays of micrometer-sized liquid-gas menisci formed at superhydrophobic surfaces immersed into water. By measuring the intensity of optical diffraction peaks in real time we are able to resolve nanometer scale oscillations of the menisci with sub-microsecond time resolution. Upon driving the system with an ultrasound field at variable frequency we observe a pronounced resonance at a few hundred kHz, depending on the exact geometry. Modeling the system using the unsteady Stokes equation, we find that this low resonance frequency is caused by a collective mode of the acoustically coupled oscillating menisci.

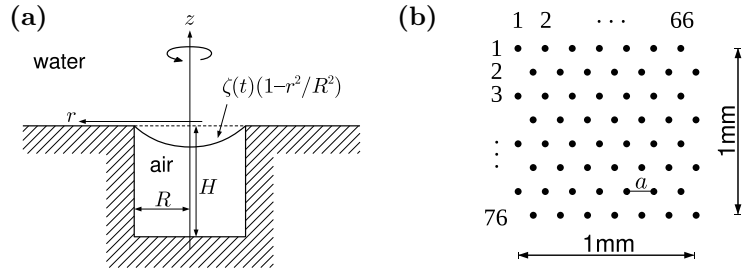

Figure 6.1: **Schematic of the experimental system. (a)** Schematic figure of a single micromeniscus. **(b)** Pattern of an array of micromenisci. Arrows denote the primitive translations and nearest neighbor distance a.

We have hitherto discussed the *static* behavior of the liquid-gas interfaces at a superhydrophobic surface. However, a diffraction type measurement as introduced in Chapter 3 allows to study also the *dynamics* of the liquid-gas interfaces [1]. This is an important problem, since in the real life of a superhydrophobic surface, the liquid-gas interfaces are frequently subject to vigorous dynamics (e.g., when a drop impacts on a superhydrophobic plant leaf). Any practical superhydrophobic surface must provide resistance to impregnation due to drop impact. In many cases, e.g. with a superhydrophobic wind shield, drop impact can be of high speed. The dynamics of the liquid-gas interfaces is therefore of great interest.

6.1 Introduction

In this chapter we will characterize the fluid mechanics of the liquid-gas interfaces and introduce an optical diffraction measurement that reveals their nanoscale motion. In particular, we measure in real time the optical diffraction intensity from a periodic array of micromenisci. Driving the system with an ultrasound field at variable frequency, we measure its frequency response and we identify a well-defined resonance peak with a center frequency well below the expectations for a single micromeniscus. Modeling the system using the unsteady Stokes equation and monopole interaction, we show that this frequency reduction is due to acoustic coupling between the menisci.

6.2 Experiments

Fig.6.1 shows the geometry of our system. It consists of $1 \times 1\text{mm}^2$ wide hexagonal and square arrays of micrometer-sized cylindrical holes (radii $R = 2\mu$m or 3μm, depth $H = 15\mu$m, nearest neighbor distance $a = 15\mu$m or 25μm). The samples were fabricated from Si (110) using standard micro lithography. Subsequently, the

[1] The detection speed is limited only by the bandwidth of the photodiode, which easily extends into the GHz range.

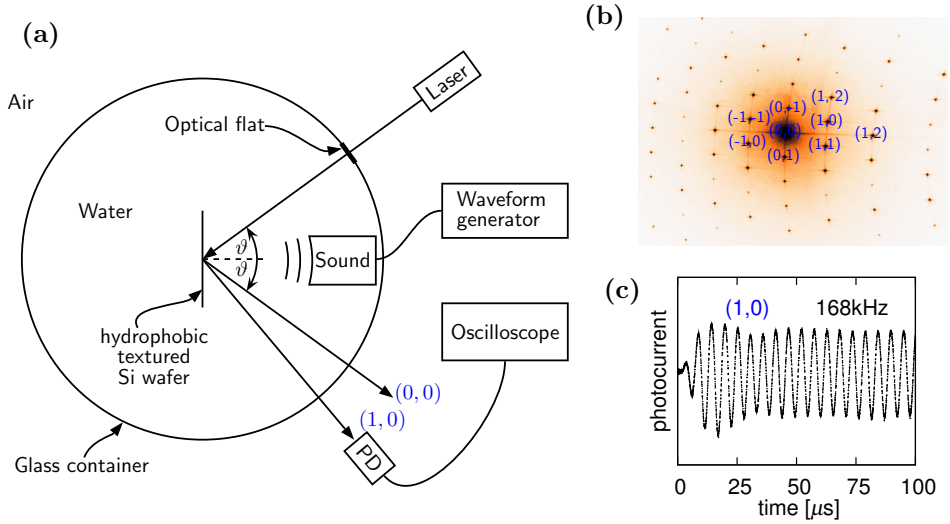

Figure 6.2: **Experiment. (a)** Schematic of the experimental setup. **(b)** Photograph of the diffraction pattern for $\vartheta \approx 60°$ as observed on a white screen (The originally black photograph with green laser spots has been color inverted.). Numbers indicate Miller indices of diffraction orders. **(c)** AC component of the light intensity measured in the (1,0) diffraction order at the beginning of an ultrasound wavetrain.

surfaces were hydrophobized by vapor deposition of a monolayer of 1H,1H,2H,2H-Perfluorodecyltrichlorosilane, following [72]. The advancing and receding contact angles on an unstructured surface are $\gamma_a = 116°$ and $\gamma_r = 104°$. Upon immersing the samples into demineralized water, ambient air is entrapped in every hole, leaving a water-air meniscus behind that is pinned at the ridge of the hole. Owing to the hydrostatic pressure, the menisci are bent inwards with equilibrium curvature $\kappa_0 = \rho g h/\sigma$ (as we have also checked by independent measurement), where g is the acceleration of gravity, σ is the water surface tension, and $h \approx 0.1$m is the distance between the sample and the free water surface. This implies that the system is in diffusion equilibrium and the gas pressure in the hole is the ambient pressure.

An Ar-ion laser ($\lambda = 488$nm, s-polarized) is used to illuminate the sample under an angle typically between 60° to 70° with respect to normal incidence (see Fig.6.2). The laser's beam waist measures 1.5mm such that the intensity varies by less than a few percent over the sample area. The diffracted intensity is measured with a photodiode positioned at a selected diffraction peak, typically chosen in the vicinity of the specular reflected beam. A broadband piezoelectric ultrasound transducer is placed at its focal distance from the sample. The ultrasound transducer is excited to emit finite wavetrains [2] using an arbitrary function generator. The ultrasound pressure at the sample is of the order 10^2 to 10^3 Pa, which is small compared to a critical static pressure above which filling occurs $P_c = 2\sigma\cos(\gamma_a)/R \approx 2.1 \cdot 10^4$Pa.

[2] Finite wavetrains are preferred to continuous waves to avoid standing waves inside the container.

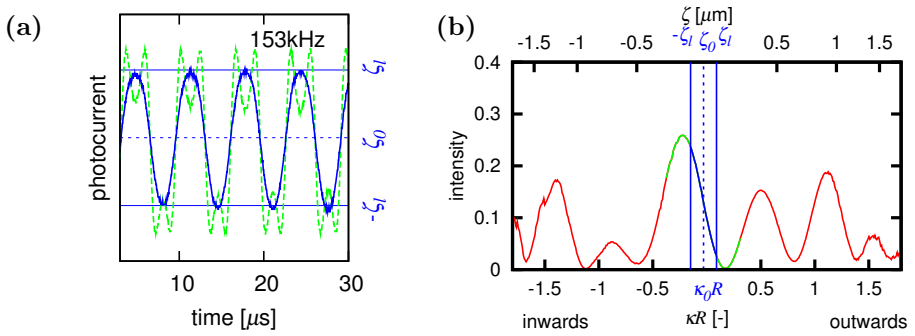

Figure 6.3: **Determination of the deflection amplitude.** **(a)** Time-resolved intensity of the $(1,0)$ diffraction order, corresponding to small ultrasound pressure ($\Delta P \approx 400$Pa), solid line, and large ultrasound pressure ($\Delta P \approx 800$Pa), dashed line. **(b)** Calculated intensity of the first diffraction order as a function of meniscus deflection for a rectangular surface profile with groove width $w = 2R$ ($\vartheta = 66°$). The data is displayed simultaneously in terms of the displacement ζ and the non-dimensionalized curvature κR. Both are related geometrically by $\zeta = 2/\kappa(1 - \sqrt{1 - R^2\kappa^2/4})$. The equilibrium curvature $\kappa_0 R = 0.04$ corresponds to $\zeta_0 = 30$nm.

To check the dynamic stability of the menisci, we increased the ultrasound pressure to much larger values and observed how the intensity oscillations disappeared at a defined threshold. The ultrasound pressure is kept constant during a frequency sweep by controlling the driving voltage according to the transducers frequency response. Fig.6.2c shows typical raw data corresponding to the beginning of a wavetrain. After a transient lasting for a few oscillation cycles, the signal becomes sinusoidal with a constant amplitude. This amplitude is extracted from the raw data by calculating the root mean square.

6.3 Deflection amplitude

The diffracted intensity depends in a highly nonlinear way on the deflection of the menisci. To assure a linear relation between the actual deflection and the measured intensity, the menisci oscillations have to be small. This can be seen in Fig.6.3a. While the diffracted intensity follows the sinusoidal driving pressure at low driving amplitudes (solid line), it is distorted at larger driving amplitudes (dashed line). Prior to an experiment, we reduce the ultrasound pressure until the undistorted sinus is observed.

To find the magnitude of the corresponding meniscus deflections, we consider the optical diffraction of the sample. In the Fraunhofer limit, the diffracted intensity is proportional to the intensity scattered by a single unit cell, and for each unit cell, the scattered intensity is governed by the interference of the elementary waves emitted from the cell volume [15]. In our case the incident angle is large and no light reaches

the bottom of the holes such that the interference takes place between the waves emitted from the plane silicon surface and the waves emitted from the meniscus. Qualitatively, as the meniscus is deflected – consider the position ζ of the apex of the meniscus – the intensity of a diffraction order (with diffraction angle $\approx$ incident angle) changes sinusoidally with a period $T = \lambda/(2n\cos(\vartheta))$, where $n = 1.33$ is the refractive index of water. To analyze these simple observations in detail, we performed a diffractive optics calculation using the multilayer rigorous coupled wave analysis in the formulation of [77]. This method allows for calculating an exact solution to the Maxwell equations for the optical response of arbitrary periodic surface profiles. In Fig.6.3b we show the resulting diffraction intensity as a function of the meniscus deflection. The typical distance between two adjacent peaks corresponds to the period evaluated from the simple Fraunhofer arguments above. The result shows that the diffracted intensity is indeed linear in the meniscus deflection in a range $[-\zeta_l .. + \zeta_l]$ around the meniscus equilibrium position ζ_0 and we find $\zeta_l \approx 90$nm. Note that the extent of the linear range depends on the incident angle ϑ. It is larger for larger incident angles, as can be seen readily from the simple expression for T. Thus, the large angles that are used in experiment allow for large meniscus oscillations. For incident angles above the angle of total reflection between water and air 48.6°, in addition the relative contribution of the menisci to the scattered intensity is large.

The theoretical result for the linear range is the key to convert the measured intensity variations into absolute meniscus deflections. Since we have to assure linearity between intensity and meniscus deflection at *all* ultrasound frequencies, the peak of the resonance curve shown in the following has the height ζ_l. The slope of the linear range together with the relative noise of the photodiode determines the resolution of the deflection measurement. It is of the order 1nm under given conditions.

6.4 Frequency response

Fig.6.4 shows a typical measured frequency response. The sample displays a single resonance at $f_r = 153 \pm 5$kHz. Similar curves were obtained for all samples. Table 6.1 shows that the observed resonance frequency increases both with increasing nearest neighbor distance and with decreasing hole size.

6.5 Theory of a single cavity-meniscus system

To understand the observations quantitatively, we consider first the response of a single meniscus under the influence of the pressure field $P(t) = P_0 + \Delta P e^{i2\pi ft}$, where f is the ultrasound frequency, P_0 is the ambient pressure and ΔP is the amplitude of the ultrasound pressure. Since $\zeta_0 \ll \Delta\zeta, R$, as follows with the values evaluated above, we approximate the meniscus as flat in equilibrium and its deflections as parabolic $\zeta(r) = \zeta(1 - r^2/R^2)$. The parabolic shape implies that the curvature is uniform up to $O(\zeta^3)$ giving right to the Laplace law. As described in [60], the smallness of the deflections $\Delta\zeta \ll R$, and the high frequency $f \gg \nu/R^2$ of the oscillations (ν kinematic viscosity), allow us to omit the non-linear term in the Navier-Stokes

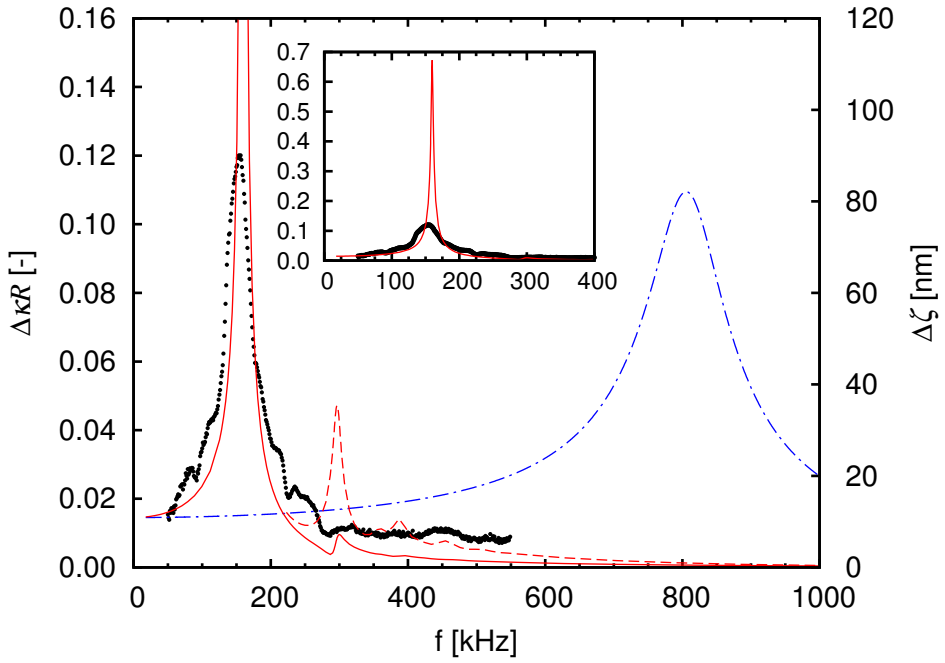

Figure 6.4: **Frequency response** The plot shows the frequency response of an array of micromenisci with hexagonal pattern, $a = 15\mu$m and $R = 3\mu$m. Experimental data (crosses) is compared to theory (lines). The dash-dotted line shows the theory for a single meniscus. Theoretical data for the array is displayed in terms of the mean (solid line) and the root mean square deflection (dashed line).

$R[\mu\text{m}]$	$a[\mu\text{m}]$	pattern	N	M	f_s[kHz]	f_c[kHz]	f_r[kHz]
3	15	H	66	76	805	159	153±5
3	15	S	67	67	805	170	177±5
3	25	H	40	46	805	258	230±20
3	25	S	41	41	805	275	240±20
2	15	H	66	76	1433	346	285±20
2	15	S	67	67	1433	368	290±20
2	25	H	40	46	1433	549	400±20
2	25	S	41	41	1433	584	410±20

Table 6.1: Resonance frequencies of the lowest collective mode f_c as a function of lattice constant, pattern geometry and menisci radius. 'H' and 'S' denote hexagonal and square pattern, respectively. f_s denotes the resonance frequency of a corresponding single meniscus, f_r the experimental result.

equation and hence the dynamics of the system is governed by the unsteady Stokes equation. The system can then be described as a harmonic oscillator

$$\{\Phi(\omega^*) + \mathrm{i}\Psi(\omega^*) + K\}\,\Delta\zeta^* = -\Delta P^*. \tag{6.1}$$

The transfer functions Φ and Ψ account for the inertia and the viscous damping due to the oscillatory flow fields. All quantities are non-dimenionalized $\omega^* = 2\pi f R^2/\nu$, $\Delta\zeta^* = \zeta/R$ and $\Delta P^* = \Delta P R^2/(\rho\nu)$. Since polytropic and thermal dissipative effects [22] can be neglected, the potential term reduces to a dimensionless spring constant $K = R/(\rho\nu^2)\left(P_0 R^2/(2H) + 4\sigma\right)$. The first term with the ambient pressure is due to the isothermal compression of the gas and is negligible throughout this work, and the second term with the surface tension σ is due to the surface energy of the liquid-gas interface. The computation of Φ and Ψ is performed by solving the unsteady Stokes equation in cylindrical coordinates with classical no-slip and free slip boundary conditions at the solid-liquid and the liquid-gas interface, respectively. A detailed account of the calculations will be given elsewhere [102]. While analytical expressions can be found both for the high and for the low frequency limit, Φ and Ψ have to be computed numerically in the intermediate frequency range $10^0 < \omega^* < 10^2$, which is relevant for the present experiments. The dash-dotted line in Fig.6.4 shows the solution for a $R = 3\mu$m hole with physical parameters of water $\rho = 10^3\mathrm{kg/m}^3$, $\nu = 10^{-6}\mathrm{m}^2/\mathrm{s}$, $\sigma = 73 \cdot 10^{-3}\mathrm{N/m}$ and ultrasound pressure $\Delta P = 390$Pa as used in the respective experiment. The obtained resonance frequency is approximately five times larger than the one observed experimentally. Clearly, the single meniscus theory fails to describe the dynamics of the system.

6.6 Hydrodynamic interaction

To resolve the discrepancy, we consider the dynamic coupling between the menisci. As the menisci oscillate in the external pressure field, they emit pressure waves that affect the other menisci. Denoting the non-dimensionalized distance between the i-th and the j-th meniscus by $d^*_{ij} = d_{ij}/R$, the additional force acting on the i-th meniscus can be expressed in terms of a multipole expansion $-\Delta\zeta^*_j \omega^{*2}/(4d^*_{ij}) + O({d^*_{ij}}^{-2})$, where ${\Delta\zeta_j}^*$ is the deflection amplitude of the j-th meniscus (see e.g., [62], [16]). In this expression, we assume that the distance between the i-th and the j-th meniscus is much larger than R and we neglected the finite propagation speed of the pressure wave. To analyze the dynamics of the entire meniscus array, we extend the equation of motion of the single meniscus, Eq. (6.1), by the additional forces generated by all other menisci keeping only the monopole term. We arrive at the coupled equations of motion

$$\{\Phi(\omega^*) + \mathrm{i}\Psi(\omega^*) + K\}\,\Delta\zeta^*_i = -\Delta P^* + \sum_{i\neq j}^{N\cdot M} \frac{\omega^{*2}}{4d^*_{ij}} {\Delta\zeta_j}^*. \tag{6.2}$$

The coupling term gives rise to an additional effective mass, which reduces the resonance frequency, as required. We solve Eq. (6.2) for the individual deflection ampli-

tudes $\Delta\zeta_i{}^*$ by numerical matrix inversion. From the result we evaluate the mean

$$\langle \Delta\zeta^* \rangle = |\sum_{i=1}^{NM} \Delta\zeta_i{}^*|/NM \tag{6.3}$$

and the root mean square

$$\langle \Delta\zeta^{*2} \rangle^{1/2} = (\sum_{i=1}^{NM} |\Delta\zeta_i{}^*|^2)^{1/2}/NM \tag{6.4}$$

deflection amplitude (see discussion below). The results are shown in Fig.6.4 with the solid and dashed line, respectively. For the moment note that both curves are nearly identical up to frequencies well above the lowest resonance. The theoretically obtained resonance frequency $f_c = 159$kHz is in excellent agreement with the experimental data, showing that collective effects are crucial for the dynamics of the system. Moreover, the good agreement shows that monopole interaction is effective beyond its obvious range of applicability where $a \gg R$.

6.7 Correct averaging

As can be seen in the inset of Fig.6.4, the theory overestimates the amplitude of the resonance which is presumably due to the neglectance of the bulk dissipation that arises in the collective flow field. Second, and more interestingly, the theoretical data for the root mean square displays a second resonance at 290kHz which is absent in the experimental data. To understand the latter effect we plot the calculated amplitude and phase for the two lowest resonances as a function of the meniscus position within the array in Fig.6.5. For the lowest resonance all menisci oscillate essentially in phase, whereas at the second resonance, the menisci in the center of the array and the ones along the edge oscillate 180° out of phase and the amplitude displays a node at the ring shaped boundary between the two regions. To evaluate the diffraction intensity for such arrays of non-identical scatterers, we note that the variation of the meniscus deflection gives rise to phase differences between the waves emitted from different unit cells that are much smaller than 2π – owing to the particular experimental condition assuring that the diffracted intensity is linear in the meniscus displacement. Extending the above Fraunhofer picture, we show in appendix B that the diffraction intensity is linear in the individual menisci deflections, and thus the experiment measures the mean deflection. Thus, we have to compare the experiment to the theoretical mean deflection, where the second resonance is indeed nearly invisible. Note that the expression for the mean as given above accounts for the phase since the deflection amplitudes $\Delta\zeta_i^*$ are complex.

The reduction of the resonance frequency predicted by the theory is confirmed for all surface patterns investigated in experiment (see Table 6.1). Since the coupling between the menisci is inversely proportional to the distance, the frequency reduction is more pronounced for smaller lattice constants. Similarly, it is more pronounced for

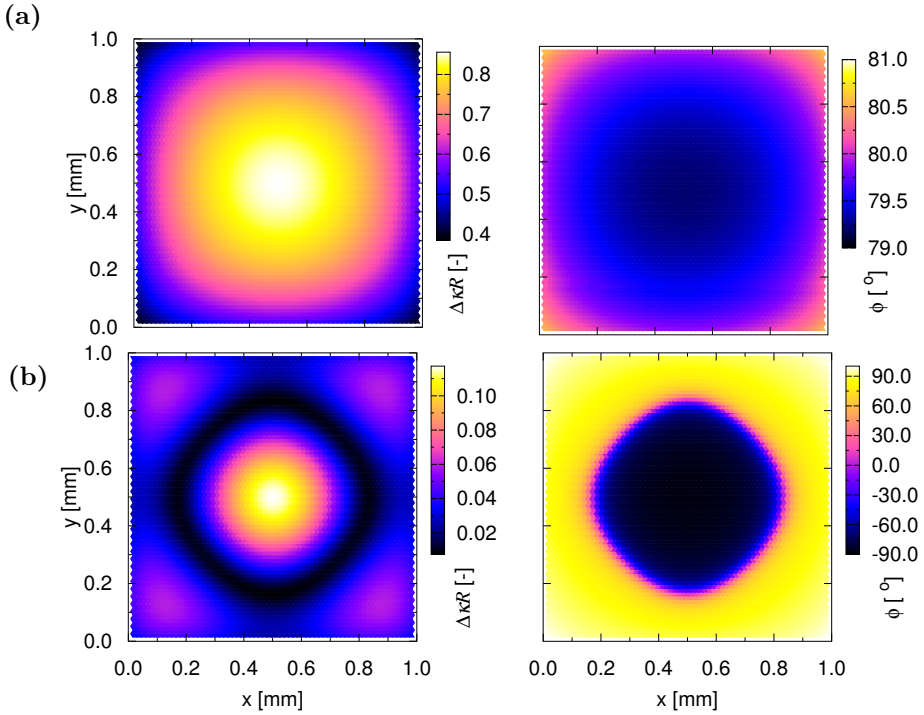

Figure 6.5: **Amplitude and phase maps.** The plots show the amplitude and phase over an array of micromenisci with hexagonal pattern, $a = 15\mu$m and $R = 3\mu$m **(a)** at the fundamental collective mode (159kHz), and **(b)** at the second collective mode (290kHz). Note that the color scale for the phase is narrower in (a) as compared to (b).

the hexagonal lattices than for the square ones, owing to the larger number of nearest neighbors. At this moment we have no clear explanation for the slight overestimation of the resonance frequency for the samples with smaller radius.

6.8 Summary and conclusions

We have studied the collective dynamics of microscopic liquid-gas interfaces formed at the openings of hydrophobic micro-cavities, under the influence of a driving ultrasound field, through a time resolved optical diffraction experiment. We described measured resonance curves through a model that evaluates the unsteady Stokes flow equations for a single cavity-meniscus system and accounts for hydrodynamic interaction in terms of a monopole approximation. We find that the dynamics of arrays of cavity-meniscus systems are determined by collective oscillation modes with resonance frequencies that are much smaller than the resonance frequency expected for a single isolated cavity-meniscus system. In terms of interface dynamics at a typical

superhydrophobic surface, those surfaces that provide a particularly small solid surface fraction, i.e. large contact angles and large slip length, are expected to show the lowest resonance frequencies. Optical diffraction has proven an accurate tool to study superhydrophobic surfaces and their nanoscopic hydrodynamics. It remains a challenge to develop a technique for detecting the oscillations of a single micromeniscus, and to confirm the unsteady Stokes flow theory for a single cavity-meniscus system, in particular to confirm the predicted height of the resonance peak, and the related prediction that viscous dissipation is dominated by vorticity generation inside the boundary layer. One suitable approach could be a confocal type detection scheme. The successful realization of such a measurement is demonstrated in appendix I. Furthermore, the present system shows a great sensitivity to ultrasound. This suggests that one or more cavity-meniscus systems could potentially be used to detect ultrasound. A readily integrated device could be based on a superhydrophobic photonic crystal. Such an approach along with first preliminary results is discussed in appendix H. In the following chapter we will demonstrate the successful measurement of a single cavity-meniscus system through a fiber optical micro interferometer and confirm the related unsteady Stokes flow theory. At the same time, the device could readily serve as a next generation ultra sensitive ultrasound sensor.

Chapter 7

Dynamics of a single cavity-meniscus system

We study the ultrasound-induced dynamics of the surface of a gas bubble trapped inside an optical microcavity that was fabricated at the end face of a hydrophobized optical fiber. Using an optical fiber interferometer, we determine the deflection of this air-water interface with nanometer resolution. The frequency-dependent response agrees well with a previously developed hydrodynamic model and demonstrates the potential for low noise level ultrasound sensing.

7.1 Introduction

Due to the low compressibility of condensed matter, the characteristic displacements caused by the propagation of an acoustic wave through a solid or liquid are typically below the nanometer scale. This makes the measurement of weak ultrasound signals a formidable task [4, 47, 58, 10]. In the traditional detection scheme a piezo-electric crystal is used to convert the ultrasound induced displacement directly into an electrical signal. Recently a number of new technologies have emerged to satisfy the ever increasing need for high ultrasound bandwidth (spatial resolution) and low noise detection (e.g. imaging depth in medical ultrasound diagnostics), including capacitive sensing of the displacement of micro machined membranes (so called cMUTs) [89], optical detection of a micromechanical cantilever [100], and a variety of optical techniques based on an interferometric detection of the ultrasound induced displacement [19, 11, 47, 58, 4]. All techniques ultimately rely on an efficient conversion of the ultrasound pressure into a mechanical displacement.

Here we introduce the use of a microscopic liquid-gas interface for acoustic detection to provide a novel approach to a sensitive pressure-to-displacement conversion. The interface is created by milling a microscopic hole into the end face of an optical fiber and subsequently hydrophobizing it. After immersing the fiber in water, a microscopic liquid-gas interface spans the opening of the hole. The restoring force acting on the interface is governed by surface tension alone, such that the interface acts like an extremely soft spring (as compared to a bulk detection medium or solid membrane). Nanometer scale detection of the microscopic liquid-gas interface is achieved through fiber optical interferometry. Our measurements also confirm a previously suggested model for the microscopic hydrodynamics of a meniscus-cavity system based on unsteady Stokes flow theory [103].

7.2 Experiments

Fig. 7.1 shows our device. A cylindrical hole is milled into the cleaved end of a 633 nm single mode optical fiber (core diameter 4.1μm) using a focused ion beam (FIB) (in this chapter, results are presented for three different samples with radii 3.25, 2.2, and 1.25 μm, and depths 6.15, 5.0, respectively 3.9 μm, as determined by SEM). Prior to the FIB process, the fiber is coated with a 5 nm conductive Pd-Au coating, which is stripped afterwards by dipping the sample in aqua regis. Subsequently the sample is hydrophobized by vapor deposition of a self assembled monolayer of an alkylsilane (1H,1H,2H,2H-Perfluorodecyltrichlorosilane), following [72]. This process results in a hydrophobic layer that is typically $1.5-1.6$ nm thick [1], and has a contact angle against water of about 115°. This large angle characterizes the hydrophobicity of the sample, and ensures that it will be in the superhydrophobic state, where a liquid-gas interface spans the opening of the cavity and the three-phase contact line is pinned at the ridge of the hole [57]. The zoom view in Fig.7.1(c) shows a microscope image of the device

[1] as determined by ellipsometry on a flat Si-wafer, assuming the bulk dielectric constant for the alkylsilane

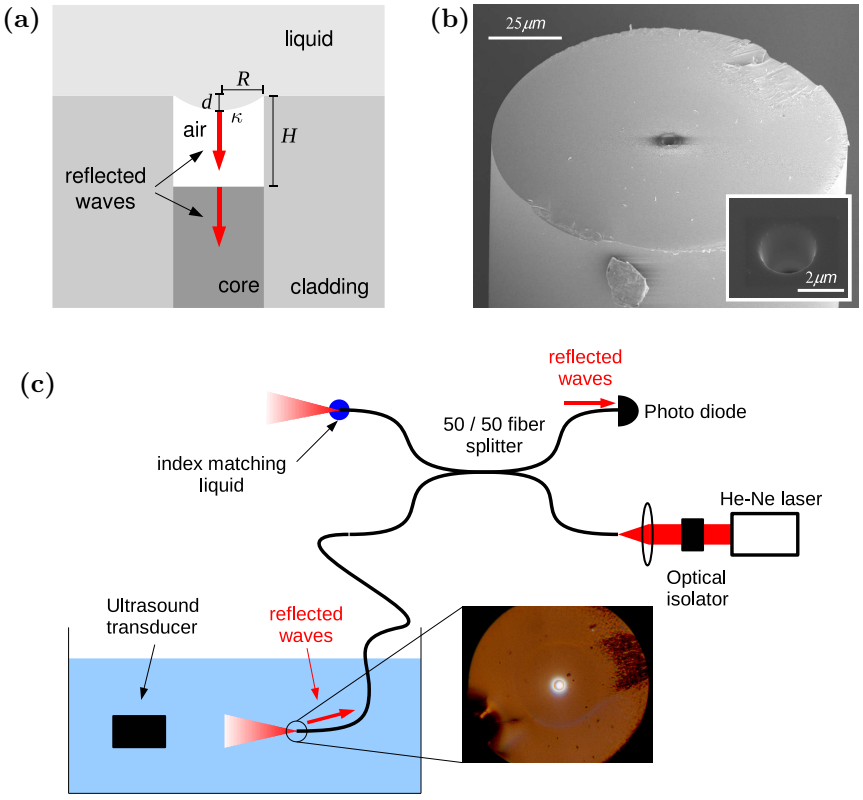

Figure 7.1: **Device and setup for experimental characterization.** **(a)** schematic and **(b)** SEM image of the device. **(c)** Schematic of the experimental setup. The zoom view shows a bright field microscope image of the device after immersion in water. The water-air interface appears as a bright circle in the center of the image.

after immersion in water. The water-air interface appears as a bright reflection in the center of the image. At rest, the interface is curved downwards, with a curvature $\kappa_0 = P_h/\sigma$ determined by a balance between the Laplace pressure $P_L = \sigma\kappa_0$ and the hydrostatic pressure $P_h = \rho g h$. Here, σ is the surface tension, ρ is the density of the liquid, g is the acceleration of gravity, and h is the depth of immersion below the water surface. The deflection d in the apex of the liquid-gas interface is related to its curvature by geometry (spherical cap) through $d = 2/\kappa\left(1 - \sqrt{1 - 4R^2\kappa^2}\right)$, where R is the hole radius. For small curvature, the latter reduces to $d \approx \kappa R^2/4$. Upon exposing the meniscus to an ultrasound field, it performs nm-scale oscillations around its rest curvature. Its dynamics are described by unsteady Stokes flow theory [103] resulting in an effective harmonic oscillator model characterized by a spring constant $K = P_0 R^2/(2RH) + 4\sigma/R$. For small cavities (as in the present experiments), the second term due to surface tension dominates over the first term that accounts for

isothermal gas compression inside the cavity.

Upon exposing the meniscus to an ultrasound field, it performs nm-scale oscillations around its rest curvature. In our characterization measurements, we place an ultrasound transducer parallel to and at few cm distance from the end face of the fiber. The ultrasound transducer is excited to emit finite wavetrains (length 100μs, repetition rate 10ms). We ensure that the ultrasound pressure is constant over the investigated frequency range, by adapting the driving voltage at the ultrasound transducer (Panametrics V309 and Olympus C308 in the range 0.1-2MHz respectively 1-5MHz) according to a calibration that was recorded previously using a hydrophone (precision acoustics HP 1.0mm). To detect nm-scale oscillations of the liquid-gas interface, we measure the interference of the two guided optical waves reflected from the meniscus-cavity system. Fig. 7.2 shows the expected electric field intensity inside the fiber optical micro interferometer, calculated by means of a fully vectorial mode solver and coupled wave formalism as provided by the CAMFR package [12]. All modes in the cavity region are leaky modes (non-guiding), their effective propagation constant is close to the free space propagation constant such that the period of the standing wave inside the interferometer is close to the free space wavelength (in contrast to the guiding region of the fiber where the period is smaller). To measure the guided waves reflected from the interferometer, we essentially have to perform a reflection loss measurement of the fiber end face. Fig.7.1(c) shows an optical setup that allows to do this. A 10 mW He-Ne laser (linear polarized) is coupled into a single mode fiber splitter with a splitting ratio 50/50. Optical feedback into the laser is suppressed by an optical isolator. The light leaves the fiber splitter trough two arms. One of them is connected to the microstructured fiber, the other is left open. To avoid a reflection from the open arm that would interfere with the actual signal wave, the open end face is immersed into an index matching liquid. The two waves reflected from the meniscus-cavity system travel back into the fiber splitter. Half of the reflected wave is detected with a photodiode, and the other half is dumped onto the optical isolator.

7.3 Deflection amplitude

Fig. 7.3 shows current traces measured at the photodiode with increasing ultrasound pressure. At low pressure, the signal is sinusoidal and proportional to the driving ultrasound pressure. At larger pressures, the signal is increasingly distorted. The minima and maxima of the sine appear flipped. This nonlinear behavior is the key to an absolute measurement of the deflection amplitude.

The reflected intensity is approximately a two-beam interference, thus, as the meniscus oscillates, the interference intensity changes with time as

$$I = \Delta I \left(\sin[\Delta\varphi \sin[2\pi f t + \alpha] + \varphi_0]\right) + I_0 \tag{7.1}$$

ΔI is an intensity amplitude, I_0 is the DC intensity, f is the ultrasound frequency, α is an arbitrary phase delay of the ultrasound, φ_0 is an optical phase offset, determined by the rest position of the meniscus, and $\Delta\varphi$ is the amplitude of the meniscus oscillations in terms of optical phase, in the following termed phase amplitude, and

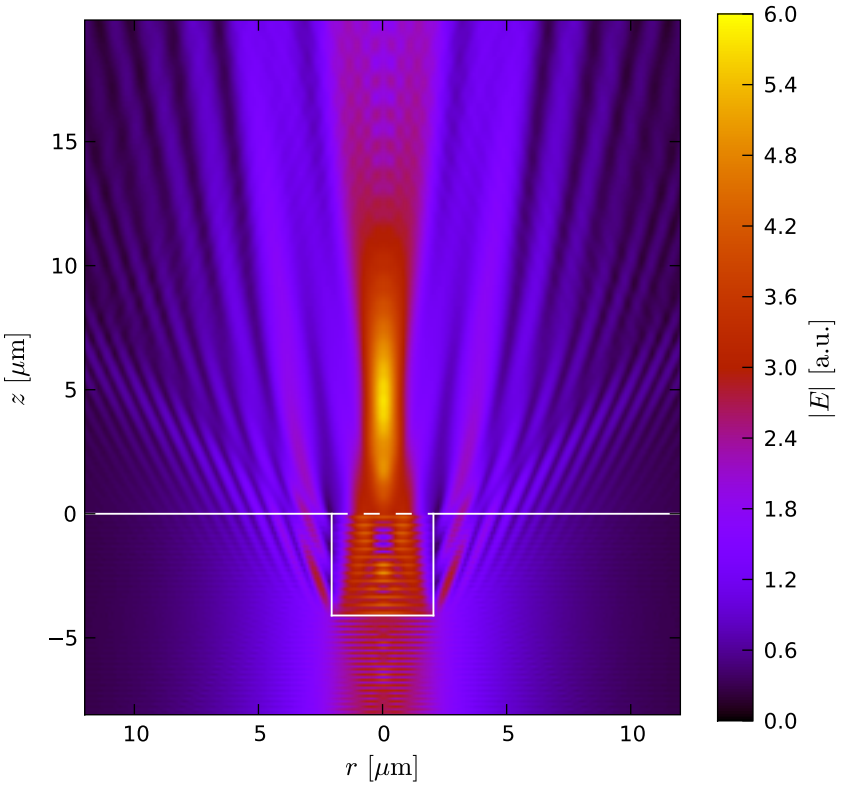

Figure 7.2: **Field distribution.** The plot shows the field intensity inside the fiber optical interferometer as calculated assuming a flat meniscus and cavity of aspect ratio one with a diameter $D = 4.1$ equal to the diameter of the fiber core. The end face of the fiber with the cavity and the liquid-gas interface are shown by solid and dashed white lines, respectively. In this calculation the refractive index of the cladding and core were taken as $n_l = 1.45$, respectively $n_c = 1.451$, and a step wise increase of the refractive index was assumed. The refractive index of water was taken as $n = 1.33$.

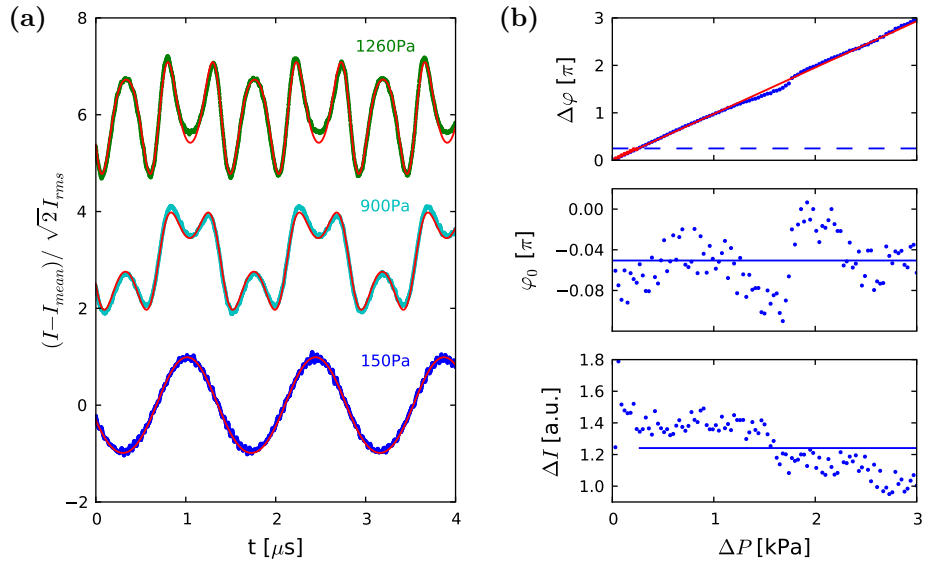

Figure 7.3: **Measurement of the deflection amplitude. (a)** Current traces measured at the photodiode with increasing ultrasound pressure. The current is normalized by subtracting its *mean*, and dividing through $\sqrt{2}$ times the *rms*. The red lines are fits to a modulated sine, as expected for two-beam interference (Eq. (7.1)). **(b)** Evolution of the fit parameters with increasing ultrasound pressure. The top panel show the phase amplitude $\Delta\varphi$. The red line displays a linear fit. The dashed line marks the onset of nonlinear current traces at about $\pi/4$. The middle panel shows that the phase offset due to the meniscus rest position has successfully been adjusted to approximately zero. The bottom panel plots the evolution of the intensity amplitude, revealing a negligible drift.

related to the mechanical deflection amplitude Δd by $\Delta\varphi = 4\pi\Delta d/\lambda$. To perform an absolute measurement of the deflection amplitude Δd, we determine the phase amplitude $\Delta\varphi$. Let us assume for the moment, that the phase offset φ_0 is zero. Then, a phase amplitude $\Delta\varphi = \pi/2$ corresponds to a current trace with flattened minima and maxima, just before the onset of flipping. Likewise, a phase amplitude $\Delta\varphi = \pi$ corresponds to a current trace that features minima and maxima that are flipped one time, reaching back to the zero line. And so forth. Thus, to determine the phase amplitude, we drive the menisci at large amplitude, and fit the resulting current trace to Eq. (7.1), determining $\Delta\varphi$. In practice, this is a formidable task. The high correlation between the fit parameters paired with the presence of multiple deep adjacent minima in the χ^2-landscape renders the problem unsuitable for Levenberg-Marquardt (LM), as well as simulated annealing [97]. We thus fit the truncated Fourier series of the current trace to the Fourier expansion of the target function. The latter is doable through LM. The red lines in the left panel of Fig.7.3 show such fits. A full calibration

measurement consist of a series of current traces with increasing ultrasound pressure, obtained at a frequency close to the resonance frequency of the meniscus. For each trace, the phase amplitude is determined. The upper right panel of Fig.7.3 shows the evolution of the phase amplitude with the driving ultrasound pressure. The amplitude is to a very good approximation linear in the driving pressure. The small kink observed around the center of the plot is a consequence of the inevitable correlation of the fit parameters, as is seen directly by the correlated kink in the phase offset (middle panel), and is not a concern. At small deflection amplitude $\Delta\varphi$, Eq. (7.1) is linear in the meniscus deflection. The proportionality constant is determined by φ_0, and is maximal on the flank between a minimum and maximum, where $\varphi_0 = 0$. This is an optimal setting for the measurement of the frequency response. Thus, to measure the frequency response, we adjust the hydrostatic pressure such that $\varphi_0 \approx 0$, and decrease the ultrasound pressure such that the phase amplitude is smaller than about $\pi/4$. The current trace is then sinusoidal, and its amplitude is found by evaluating the *rms* current of the raw data. Through the previous calibration measurement the corresponding phase amplitude is known. The frequency response is then obtained, by sweeping the ultrasound frequency, and extracting the amplitude of every recorded current trace.

7.4 Frequency response

Fig. 7.4 shows the measured frequency response of the fabricated cavity-meniscus systems (dots). The experimental data is well described by unsteady Stokes flow theory (lines), thus confirms the theoretical model for a single isolated cavity-meniscus system as developed in Sec. 2.3. In contrast to previous experimental data obtained with arrays of hydrodynamically coupled menisci, the theory accounts for the height and width of the resonance peaks, i.e., it captures the relevant dissipation mechanisms. We thus conclude, that the reason for the previous disagreement lied indeed in the neglection of the dissipation arising in the global flow field that was present above the arrays of menisci, as speculated previously. Moreover, and more importantly, the good agreement observed here opposes potential flow theory, that accounts for viscous dissipation in terms of bulk dissipation integrals and does *not* capture dissipation correctly (inset of Fig.7.4). The comparison, and the experimental confirmation of the unsteady Stokes flow theory reveals that viscous dissipation in this system is dominated by vorticity generation at the solid boundary. This behavior is in gross contrast to free bubbles in an unbounded medium [61], and is a unique consequence of the proximity of the system to a solid wall.

7.5 Pressure-to-displacement conversion

We finally evaluate the prospects of the device for low noise level ultrasound detection. To do so, we compare the device to the state of the art, defined by a recently developed fiber optical hydrophone [10]. Like the device presented here, the latter hydrophone is based on a microscopic optical interferometer fabricated on the end face of an optical

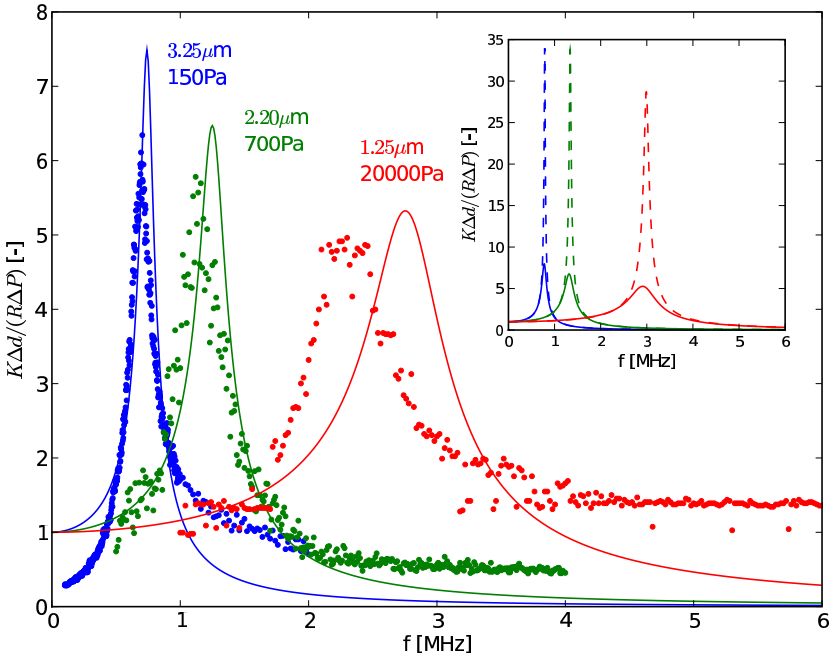

Figure 7.4: **Frequency response.** The plot shows the ultrasound frequency response of single cavity-meniscus systems with decreasing radius. Experimental data (dots) are compared to unsteady Stokes flow theory (solid lines). The Color codes blue, green, and red, correspond to cavity radii 3.25, 2.2, and 1.25 μm, respectively. To facilitate comparison between the different sample geometries, the amplitude is plotted in its dimensionless form, normalized through the hole radius and ultrasound pressure ΔP, and scaled by the systems spring constant $K = P_0R^2/(2RH) + 4\sigma/R$. The data for the larger radii were obtained at small ultrasound pressure, in the linear regime (150Pa and 700Pa, respectively), by evaluating the *rms* of the underlying current traces, as described in the text. To cope with low signal level at small interferometer radius, the data for the smallest cavity was obtained at larger ultrasound pressure (20kPa), by directly fitting each underlying current trace to Eq. (7.1). The inset compares unsteady Stokes flow theory (solid lines) and potential flow theory (dashed lines).

fiber, though, in contrast to the present device, a polymer provides the pressure-to-displacement conversion. However, the subsequent interferometric measurement of the displacement, and conversion into an electrical signal (limited ultimately by shot noise), is the same in both devices, such that we can directly benchmark the present device by comparing its pressure-to-displacement conversion. The pressure-to-displacement conversion follows from the balance of the Laplace pressure and the ultrasound pressure, together with the geometric relation between the curvature and the deflection as $\Delta d/\Delta P = R^2/(4\sigma)$ (see appendix F for details). The resonance frequency of the cavity-meniscus system is approximately $f_R = 1/\pi(2\sigma/(\rho R^3))^{1/2}$ [103]. Thus, a device with 10MHz ultrasound bandwidth requires a cavity radius of about 500 nm, and the pressure-to-displacement conversion is about 10^{-12}m/Pa. In comparison, above cited device features a pressure-to-displacement conversion of about $4 \cdot 10^{-15}$m/Pa. Thus, the device presented here offers great prospects for future ultra sensitive ultrasound detection. It allows us to hear with a bubble.

7.6 Summary and conclusions

We have realized a single cavity-meniscus system on a micro structured superhydrophobic optical fiber. Ultrasound induced nanometer scale oscillations of the suspended liquid-gas interface were detected through optical micro interferometry. The device opens new perspectives for low noise ultrasound detection. Determining the frequency response of the system, we confirmed an unsteady Stokes flow model of a single isolated cavity-meniscus system (Chapter 8). The experiment offers unique perspectives for studying the dynamics of capillaries and bubble-like objects on the micro-scale, in real time, with nanometer resolution. When driving the menisci with large pressure far above their fundamental resonance frequency, we could see the signatures of higher order modes appear in the current traces, i.e., we are beginning to see the modes of a micrometer sized liquid drum.

Chapter 8

Stokes flow theory of oscillating menisci

During my PhD, I had the honor to collaborate with Kazuyasu Sugiyama (now at Tokyo University) who was at that time a postdoc in Detlef Lohse's group, on a problem that seemed initially entirely academic, however later even led to the filing of a patent. It concerns the (collective) dynamics of one or more microscopic liquid-gas interfaces as they are found at the texture of a superhydrophobic surface (Chapter 6 and 6). In a sense, it was the first time, that somebody had looked at the ultrasonic hydrodynamics *of a superhydrophobic surface. Consequently, the theory had to be developed 'from scratch'. This section is due to the ingenuity of Kaz, who formulated that theory.*

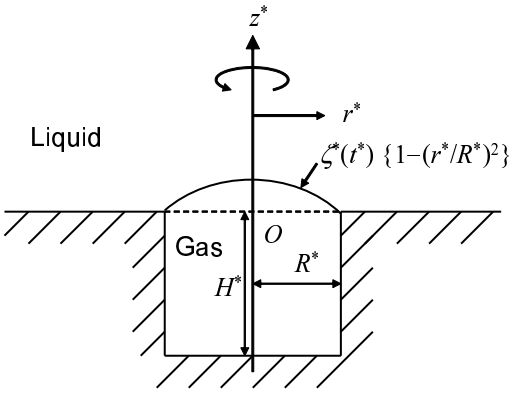

Figure 8.1: **Schematic of the theoretical model for a single cavity-meniscus system** Dimensional quantities such as the radius R^* and depth H^* of the cavity are denoted with a $*$. The interface is pinned at the edge of the cavity, and undergoes small amplitude parabolic deformations.

We address the resonance frequency in a multi-meniscus system. First, we derive a transfer function accounting for a relation between a deflection of a single meniscus and the external forcing. Second, using the obtained transfer function, we consider the collective effect.

8.1 Single cavity-meniscus system

We shall now derive an unsteady Stokes flow model for a single cavity-meniscus system. Fig. 8.1 shows a schematic of the theoretical model. Dimensional quantities such as the radius R^* and depth H^* of the cavity are denoted with a $*$. The following approximations are introduced.

(1) we assume the meniscus is flat in equilibrium. This condition is satisfied when the deflection at rest is much smaller than the deflection amplitude and the radius of the cavity, $|\zeta_0^*| \ll R^*, \Delta\zeta^*$.

(2) we assume that the acoustic field is a function of the time alone, expressed as $P^* = P_0^* + \Delta P^* \exp(\omega^* t^*)$, corresponding to a 'global' pressure change. This requires that the ultrasound wavelength λ^* is much larger than the system size $R^* \ll \lambda^*$.

(3) We assume that the interface is pinned at the edge of the cavity, and undergoes small amplitude parabolic deformations

$$\zeta^*(t^*)(1 - r^{*2}/R^{*2}), \tag{8.1}$$

where $\zeta^*(t^*)$ is the deflection of the interface on the axis $r^* = 0$ and r^* is the radial coordinate. This assumption has been employed by [73]. In an experiment it requires that $|\zeta^*| \ll R^*$ and $|\zeta^*| \ll H^*$. As shown below, the parabolic shape implies that the curvature of the interface is approximately uniform for a given ζ^*, as far as

$|\zeta^*| \ll R^*$, giving right to Laplace's law. It should be noted that the 'imposed shape' cannot be strictly verified. In a more realistic case, the local deformation of the interface should be taken into account, and Laplace's law should be applied locally at every point of the interface. Instead, we impose the shape of the interface. The parabolic shape implies that the interface oscillates with its fundamental oscillation mode. This approximation should describe the behavior of the system for small ultrasound frequencies and up to the fundamental resonance frequency. At much higher frequencies, the interface may deform following other shapes, corresponding to higher order oscillation modes, as known e.g. from oscillation modes of a circular plate. Such oscillations are not included in the present model.

(4) We assume that far away from the meniscus the flow vanishes. We consider three cases for the boundary conditions. (i) no-slip on both the liquid-gas interface and the solid wall, (ii) free-slip on both the liquid-gas interface and the solid wall, (iii) free-slip on the liquid-gas interface and no-slip on the solid wall

(5) Considering discussions in [60] we appreciate that the oscillating motion of a solid body in a liquid generates vorticity in a layer of a characteristic thickness $\delta = \sqrt{2\nu/\omega}$, while at larger distances the flow decays to potential flow. Here ν is the kinematic viscosity and ω is the oscillation frequency. Let l be the size of the body and a be the amplitude of the oscillations. If $l \gg \delta$ and $a \ll \delta$, the time derivative and $(\boldsymbol{v}\cdot\boldsymbol{\nabla})\boldsymbol{v}$ term in the Navier-Stokes equation are of the order $\partial_t v \approx v\omega \approx a\omega^2$ and $(\boldsymbol{v}\cdot\boldsymbol{\nabla})\boldsymbol{v} \approx v^2/l \approx a^2\omega^2/l$, such that the $(\boldsymbol{v}\cdot\boldsymbol{\nabla})\boldsymbol{v}$ term can be neglected.

8.1.1 Inertia and damping

To evaluate the inertia and damping, we deal with a harmonic oscillation of the interface in accordance with temporally periodic motions of liquid, and then evaluate the normal stress averaged over the interface. Here, we assume unsteady creeping flows.

Governing equations and non-dimensionalization

The flow is governed by the continuity and unsteady Stokes equations written as

$$\nabla^* \cdot \boldsymbol{u}^* = 0 \tag{8.2}$$

$$\partial_{t^*}\boldsymbol{u}^* = -\frac{\nabla^* p^*}{\rho_L^*} + \nu^* {\nabla^*}^2 \boldsymbol{u}^*, \tag{8.3}$$

where $\boldsymbol{u}$, ρ_L, p and ν denote the velocity vector, the liquid density, the dynamic pressure and the kinematic viscosity, respectively. We introduce an acoustic field as the driving pressure P_D given by

$$P_D^* = P_0^* + \Delta^* \exp(i\omega^* t^*), \tag{8.4}$$

where ω denotes the angular frequency and Δ the pressure amplitude. In virtue of the axial symmetry, we introduce a separation of variables for the velocity components,

the pressure, and the deflections in the following form

$$\begin{aligned} u_r^*(r^*, z^*, t^*) &= \hat{u}_r^*(r^*, z^*) \exp(i\omega^* t^*), \\ u_z^*(r^*, z^*, t^*) &= \hat{u}_z^*(r^*, z^*) \exp(i\omega^* t^*), \\ p^*(r^*, z^*, t^*) &= \hat{p}^*(r^*, z^*) \exp(i\omega^* t^*) + P *_D (t^*), \\ \zeta^*(t^*) &= \hat{\zeta}^* \exp(i\omega^* t^*). \end{aligned} \tag{8.5}$$

For ease in solving the unsteady Stokes equation, all quantities are non-dimensionalized by using the radius of the groove R^*, the liquid density ρ_L^*, and the kinematic viscosity ν^*, i.e.,

$$\begin{gathered} H = \frac{H^*}{R^*}, \quad r = \frac{r^*}{R^*}, \quad z = \frac{z^*}{R^*}, \quad \zeta = \frac{\zeta^*}{R^*}, \\ \omega = \frac{\omega^* R^{*2}}{\nu^*}, \quad p = \frac{p^* R^{*2}}{\rho_L^* \nu^*}, \quad \Delta = \frac{\Delta^* R^{*2}}{\rho_L^* \nu^*}, \quad \boldsymbol{u} = \frac{\boldsymbol{u}^* R^*}{\nu^*}, \\ \sigma = \frac{\sigma^* R^*}{\rho_L^* \nu^{*2}}, \quad \kappa = \kappa^* r^*, \end{gathered} \tag{8.6}$$

where σ and κ denote the surface tension and curvature of the interface, respectively. In this way, we obtain dimensionless governing equations

$$D_* \hat{u}_r + \partial_z \hat{u}_z = 0, \tag{8.7}$$

$$\begin{aligned} i\omega \hat{u}_r &= -\partial_r \hat{p} + (DD_* + \partial_z^2)\hat{u}_r, \\ i\omega \hat{u}_z &= -\partial_z \hat{p} + (D_* D + \partial_z^2)\hat{u}_z, \end{aligned} \tag{8.8}$$

where $D = \partial_r$ and $D_* = \partial_r + 1/r$. We now introduce a Stokes stream function ψ and provide the velocity components as

$$\hat{u}_r = \frac{i}{\omega}\partial_r \hat{p} - \frac{1}{r}\partial_z \psi, \quad \hat{u}_z = \frac{i}{\omega}\partial_z \hat{p} + \frac{1}{r}\partial_r \psi, \tag{8.9}$$

to identically satisfy Eq. (8.7). We replace the Stokes equation Eq. (8.8) with the Helmholtz equation

$$\left(DD_* + \partial_z^2 - i\omega\right)\frac{\psi}{r} = 0, \tag{8.10}$$

and the Laplace equation

$$\left(D_* D + \partial_z^2\right)\hat{p} = 0. \tag{8.11}$$

To determine the velocity components and the pressure, we analytically solve Eq. (8.10) and (8.11).

Boundary conditions

On the interface and wall ($z = 0$) as shown in Fig. 2.13, we write the kinetic condition as

$$\hat{u}_z = \begin{cases} i\omega\hat{\zeta}(1 - r^2) & \text{for} \quad r \le 1, \\ 0 & \text{for} \quad r > 1. \end{cases} \tag{8.12}$$

The condition at the large distance from the interface implies

$$\hat{u}_r \to 0, \quad \hat{u}_z \to 0 \quad \text{as} \quad z \to \infty. \tag{8.13}$$

No-Slip (NS) condition is expressed as

$$\hat{u}_r = 0 \quad \text{at} \quad z = 0, \tag{8.14}$$

while Free-Slip (FS) one as

$$\partial_z \hat{u}_r = 0 \quad \text{at} \quad z = 0. \tag{8.15}$$

We will consider three cases shown below:

(i) : NS interface and NS wall
(ii) : FS interface and FS wall
(iii) : FS interface and NS wall

Our primary concern is laid on the mixed boundary problem (case (iii)) to be compared with the experiment. We analyze the non-mixed boundary problems, i.e., cases (i) and (ii), which are more easily and rigorously solved than case (iii), to comparatively investigate the effect of the vorticity generation of the wall on the inertia and damping.

Integral expressions of solution

With the aid of Hankel's transforms such as

$$F(\lambda) = \int_0^\infty \mathrm{d}\bar{r}\ f(\bar{r})\bar{r}J_0(\lambda\bar{r}), \quad f(r) = \int_0^\infty \mathrm{d}\lambda\ F(\lambda)\lambda J_0(\lambda r),$$

where J_n denotes a Bessel function of the first kind and with the consideration of

$$\partial_r(rJ_1(\lambda r)) = \lambda r J_0(\lambda r), \quad \partial_r J_0(\lambda r) = -\lambda J_1(\lambda r),$$

$$\int_0^1 \mathrm{d}r\ rJ_0(\lambda r) = \frac{J_1(\lambda)}{\lambda}, \quad \int_0^1 \mathrm{d}r\ (1-r^2)rJ_0(\lambda r) = -\frac{2J_0(\lambda)}{\lambda^2} + \frac{4J_1(\lambda)}{\lambda^3},$$

we determine the solutions of Eq. (8.10) and (8.11)

$$\hat{p} = i\omega \int_0^\infty \mathrm{d}\lambda\ F(\lambda)J_0(\lambda r)\exp(-\lambda z), \tag{8.16}$$

$$\psi = r\int_0^\infty \mathrm{d}\lambda\ G(\lambda)J_1(\lambda r)\exp(-\sqrt{\lambda^2 + i\omega}z), \tag{8.17}$$

where we choose the sign inside the exponential function to be consistent with Eq. (8.13). From Eq. (8.9), we determine the velocity components in the explicit form

$$\begin{aligned}
\hat{u}_z &= \int_0^\infty \mathrm{d}\lambda\ F(\lambda)\lambda J_0(\lambda r)\exp(-\lambda z) + \int_0^\infty \mathrm{d}\lambda\ G(\lambda)\lambda J_0(\lambda r)\exp(-\sqrt{\lambda^2 + i\omega}z), \\
\hat{u}_r &= \int_0^\infty \mathrm{d}\lambda\ F(\lambda)\lambda J_1(\lambda r)\exp(-\lambda z) + \int_0^\infty \mathrm{d}\lambda\ G(\lambda)\sqrt{\lambda^2 + i\omega}J_1(\lambda r)\exp(-\sqrt{\lambda^2 + i\omega}z).
\end{aligned} \tag{8.18}$$

Eq. (8.12) is satisfied provided

$$F+G=\int_0^\infty \mathrm{d}\bar{r}\ \hat{u}_z|_{z=0}\bar{r}J_0(\lambda\bar{r})=i\omega\hat{\zeta}\left\{-\frac{2J_0(\lambda)}{\lambda^2}+\frac{4J_1(\lambda)}{\lambda^3}\right\}. \tag{8.19}$$

Considering the following relations

$$\hat{u}_r|_{z=0}=\int_0^\infty \mathrm{d}\lambda\ \left(\lambda F(\lambda)+\sqrt{\lambda^2+i\omega}G(\lambda)\right)J_1(\lambda r),$$

$$\partial_z\hat{u}_r|_{z=0}=-\int_0^\infty \mathrm{d}\lambda\ \left(\lambda^2F(\lambda)+(\lambda^2+i\omega)G(\lambda)\right)J_1(\lambda r),$$

$$\partial_r\hat{u}_z|_{z=0}=-2r=-\int_0^\infty \mathrm{d}\lambda\ \lambda^2\left(F(\lambda)+G(\lambda)\right)J_1(\lambda r),$$

we determine F and G for the NS interface and NS wall ($\hat{u}_r|_{z=0}=0$)

$$\begin{aligned}F=&\hat{\zeta}\left(-\frac{2J_0(\lambda)}{\lambda^2}+\frac{4J_1(\lambda)}{\lambda^3}\right)\left(\lambda^2+i\omega+\lambda\sqrt{\lambda^2+i\omega}\right),\\ G=&\hat{\zeta}\left(-\frac{2J_0(\lambda)}{\lambda^2}+\frac{4J_1(\lambda)}{\lambda^3}\right)\left(-\lambda^2-\lambda\sqrt{\lambda^2+i\omega}\right),\end{aligned} \tag{8.20}$$

while those for the FS interface and FS wall ($(\partial_z\hat{u}_r+\partial_r\hat{u}_z)_{z=0}=0$)

$$\begin{aligned}F=&\hat{\zeta}\left(-\frac{2J_0(\lambda)}{\lambda^2}+\frac{4J_1(\lambda)}{\lambda^3}\right)\left(2\lambda^2+i\omega\right),\\ G=&\hat{\zeta}\left(-\frac{2J_0(\lambda)}{\lambda^2}+\frac{4J_1(\lambda)}{\lambda^3}\right)\left(-2\lambda^2\right).\end{aligned} \tag{8.21}$$

For the potential flow, since the irrotational velocity field is achieved by setting $\psi=0$, we determine F and G

$$\begin{aligned}F=&i\omega\hat{\zeta}\left\{-\frac{2J_0(\lambda)}{\lambda^2}+\frac{4J_1(\lambda)}{\lambda^3}\right\},\\ G=&0.\end{aligned} \tag{8.22}$$

For the mixed boundary problem (case (iii)), it is difficult to determine F and G by use of the Hankel transform. Instead of using the integral expression, we solve the governing equations (8.7) and (8.8) by means of the direct numerical simulation. To discretize the governing equations, we employ the second-order finite difference scheme.

Surface averaged normal stress

For the stokes flow, we write a normal stress due to the deflection $\hat{\zeta}$ on the interface in a general form

$$\left(-\hat{p}+2\partial_z\hat{u}_z\right)_{z=0}=-\int_0^\infty \mathrm{d}\lambda\ (2\lambda^2+i\omega)F(\lambda)J_0(\lambda r)-2\int_0^\infty \mathrm{d}\lambda\ \lambda\sqrt{\lambda^2+i\omega}G(\lambda)J_0(\lambda r). \tag{8.23}$$

Further we take the surface average over the interface to obtain

$$\begin{aligned}\langle -\hat{p} + 2\partial_z \hat{u}_z \rangle_S =& 2\int_0^1 \mathrm{d}r\ r\left(-\hat{p} + 2\partial_z \hat{u}_z\right)_{z=0} \\ =& -2\int_0^\infty \mathrm{d}\lambda\ \frac{(2\lambda^2 + i\omega)F(\lambda)J_1(\lambda)}{\lambda} - 4\int_0^\infty \mathrm{d}\lambda\ \sqrt{\lambda^2 + i\omega}G(\lambda)J_1(\lambda) \\ =& \left(\Phi(\omega) + i\Psi(\omega)\right)\hat{\zeta},\end{aligned} \tag{8.24}$$

where Φ and Ψ denote transfer functions, which indicate the ratio of the normal stress to the amplitude of the deflection. The total normal stress of liquid on the interface is written as

$$P_L = P_0 + \Delta\exp(i\omega t) - \langle -\hat{p} + 2\partial_z \hat{u}_z \rangle_S \exp(i\omega t). \tag{8.25}$$

In the next section, we obtain the transfer functions.

Transfer functions

Here, we numerically evaluate the transfer functions.
NS interface and NS wall (case i)

For the NS interface and NS wall the normal stress is given by

$$\left(-\hat{p} + 2\partial_z \hat{u}_z\right)_{z=0} = i\omega\hat{\zeta}\int_0^\infty \mathrm{d}\lambda\ \left(\lambda^2 + i\omega + \lambda\sqrt{\lambda^2 + i\omega}\right)\left(\frac{2J_0(\lambda)}{\lambda^2} - \frac{4J_1(\lambda)}{\lambda^3}\right)J_0(\lambda r), \tag{8.26}$$

and the surface averaged stress is

$$\langle -\hat{p} + 2\partial_z \hat{u}_z \rangle_S = \hat{\zeta}\int_0^\infty \mathrm{d}\lambda\ i\omega(\lambda^2 + i\omega + \lambda\sqrt{\lambda^2 + i\omega})H(\lambda), \tag{8.27}$$

where

$$H(\lambda) = \left(\frac{4J_0(\lambda)}{\lambda^3} - \frac{8J_1(\lambda)}{\lambda^4}\right)J_1(\lambda). \tag{8.28}$$

The transfer functions are written as

$$\begin{aligned}\Phi(\omega) &= \int_0^\infty \mathrm{d}\lambda\ \left(-\omega^2 - \omega\lambda\sqrt{\frac{-\lambda^2 + \sqrt{\lambda^4 + \omega^2}}{2}}\right)H(\lambda), \\ \Psi(\omega) &= \int_0^\infty \mathrm{d}\lambda\ \left(\omega\lambda^2 + \omega\lambda\sqrt{\frac{\lambda^2 + \sqrt{\lambda^4 + \omega^2}}{2}}\right)H(\lambda).\end{aligned} \tag{8.29}$$

We take the numerical integrals by means of the trapezoidal rule. To ensure the numerical convergence, we take care of the resolution and the integral range. We set

the sufficiently small sampling interval of $\Delta\lambda = 3\cdot 10^{-5}$. Instead of half-infinite range $\lambda \in [0,\infty)$, we take the integral within the truncated domain $\lambda \in [0,\Lambda]$ based on

$$\Phi = \int_0^\Lambda \mathrm{d}\lambda \ \left(-\omega^2 - \omega\lambda\sqrt{\frac{-\lambda^2+\sqrt{\lambda^4+\omega^2}}{2}}\right) H(\lambda) + O(\Lambda^{-4}),$$
$$\Psi = \int_0^\Lambda \mathrm{d}\lambda \ \left(\omega\lambda^2 + \omega\lambda\sqrt{\frac{\lambda^2+\sqrt{\lambda^4+\omega^2}}{2}}\right) H(\lambda) + \frac{2\omega}{\pi\Lambda^2}\left(4\cos\Lambda\sin\Lambda - 3\right) + O(\Lambda^{-3}), \tag{8.30}$$

in which the last terms corresponds to the decaying behavior of the truncated error. To make the the truncated error sufficiently small, we set $\Lambda = 3000$. In evaluating the Bessel functions, we use the subroutines of '*Numerical Recipes in Fortran*'. As deduced from the numerical tests, in which the resolution, the integral domain and the parameter ω are varied, the accuracy of the transfer functions is more than six significant digits. For validation of the numerical integrals, we make comparison with the analytical behaviors of transfer functions both for $\omega \ll 1$ and for $\omega \gg 1$. The parts of the integral kernels for $\omega \ll 1$ asymptotically behave

$$-\omega^2 - \omega\lambda\sqrt{\frac{-\lambda^2+\sqrt{\lambda^4+\omega^2}}{2}} \to -\frac{3}{2}\omega^2, \quad \omega\lambda^2 + \omega\lambda\sqrt{\frac{\lambda^2+\sqrt{\lambda^4+\omega^2}}{2}} \to 2\lambda^2\omega,$$

while those for $\omega \gg 1$ behave

$$-\omega^2 - \omega\lambda\sqrt{\frac{-\lambda^2+\sqrt{\lambda^4+\omega^2}}{2}} \to -\omega^2 - \frac{\sqrt{2}}{2}\omega^{3/2}\lambda \quad \omega\lambda^2 + \omega\lambda\sqrt{\frac{\lambda^2+\sqrt{\lambda^4+\omega^2}}{2}} \to \frac{\sqrt{2}}{2}\omega^{3/2}\lambda + \omega\lambda^2.$$

We obtain the asymptotic solutions for $\omega \ll 1$,

$$\Phi = \frac{32}{15\pi}\omega^2 + \ldots, \quad \Psi = -\frac{16}{3\pi}\omega + \ldots, \tag{8.31}$$

while those for $\omega \gg 1$,

$$\Phi = \frac{64}{45\pi}\omega^2 + \frac{\sqrt{2}}{4}\omega^{3/2} + \ldots, \quad \Psi = -\frac{\sqrt{2}}{4}\omega^{3/2} - \frac{8}{3\pi}\omega + dots \tag{8.32}$$

The transfer functions for the no-slip interface and wall are shown in Fig. 8.2. The agreements with the asymptotic solutions both for $\omega \ll 1$ and $\omega \gg 1$ may validate the present numerical determinations.

FS interface and FS wall (case ii)

For the FS interface and FS wall, we obtain

$$(-\hat{p} + 2\partial_z\hat{u}_z)_{z=0} = \hat{\zeta}\int_0^\infty \mathrm{d}\lambda \ \left(4\lambda^4 + 4i\omega\lambda^2 - \omega^2 - 4\lambda^3\sqrt{\lambda^2+i\omega}\right)\left(\frac{2J_0(\lambda)}{\lambda^2} - \frac{4J_1(\lambda)}{\lambda^3}\right) J_0(\lambda r), \tag{8.33}$$

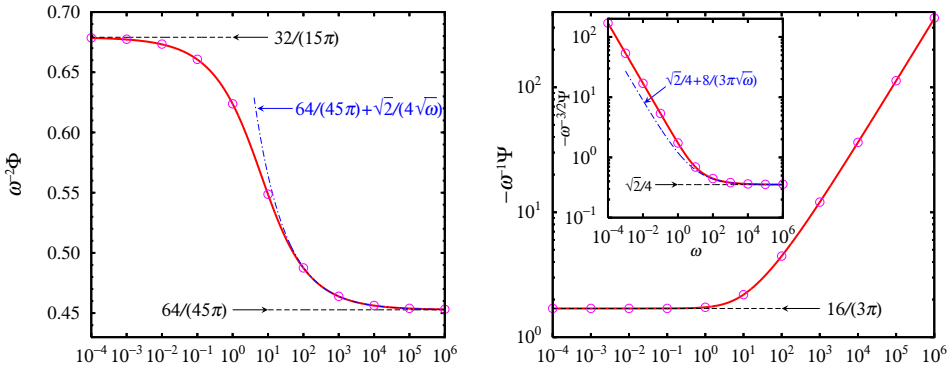

(a) $\omega^{-2}\Phi$ (b) $-\omega^{-1}\Psi$ and $-\omega^{-3/2}\Psi$

Figure 8.2: Transfer functions Φ and Ψ versus the angular frequency ω for the no-slip interface and wall. The solid line shows the numerical evaluation. The symbol shows the finite difference solution. The dashed and alternatively dashed and dotted lines show the asymptotic solutions.

$$\langle -\hat{p} + 2\partial_z \hat{u}_z \rangle_S = \hat{\zeta} \int_0^\infty \mathrm{d}\lambda \ \left(4\lambda^4 + 4i\omega\lambda^2 - \omega^2 - 4\lambda^3 \sqrt{\lambda^2 + i\omega} \right) H(\lambda). \tag{8.34}$$

The transfer functions are written as

$$\begin{aligned} \Phi(\omega) &= \int_0^\infty \mathrm{d}\lambda \ \left(4\lambda^4 - \omega^2 - 2\lambda^3 \sqrt{2(\lambda^2 + \sqrt{\lambda^4 + \omega^2})} \right) H(\lambda), \\ \Psi(\omega) &= \int_0^\infty \mathrm{d}\lambda \ \left(4\omega\lambda^2 - 2\lambda^3 \sqrt{2(-\lambda^2 + \sqrt{\lambda^4 + \omega^2})} \right) H(\lambda). \end{aligned} \tag{8.35}$$

Taking the integral within the truncated domain $\lambda \in [0, \Lambda]$, we can estimate the truncated error from

$$\begin{aligned} \Phi(\omega) &= \int_0^\Lambda \mathrm{d}\lambda \ \left(4\lambda^4 - \omega^2 - 2\lambda^3 \sqrt{2(\lambda^2 + \sqrt{\lambda^4 + \omega^2})} \right) H(\lambda) + O(\Lambda^{-4}), \\ \Psi(\omega) &= \int_0^\Lambda \mathrm{d}\lambda \ \left(4\omega\lambda^2 - 2\lambda^3 \sqrt{2(-\lambda^2 + \sqrt{\lambda^4 + \omega^2})} \right) H(\lambda) + \frac{2\omega}{\pi\Lambda^2} (4\cos\Lambda \sin\Lambda - 3) + O(\Lambda^{-3}). \end{aligned} \tag{8.36}$$

Since the decaying behavior of the truncated error with respect to Λ is similar to Eq. (8.30), we employ the same numerical procedure to evaluate the transfer functions as that for the NS interface and NS wall. Asymptotic behaviors of the integral kernels are summarized below:

$$4\lambda^4 - \omega^2 - 3\lambda^3 \sqrt{2(\lambda^2 + \sqrt{\lambda^4 + \omega^2})} \to \begin{cases} -\dfrac{3}{2}\omega^2 & (\omega \to 0) \\ -\omega^2 - 2\sqrt{2}\lambda^3 \omega^{1/2} & (\omega \to \infty) \end{cases}$$

$$4\omega\lambda^2 - 2\lambda^3\sqrt{2(-\lambda^2+\sqrt{\lambda^4+\omega^2})} \to \begin{cases} 2\lambda^2\omega & (\omega \to 0) \\ 4\lambda^2\omega - 2\sqrt{2}\lambda^3\omega^{1/2} & (\omega \to \infty) \end{cases}$$

We obtain the asymptotic solutions for $\omega \ll 1$,

$$\Phi = \frac{32}{15\pi}\omega^2 + \ldots, \quad \Psi = -\frac{16}{3\pi}\omega + \ldots, \tag{8.37}$$

while those for $\omega \gg 1$,

$$\Phi = \frac{64}{45\pi}\omega^2 + 4\sqrt{2}\omega^{1/2} + \ldots, \quad \Psi = -\frac{32}{3\pi}\omega + 4\sqrt{2}\omega^{1/2} + \ldots \tag{8.38}$$

With respect to ω, the leading exponent of Ψ as $\omega \to \infty$ is 1 which is different from 3/2 for the no-slip interface and wall. We interpret that the difference stems from the different generation mechanism of the kinetic energy dissipation. For the NS wall, the vorticity is generated at the wall due to the shearing motion of the fluid and then diffuses in the vertical direction. As a consequence, the bulk region contains the significant energy dissipation rate, which is necessarily maintained by the kinetic energy production by way of the interface oscillation. In contrast, such an additional energy production is not present for the FS wall since the vorticity is not generated at the wall. The behaviors of Ψ as $\omega \to 0$ and the leading term of Φ as $\omega \to \infty$ are same as those for the no-slip interface and wall.

The transfer functions for the free-slip interface and wall are shown in Fig. 8.3. The agreements with the asymptotic solutions both for $\omega \ll 1$ and $\omega \gg 1$ may validate the present numerical evaluation.

FS interface and NS wall (case iii)

By means of the direct numerical simulation, we solve the governing equations (8.7) and (8.8) with the boundary conditions (8.12) and (8.15) to determine the transfer functions Φ and Ψ. We employ the finite difference scheme. On the staggered grid, the space derivatives are approximated by the second-order central difference scheme. Introducing the pseudo-time τ, we integrate the following equation in time by using the first-order implicit Euler scheme until the convergence of the steady solution.

$$\frac{\partial \hat{\boldsymbol{u}}}{\partial \tau} = -\nabla p + (\nabla^2 - i\omega)\hat{\boldsymbol{u}}.$$

We choose the time step $\Delta\tau = 0.5\omega^{-1}$. The solenoidal condition of the velocity vector is satisfied by solving a Poisson equation for the pressure. We employ a simplified-marker-and-cell procedure and solve the pressure equation in an iterative way by means of the tridiagonal matrix algorithm and the successive over relaxation method. The number of the grid point for the interface ($0 \le r \le 1$ and $z = 0$) is taken $N_I = 50$. The extent of the simulation domain is $r_{\max} \times z_{\max} = 741 \times 1000$ which is divided

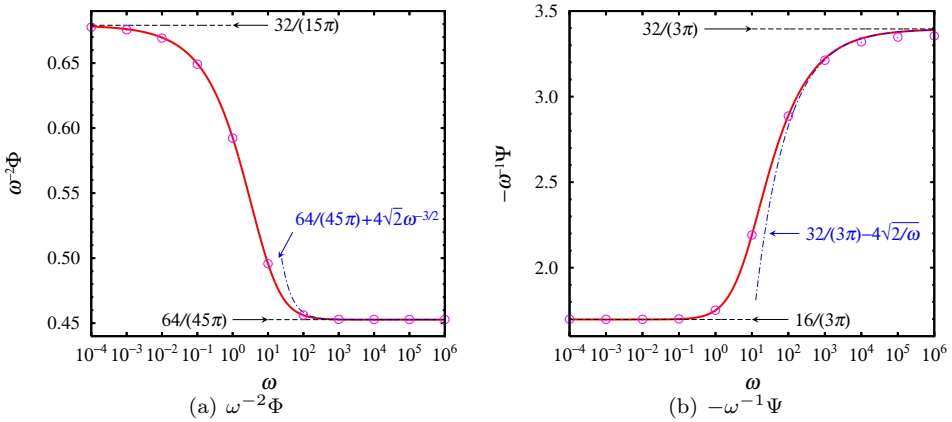

(a) $\omega^{-2}\Phi$ (b) $-\omega^{-1}\Psi$

Figure 8.3: Transfer functions Φ and Ψ versus the angular frequency ω for the free-slip interface and wall. The solid line shows the numerical evaluation. The symbol shows the finite difference solution. The dashed and alternatively dashed and dotted lines show the asymptotic solutions.

into $N_r \times N_z = 300 \times 300$. The grid width is written in a geometric series form, i.e.,

$$\begin{aligned}
\Delta r_j &= \alpha_r \Delta r_{j-1} && \leq j \leq N_I/2 \\
\Delta r_j &= \Delta r_{j-1} && j = N_I/2 + 1 \\
\Delta r_j &= \alpha_r^{-1} \Delta r_{j-1} && N_I/2 + 1 \leq j \leq N_I/2 \\
\Delta r_j &= \alpha_r \Delta r_{j-1} && N_I + 1 \leq j \\
\Delta z_j &= \alpha_z \Delta z_{j-1} && \forall j,
\end{aligned}$$

where $\alpha_r = 1.03$ and $\alpha_z = 1.04$. The boundary condition (8.13) at the large distance from the interface is replaced by the free-slip condition $u_z = \partial_z u_r = 0$ at $z = z_{\max}$.

The finite difference evaluations for the NS interface and wall (case i) and FS interface and wall (case ii) are shown as the circle symbols, respectively, in figure 8.2 and figure 8.3. The both simulation results show good agreement with the solid lines, corresponding to the high-accurate numerical evaluations written in the integral forms Eq. (8.30) and (8.36). For the NS interface and wall, the relative errors of Φ and Ψ are less than 0.035% and 1.2%, respectively, while for the FS interface and wall, those are less than 0.080% and 1.0%. In particular, the simulation results are accurate enough within a range of $10^0 \leq \omega \leq 10^2$, in which all the experimental conditions lie, namely, the relative errors of Φ and Ψ are less than 0.028% and 0.026%, respectively, while for the FS interface and wall, those are less than 0.038% and 0.098%. The transfer functions for the FS interface and NS wall are shown in figure 8.4. To numerically evaluate them, we use the same simulation code for the symbols shown in figure 8.2 and figure 8.3. Thus, we expect the comparable accuracies to the above-mentioned ones. As deduced from figure 8.4, the asymptotic solutions for $\omega \ll 1$ may be written

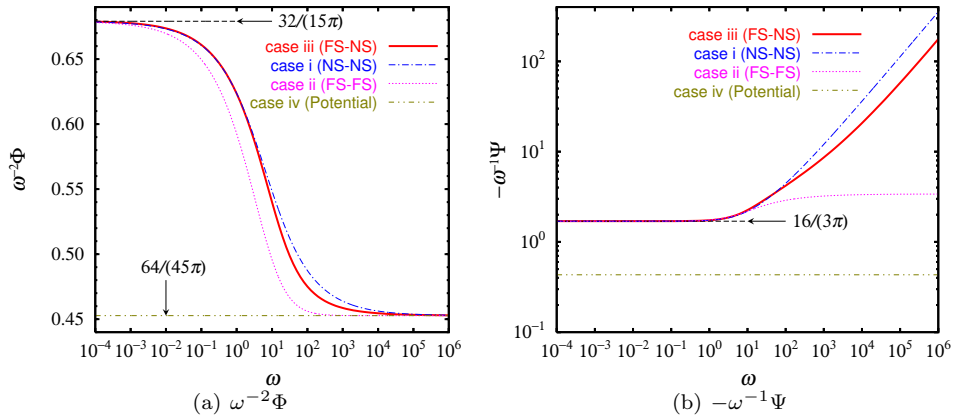

(a) $\omega^{-2}\Phi$ (b) $-\omega^{-1}\Psi$

Figure 8.4: Transfer functions Φ and Ψ versus the angular frequency ω for various boundary conditions.

as

$$\Phi = \frac{32}{15\pi}\omega^2 + \ldots, \quad \Psi = -\frac{16}{3\pi}\omega + \ldots. \tag{8.39}$$

For $\omega \gg 1$, Φ may approach to

$$\Phi = \frac{64}{45\pi}\omega^2 + \ldots. \tag{8.40}$$

and $-\Psi \propto \omega^{3/2}$. The profiles of the transfer functions for the FS interface and NS wall are globally nearer to those for the NS interface and wall than those for the FS interface and wall. This tendency indicates that the NS wall, which generates the considerable bulk energy dissipation rate, is more significant for the transfer functions than the FS interface.

8.1.2 Potential

Considering the compressibility of gas, we now evaluate the potential force. Here, we use the same non-dimensionalization using the kinematic viscosity as that in Sec. 8.1.1. We should take care of this dimensionless treatment for the gas pressure, which is usually normalized by using the stationary pressure, in estimating the resonance characteristics in the *dimensional* form. Supposing that a speed of sound is high enough compared with the velocity of the interface, we recognize that the gas pressure P_G is spatially homogeneous inside the groove. In the stationary state, the gas pressure balances with the liquid one, i.e., $P_{G0} = P_0$. When assuming the isothermal volume

change of gas, we determine the gas pressure in accordance with the deflection ζ,

$$P_G = \frac{HP_0}{H + 2\zeta \int_0^1 \mathrm{d}r\ (1-r^2)r}, \tag{8.41}$$

which would be approximated with the condition $\zeta/H \ll 1$ by

$$P_G = P_0 - \frac{P_0}{2H}\hat{\zeta}\exp(i\omega t) + O((\hat{\zeta}/H)^2). \tag{8.42}$$

We can additionally introduce the thermal damping effect to this expression. We assume that the temperature on the groove walls and the gas-liquid interface is fixed at the undisturbed temperature T_0 because of the large heat capacity of solid and liquid. According to the linear analysis for the cylindrical groove, performed by Chen & Prosperetti (1998, J. Acoust. Soc. Am., **104**, 1389), we write the gas pressure as

$$P_G = P_0 - \frac{\gamma P_0}{2H\left\{1 + 4(\gamma-1)\sum_{n=1}^{\infty}\left(\frac{1}{k_n^2} + \frac{2i\omega\tanh(k_nH/2)}{Hk_n^3\alpha_n^2 D}\right)\right\}}\hat{\zeta}\exp(i\omega t) + O((\hat{\zeta}/H)^2), \tag{8.43}$$

where

$$k_n = \sqrt{\alpha_n^2 + \frac{i\omega}{D}} = \sqrt{\frac{\alpha_n^2}{2} + \frac{1}{2}\sqrt{\alpha_n^4 + \frac{\omega^2}{D^2}}} + i\sqrt{-\frac{\alpha_n^2}{2} + \frac{1}{2}\sqrt{\alpha_n^4 + \frac{\omega^2}{D^2}}}, \tag{8.44}$$

α_n denotes the nth zero of $J_0(\alpha_n)$ and D represents the gas thermal diffusivity.

8.1.3 Relation between the deflection and driving pressure amplitudes

We now consider the Laplace law

$$P_G - P_L = \sigma\kappa, \tag{8.45}$$

where the curvature κ is given by

$$\kappa = \nabla\cdot\left(\frac{\nabla(z-\zeta(1-r^2))}{|\nabla(z-\zeta(1-r^2))|}\right) = 4\zeta + O(\zeta^3), \tag{8.46}$$

which indicates the curvature can be recognized uniform for given ζ as far as the deflection ζ is small enough. Substituting Eq. (8.25) and (8.42) into (8.45), we arrive at a relation between the deflection and the driving pressure amplitude

$$L(\omega, K)\hat{\zeta} = -\Delta, \tag{8.47}$$

where L is expressed as

$$L = -\Phi(\omega) - i\Psi(\omega) + K,$$

and K represents the rigidity, which is equivalent to the spring constant in the spring-mass system. K is dependent on the the angular frequency ω

$$K(\omega) = \frac{\gamma P_0}{2H\left\{1 + 4(\gamma-1)\sum_{n=1}^{\infty}\left(\frac{1}{k_n^2} + \frac{2i\omega\tanh(k_nH/2)}{Hk_n^3\alpha_n^2 D}\right)\right\}} + 4\sigma. \tag{8.48}$$

8.2 Hydrodynamic interaction

We now derive the interactive force among multiple menisci. Here, we consider two menisci labeled i and j. We take two cylindrical coordinates (r_i, θ_i, z) and (r_j, θ_j, z) from the origins at the the centroids of the i-th and j-th interfaces. The surface averaged normal stress on the j-th interface due to the i-th interfacial motion is written as

$$\begin{aligned}\langle -\hat{p}_i + 2\partial_z\hat{u}_{zi}\rangle_{S_j} =& \frac{1}{\pi}\int_0^{2\pi}\mathrm{d}\theta\int_0^1 \mathrm{d}r_j\ r_j(-\hat{p}_i + 2\partial_z\hat{u}_{zi})_{z=0} \\ =& -\int_0^{\infty}\mathrm{d}\lambda\langle J_0(\lambda r_i)\rangle_{S_j}\left\{(2\lambda^2 + i\omega)F(\lambda) + 2\lambda\sqrt{\lambda^2+i\omega}G(\lambda)\right\},\end{aligned} \tag{8.49}$$

where

$$\langle J_0(\lambda r_i)\rangle_{S_j} = \frac{1}{\pi}\int_0^{2\pi}\mathrm{d}\theta\int_0^1\mathrm{d}r_j\ r_j J_0(\lambda r_i). \tag{8.50}$$

Let d_{ij} be a distance between the i-th and j-th centroids, we rewrite $\langle J_0(\lambda r_i)\rangle_{S_j}$ as

$$\begin{aligned}\langle J_0(\lambda r_i)\rangle_{S_j} =& \int_0^1\mathrm{d}r_j\ \frac{r_j}{\pi}\int_0^{2\pi}\mathrm{d}\theta\ J_0(\lambda\sqrt{r_j^2 - 2r_jd_{ij}\cos\theta_j + d_{ij}^2}) \\ =& \int_0^1\mathrm{d}r_j\ \sum_{n=0}^{\infty}\frac{(-1)^n\lambda^{2n}J_0(\lambda d_{ij})r_i^{2n+1}}{2^{2n-1}(n!)^2} \\ =& \sum_{n=0}^{\infty}\frac{\left(\partial_{d_{ij}}^2 + d_{ij}^{-1}\partial_{d_{ij}}\right)^n J_0(\lambda d_{ij})}{4^n(n+1)(n!)^2},\end{aligned} \tag{8.51}$$

in which the higher-order contribution is negligible, i.e., $\langle J_0(\lambda r_i)\rangle_{S_j} \approx J_0(\lambda d_{ij})$, if $d_{ij} \gg 1$ and $\omega \gg 1$, In this case, the averaged stress is well approximated by

$$\langle -\hat{p}_i + 2\partial_z\hat{u}_{zi}\rangle_{S_j} = \frac{\hat{\zeta}_i\omega^2}{4d_{ij}} + o(d_{ij}^{-1}). \tag{8.52}$$

Hence, for a multi-meniscus system, the i-th displacement $\hat{\zeta}_i$ is governed by

$$L(\omega, K)\hat{\zeta}_i = -\Delta + \sum_{i\neq j}\frac{\omega^2\hat{\zeta}_j}{4d_{ij}}, \tag{8.53}$$

of which the second term in the r.h.s accounts for the effect from other menisci motions. The interaction is monopole, which is similar to that for the spherical bubbles suspended in liquid. Note that since this term contains ω^2, it leads to the increase of the virtual mass. For the multiple body problem, we write the simultaneous equations (8.53) in a matrix form with complex numbers, and numerically solve them to determine the deflection $\hat{\zeta}_i$. If the number of menisci is N, the size of the matrix to be inverted is $N \times N$.

Appendix A

Multilayer Rigorous Coupled Wave Analysis

We aim to calculate exactly the intensity of the light diffracted from an optical grating with arbitrary profile, made of an arbitrary number of isotropic (n scalar), dielectric (n real) or absorbing (n complex) materials. A method that allows to do so, is the Rigorous Coupled Wave Analysis (RCWA), that was pioneered in the 1980-90 [74, 75, 76, 39, 77, 93]. In this chapter, we will review this method, and present the steps that are necessary to write an efficient numerical implementation. At the end of the chapter, we will pay attention on the choice of the programming language(s) and the coding philosophy that was adopted in this work. These aspects are often overlooked, though of paramount importance, if we are aiming for modeling tools that provide a high numerical performance, paired with a flexible user interface, that is easily maintained and extended. It is the aim of those sections to unveil some of the benefits that are provided by recent generations of programming languages to scientific computing.

A.1 Analytic formulation

To be able to write an efficient implementation of the RCWA, we have to go through its derivation, and we have to understand its numerical tricks and tweaks. So let's do it.

A.1.1 Single layer grating

We start by considering a single layer diffraction grating, that is, the dielectric constant in the grating region is a function of y alone. Fig. A.1 shows a schematics of such a grating. The grating has a period T and thickness d. Space is divided into three regions. The reflection region R, characterized by a real dielectric constant ϵ^R, the grating region G with periodic (generally complex) dielectric constant

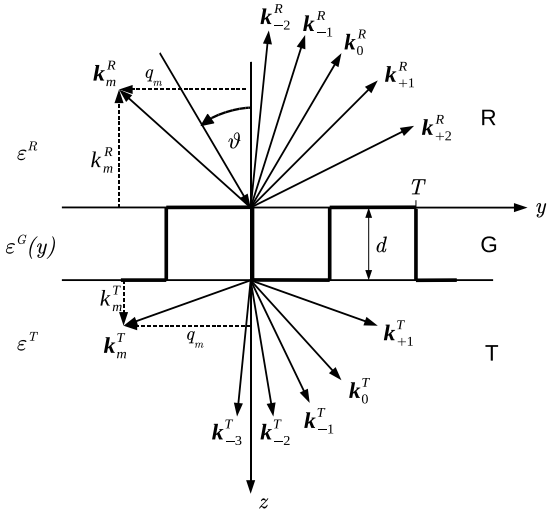

Figure A.1: Waves involved in the diffraction at an optical grating.

$\epsilon^G(y) = \epsilon^G(y+T)$, and the transmission region T, with a (generally complex) dielectric constant ϵ^T. The grating is illuminated from the reflection region under an incident angle ϑ_0.

Generally, as an optical grating is illuminated with a plane wave, a number of plane waves are scattered from the grating. Associated with every wave is a wave vector and an amplitude. It is convenient to express the spatial coordinate in units of $2\pi/\lambda$, i.e. $r \mapsto 2\pi r/\lambda$. Then the square of every wave vector in the reflection and transmission region is ϵ^R, respectively ϵ^T. We denote y-components of wave vectors by q's and z-components by k's. We denote the wave vector of the incident wave by k_0 and q_0. All other wave vectors obtain superscripts denoting the region, such as k^R_0. The y-components of the wavevectors follow from Floquet's theorem, as

$$q_n = q_0 + nQ, \tag{A.1}$$

where $n = -\infty \cdots + \infty$ is the diffraction order, $Q = \lambda/T$ and $q_0 = \sqrt{\epsilon^R}\sin\vartheta$. The z-components of the wave vectors require an individual treatment in each region. They generally follow from the Maxwell equations through a suitable secular equation. In the reflection and transmission region, this is the kernel of the wave equation in free space, and the z-components of the wave vectors follow as

$$\begin{aligned} k_0 &= (\epsilon^R - q_0^2)^{1/2} \\ k^R_n &= (\epsilon^R - q_n^2)^{1/2} \\ k^T_n &= (\epsilon^T - q_n^2)^{1/2}. \end{aligned} \tag{A.2}$$

A real k represents a visible diffraction order, a complex k represents an evanescent order. To accept only waves that travel in a physically meaningful direction, and

evanescent orders that do not diverge towards infinity, we require that $k_0 > 0$, $k_m^R < 0$, $k_m^T > 0$ respectively $\mathrm{Im}(\mathrm{k_m^R}) \leq 0$, $\mathrm{Im}(\mathrm{k_m^T}) \geq 0$.

In the grating region, the z-components of the wavevectors require a more elaborate treatment. From here on the two polarization directions s and p need to be distinguished. We consider first the technically less involved case of s-polarization. The derivation for p-polarization is presented thereafter.

Secular equation

With an s-polarized wave, the electric field vector is perpendicular to the scattering plane (s stands for the German word 'senkrecht' meaning perpendicular), such that only its x-component is non-zero, and we need to deal only with a scalar wave equation

$$\Delta E + \epsilon E = 0 \tag{A.3}$$

We expand the electric field into plane waves,

$$E = \sum_n S_n(z) e^{iq_n y}, \tag{A.4}$$

and the dielectric constant into a Fourier series,

$$\epsilon = \sum_m \epsilon_m e^{imQy}. \tag{A.5}$$

This goes into Eq. (A.3). We evaluate the operators

$$\Delta E = \sum_n \left(-q_n^2 S_n + S_n''\right) e^{iq_n y} \tag{A.6}$$

$$\begin{aligned} \epsilon E &= \sum_m \epsilon_m e^{imQy} \sum_n S_n e^{inQy} e^{iq_0 y} \\ &= \sum_n \sum_m \epsilon_{n-m} S_m e^{inQy} e^{iq_0 y} \\ &= \sum_n \sum_m \epsilon_{n-m} S_m e^{iq_n y}. \end{aligned} \tag{A.7}$$

Here we have made use of a discrete analog of the convolution theorem of the Fourier transformation. Now we use the fact that the plane waves form an orthogonal basis of the space of functions with period T, to say 'if two infinite sums over plane waves are equal, every single summand must be equal', and we write the equation for the n^{th} summand

$$-q_n S_n + S_n'' + \sum_m \epsilon_{n-m} S_m = 0 \tag{A.8}$$

This is a coupled second order ODE with constant coefficients. In principle these are infinitely many equations, however, in practice the system can be truncated and

solved. For the later numerical implementation, a representation in matrix form is useful

$$S'' - AS = 0, \tag{A.9}$$

with

$$A = \begin{pmatrix} (q_{-N}^2 - \epsilon_0) & -\epsilon_{-1} & \dots & -\epsilon_{-2N} \\ -\epsilon_1 & (q_{-N+1}^2 - \epsilon_0) & & \vdots \\ & \ddots & & \\ \vdots & & (q_{N-1}^2 - \epsilon_0) & -\epsilon_{-1} \\ -\epsilon_{2N} & \dots & -\epsilon_1 & (q_N^2 - \epsilon_0) \end{pmatrix} \tag{A.10}$$

Eq. (A.9) has the well known solution

$$S = \sum_m v_m \left(c_m^+ e^{\sqrt{\lambda_m} z} + c_m^- e^{-\sqrt{\lambda_m} z} \right), \tag{A.11}$$

where v_m and λ_m are the eigenvectors and eigenvalues of the matrix A, respectively, and c_m^+ and c_m^- are unknown coefficients.

Electric fields

With the knowledge of the wave vectors, the expansion of the electric fields into plain waves can be formulated in all regions. We consider first s-polarization. The expansion in the incident region contains the coefficients of the back-scattered waves R_n, that we eventually wish to calculate

$$E_n^R = e^{i(q_0 + k_0 z)} \delta_{n0} + R_n e^{i(q_n y + k_n^R z)}, \tag{A.12}$$

where δ is the Kronecker delta. The expansion in the transmission region contains equivalent transmission coefficients. We introduce already here a shift of the spacial coordinate to the boundary at $z = 0$, that will later be important in the multilayer method below, to avoid a loss of numerical precision in the exponential

$$E_n^T = T_n e^{i(q_n y + k_n^T z)} = \tilde{T}_n e^{i(q_n y + k_n^T (z-d))}. \tag{A.13}$$

For the field in the grating region, we introduce a similar shift of the spatial coordinate

$$\begin{aligned} E_n^G &= \sum_m v_{nm} \left(c_m^+ e^{\sqrt{\lambda_m} z} + c_m^- e^{-\sqrt{\lambda_m} z} \right) e^{i q_n y} \\ &= \sum_m v_{nm} \left(\tilde{c}_m^+ e^{\sqrt{\lambda_m} (z-d)} + \tilde{c}_m^- e^{-\sqrt{\lambda_m} z} \right) e^{i q_n y} \end{aligned} \tag{A.14}$$

The expansion coefficients determine the intensities of the diffracted waves through the Poynting vector as

$$\begin{aligned} I_n^R &= R_n R_n^* \frac{k_n^R}{k_0} \\ I_n^T &= T_n T_n^* \frac{k_n^T}{k_0} \end{aligned} \tag{A.15}$$

for s-polarization, and

$$\begin{aligned} I_n^R &= R_n R_n^* \frac{k_n^R}{k_0} \\ I_n^T &= T_n T_n^* \frac{k_n^T \epsilon^R}{\epsilon^T k_0} \end{aligned} \tag{A.16}$$

for p-polarization. In case all materials are transparent, energy conservation requires that

$$\sum_n I_n^R + I_n^T = 1, \tag{A.17}$$

which can serve to test the numerical accuracy of the calculation.

Field matching

From the Maxwell equations in integral form, one derives continuity conditions for the electric and magnetic fields at a boundary, using Gauß' theorem (by shrinking the integration volume in a suitable manner). In the case of s-polarized waves, considered here, these reduce to requiring that E and $\partial_z E$ be continuous. We evaluate the derivatives in each region.

$$\begin{aligned} \partial_z E_n^R &= ik_0 e^{i(q_0 + k_0 z)} \delta_{n0} + ik_n^R R_n e^{i(q_n y + k_n^R z)} \\ \partial_z E_n^G &= \sum_m \sqrt{\lambda_m} v_{nm} \left(\tilde{c}_m^+ e^{\sqrt{\lambda_m}(z-d)} - \tilde{c}_m^- e^{-\sqrt{\lambda_m} z} \right) e^{iq_n y} \\ \partial_z E_n^T &= k_n^T \tilde{T}_n e^{i(q_n y + k_n^T (z-d))} \end{aligned} \tag{A.18}$$

We substitute the boundaries into E and $\partial_z E$. At $z = 0$, we have

$$\begin{aligned} \delta_{n0} + R_n &= \sum_m v_{nm} \left(\tilde{c}_m^+ e^{-\sqrt{\lambda_m} d} + \tilde{c}_m^- \right) \\ ik_0 \delta_{n0} + ik_n^R R_n &= \sum_m \sqrt{\lambda_m} v_{nm} \left(\tilde{c}_m^+ e^{-\sqrt{\lambda_m} d} - \tilde{c}_m^- \right), \end{aligned} \tag{A.19}$$

and at $z = d$

$$\begin{aligned} \sum_m v_{nm} \left(\tilde{c}_m^+ + \tilde{c}_m^- e^{-\sqrt{\lambda_m} d} \right) &= \tilde{T}_n \\ \sum_m \sqrt{\lambda_m} v_{nm} \left(\tilde{c}_m^+ - \tilde{c}_m^- e^{-\sqrt{\lambda_m} d} \right) &= ik_n^T \tilde{T}_n \end{aligned} \tag{A.20}$$

This is a $4N \times 4N$ linear system, where $N = -M + P + 1$ is the total number of diffraction order retained in the expansion (M and P, being the positive and negative cut off). Written in matrix form, it reads

$$\begin{array}{cccc} R & \tilde{c}^+ & \tilde{c}^- & \tilde{T} \\ -I & VX & V & \\ -iK^R & V\Lambda X & -V\Lambda & \\ & -V & -VX & I \\ & -V\Lambda & V\Lambda X & iK^T \end{array} = \begin{array}{c} \delta \\ ik_0\delta \\ 0 \\ 0 \end{array}, \tag{A.21}$$

where R, $\tilde{c}^+$, $\tilde{c}^-$, and $\tilde{T}$ are coefficient lists identifying the columns of the matrix, V is a matrix containing the eigenvectors v_{nm}, Λ is a diagonal matrix containing the roots of the eigenvalues $\sqrt{\lambda_m}$, and X is diagonal matrix containing the exponents $e^{-\sqrt{\lambda_m}d}$. K^R and K^T are diagonal matrices containing the z-components of the wave vectors in the reflection and transmission region. By solving above linear system, the coefficients for the expansion into plain waves are found in all region in space, and a complete solution to the Maxwell equations is obtained. The solution can in principle be made arbitrarily accurate, by retaining a sufficiently large number of diffraction orders in the expansion. However, so far we have only considered a single layer grating, and the real strength in the RCWA lies in its ability to describe gratings with an arbitrary profile as a stack of sufficiently thin layers. We will thus not pursue the solution of above linear system in further detail, and postpone the final step of linear algebra to Sec. A.1.2, where we treat at once the multilayer system. Before we turn to the multilayer system, we shall however repeat our calculation for the p-polarization case.

p-polarization

We consider both Maxwell equations.

$$\begin{aligned} \nabla \times H &= \frac{1}{c}\partial_t \epsilon E \\ \nabla \times E &= -\frac{1}{c}\partial_t \epsilon H \end{aligned} \tag{A.22}$$

Substituting plain waves, we have

$$\begin{aligned} \nabla \times H &= -\frac{i\omega}{c}\epsilon E \\ \nabla \times E &= \frac{i\omega}{c}\epsilon H \end{aligned} \tag{A.23}$$

Thus

$$\begin{aligned} \partial_z H_x &= -\frac{i\omega}{c}\epsilon E_y \\ \partial_y E_z - \partial_z E_y &= \frac{i\omega}{c} H_x \\ \partial_y H_x &= \frac{i\omega}{c}\epsilon E_z \end{aligned} \tag{A.24}$$

We expand the fields

$$\begin{aligned} H_x^G &= \sum_n U_n e^{iq_n y} \\ E_y^G &= \frac{ic}{\omega}\sum_n S_n e^{iq_n y} \\ E_z^G &= \frac{ic}{\omega}\sum_n P_n e^{iq_n y} \end{aligned} \tag{A.25}$$

and the dielectric constant

$$\epsilon = \sum_m \epsilon_m e^{imQy}. \tag{A.26}$$

Substitution yields

$$\begin{aligned} U'_n &= \sum_m \epsilon_{n-m} S_m \\ \frac{ic}{\omega} i q_n P_n - \frac{ic}{\omega} S'_n &= \frac{i\omega}{c} U_n \\ i q_n U_n &= \sum_m \epsilon_{n-m} P_m \end{aligned} \tag{A.27}$$

We introduce the matrix $\epsilon_{nm} = \epsilon_{n-m}$. The first line reads

$$U_n = \sum_m \epsilon_{nm} S_m, \tag{A.28}$$

the second line is rearranged to

$$-q_n P_n - i S'_n = i \frac{\omega^2}{c^2} U_n \tag{A.29}$$

And the third line is inverted

$$\sum_m q_m \epsilon^{-1}_{nm} i q_m U_m = -q_n Pn \tag{A.30}$$

The second and third line yield together

$$\sum_m q_m \epsilon^{-1}_{nm} i q_m U_m - i S'_n = i \frac{\omega^2}{c^2} Un \tag{A.31}$$

The first line yields

$$\sum_m \epsilon^{-1}_{nm} U''_m = S'_n, \tag{A.32}$$

thus

$$\sum_m q_n \epsilon^{-1}_{nm} i q_m U_m - i \sum_m \epsilon^{-1}_{nm} U''_m = i \frac{\omega^2}{c^2} U_n, \tag{A.33}$$

which, after some rearrangement yields

$$U''_n - \sum_{k,m} \epsilon_{nk} \left(q_k - \epsilon^{-1}_{km} q_m - \delta_{km} \right) U_m = 0 \tag{A.34}$$

The boundary conditions are a potential pitfall. They are really that E_x, E_y, H_x, H_y be continuous, and *not* generally any of the derivatives such as $\partial_z H_x$. In this case the H_x one and the E_y one are those to be considered. Substitution of plane waves in the Maxwell equation, yields

$$-\frac{i\omega}{c} \epsilon E_y = \partial_z H_x, \tag{A.35}$$

thus, in the incident and transmission region, we have

$$-\frac{i\omega}{c}\epsilon E_y = \partial_z H_x, \tag{A.36}$$

however, in the grating region we have

$$-\frac{i\omega}{c}\epsilon E_y = \sum_n S_n e^{iq_n y} = \sum_{m,n} \epsilon^{-1}_{nm}\partial_z U_m e^{iq_n y} = \boldsymbol{\epsilon}^{-1} H_x^G, \tag{A.37}$$

where $\boldsymbol{\epsilon}^{-1}$ is the inverse epsilon matrix. Thus, the n^{th} order of the field and derivative in each region in space reads

$$\begin{aligned}
H_n^R &= \delta_{n0} e^{i(q_0 y + k_0^R z)} + R_n e^{i(q_n y + k_n^R z)} \\
\frac{1}{\epsilon^R}\partial_z H_n^R &= \frac{ik_0}{\epsilon^R}\delta_{nn_0} + \frac{ik_n^R}{\epsilon_R} R_n e^{i(q_n y + k_n^R z)} \\
H_n^G &= \sum_m v_{nm}\left(\tilde{c}_m^+ e^{\sqrt{\lambda_m}(z-d)} + \tilde{c}_m^- e^{-\sqrt{\lambda_m} z}\right) e^{iq_n y} \\
\boldsymbol{\epsilon}^{-1}\partial_z H_n^G &= \sum_k \epsilon^{-1}_{nk} \sum_m \sqrt{\lambda_m} v_{km}\left(\tilde{c}_m^+ e^{\sqrt{\lambda_m}(z-d)} - \tilde{c}_m^- e^{-\sqrt{\lambda_m} z}\right) e^{iq_n y} \\
H_n^T &= \tilde{T}_n e^{i(q_n y + k_n^T (z-d))} \\
\frac{1}{\epsilon^T}\partial_z H_n^T &= \frac{ik_n^T}{\epsilon^T}\tilde{T}_n e^{i(q_n y + k_n^T (z-d))}
\end{aligned} \tag{A.38}$$

We evaluate the boundaries. At $z = 0$ we have

$$\begin{aligned}
\delta_{n0} + R_n &= \sum_m v_{nm}\left(\tilde{c}_m^+ e^{-\sqrt{\lambda_m} d} + \tilde{c}_m^-\right) \\
\frac{ik_0}{\epsilon^R}\delta_{n0} + \frac{ik_n^R}{\epsilon^R} R_n &= \sum_{k,m} \epsilon^{-1}_{nk} v_{km}\sqrt{\lambda_m}\left(\tilde{c}_m^+ e^{-\sqrt{\lambda_m} d} - \tilde{c}_m^-\right)
\end{aligned} \tag{A.39}$$

and at $z = d$

$$\begin{aligned}
\sum_m v_{nm}\left(\tilde{c}_m^+ + \tilde{c}_m^- e^{-\sqrt{\lambda_m} d}\right) &= \tilde{T}_n \\
\sum_{k,m} \epsilon^{-1}_{nk} v_{km}\sqrt{\lambda_m}\left(\tilde{c}_m^+ - \tilde{c}_m^- e^{-\sqrt{\lambda_m} d}\right) &= \frac{ik_n^T}{\epsilon^T}\tilde{T}_n
\end{aligned} \tag{A.40}$$

In matrix form,

$$\begin{matrix} R \\ -I \\ -\frac{i}{\epsilon^R}K^R \\ \\ \end{matrix}
\begin{matrix} \tilde{c}^+ & \tilde{c}^- & \tilde{T} \\ VX & V & \\ \boldsymbol{\epsilon}^{-1}V\Lambda X & -\boldsymbol{\epsilon}^{-1}V\Lambda & \\ -V & -VX & I \\ -\boldsymbol{\epsilon}^{-1}V\Lambda & \boldsymbol{\epsilon}^{-1}V\Lambda X & \frac{i}{\epsilon^T}K^T \end{matrix}
= \begin{matrix} \delta \\ i\frac{k_0}{\epsilon^R}\delta \\ 0 \\ 0 \end{matrix}, \tag{A.41}$$

, This is in large analogy to the *s*-polarization case, which is great, because it means we will be able to reuse a large amount of the numerical code.

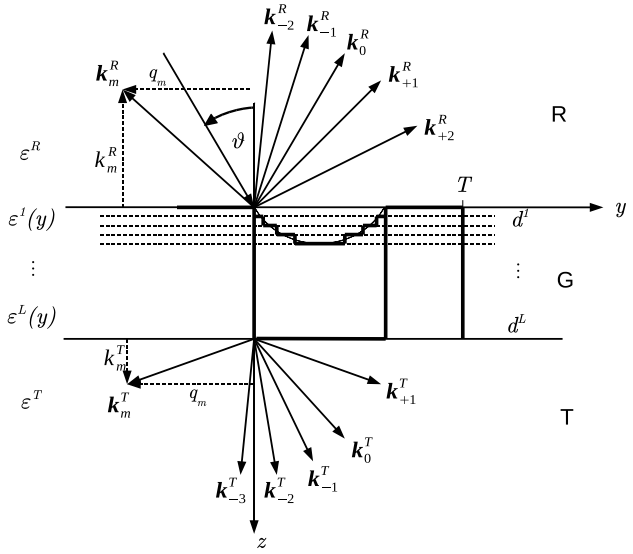

Figure A.2: Description of a grating with arbitrary surface profile through Rigorous Coupled Wave Analysis.

A.1.2 Multilayer grating

In the previous section we considered a single layer grating, characterized by a dielectric constant in the grating region that is a function of y alone. Most gratings met in real life, such as blazed gold gratings, and in particular also the superhydrophobic grating with the curved liquid-gas interfaces on top of its grooves studied in this work, do however not satisfy this assumption. The real strength in the RCWA lies in its ability to describe also these types of gratings, and generally gratings with arbitrary surface profile, with in principle arbitrary accuracy, as a stack of sufficiently thin grating layers. In this section we will go through the steps that are required to extend the rigorous coupled wave analysis to these types of gratings.

Fig. A.2 shows the schematics of a general grating. To describe an arbitrary surface profile –in this case the curved liquid-gas interface–, the grating is sliced into layers parallel to the surface. The curved interface is approximated by layers with a thickness much smaller than the wavelength, such that in each layer, the dielectric constant is again a function of y alone. The grating is thus represented by a stack of layers with periodic, generally complex dielectric constant $\epsilon^l(y) = \epsilon^l(y+T)$, $l = 1, \ldots, L$. Each layer is now treated separately to arrive at a secular equation, and subsequently the boundary conditions of the electric fields are evaluated at the boundary between each two layers. This results in $L+1$ matrix equation analogue to Eq. (A.21). It is tempting to go ahead and solve this system by successively inverting the equation for each boundary, and substituting the result in the next one. This works well analytically (forgetting for the moment, that the matrices are in principle

infinitely large, and we do not have a rigorous way of determining the regularity of the truncated matrices), however, numerically this fails horribly, since the matrix to be inverted, though regular, may have arbitrarily small diagonal elements, and inversion means division, such that we divide by something close to zero, and due to the finite number space of the computer the numerical error becomes arbitrarily large. And indeed, one of the most important maxims of numerical linear algebra is, that on usually does *not* invert a matrix, instead, one aims for finding one (or more) *solutions* to a linear system in an iterative manner. Therefore, one way –the safe way– to solve the $L+1$ matrix equations, is to write them as 'big' linear system and solve it at once (by means of one of the suitable algorithms, such as LU decomposition or singular value decomposition). It is appropriate to consider this method first.

Full solution

We consider first the case of s-polarization. From equations such as Eq. (A.21), the global linear system follows as

$$\begin{array}{cccccccccccccc}
[R] & [\bar{c}_1^+] & [\bar{c}_1^-] & [\bar{c}_2^+] & [\bar{c}_2^-] & \cdots & [\bar{c}_{L-1}^+] & & [\bar{c}_{L-1}^-] & & [\bar{c}_L^+] & [\bar{c}_L^-] & [\tilde{T}] & \\
-I & V^1X^1 & V^1 & & & & & & & & & & & \delta \\
-iK^R & V^1\Lambda^1X^1 & -V^1\Lambda^1 & & & & & & & & & & & i\frac{k_0}{\epsilon^R}\delta \\
 & -V^1 & -V^1X^1 & V^2X^2 & V^2 & & & & & & & & & 0 \\
 & -V^1\Lambda^1 & V^1\Lambda^1X^1 & V^2\Lambda^2X^2 & -V^2\Lambda^2 & & & & & & & & & \\
 & & & & & \ddots & & & & & & & & = \\
 & & & & & & -V^{L-1} & & -V^{L-1}X^{L-1} & & V^LX^L & V^L & & \vdots \\
 & & & & & & -V^{L-1}\Lambda^{L-1} & & V^{L-1}\Lambda^{L-1}X^{L-1} & & V^L\Lambda^LX^L & -V^L\Lambda^L & & \\
 & & & & & & & & & & -V^L & -V^LX^L & I & \\
 & & & & & & & & & & -V^L\Lambda^L & V^L\Lambda^LX^L & iK^T & 0
\end{array} \tag{A.42}$$

Note that symbols in square brackets are column designators. The solution to this $2N(l+1) \times 2N(l+1)$ system provides the expansion coefficients of the fields in *all* regions in space. The result for p-polarization is obtained by inserting $1/\epsilon$'s, respectively $\boldsymbol{\epsilon}_l^{-1}$'s at the appropriate places. This is the easiest way of obtaining the expansion coefficients, and indeed, it is the best way if *all* coefficients are needed, e.g., if one wishes to calculate the field distribution inside the grating. And, it is also feasible, when the number of grating layers is small. However, when a large number of grating layers is required, and the grating period is large, such that a large number of diffraction orders need to be retained in the expansion, the linear system quickly blows up and exceeds the capabilities of current computer technology, both in terms of computational power and memory. E.g., for the superhydrophobic surfaces with 12μm period, studied in this paper about $\pm$128 diffraction orders are required to obtain accurate results (generally about $10\dot{n}T/\lambda$ order are required). The large dimensions require additionally a large number of slices. Generally the discretization is accurate, when the thickness of the layers is smaller than about $1/10\lambda/n$. With a meniscus that is curved downwards by 3μm, about 100 slices are required. We thus end up with a $50\,000 \times 50\,000$ matrix. Assuming 4 byte floating point representation (single precision), and taking into account that the storage of a complex number requires double the amount, we find, that no less than 20Gbyte of memory would be required only to store the matrix. Additionally matrix inversion scales with N^3, and it is unlikely that we would obtain results within a reasonable computation time. Thus, a smarter way for solving the global linear system is required. A clever scheme was suggested in [77]. It is based on iteratively solving the individual equation at

each boundary without performing numerically ill conditioned matrix inversions. The equation is cast into a form that allows to separate the well-conditioned part of the matrix from the ill-conditioned one, and perform inversion only on the former. In the end, one obtains only the reflected waves (or only the transmitted waves), while all information about the expansion coefficients of the waves in the grating layers is lost. In most cases, this is however not a concern, since one is indeed only interested of the reflected or transmitted waves. This scheme is invaluable for the type of calculations performed in this work. The following section is devoted to its analytic formulation.

Partial solution

We consider first the conceptually easier case for the reflected waves. The derivation for the transmitted waves is presented thereafter. As before, the form of the equations is identical for s- and p-polarization, only the numerical values of the matrices differ by additional $1/\epsilon$'s and $\boldsymbol{\epsilon}_l^{-1}$'s. We present here the case for s-polarization. We start by rewriting the equation at the last boundary. We denote this the $L+1^{th}$ boundary. According to Eq. A.21 we have at the last boundary (as before, symbols in square brackets are column designators)

$$\begin{matrix}[\tilde{c}_L^+] & [\tilde{c}_L^-] & & [\tilde{T}] \\ V^L & V^L X^L & = & f^{L+1} \\ V^L\Lambda^L & -V^L\Lambda^L X^L & & g^{L+1}\end{matrix}, \tag{A.43}$$

where $f^{L+1} = I$, and $g^{L+1} = iK^T$. The trouble in inverting above equation is cause by the column containing the X's, since those contain phase factors, and those can be zero. We thus rearrange the columns in the following way

$$\begin{matrix}[\tilde{c}_L^-] & & [\tilde{c}_L^+] & [\tilde{T}] \\ V^L X^L & = & -V^L & f^{L+1} \\ -V^L\Lambda^L X^L & & -V^L\Lambda^L & g^{L+1}\end{matrix}, \tag{A.44}$$

and we invert the latter, obtaining

$$\begin{pmatrix} -V^L & f^{L+1} \\ -V^L\Lambda^L & g^{L+1}\end{pmatrix}^{-1} \begin{pmatrix} V^L X^L \\ -V^L\Lambda^L X^L\end{pmatrix} [\tilde{c}_L^-] = \begin{bmatrix} \tilde{c}_L^+ \\ \tilde{T}\end{bmatrix} \tag{A.45}$$

From this equation we extract the upper row, that links the $\tilde{c}_L$'s. We write it as

$$a^L \tilde{c}_L^- = \tilde{c}_L^+. \tag{A.46}$$

This identity is used to substitute the $\tilde{c}+_L$ in the right-hand-side of the equation for the next lower boundary, here the L^{th} boundary. We thus obtain

$$\begin{matrix}[\tilde{c}_{L-1}^+] & [\tilde{c}_{L-1}^-] & & [\tilde{c}_L^-] & [\tilde{c}_L^-] \\ V^{L-1} & V^{L-1}X^{L-1} & = & a^L V^L X^L + V^L & =: f^L \\ V^{L-1}\Lambda^{L-1} & -V^{L-1}\Lambda^{L-1}X^{L-1} & & a^L V^L\Lambda^L X^L - V^L\Lambda^L & g^L\end{matrix}, \tag{A.47}$$

such that we end up with an equation that has the same form as considered previously. We go on like this until we reach the first boundary, where we face

$$\begin{matrix}[R] & & & [\tilde{c}_1^-] \\ I & \delta & = & f^1 \\ iK^R & ik_0\delta & & g^1 \end{matrix}, \tag{A.48}$$

which we rewrite as

$$\begin{matrix}[R] & [\tilde{c}_1^-] & & \\ -I & f^1 & = & \delta \\ -iK^R & g^1 & & ik_0\delta \end{matrix}. \tag{A.49}$$

This is a regular $2N \times 2N$ system that can be solved in a straight forward manner. Under the line, we have converted the inversion of one $2N(L+1) \times 2N(L+1)$ system into L+1 successive inversions of a $2N \times 2N$ system. Thus we have essentially transformed the computational problem from an N^9 problem to an N^7 problem. This provides us a great gain in computational speed and memory efficiency.

It remains to go through the fast scheme for the transmitted waves. We begin by considering the equation at the first boundary.

$$\begin{matrix}[R] & & & [\tilde{c}_1^+] & [\tilde{c}_1^-] \\ f_0 & + & a_0 & = & V^1X^1 & V^1 \\ g_0 & & b_0 & & V^1\Lambda^1X^1 & -V^1\Lambda^1 \end{matrix}, \tag{A.50}$$

where $f_0 = I$, $g_0 = iK^R$, and $a_0 = \delta$, $b_0 = ik_0\delta$. Thus

$$\begin{matrix}[R] & [\tilde{c}_1^-] & & [\tilde{c}_1^+] & & \\ f_0 & -V^1 & = & V^1X^1 & - & a_0 \\ g_0 & V^1\Lambda^1 & & V^1\Lambda^1X^1 & & b_0 \end{matrix}. \tag{A.51}$$

Thus

$$\begin{bmatrix} R \\ \tilde{c}^- \end{bmatrix} = \begin{pmatrix} f_0 & -V^1 \\ g_0 & V^1\Lambda^1 \end{pmatrix}^{-1} \begin{pmatrix} V^1X^1 \\ V^1\Lambda^1X^1 \end{pmatrix} [\tilde{c}_1^+] - \begin{pmatrix} f_0 & -V^1 \\ g_0 & V^1\Lambda^1 \end{pmatrix}^{-1} \begin{pmatrix} a_0 \\ b_0 \end{pmatrix}. \tag{A.52}$$

From this equation we extract the lower row and write it as

$$\tilde{c}_1^- = m^1\tilde{c}_1^+ - s^1 \tag{A.53}$$

Substitution in the equation for the second boundary yields

$$\begin{matrix} & [\tilde{c}_2^+] & & [\tilde{c}_2^+] & [\tilde{c}_2^-] \\ V^1 + V^1X^1m^1 & + & -V^1X^1s^1 & = & V^2X^2 & V^2 \\ V^1\Lambda^1 - V^1\Lambda^1X^1m^1 & & V^1\Lambda^1X^1s^1 & & V^2\Lambda^2X^2 & -V^2\Lambda^2 \end{matrix} \tag{A.54}$$

thus

$$\begin{matrix}[R] & & & [\tilde{c}_2^+] & [\tilde{c}_2^-] \\ f_0 & + & a_0 & = & V^2X^2 & V^2 \\ g_0 & & b_0 & & V^2\Lambda^2X^2 & -V^2\Lambda^2 \end{matrix}, \tag{A.55}$$

At the last boundary we face

$$\begin{matrix}[\tilde{c}^+] & & & [\tilde{T}] \\ f_L & + & a_L & = & I \\ g_L & & b_L & & iK^T \end{matrix} , \tag{A.56}$$

which we rewrite as

$$\begin{matrix}[\tilde{T}] & [\tilde{c}^+] & & \\ I & -f_L & = & a_L \\ iK^T & -g_L & & b_L \end{matrix} , \tag{A.57}$$

arriving at a final $2N \times 2N$ system that can be solved in a straight forward manner.

This finishes our analytic treatment of the Rigorous Coupled Wave Analysis. Having come this far, one may be inclined to ask 'What is next?'. For us the next steps will be a practical numerical implementation of the latter analytical treatment. On the analytical level, the next step would be to consider the case when light impinges on the grating in an incident plane that is *not* perpendicular to the grating grooves, known as the conical mount, and moreover, to give up the separation into s- and p-polarization, which led to scalar wave equations, and to consider instead anisotropic materials, such as birefringent and ferromagnetic materials, that are described by a dielectric tensor with generally nine independent elements, that makes it necessary to consider the full vectorial wave equation. An implementation of the latter is described in [39]. This is however beyond the scope of this work. And indeed, this situation is rarely met in practice, the only notable exception being diffractive x-ray optics, where many of the commonly used materials are birefringent. Noteworthy is also the work of Lifeng Li [64], who defined the state of the art by providing an efficient numerical method for crossed gratings, that is applicable to gratings with a two-dimensional profile.

A.2 Numerical formulation

The presented analytical formulation of the Rigorous Coupled Wave Analysis describes how to obtain –in theory– a solution to the Maxwell equations for the problem of diffraction of a plain wave from an optical grating. This is however really only half of the work. In practice, the analytic equations have to be cast into the form of an efficient computer code, that employs a set of delicate numerical algorithms. Choices have to be made, which computer language should be used, and how the code should be structured. These aspects are often overlooked. Nevertheless, they are of paramount importance, if we want to provide a code that is at the same time fast, flexible, and easy to use and maintain. This section is devoted to describe the numerical code written for this work, and the paradigms that stand behind it. A coding philosophy was adopted that aims at combining the unsurpassed numerical power of traditional procedural programming languages such as FORTRAN90, with the ability to combine functions and data to well structured entities provided by modern dynamic object oriented (OO) programming languages. We will refrain from justifying this approach (an excellent motivation can be found in [12]). We will rather

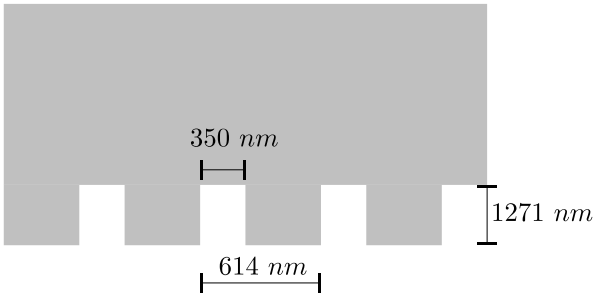

Figure A.3: Schematic of a rectangular profile dielectric transmission grating.

use the following subsections to explain the code and its user interface in greater detail. The user level code is described in the following subsection. The numerical core routines are briefly discussed in the subsection thereafter.

A.2.1 User level code

The definition of a grating geometry that is to be analyzed by RCWA can naturally be done on two rather different levels. On the one hand, the user may provide directly one or more grating layers, each characterized by its thickness and its dielectric function in y-direction – the latter possibly being supplied in form of a series of discrete values. On the other hand, the user may request: 'Calculate me the diffraction from a grating whose unit cell is described by a gold triangle with blaze angle 30°!', that is he or she may want to give the description of the unit cell in terms of a set of geometrical objects with certain properties. To give right to these rather different user interactions, the present code provides two levels of abstraction. In the following subsections we will describe both of them using a binary (rectangular profile) grating, respectively a grating with a curved meniscus on top of the groove as an example. We aim to illustrate thereby the power of abstraction provided through the OO approach, and introduce some of the features of the particular computer language that was chosen here, namely Python.

Binary grating

Suppose we want to describe a binary (rectangular profile) transmission grating as described in Fig. A.3. The grating consists of two halfspaces (the reflection and the transmission region) and one slice. We can simplify this even further and say, the grating consists of three slice (where two of them are infinitely thick and have a constant dielectric function in y–direction). The present code allows us to describe this stack simply by

```
[ reflection, binary, transmission ]
```

The brackets represent a list in Python, which may be thought of as an ordered sequence of arbitrary objects (the order really matters; if we do `list[0]` with a list

called `list`, we get back the first object, and not anything else). In this case, the three objects are the reflection, grating, and transmission slices. It is important to realize, that, though we could put arbitrary objects in our list (Python allows us to do so; we could write `[ 71.9, binary, 'hello' ]`, where `71.9` is just a floating point number, and `'hello'` is a string containing the word 'hello'), in our case the objects are all 'slice objects'. So how do we get these objects? To create a slice, we write

```
binary = slice( 1271, [ [350, air], [614, glass] ] )
```

The slice has a thickness of 1, and comprises two steps. Starting from 0, until 350, the material is air, and until 614 the material is Si. What are the units of these numbers? It does not matter. It only matters that the same unit is used throughout the computation, in particular, the wavelength should be specified in the same unit. For the purpose of this example, let us assume, these are micrometers. Above slice represents then the grating layer of a highly efficient high dispersion fused silica transmission grating as described in Chapter 5. Note, that the refractive index steps are again provided as a list. Generally, there can be an arbitrary number of steps, each consisting of a coordinate and a material. We are nearly done! The last thing that remains, is to specify what the materials `air` and `glass` really are. Here, we meet the full power of modern OO computer languages, in particular, we get involved with a feature called polymorphism. In the most simple case, we can write

```
air   = material(1.0)
glass = material(1.45)
```

And this does really what one would expect it does, it makes `air` a material with refractive index 1.0, and `glass` a material with refractive index 1.45. On many occasions we may however want to take into account that the refractive index of the material depends on the wavelength of the light. E.g., we may want to specify a series of tuples (λ_i, n_i), that describe the dielectric function over a certain wavelength range (possibly along with a directive how the code should interpolate between those numbers), or we may even go further and provide an arbitrary function that describes the wavelength dependency of the refractive index. It is important to stress that we want to specify this only here, at the moment when we define the material. At a later stage in the computation, we don't want to worry about such details any more, instead, we want to deal with a material by refering only to its name. The present code allows to do all this. E.g., we may write

```
gold  = material( [ [ 0.4000, (1.658 + 1.956j) ],
                    [ 0.4592, (1.426 + 1.846j) ],
                    [ 0.4769, (1.242 + 1.796j) ],
                    [ 0.4959, (0.916 +  1.84j) ],
                    [ 0.5166, (0.608 +  2.12j) ],
                    [ 0.5391, (0.402 +  2.54j) ],
                    [ 0.5636, (0.306 +  2.88j) ],
                    [ 0.5904, (0.180 +  2.84j) ],
                    [ 0.6199, (0.130 +  3.16j) ],
```

```
                    [ 0.6526, (0.166 +  3.15j) ],
                    [ 0.6888, (0.160 +   3.8j) ] ]  )
```

to describe the dispersion of gold through linear interpolation between tabulated experimental values. Or we may provide the dispersion of diamond through a Herzberger-type formula [45], as suggested in [90] by writing

```
def n(l):
   A = 2.37837
   B = 1.18897e-2
   C = -1.0083e-4
   D = -2.3676e-5
   E = 3.24263e-8
   L = 1/(l**2-0.0028)

   return A + B*L + C*L**2 + D*l**2 + E*l**4

diamond = material( n )
```

This provides an enormous amount of flexibility. The mechanism behind this is polymorphism, meaning that the objects, though providing the same functionality, are rather different (poly morph). E.g., in the case of the simplest material with wavelength independent refractive index, only one number needs to be stored along with the object, while in case of a tabulated refractive index, a sequence of tuples needs to be stored, along with code that is capable to perform interpolation between the values. But back to our example. We have provided a top-down description of the code necessary to define an optical grating (typically this is also the approach during programming; one starts with the 'big' global objects, and breaks them down into smaller and smaller pieces, until one ends up on the level of the actual code). Nevertheless, like most other programming languages, Python will complain if we refer to objects that are not yet known. Let us thus first summarize the lines of code in the correct order.

```
air   = material(1.0)
glass = material(1.45)

incident     = slice( inf,  [             [614, glass] ] )
binary       = slice( 1271, [ [350, air], [614, glass] ] )
transmission = slice( inf,  [             [614, air]   ] )
```

To embed the list of slices into a full computational task, it remains to write

```
grating = stack( [ incident, binary, transmission ] )
```

The resulting object, here named `grating`, comprises a full computational task. To adapt it to our needs, we may specify the incident angle and wavelength and polarization of the light, by writing

```
grating.theta = 36.67
grating.l     = 1064
grating.pol   = 'TE'
```

It remains to set the single computational parameter that enters the computation, namely the number of positive and negative orders retained in the plain wave expansion

```
grating.order = (-12, 12)
```

Through the '.' syntax, we have accessed particular data entities (designated by their name `theta pol`, etc.) that belong to the `grating` object. Generally, in OO programming, objects can not only have data entities attached to them. They can also contain functions ('methods' in OO parlance). This allows us to execute the at last the RCWA computation simply by writing

```
grating.compute()
```

This will return the diffraction intensities of the reflected and transmitted waves as represented by Eq. (2.63). The empty brackets of the call to the `.compute()` method represent a situation that is frequently encountered in OO programming. Generally, the method could take arbitrary arguments (since it is just a function as any other), however, in many cases, and as is also the case here, the method will operate on the object itself (that is the reason why it is stored together with the object), and all the data on which the method is supposed to operate are as well stored with the object, and the method knows where to find it. For this reason we don't need to specify anything further in the call of the `compute()` method. Looking back, we have described the computation of a custom dielectric transmission grating in just ten lines of very readable and intuitive code (in fact, we could do with six lines, if we combine the last five lines to `stack( [ incident, binary, transmission ], theta=60, pol='TE', order=(-12,12) ).compute()`).

To optimize a specific optical grating to provide peak performance in a certain wavelength range, one often needs to compute the diffraction characteristics of the grating for a large number of parameter choices, e.g., for the silica grating considered in this example, one typically varies the width and the depth of the grating grooves, and evaluates which combination provides the highest diffraction efficiency. In the remainder of this subsection we will show how this can be implemented in a straight forward manner, by embedding the previous code snippets into few lines of pure Python code

```
T = 614
air   = material(1.0)
glass = material(1.45)

incident     = slice( inf,   [               [T, glass] ] )
binary       = slice( 1271,  [ [0.5*T, air], [T, glass] ] )
transmission = slice( inf,   [               [T, air]   ] )
```

```
grating = stack( [ incident, binary, transmission ] )
grating.theta = 36.67
grating.l     = 1064
grating.pol   = 'TE'
grating.order = (-12, 12)

depth = arange(0.1, 1, 0.1)
width = arange(0.1, 1, 0.1)

result = []
for d in depth:
   binary.d = d * T
   for w in width:
      binary.steps[0][0] = w * T
      result += [ grating.compute() ]
```

Inside the loops, the relevant geometric properties of the binary layer (that is, its thickness, and the width of the air step, that defines the width of the groove) are repeatedly modified, and for each setting the diffraction intensities are computed. The results are accumulated in a list. At the end of the run the result may be further processed, e.g., we may save them by exporting the `result` variable to a file, or do some interactive plotting. This functionality is provided by existing Python modules that are readily available. The latter code is indeed all that is required to obtain the data that underlies Fig. 5.8.

Complex geometries

Above approach is useful to describe rather simple grating geometries, i.e., those that contain only of few grating layers. However, if the grating profile involves complicated shapes, it may be not straight forward to express it in terms of a series of grating layers. Thus, a simpler geometric approach is needed to define the geometry, and the process of deriving suitable slices is to be left to the computational routines. Suppose we want to describe the geometry of an optical grating that features a curved liquid-gas interface on top of its groove, as shown in Fig. A.4(a). Generally, a reasonably arbitrary two-dimensional geometry may be constructed by piling on top of each other a number of geometric objects, such as rectangles, circles, triangles, etc., that may overlap and partially cover each other, and consider the resulting 'image' as the final geometric object, just as one often does when preparing graphic illustrations for a presentation. In this case it would be natural to define first a box, that describes the extension of the unit cell, and then place geometric objects inside. 'inside' should not be taken too serious. Possibly one will allow the geometric objects to extend over the boundary of the box, i.e., the box may be thought of merely as a frame that is put on top of the pile of objects. Fig. A.4(b) illustrates this approach. How could this process look like in OO programming? Possibly one would start by creating a box. In the present case the box has a width of 8μm (that will later be the period T of the

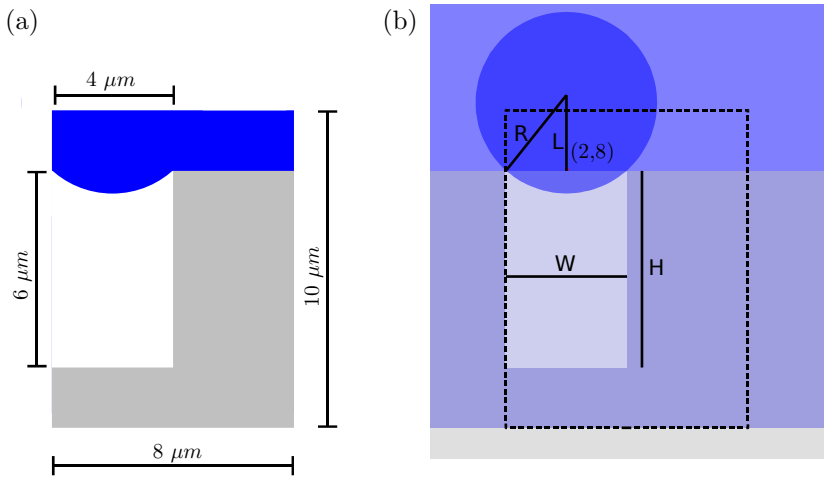

Figure A.4: (a) Schematic of a superhydrophobic grating featuring a curved liquid-gas interfaced on top of its groove. (b) Description of the grating geometry by piling partially overlapping geometric objects on top of each other. The illustration displays the same objects, in the same order as in (a), however all objects have a transparency of 50%.

grating, and some height H. Generally we don't know a priori how high the box needs to be to fit all objects inside, so we would like to make it rather large, say 10μm. For reasons that are dictated by the coding logic, it is necessary to specify a background material of the box that is to be used if an area is not covered by any object (if we would not do so, the code would have to invent a background, and to this end it would create certain objects that could interfere with user activity; alternatively we could refrain from making the code invent a background, but then the risk is high that the user may forget to specify the background himself). In the present case we use water as the background. The box is created simply by writing

```
T = 8
H = 10
water = material(1.33, 'blue')

box = cell(T,H,water)
```

Here, we get involved with an additional feature of Python, namely optional arguments. When creating a material instance, a color specification *may* be passed (if we don't pass anything, the default color 'white' is attributed to the material). The specified color will be used later to represent the material when we request a fake color image of the unit cell. As we write this, a first object (the lowest lying object) will already be included in the box, namely its background object. We may now go ahead and pile other objects on top of it. To make this easier, we may want to define a coordinate origin (or 'anchor') for the objects that we are planning to add. In this

case we choose the top grating surface, in the middle of the groove as an anchor, as shown in Fig. A.4(b). This is done through

```
domain.anchor = (2,8)
```

Behind the scenes, this operation unleashes the power of OO programming. The symbol `domain` may be understood as a unification of all types of objects that we may want to put into the box (a domain can be understood as an arbitrary domain in R^2). In OO programming this is called a 'class'. In fact, here, it is a 'base class' that serves as a template for defining more specific classes such as a `circle` class, a `halfspace` class, etc.. Through above operation, we modify one of the data items attributed to the base class, namely its `anchor`. The anchor is known to all derived classes, such that all geometric objects are aware of this change (generally a derived class knows all items of it parent class). This mechanism is called 'inheritance'. Above code line contains, yet another language feature of Python, namely its *dynamic* character, meaning that many things can be modified at run time. While we have previously manipulated only objects, here we manipulate a class (the symbol `domain` represents the class definition). Thus, with Python even the *definition* of a class can be changed during execution. Dynamic OO programming is a rather new development, that distinguishes recent generations of computer languages from original static OO languages, such as C++. Let us however return from this excursion about classes to the example of the superhydrophobic grating. To describe the geometry, we place first a silicon halfspace into the box. We can do this through

```
box + halfspace(-inf,0,SiO2)
```

Here, we have made use of another powerful feature of OO programming, namely, the ability to define operators and relations between abstract objects allowing to use them in an intuitive manner. The present code assigns to the '+' operator the function that it should 'add' the specified object to the pile of known objects stored with the box. Behind this lies a complicated operation. However, the user does not need to be concerned about that. For him or her it is sufficient to deal with a simple +. We complete the grating geometry by

```
box + halfspace(-inf,0,SiO2)
box + rectangle(W, H, air, (0, -0.5*H) )
box + circle(R, water, (.0,L))

box + rectangle()
```

It remains to call the `slice()` method to obtain a sequence of slices representing the unit cell. This sequence of slices is readily a list of slice objects as required for the creation of a stack object as described above, i.e., we may use it directly to create a full computational task and write

```
grating = stack( box.slice() )
```

To visualize the result, we may invoke the stack's `paint()` method

```
grating.paint().save('grating.jpg')
```

Here we have directly saved the resulting image object to a file. It remains to define the computational parameters of the `grating` object and run the computation as described in the previous section.

We close this section by taking a deeper look at the coding logic of the `slice()` method. How is the 'piling of overlapping objects and considering the final image' cast into a computer code? To know what we 'see' at an arbitrary point inside the box, we walk through the pile of domain objects starting from the uppermost one, and for each domain, we ask: 'are we inside?'. If so, the material of this domain is the one 'seen' at this point. To facilitate this operation, each domain has an `inside(r)` method attributed to it, that returns for a given `r` true or false, depending on whether or not the point lies inside. This makes clear what the `domain` class really is on the coding level: it represents the class of objects that are equipped with a position (their own coordinate), and an `inside(r)` method. To obtain grating slices suitable for the creation of a stack, the 'inside-check' is done on a two-dimensional mesh that spans the entire box. Subsequently, in each cut along the x-direction, adjacent steps that feature the same material, are merged. Likewise, thereafter identical slices in y-direction are merged. A thorough merging is of uttermost importance to avoid an unnecessary increase of the number of slices, that can otherwise result in a dramatic increase of the computational time.

Above example illustrates the flexibility that is enabled through an OO programming approach. The precise delineation of what functionality and data should be provided by different entities of the code, makes it extremely easy to extend existing programs and implement flavors of objects and novel algorithms in ways that were not even envisaged originally. This facilitates the combination of previously unrelated code packages, and typically results in a great reusage of existing code, such that complex computational tasks can be coded in a short amount of time. Here lies its great significance for scientific computing. OO programming really allows to encode a large class of numerical tasks, that otherwise (through a traditional procedural approach) could not be implemented within a reasonable amount of programming time.

It should however not be forgotten, that, at the heart of every scientific computation lies a numerical algorithm that spawns a vast amount of floating point operations to the cpu, and frequently manipulates large amounts of memory. However useful an OO approach may be for providing a flexible and well structured user interface, in practice only a negligible amount of run time will be spend on things such as interpreting the user input and setting up the computational cell. By far the largest amount of time will be spend in the low level computational routines. The performance of the computation depends thus ultimately on a rigorous and efficient implementation of the underlying numerical algorithms. The following section is devoted to such aspects.

A.2.2 Numerical core routines

The presented analytical scheme requires a number of non-elementary numerical operations, that can be put into two groups. The first one is Fourier transformation, or

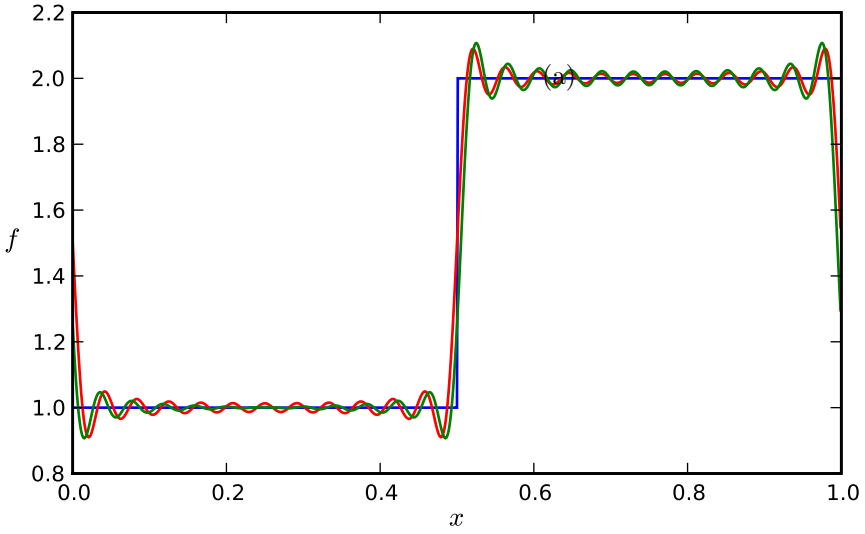

Figure A.5: Fourier expansion of a step function (blue line). The red line displays the expansion based on the exact evaluation of the Fourier coefficients. The green line displays the FFT result sampled on 100 points over the period. Expansions are evaluated up to the 24^{th} harmonic. The FFT result is shifted as compared to the exact result due to bandwidth limitation.

more precisely Fourier series expansion (to compute the representation of the dielectric function in each grating layer), the second is linear algebra, including eigenvalue problems (the secular equation in each grating layer), matrix inversion (for the partial solution schemes), and solution of regular linear systems. The following two subsections briefly discuss the prior respectively the latter.

Fourier expansion

One may be inclined to say that the numerical calculation of a Fourier series representation of a grating layer is straight forward, one only needs to employ the well known FFT algorithm [97]. However, most gratings that we want to compute here, are represented by layers that consist of only few discrete steps, representing large discontinuities. Fig. A.5 illustrates a structure consisting of only one step. The Fourier transform of such a structure requires a large number of harmonics. The FFT algorithm computes *all* harmonics, (with frequencies $1/T \ldots N/T$, where N is the number of samples) *at the same time*. On the one hand this is great (this is what makes the algorithm so fast), on the other hand it means that any effect caused by high harmonic cut off, such as aliasing or leakage of spectral density, can contaminate the hole result. Thus, if a numerically accurate representation of a generally rather discontinuous function is required, great care has to be taken about proper sampling.

Depending on the function, the required sampling density may differ. Indeed, there is no fundamental numerical criterion that tells us what sampling density is required for a particular function. Only the opposite is possible. The sampling theorem, or Nyquist theorem tells us that, if a function is truely bandwidth limited, meaning that it has exactly zero spectral density above a certain frequency, then the FFT gives us indeed the exact result. On the other hand, it states that, if the function is *not* bandwidth limited, *all* missed spectral density is spuriously moved into the range used in the computation. Thus, FFT may not be the safest choice for the calculation of the Fourier representation of the grating slices considered here. On the other hand, in the present case of piecewise constant functions (the representation of the dielectric function in terms of steps is exactly this), the Fourier series representation can be calculated very easily by directly evaluating the analytical expression. In this case, in contrast to the FFT, every Fourier coefficient is evaluated independently, and a contamination of the result due to bandwidth limitation is not encountered. Moreover, with the mostly small number of steps, only very few floating point operations are required. In contrast, to compute the Fourier representation of a few step function (that is represented by only few numbers), one would first need to resampled the function on a dense mesh, and then pass a large number of floating point values to the routine. That seems indeed not very efficient. Thus, we use a direct numerical representation of the analytic expression

$$\begin{aligned} c_k &= \int_0^T f(x)\exp(-i2\pi kx/T)dx \\ &= \frac{i}{2\pi k}\left[f_N - f_1 + \sum_{n=1}^{N-1}(f_n - f_{n+1})\exp(-i2\pi kx_n/T)\right], \end{aligned} \tag{A.58}$$

where $f(x)$ is a periodic function on the interval T, and piece wise constant with value f_n on the interval $(x_{n-1}, x_n]$.

Linear algebra

The presented careful evaluation of the Fourier expansion of the dielectric function in the grating slices is undoubtedly important for a successful initialization of the numerical routines, however, the largest amount of numerical operations is performed by the linear algebra routines that provide eigenvalues of the secular equation, and solutions to the linear systems that represent the field matching at the boundaries of the grating layers. It is here, where highly efficient numerical code can really make a difference. A number of delicate numerical algorithms have been devised over the past decades, that can perform such tasks. Which algorithm is most suitable for a specific computational problem depends on the *shape* of the matrix, e.g., whether it represent a regular, over-determined or under-determined system, whether it is symmetric or triangular, etc., and on its *condition*, that is, whether it has many elements close to zero, whether it is densely or sparsely populated, etc.. The linear systems that are encountered with above analytical formulation, are all regular, and, when following the presented solution scheme, rather well conditioned. A popular

algorithm that is suitable for solving such systems is the LU factorization, where the matrix is first factorized into a lower 'L', and upper 'U' triangular part, and the solution is afterwards obtained by a computationally inexpensive substitution process. This is the default solution method adopted in the present code. The solution of a linear system is however the less sophisticated linear algebraic problem that has to be tackled. A harder nut to crack is the eigenvalue problem represented by the secular equation for the propagation constants. By its very nature, an eigenvalue problem is a much less predictable computational task as is the solution of a linear system. Most modern eigenvalue routines grind the matrix to diagonal form by applying in an iterative manner a sequence of similarity transformations. Typically a combination of *factorization methods* and *atomic transformation* results in the most successful approach. A reference implementation of above mentioned schemes is provided in the linear algebra code package LAPACK, which was conceived in the early 1980's as a successor of the LINPACK library, originally intended for the use on supercomputers. Both code packages are written in FORTRAN77, and rely heavily on the BLAS (Basic Linear Algebra Subprograms) routines. It is indeed remarkable that this code, written in the 1970's is still used today in its original form, to provide the basis of nearly all scientific computing (the reader is encouraged to browse into the '\bin\win32' subfolder of a MATLAB$^{\text{TM}}$ installation to spot a file named 'lapack.dll', or to type 'lapack' into the search bar of the MATLAB$^{\text{TM}}$ help browser). Possibly the fastest embodyment of the LAPACK library available to date for intel$^{\text{TM}}$ IA-32, EM64 and AMD64$^{\text{TM}}$ architectures is the intel$^{\text{TM}}$Math Kernel Library, available for free for non-commercial use under Linux. The binaries include highly optimized code that is capable of employing the newest features of recent processor generations such as SSE instructions and the like for its needs. Indeed, this code typically runs 2-3 times faster than code derived with free compilers. Whenever possible, it is highly recommended to use such vendor supplied libraries.

Appendix B

On the effect of inhomogeneous meniscus displacement

We consider the light diffracted by N micromenisci. The problem is well described by Fraunhofer diffraction since $\lambda \ll a, R$. Following [15] Eq.8.5.23 on pp.445, the intensity I at a point far away from the grating is

$$I = \left| \sum_n e^{i\phi_n} z_n \right|^2 , \tag{B.1}$$

where ϕ_n is the phase and z_n the integral of the disturbance over the unit cell for the n-th meniscus. Owing to the simple picture that the intensity diffracted from the unit cell is governed by the interference between two waves, namely the light emitted from the Si-surface and the light emitted from the water-air interface, we realize that

$$z_n = e^{i\alpha} + e^{i(\alpha+\alpha_0+\delta\alpha_n)}. \tag{B.2}$$

In the homogeneous case $\delta\alpha_1 = \delta\alpha_1 = \cdots = \delta\alpha_N =: \delta\alpha$, i.e, $z_1 = z_2 = \cdots = z_N =: z$ the diffracted intensity reduces to the known separable expression

$$I = \left| \sum_n e^{i\phi_n} \right|^2 |z|^2 . \tag{B.3}$$

In a diffraction order, the incident and observation angle are such that the phases ϕ_n are the same for all unit cells, i.e. $\phi_1 = \phi_2 = \cdots = \phi_N =: \phi$ and indeed

$$I = \left| \sum_n e^{i\phi_n} \right|^2 \left| e^{i\alpha} \right|^2 \left| 1 + e^{i(\alpha_0+\delta\alpha)} \right|^2 = N^2 \left[2 + 2\cos(\alpha_0 + \delta\alpha) \right]. \tag{B.4}$$

In the inhomogeneous case

$$I = \left| \sum_n e^{i\phi_n} e^{i\alpha} \left(1 + e^{i(\alpha_0 + \delta\alpha_n)}\right) \right|^2 \tag{B.5}$$

and in a diffraction order

$$\begin{aligned} &= \left|e^{i\phi}\right|^2 \left|e^{i\alpha}\right|^2 \sum_n \left(1 + e^{i(\alpha_0+\delta\alpha_n)}\right) \sum_m \left(1 + e^{-i(\alpha_0+\delta\alpha_m)}\right) \\ &= N^2 + N \sum_n \left[e^{i(\alpha_0+\delta\alpha_n)} + e^{-i(\alpha_0+\delta\alpha_n)}\right] + \sum_{n,m} e^{i(\delta\alpha_n - \delta\alpha_m)}. \end{aligned} \tag{B.6}$$

We can chose α_0 such that $\sum_n \delta\alpha_n = 0$, and since $\delta\alpha_n \ll \alpha_0, 2\pi$, the second term reduces to

$$N \sum_n 2\cos(\alpha_0 + \delta\alpha_n). \tag{B.7}$$

Observing that the hole expression is real, we realize that the result is unchanged if we replace the third term by its real part

$$\sum_{n,m} \cos(\delta\alpha_n - \delta\alpha_m). \tag{B.8}$$

Thus,

$$I = N^2 + N \sum_n 2\cos(\alpha_0 + \delta\alpha_n) + \sum_{n,m} \cos(\delta\alpha_n - \delta\alpha_m) \tag{B.9}$$

Owing to the fact that the meniscus equilibrium position is in the center of a linear range with positive slope, we realize that $\alpha_0 \approx -\pi/2$. The sinus function has a relative error from the straight less than 20% in the interval [-1,1], thus the linear range extends approximately over 1/3 of the full period thus the deflection at resonance ζ_r corresponds to a phase of approximately $2\pi/6$, thus

$$\alpha_n = \frac{2\pi}{6\zeta_r}\zeta_n - \pi/2, \tag{B.10}$$

where ζ_n is the deflection of the n-th meniscus. Substituting $2\pi/(6\zeta_r) =: c$ and expanding the trigonometric functions, we obtain

$$\begin{aligned} I =& N^2 + 2N \sum_n \left[c\zeta_n - \frac{1}{3!}(c\zeta_n)^3 + \dots\right] + \sum_{n,m} \left[1 - \frac{1}{2!}(c(\zeta_n - \zeta_m))^2 + \dots\right] \\ =& 2N^2 + 2N \sum_n \left[c\zeta_n - \frac{1}{3!}(c\zeta_n)^3 + \dots\right] + \sum_{n,m} \left[-\frac{1}{2!}c^2(\zeta_n - \zeta_m)^2 + \dots\right] \end{aligned} \tag{B.11}$$

keeping terms up to second order, we have

$$I = 2N^2 + 2Nc \sum_n \zeta_n - \frac{c^2}{2} \sum_{n,m} (\zeta_n - \zeta_m)^2. \tag{B.12}$$

Owing to the experimental test of the homogeneity that confirmed

$$I = I_0 + \delta I(r\zeta_1, \ldots, r\zeta_N) = I_0 + r\delta I(\zeta_1, \ldots, \zeta_N), \tag{B.13}$$

for $r \in \mathbb{R}$, $r \ll 2\pi$, we conclude that

$$I = 2N^2 + 2Nc\sum_n \zeta_n, \tag{B.14}$$

thus,

$$I = N^2[2 + 2c\langle\zeta_n\rangle]. \tag{B.15}$$

Expressing the homogeneous case in terms of the deflection results in

$$I = N^2[2 + 2c\zeta_0], \tag{B.16}$$

thus, the intensity of N menisci with *inhomogeneous* deflections $\zeta_1, \ldots, \zeta_n$ is indeed the same as the intensity of N menisci with *homogeneous* deflections $\zeta_1 = \cdots = \zeta_N = \langle\zeta_n\rangle_n$ equal to the *mean*.

Appendix C

A setup for vapor deposition of self assembled silane monolayers

This appendix describes the development of a vapor deposition setup that provides hydrophobic self assembled monolayers of an alkylsilane (typically 1H,1H,2H,2H-Perfluorodecyltrichlorosilane), in a highly reproducible manner, following [72]. The layers are typically 1.5 to 1.6nm thin (as determined by ellipsometry assuming the bulk dielectric constant of the alkylsilane), and the advancing an receding contact angles on a plane substrate are $\vartheta_a = 116 \pm 2$ respectively $\vartheta_r = 104 \pm 2$. Vapor deposition of alkylsilanes was initially performed following a commonly used technique that is performed under ambient conditions. Though wide spread, this technique provided however highly unreproducible, often unexceptable results. E.g., in one case, the sample consisted of an array of cylindrical holes with 3μm radius, etched into silicon. When inspecting the coated and cleaned sample under an optical microscope, some of the holes were filled, only few were empty, and cylindrical pieces of material where observed on the sample. This ruled out the traditional vapor deposition method for this work. And indeed, this method admits the silane reagent to the object that is to be coated, in an unpredictable thermodynamic state, as we will describe in the following section. This suggested however, that the method should be easily fixed, and converted into a well controlled setup for hydrophobic coating production, as is described in the subsequent section.

C.1 Traditional vapor deposition technique

In the traditional vapor deposition technique, a small amount of the liquid silane is extracted from the stock bottle using a syringe or pipette. This is done either inside a glove box providing a dry environment, or under a stream of dry nitrogen. The syringe

is then quickly brought to a desiccator, and a drop of silane is placed on the bottom of the vessel. The sample is quickly placed inside the vessel, the vessel is closed and evacuated using a membrane pump. Subsequently the valve between the vessel and the pump is closed, and the silane is admitted to react with the sample surface for some time. The desiccator is vented, and the sample is removed and cleaned, typically with one or more organic solvents and water, possibly in an ultrasonic bath.

The underlying chemical process is the following. Generally, the reactive group of the silane is a silicon atom that is linked to the functional part of the molecule through a single covalent bond. The three remaining bonds are terminated by chloride atoms. The covalent binding of the silane to a silicon / silicon oxide surface occurs through the formation of Si–O–Si bonds. This requires the removal of the three chloride atoms. Generally this is provided by water. The hydrogen atoms gained from the water react with the chloride to form HCl, and the oxygen atom provides the link in the Si–O–Si bond. The stochiometry of the reaction is satisfied, by requiring that a fraction of the reactions takes its oxygen from the SiO_2 surface.

The problem of above traditional technique is, that an undefined mixture of silane and water is admitted to the sample, that results in an uncontrolled polymerization reaction. In particular, the highly reactive silane begins to polymerize already in the vapor phase, before adsorbing to the sample surface, and the polymerization reaction continues beyond the formation of a monolayer. To provide a controlled polymerization reaction, the following approach is adopted.

C.2 Controlled vapor depostion

Fig. C.1 shows a schematic of the vapor deposition setup. Two reservoirs containing the silane, respectively water, are connected to a reaction chamber through valves. A rotary pump, is connected to the chamber through a buffer compartment, that is equipped with a vacuum gage and separated from the chamber and the pump by an additional valve. The chamber and reagent reservoirs, including all valves, are made of glass. All valves are silicone smeared glass valves. The silane reservoir has been filled under dry conditions inside a glove box. Initially, the valves between the reservoirs and the chamber are closed. The initial setup scheme start by evacuating the chamber. Subsequently the water is degassed by opening the valve between the water reservoir and the chamber for few minutes, while continuing to pump. Before degassing the silane, the valve between the water reservoir and the chamber is closed, and the chamber is evacuated again to the end pressure of the rotary pump. The silane is degassed, by opening the valve between the silane reservoir and the chamber for a few minutes. The valve between the chamber and the silane reservoir closed, the pump turned off, and the chamber vented. This finalizes the initial setup scheme.

To perform a vapor deposition of a self assembled silane coating, the sample is placed in the reaction chamber. The chamber is closed and evacuated to the end pressure of the rotary pump. The pressure reached in this way (typically about $5 \cdot 10^{-2}$mbar), is below the vapor pressure of the silane (≈ 0.4mbar). Subsequently all valves of the buffer compartment are closed, and the pump is turned off. Subsequently

(a)

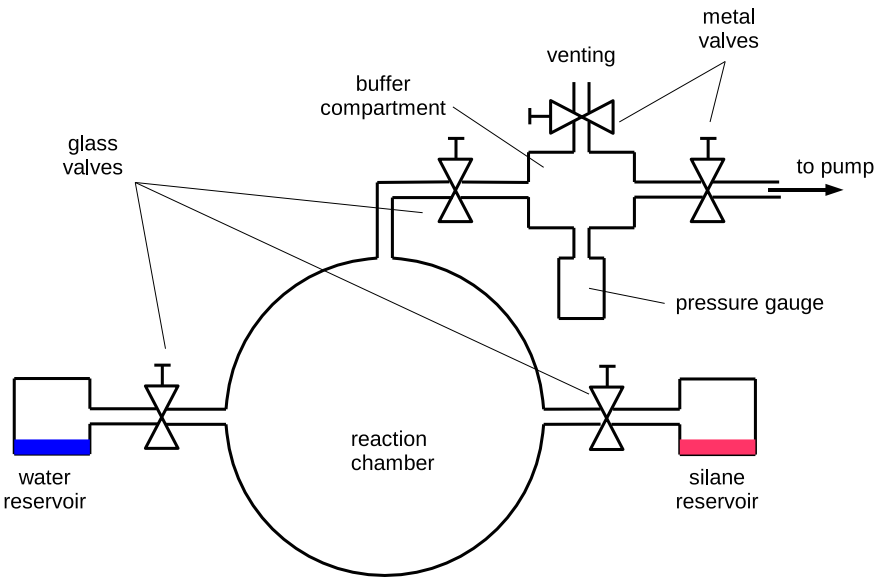

(b)

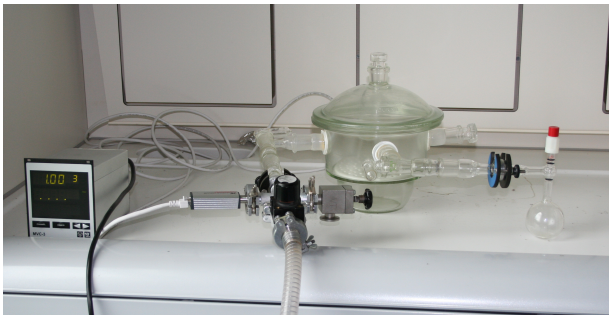

Figure C.1: Schematic (a) and photograph (b) of the setup for controlled vapor deposition of an alkylsilane.

the valve between the silane reservoir and the chamber is opened for a short time (typically 5 min). This results in silane gas at the vapor pressure filling the reaction chamber, and a layer of silane molecules adsorbing to the sample surface. The valve between the silane reservoir and the chamber is closed, and the valve between the water reservoir and the chamber is opened for few seconds. This results in a pressure increase in the chamber to the vapor pressure of water, and water vapor filling the chamber. The reagents are allowed to react for some time (in this work, the waiting time was typically 30min, but probably a much shorter time works equally well). Subsequently the chamber is vented through the following procedure. First the valve between the buffer compartment and the chamber is opened. This results in a gas flow from the chamber to the buffer compartment. Subsequently the venting valve of the buffer compartment is opened, such that the entire system is vented. The latter venting procedure is of uttermost importance for the successful completion of a clean coating process, and becomes necessary due to the grease smeared glass valves used at the reaction chamber. In an earlier design of the setup, the buffer compartment was not implemented, and the chamber was vented directly through a glass valve. As a result, the sample was often contaminated by fine drops of grease, that were dragged from the valve by the vigorous initial air flow arising in the first moment when opening the valve. In contrast, the outermost valve of the buffer compartment is not smeared, such that no grease drops are produced, and the gas flow through the grease smeared valve between the buffer compartment and the chamber is not a concern when the valve is fully opened, and the flow is slow. For this reason, the buffer compartment is of uttermost importance for the production of a clean coating. This raises the question whether it would not be simpler to replace the grease smeared valves by unsmeared ones. And indeed it would, however, it is at the same time necessary to keep the chamber and all its valves entirely in glass (and possibly some polymer). To the best of our knowledge no unsmeared glass valves are available, that can provide a sufficiently low leakage rate. The all-in-glass design is necessary because of the aggressive reaction product HCl. Indeed, a first version of the chamber, made of stainless steel, was highly corroded (all chamber surface was covered with fine rust particles) after few weeks of operation. For this reason we believe that the all in glass design is the only reliable layout, that can provide high quality coating fabrication over long terms. The grease smeared valves caused however another problem. Namely, repeatedly, after several weeks of operation, the valve between the silane reservoir and the chamber got stuck, resulting in a fatal failure of the system. The valve could only be recovered by heating valve and reservoir to 400° in an oven (after wrapping it in a large amount of aluminum foil to prevent damage of the device and the oven during the vigorous separation). For this reason, at the time of writing the traditional type glass valve is replaced by an (also grease smeared) glass valve featuring a Teflon screw and a rubber gasket.

Appendix D

Design of a chamber for diffraction measurements in pressure controlled liquid environment

We now estimate the angle between two diffraction orders. Fig. D.1 shows wavevectors in optical grating diffraction. We have

$$dk \approx |\boldsymbol{d}k|$$

for not too flat angles, and

$$|\boldsymbol{d}k| = |\boldsymbol{k}|\, d\varphi,$$

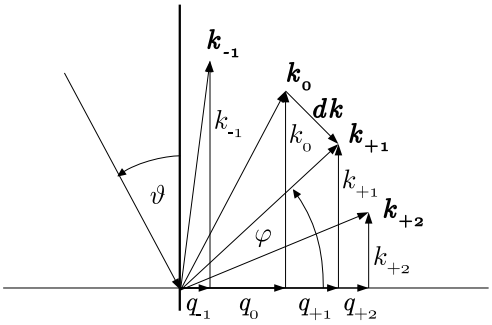

Figure D.1: **Wave vectors in optical grating diffraction.**

thus

$$d\varphi \approx \frac{dk}{|\boldsymbol{k}|}.$$

We have

$$\boldsymbol{k_0} = \frac{2\pi n}{\lambda},$$

$$k_0 = \frac{2\pi n}{\lambda}\sin(\vartheta),$$

$$K = \frac{2\pi}{T}$$

and

$$k_m = k_0 + mK,$$

where n is the refractive index of the medium of incident and diffracted beams, λ is the wavelength of the light, m is the diffraction order and T is the grating period. Thus

$$dk = K$$

and

$$d\varphi = \frac{\lambda}{T}.$$

We have $\lambda = 488\text{nm}$, $T = 16\mu\text{m}$, thus,

$$d\varphi \approx \frac{1}{32}.$$

On the other hand we have

$$d\varphi > \frac{dl}{R},$$

where dl is the separation between two beams at radius R, where the photodiode is located. We require a diameter d of the laser beam that is large enough such that it hits many lines of the grating, say (1000 lines), thus $d \approx 10mm$. To ensure measurement of the total intensity of exactly one diffraction order we require a size w of the active area of the photodiode of $w \approx d$. We require some separation between the beams and some freedom for the alignment of the photodiode, thus we choose $dl = 20mm$. Thus

$$\frac{1}{32} = \frac{20\text{mm}}{R} \tag{D.1}$$

We now turn to the lens effect of the cylindrical glass container filled with water. If we had no container, we could always satisfy Eq. (D.1) by increasing R. However, a container acts like a cylindrical lens that causes the diffracted beams to diverge such that beams of different order overlap for large enough R. As can be seen in Fig. D.2(a), indeed for any container radius R_0 and angular separation $d\varphi$ there is a radius R at which the beams overlap. We have from Fig. D.2(a)

$$R = R_0 + 2f, \tag{D.2}$$

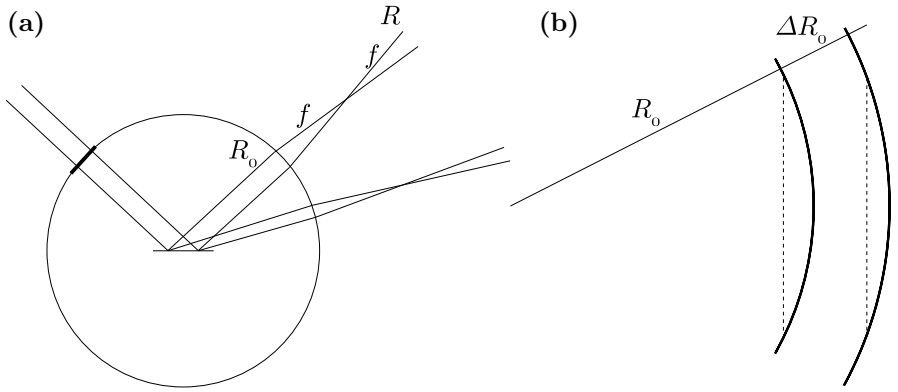

Figure D.2: **Lens effect of a water-filled glass container. (a)** Refraction at the container wall causes the diffracted beams first to converge and later to diverge again. **(b)** A cylindrical wall acts as two thin plan-convex lenses.

where f is the focal length of the container.

We now evaluate a focal length of a glass container filled with water. We can describe the lens effect of the container as a compound lens consisting of two thin plan-convex lenses, see Fig. D.2(b). We have a *lens-maker* equation, for the focal length f of a thin lens with radii r_1 and r_2 and refractive index n_l of the lens material and refractive index n_m of the surrounding medium

$$\frac{1}{f} = \left(\frac{n_l}{n_m} - 1\right)\left(\frac{1}{r_1} - \frac{1}{r_2}\right). \tag{D.3}$$

The radius r_1 corresponds to the surface near to the light source. Positive radius corresponds to origin of radius on the side of the outgoing beam. A radius is ∞ if a surface is planar. We have no refraction at the planar surface of a plan-convex lens, thus the medium at the planar side is arbitrary, thus we can use Eq. (D.3) for our case with a water lens surrounded by glass with focal length f_1 and a glass lens surrounded by air with focal length f_2. The focal length of two thin lenses with a distance between each other that is small compared to both individual focal lengths is

$$\frac{1}{f} = \frac{1}{f_1} + \frac{1}{f_2},$$

thus

$$\frac{1}{f} = \left(\frac{n_w}{n_g} - 1\right)\frac{1}{R_0} + \left(\frac{n_g}{n_a} - 1\right)\frac{1}{R_0 + \Delta R_0},$$

where n_w is the refractive index of water, n_g is the refractive index of glass and n_a is the refractive index of air. We have $n_w \approx 1.33$, $n_g \approx 1.48$, $n_a \approx 1$, thus

$$\frac{1}{f} \approx \left(\frac{1.33}{1.48} - 1\right)\frac{1}{R_0} + (1.48 - 1)\frac{1}{R_0 + \Delta R_0}$$

$$f = R_0 \frac{1}{0.48 \frac{1}{1+\frac{\Delta R_0}{R_0}} - 0.1}.$$

For $\Delta R_0 \ll R_0$

$$f \approx 2.6 R_0$$

Substituting in Eq. (D.2), we have

$$R \approx 6 R_0.$$

Together with Eq. (D.1), we have

$$R_0 = 20\text{mm} \frac{32}{6} \approx 10\text{cm},$$

which is close to our previous estimation, $R_0 \approx 15$cm, based on $f \approx R_0$ and $R \approx R_0 + f$ to be on the save side. The result is consistent with the approximation of thin lenses and $\Delta R_0 \ll R_0$. With $R_0 = 150$mm, we have

$$f \approx 390\text{mm}.$$

For a diffraction measurement under water-vapor as well as under ambient conditions, a setup is designed as shown in Fig. D.3. The sample is illuminated with the 488nm line of an Ar-ion laser (coherent, Innova 90c). To chose *s*- or *p*-polarization of the incident light, The number and orientation of mirrors in the illuminating beam path is chosen accordingly. The optical beam reaches the sample at last via two mirrors. The farther of the two directs the beam vertically upwards, the closer (last) mirror directs the beam parallel to the optical table onto the sample. A tilt of the closer mirror changes primarily the angle of the laser beam, while a tilt of the farther mirror changes primarily its position. The mirrors are always used in this way to change independently the position and angle of the laser beam.

We now describe how the sample is aligned, the rotation axis of the detector stage is aligned collinear to the rotation axis of the cell stage, and the laser beam is brought into perpendicular incidence on the center of the sample. The tolerances of all parts that determine the position of the sample holder (such as the mounting holes of the plate that connects the cell rotation stage and the bottom flange of the cell, the blind holes that determine the position of the sample tripod, etc.) are $\approx 0.1mm$, such that, after placing the sample holder (with a mounted sample), the axis of the cell rotation stage lies on the vertical middle line of the sample surface with an error of typically less than 1mm. This will result in the worst case in a 'drift' of the laser spot on the photodiode during an angular scan of less than 1mm. Given the diameter of the active area of the photodiode of about 1cm, and a width of the laser spot on the diode of few mm (depending on the diffraction angle and order) this is just acceptable. Next, the axis of the cell rotation stage is nearly perpendicular to the optical table, such that the inclination of the sample surface can be adjusted by bringing the laser beam into a plane parallel to the optical table (by measuring the beam height with a ruler), and adjusting the sample tripod such that the reflected beam is collinear to the

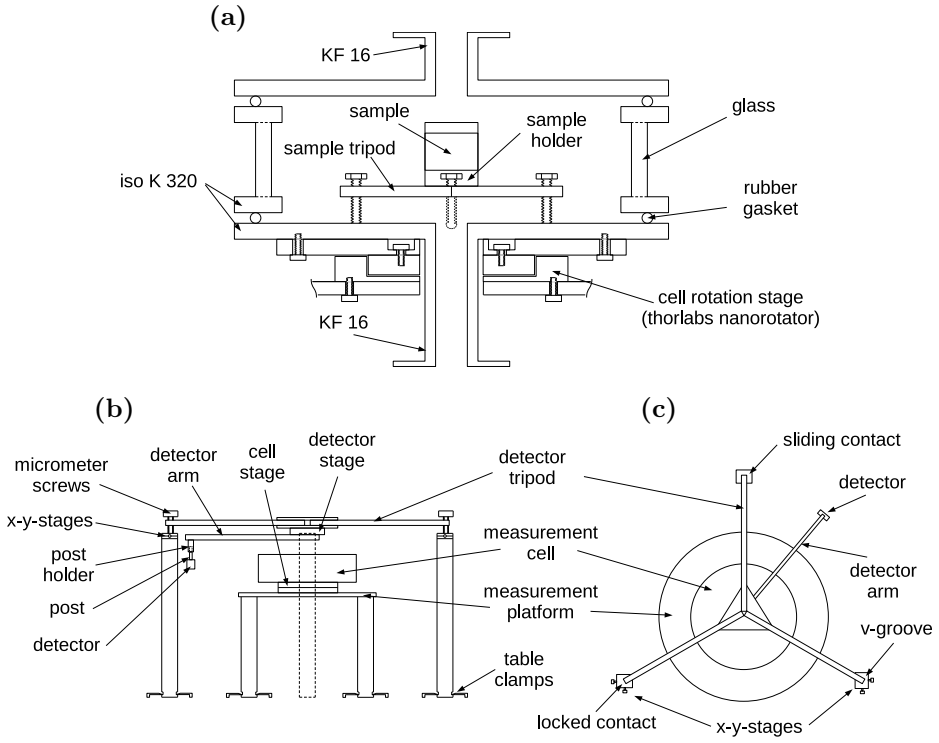

Figure D.3: **Setup for angle resolved diffraction measurements under pressure controlled conditions under vapor as well as ambient atmosphere. (a)** Vacuum- and high pressure measurement cell (cross section). **(b-c)** Setup for angle resolved diffraction measurements. **(b)** side view **(c)** top view.

incident beam (after having rotated the sample to zero incident angle). The sample is rotated and it is ensured that all diffracted beams are in the same plane parallel to the optical table. At last, the laser beam is brought in perpendicular incidence on the vertical center line of the sample by using the center line markers on the sample to find the position, and the reflection from the sample to find the perpendicular angle. Thereafter the illuminating beam is not changed any more. This position is defined as the zero position of the cell rotation stage. Next, the detector rotation axis is brought onto the cell rotation axis. To achieve this (1) the sample is rotated to 2°, the detector is brought onto the reflected beam, the position of the detector is defined as 4°. (2) the sample is rotated to 86°, the detector to 172°, the translation stages of the detector tripod are used to correct half of the misalignment. The remaining misalignment is corrected by manually rotating the detector arm (while the position encoder remains at 172°). (3) the sample is rotated to 45°, the detector to 90°, the translation stages are moved to correct the misalignment. (4) the micrometer screws of the detector tripod are used to align the tilt of the detector rotation plane. (5) the z-position and rotation of the photodiode is adjusted. (6) the latter steps are repeated until satisfactory alignment is reached.

Appendix E

On the estimation of the error in χ^2 fitting

In statistical analysis one defines [97]

$$\chi^2 = \sum \left(\frac{y_i - y(\alpha, x_i)}{\sigma_i} \right)^2, \tag{E.1}$$

where (x_i, y_i), $i = 1, \ldots, N$ are the measured data points, σ_i are their individual standard deviations, and $y(x) = y(x; \alpha_1, \ldots, \alpha_M$ is the functional relationship between the measured variables with M adjustable parameters α_j, $j = 1, \ldots, M$.

If the individual errors σ_i are normal distributed, the confidence interval $\delta\alpha$ is

$$\delta\alpha = \pm\sqrt{V}\sqrt{\Delta\chi^2_\mu}, \tag{E.2}$$

where V is the variance and related to the second derivative with respect to the parameter of χ^2 by

$$1/V = \frac{1}{2}\frac{\partial^2\chi^2}{\partial\alpha^2}|_{\alpha_0}, \tag{E.3}$$

and $\Delta\chi^2_\mu$ is a constant determined by the confidence level p and the number of fitting parameters μ considered simultaneously in the confidence analysis. If one is interested in the confidence interval of every fitting parameter individually, then $\mu = 1$. One is often interested in the 68.3% confidence interval. In this case $\Delta\chi^2_1 = 1$, and therefore

$$\delta\alpha = \sqrt{V} \tag{E.4}$$

Reasonably, this is called the confidence interval for $\pm 1\sigma$ confidence level.

Near a minimum α_0, χ^2 can be approximated with a parabola

$$\chi^2 \approx \chi^2(\alpha_0) + \frac{1}{2}\frac{\partial^2}{\partial\alpha^2}\chi^2|_{\alpha_0}(\alpha - \alpha_0)^2. \tag{E.5}$$

With the short notation $\chi^2(\alpha_0) =: \chi_0^2$, we have

$$\chi^2 = \chi_0^2 + \frac{1}{V}(\alpha - \alpha_0)^2. \tag{E.6}$$

The inverse is a Lorentzian

$$\frac{1}{\chi^2} = \frac{1}{\frac{1}{V}(\alpha - \alpha_0)^2 + \chi_0^2} = \frac{\sqrt{V}}{\sqrt{\chi_0^2}} \frac{\sqrt{V\chi_0^2}}{(\alpha - \alpha_0)^2 + V\chi_0^2} \tag{E.7}$$

The HWHM γ is

$$\gamma = \sqrt{V}\sqrt{\chi_0^2}. \tag{E.8}$$

In a typical fit one has $\chi_0^2 \approx \nu$, where $\nu = N - M$ is called the degree of freedom, thus

$$\gamma \approx \sqrt{V}\sqrt{\nu}. \tag{E.9}$$

If the individual errors σ_i are not known, the best guess is

$$\sigma_i^2 = \frac{1}{\nu} \sum \left(y_i - y(x_i, \alpha_0)\right)^2. \tag{E.10}$$

Plugging this back into the χ^2, we have

$$\chi_0^2 \equiv \nu. \tag{E.11}$$

In this case

$$\gamma \equiv \sqrt{V}\sqrt{\nu}. \tag{E.12}$$

In conclusion, in case of 'real' statistical analysis (σ_i are known), the HWHM can be used – together with the obtained chi-square at the minimum – to determine the confidence interval $\delta\alpha$

$$\delta\alpha = \gamma \frac{\sqrt{\Delta\chi_\mu^2}}{\sqrt{\chi_0^2}}. \tag{E.13}$$

Here χ_0^2 is typically about ν and one often asks for the 1σ-confidence interval, where $\sqrt{\Delta\chi_\mu^2} = 1$, such that

$$\delta\alpha \approx \frac{\gamma}{\sqrt{\nu}}. \tag{E.14}$$

In the case of 'formal' statistical analysis (σ_i are unknown), the HWHM can be used to determine the 'formal standard error'

$$\sqrt{V} \equiv \frac{\gamma}{\sqrt{\nu}}. \tag{E.15}$$

Fig. E.1 illustrates above results for a randomized set of data fitted to a parabola

$$y = \alpha x^2, \tag{E.16}$$

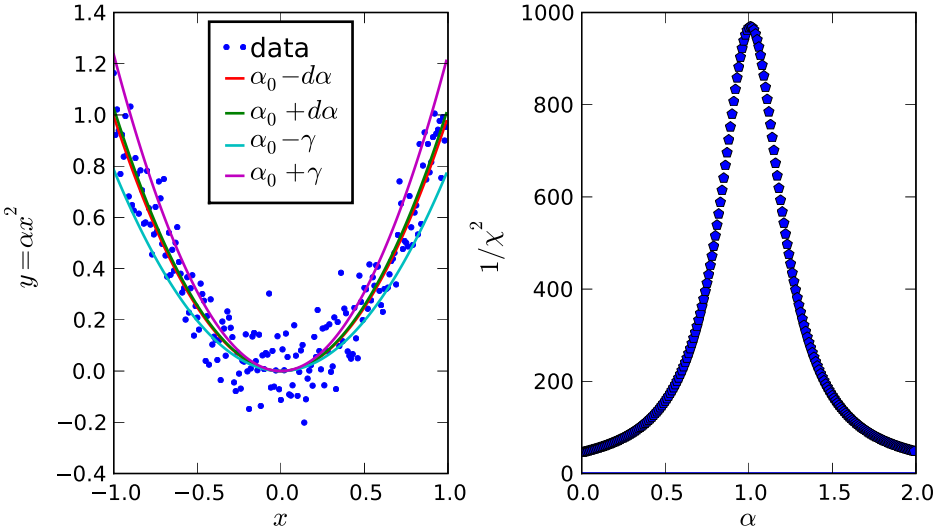

	α_0	$\delta\alpha$	$\gamma/\sqrt{\nu}$	χ_0^2
Levenberg-Marquardt	1.0148...	0.0158100709643		
'Lorentzian fit'	1.0148...	0.015810070863	0.0148	175.1

Figure E.1: Fit of 200 noisy data to a parabola $y = \alpha x^2$, where $\alpha = 1$ and the y_i are normal distributed with $\sigma_i = 0.1$. The table compares the resulting fit parameters and errors for the Levenberg-Marquardt and '$1/\chi^2$-approach'.

where $\nu = 199$ (i.e., $\Delta x = 0.01$), $\alpha = 1$, and the y_i are normal distributed with $\sigma_i = 0.1$. The solid lines show curves at the boundary of the confidence interval for the standard error $\pm\delta\alpha$, and the error $\pm\gamma$. The table in Fig. E.1 compares the underlying statistical analysis using Levenberg-Marquardt and 'Lorentzian fit'. Even for this fairly poor statistics with only 200 data points, both methods agree nearly to machine precision.

In physics one often encounters the case (nearly always) that the model is 'wrong' or 'not perfect'. If the random error of the measured data is much larger than the imperfections of the model, this is not a problem, and $\delta\alpha$ remains a well defined measure for the error. If however the random error is smaller than the imperfections of the model, the statistical analysis as described in the preceding looses its foundation. In this book, this case is encountered e.g. in Fig. 3.2. How to assess the 'quality of the fit' in such a case? It turns out that γ is a safe measure for the error of the fit. It is like evaluating the standard error but omitting the division by $\sqrt{\nu}$. This makes sense, because in such a case, acquiring more experimental data points should not reduce the error, in contrast $\delta\alpha$ would decrease. Fig. E.1(a) illustrates these aspects. Evidently, if one was not sure that the error of the experimental data was perfectly Gaussian, one would consider γ as a safer choice for an error estimate than α.

Appendix F

Noise equivalent pressure for ultrasound detection using a meniscus on a fiber

F.1 Interference signal

The reflected intensity is approximately a two beam interference

$$E = \sqrt{r_{ga}} E_1 e^{i\omega t} + \sqrt{r_{aw}} E_2 e^{i\omega t + \varphi}, \tag{F.1}$$

where r_{ga} and r_{aw} are the reflection coefficients of the glass-air and air-water interface, respectively, and $\varphi = 4\pi\zeta/\lambda$ is the phase shift (ζ meniscus deflection and λ wavelength of the light). We have $r_{ga} \approx r_{aw} =: r \approx 0.01$, thus

$$J = 2J_0 r(1 + \cos\varphi), \tag{F.2}$$

where J is the intensity at the detector and J_0 is the incident intensity. Thus, the intensity on the detector is of the order

$$J_d = 2J_0 r \tag{F.3}$$

and the signal intensity is of the order

$$J_s = 2J_0 r\varphi \tag{F.4}$$

F.2 Optical shot noise

We have

$$I\tau = \frac{e}{N}, \tag{F.5}$$

where I is the current, e is the electron charge, τ is a time interval and N is the number of electrons. I and N are random variables, thus

$$\langle I \rangle = \frac{e}{\tau}\langle N \rangle, \tag{F.6}$$

and

$$\langle I^2 \rangle = \left(\frac{e}{\tau}\right)^2 \langle N^2 \rangle. \tag{F.7}$$

Since N is Poisson distributed, its variance is equal to the mean

$$\langle N - \langle N \rangle \rangle^2 = \langle N \rangle. \tag{F.8}$$

We have an identity for the variance that holds for any random variable X

$$\langle X - \langle X \rangle \rangle^2 = \langle X^2 \rangle - \langle X \rangle^2, \tag{F.9}$$

thus,

$$\langle \Delta I^2 \rangle = \langle I^2 \rangle - \langle I \rangle^2 = \left(\frac{e}{\tau}\right)^2 \left(\langle N^2 \rangle - \langle N \rangle^2\right) = \left(\frac{e}{\tau}\right)^2 \langle N \rangle = \frac{e}{\tau}\langle I \rangle. \tag{F.10}$$

There is factor of two missing, because we actually don't ask for the probability of having a 'click' given that there was a 'click' at t_0, rather the beginning of the interval is arbitrary, i.e., actually

$$\langle \Delta I^2 \rangle = 2eI\Delta f, \tag{F.11}$$

where Δf is the bandwidth. The photocurrent is

$$I = \frac{e\eta J}{h\nu}, \tag{F.12}$$

where η is the quantum efficiency of the detector, h is Planck's constant and ν is the frequency of the light. Thus, the shot noise is

$$\delta I_{sn}/\sqrt{\Delta f} = \sqrt{\frac{2e^2\eta J}{h\nu}}, \tag{F.13}$$

With $J = 2J_0 r = 2 \cdot 10^{-4}$, $\eta = 0.5$ and $\lambda = 600$nm, we have

$$\delta I_{sn}/\sqrt{\Delta f} = 4 \cdot 10^{-12}\mathrm{A}/\sqrt{\mathrm{Hz}}. \tag{F.14}$$

F.3 Pressure to displacement conversion

We have

$$\zeta = \frac{2}{\kappa}\left(1 - \sqrt{1 - R^2\kappa^2/4}\right) \approx R^2\kappa/4 \tag{F.15}$$

and

$$P = \sigma\kappa, \tag{F.16}$$

where κ is the curvature, P is the pressure, R is the radius of the cylindrical hole and σ is the surface tension, thus

$$\zeta = \frac{R^2 P}{4\sigma}. \tag{F.17}$$

F.4 Noise equivalent pressure

We have

$$\varphi = \frac{\pi R^2}{\sigma\lambda} P, \tag{F.18}$$

$$J_s = \frac{2\pi J_0 r R^2}{\sigma\lambda} P, \tag{F.19}$$

and

$$I_s = \frac{2\pi J_0 r R^2 e\eta}{\sigma hc} P. \tag{F.20}$$

We compare the signal current to the shot noise

$$\delta I_{sn} \leq I_s \tag{F.21}$$

$$\sqrt{\frac{2e^2\eta 2J_0 r\lambda}{hc}}\sqrt{\Delta f} \leq \frac{2\pi 2J_0 R^2}{\sigma hc} P \tag{F.22}$$

$$\sqrt{\frac{hc\lambda}{J_0 r\eta}}\frac{\sigma}{\pi R^2}\sqrt{\Delta f} \leq P. \tag{F.23}$$

The resonance frequency of a meniscus is about

$$f = \frac{1}{5}\sqrt{\frac{4\sigma}{\rho R^3}}, \tag{F.24}$$

where ρ is the density of the liquid. Thus,

$$R \approx \left(\frac{\sigma}{6\rho f^2}\right)^{1/3}. \tag{F.25}$$

Thus, for water, a resonance frequency of 35MHz corresponds to $R = 200$nm. With $R = 200$nm, $P_0 = 10$mW, $r = 0.0001$, $\lambda = 600$nm, $\Delta f = 30 \cdot 10^6$, $\sigma = 73 \cdot 10^{-3}$, we have a noise equivalent pressure

$$P_{ne} = 1500\text{Pa}. \tag{F.26}$$

A resonance frequency of 1MHz corresponds to 2.3μm. With $R = 2.3\mu$m, $r = 0.01$, $\Delta f = 1$MHz, we have a noise equivalent pressure

$$P_{ne} = 0.2\text{Pa}. \tag{F.27}$$

The reason why it is much worse at higher frequencies is the small radius R, which enters quadratically and at the same time results in a much smaller reflectivity r.

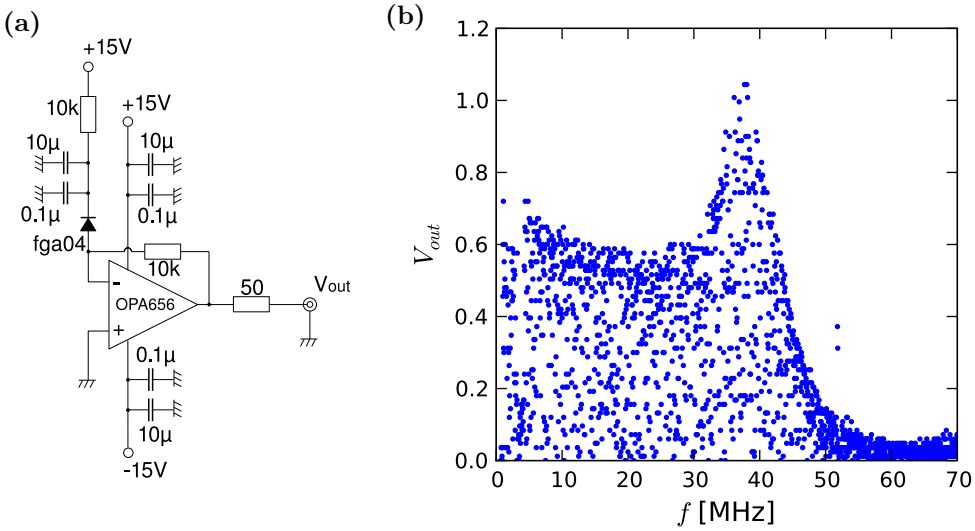

Figure F.1: **Light detection based on a photodiode.** **(a)** Schematics of an electrical circuit using thorlabs fga04 and OPA656 with 10kΩ transimpedance gain. **(b)** Measured frequency response. The detector has a slight gain peaking at around 38MHz.

F.5 Detector performance

Fig. F.1(a) shows the schematics of the detector. A thorlabs fga04 PIN diode converts the incident light into a photocurrent. The current is amplified and converted into a voltage using an OPA656 with a 10kΩ feedback resistor. The capacitance of the photodiode is reduced by applying a reverse bias. All voltage sources are buffered by suitable capacitors to satisfy fast current drains. The measured frequency response is shown in Fig. F.1(b). The device shows a slight gain peaking at around 38MHz, before it rolls off at around 40MHz.

thermal noise

The thermal noise in the transimpedance OpAmp is

$$\delta I_{jn}/\sqrt{\Delta f} = \sqrt{4k_B T/R}, \tag{F.28}$$

where k_B is the Boltzmann constant, T is the temperature and R is the resistance of feedback resistor. With $R = 10^4$ and $T = 300$, we have

$$\delta I_{jn}/\sqrt{\Delta f} = 1.3 \cdot 10^{-12}\mathrm{A}/\sqrt{\mathrm{Hz}}. \tag{F.29}$$

input noise

The OPA656 has an input current noise

$$\delta I_{cn}/\sqrt{\Delta f} = 1.3 \cdot 10^{-12}\mathrm{A}/\sqrt{\mathrm{Hz}}, \tag{F.30}$$

and an input voltage noise $\delta V_{vn}/\sqrt{\Delta f} = 7 \cdot 10^{-9} V/\sqrt{\mathrm{Hz}}$. With the 10^4 resistor, the latter translates into a current noise

$$\delta I_{vn}/\sqrt{\Delta f} = 7 \cdot 10^{-13}\mathrm{A}/\sqrt{\mathrm{Hz}}. \tag{F.31}$$

total noise

The total noise is the rms of the individual noise contributions. Thus we have an output voltage noise

$$\delta V_{out}/\sqrt{\Delta f} = 1.5 \cdot 10^{-8}\mathrm{V}/\sqrt{\mathrm{Hz}}. \tag{F.32}$$

With the 40MHz BW of the detector, we have

$$\delta V_{out} = 0.09\mathrm{mV}. \tag{F.33}$$

Fig. F.1 shows the dark output of the detector as measured with an oscilloscope. Oscillations with a characteristic frequency of around 38MHz are observed corresponding to the gain peaking. The optical shot noise, Eq. (F.14), (10mW optical power incident on the meniscus-cavity system and a reflectivity of the meniscus $r = 0.01$) translates into a voltage noise $\delta V = 0.2$mV. Due to the additional noise associated with gain peaking, the detector noise remains slightly above the optical shot noise limit.

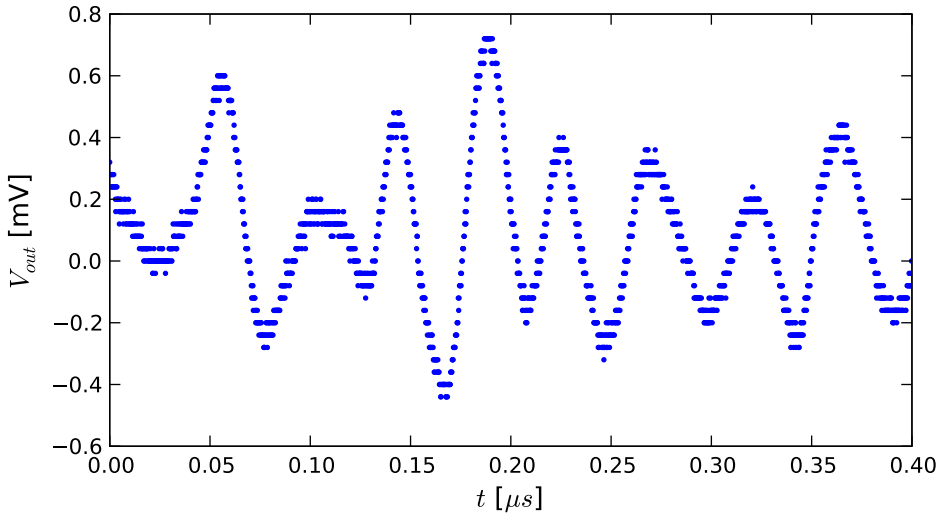

Figure F.2: **Detector dark signal.** The detector's gain peaking at around 38MHz results in an amplification of the corresponding noise component.

Appendix G

Electric driving of micromenisci

In this appendix we present experimental results on collectively oscillating micromenisci that are excited using electric forces rather than ultrasound. This seemed initially a rather academic problem. However, from a later perspective this problem seems indeed practically relevant. A large number of ultrasound application (e.g. all send-receive type measurements) rely not only on the efficient *measurement* of ultrasound rather also on its efficient *generation*. Driving a meniscus electrically could enable ultrasound generation with a meniscus-cavity system and complete a missing piece e.g. to make an optical fiber based ultrasound device that is capable is a complete ultrasound diagnosis device. We will follow a 'bottom up' approach, and start by asking whether it is actually possible to drive menisci electrically, and what are the requirements on the superhydrophobic surface, the driving voltage, conductivity of the liquid, etc., and end with presenting results along with an neat nonlinear mathematical problem.

G.1 Feasibility

Two electric driving scenarios

We now estimate what voltages are required to drive a cavity-meniscus system as described in Chapter 6 and 7 through electric forces. Fig. G.1 shows schematically two possible designs. The conducting liquid is separated from the conducting bulk substrate through an insulating layer, which may be thick compare to the size of the texture (a) or thin compared to the size of the texture (b). A voltage is applied between the liquid and the conducting part of the substrate. In (a) the liquid-gas interface mainly experiences an electrical force that pulls in downward direction, while in (b) it experiences forces pulling in different directions on different surface elements, and additionally the contact angle changes due to the so-called electrowetting effect.

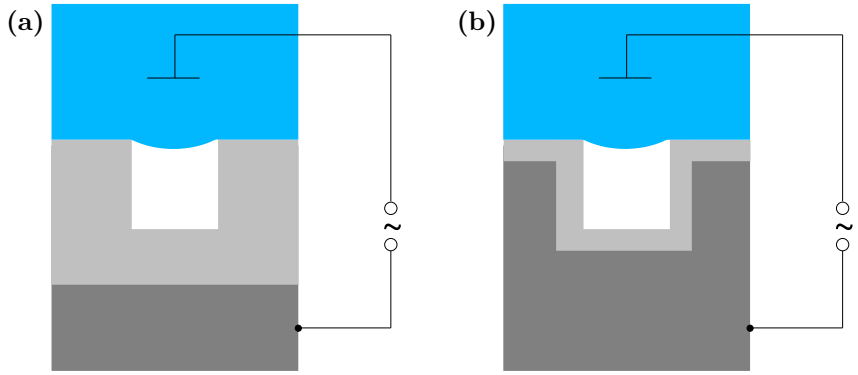

Figure G.1: **Two possible electrical geometries.** **(a)** Insulator thickness larger than texture size. **(b)** Insulator thickness smaller than texture size.

We consider first the effect of a contact angle change. We assume the sharp edge is curved on a scale much smaller than the entire meniscus. With no voltage applied, the contact line adopts a position in the center of the curved rim, determined by the Young angle and the curvature of the interface imposed by Laplace's law. As the Young angle is decreased through the electrowetting effect, the contact line moves to continuously satisfy Young's condition. As long as the Young angle remains smaller than 90° the translation is infinitesimal (at maximum as large as the radius of curvature of the edge). In this case, negligible forcing is provided by the contact angle change. If however, the contact angle is changed below 90° the meniscus will translate downwards. This corresponds to a strong forcing. In a typical electrowetting system the contact angle of a previously hydrophobic surface with a contact angle considerably larger than 90° is easily decreased well below 90°. We thus conclude, that, through the electrowetting effect, it should easily be possible to drive the meniscus to strong oscillations. This type of forcing is however rather different from a forcing through an ultrasound pressure as performed in Chapters 6 and 7. In particular, the shape of the interface does not necessarily change, i.e., there is not the type of 'surface tension spring' as encountered before. Instead two other oscillation scenarios could be encountered: (1) Oscillations are slow (below resonance) and gas compression contributes a large enough restoring force. The interface could indeed not deform at all, and only move downwards and upwards like a piston. (2) Oscillations are fast. Inertia, viscous dissipation and surface tension will counteract and cause local deformations of the liquid gas interfaces and the interface could vibrate forming complex surface modes. In both scenarios the interface additionally experiences electrostatic forces that differ depending on the position on the interface. In conclusion, the 'thin-insulator-geometry' could lead to very complicated interface motion. It may thus be beneficial to look first at a simpler system, and to search address the realization of electrically driven micromenisci on an easier route.

Dielectric strength

Let us thus consider the 'thick-insulator-geometry'. In this case, no electrowetting effect is present, and we deal only with electrostatic forces acting on the interface. Let us make a simple model. Let us assume the interface is flat in equilibrium and undergoes small spherical-cap-like deformations. In this case the deflection ζ in the apex of the interface is linked to its curvature κ through

$$\zeta = \frac{R^2\kappa}{4}, \tag{G.1}$$

where R is the cavity radius. Let us assume for simplicity that the dielectric constant ϵ of the insulator is the same as the one of the gas inside the cavity. In this case the force per unit area acting on the interface is approximately

$$\frac{F}{A} = \frac{1}{2}\epsilon\frac{U^2}{(d-\zeta)^2}, \tag{G.2}$$

where U is the applied voltage and d is the distance between the bottom electrode and the flat water surface. The force is balanced by the Laplace pressure of the curved interface thus

$$\sigma\kappa = \frac{1}{2}\epsilon\frac{U^2}{(d-\zeta)^2}. \tag{G.3}$$

Substituting Eq. (G.1) yields

$$\zeta = \frac{\epsilon R^2}{8\sigma}\frac{U^2}{(d-\zeta)^2}. \tag{G.4}$$

Let us approximate $d - \zeta \approx d$, and let us assume $R = d$. Then

$$U = \sqrt{\frac{8\sigma\zeta}{\epsilon}}, \tag{G.5}$$

and we find for 100nm deflection we need around 80V. This is quite a bit, since (1) we are planning to establish such a system on micron scales, and we must provide a sufficiently strong insulating layer and (2) we want to provide such a voltage at up to MHz frequencies. Let us check the numbers. The dielectric breakdown strength of SiO_2 is about 10-100V/μm (when obtained through dry or wet oxidization of silicon). Thus, working with micron size cavities we are indeed rather close to dielectric breakdown. In resonance, less force will be needed to achieve the same amplitude. From the experiments with ultrasound, we know that the amplitude at resonance is about 10 times higher than in the quasistatic case. On the other hand we also really want to measure off resonance to capture the full resonance curve, so in the end we will really need to work near the dielectric breakdown limit. But it could have been worse. In principle, we should at least be able to apply a voltage that is large enough to see something. So let us check whether we can actually apply such a voltage – at the required frequency.

RC frequency cut off

The electrical bandwidth of the liquid-insulator-electrode system has an RC constant which may not be so small, since the liquid resistance may generally be rather large. Let us thus estimate the RC frequency cut off for a typical sample. In the experiments performed in Chapter 6, the sample consists of a 2×5mm large piece of a silicon wafer. We suppose that a reasonable diffraction experiment can still be achieved if we place a flat electrode with the same area at 1cm distance from the surface.

The capacitance C of the insulating layer of the sample is

$$C = \epsilon\frac{A}{d}, \tag{G.6}$$

where A is the total sample area and d is the insulator thickness. The liquid between the sample surface and the electrode acts as an electrical resistor with resistance

$$R = \rho\frac{l}{A}, \tag{G.7}$$

where ρ is the resistivity of the water and l is the distance between the sample surface and the electrode. The system's RC frequency cut off occurs at frequency

$$f = \frac{1}{2\pi RC}, \tag{G.8}$$

thus

$$f = \frac{d}{2\pi\rho\epsilon l}. \tag{G.9}$$

We note that the cut off frequency depends on the ratio d/l but not on the area A. The resistivity of saturated NaCl-in-water solution is about $\rho = 5\cdot10^{-2}\Omega$/m, and we find with an insulator thickness $d = 6\mu$m (corresponding to the cavity diameter of the largest samples used in Chapter 6)

$$f \approx 200MHz. \tag{G.10}$$

For 20g/l NaCl solution the resistivity increases to $\rho = 2\cdot10^{2}\Omega$/m. In this case we have

$$f \approx 50kHz. \tag{G.11}$$

In practice we may introduce additional capacitances (e.g., at the back side of the sample) that decrease the bandwidth further. Thus, we better put half a kilo of salt on the liter (saturation) than only 20g. Moreover, it is a good idea to check the bandwidth of our system in practice before we go ahead an try to excite meniscus oscillations with a precious 'real' sample. To measure the bandwidth of an RC system one usually measures the voltage 'before' and 'after' the resistor with an oscilloscope with a calibrated voltage probe. However, this is not possible in our case, evidently since we cannot measure 'before' and 'after' the resistor. Thus we introduce another resistor that is smaller than the 'water resistor', and measure the current through this one – by measuring the voltage drop across it. In this way, it was verified that the bandwidth of a dummy sample is in practice larger than 10MHz, which was the bandwidth of the voltage source used in the measurement.

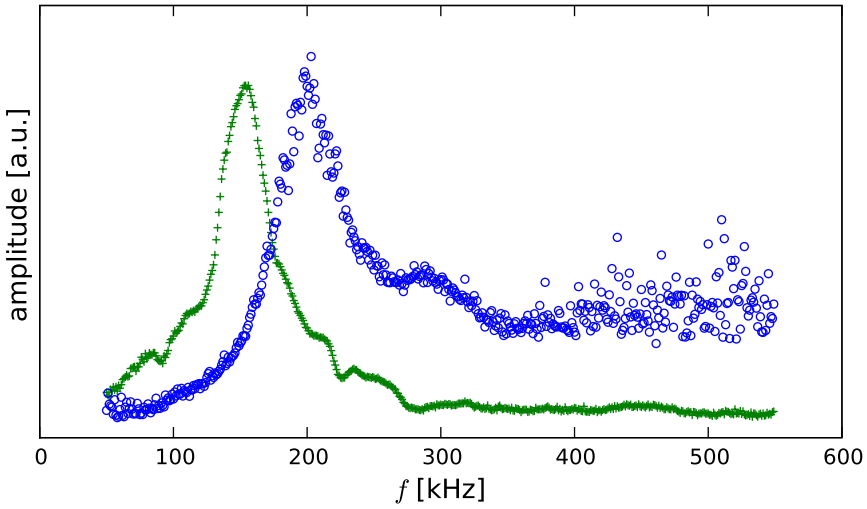

Figure G.2: **Resonance behavior of electrically driven collectively oscillating micromenisci.** An electrically driven system (open blue symbols) is compared to an equivalent pressure driven system (green '+'s). A slight increase of the resonance frequency is possibly due to a slight decrease of the diameter of the cavities due to the silicon oxidization process.

G.2 Experiment

To obtain a system suitable for electrically driven meniscus oscillation, the samples as used in Chapter 6 are modified by converting the outermost layer of the readily texture silicon surface into SiO_2 through wet oxidization. In this way an approximately 6μm thin isolating SiO_2 surface layer could be achieved. After the oxidization process, the sample is hydrophobized in the usual way. A point on the backside of the sample is scratched to remove the insulating layer and the sample is glued with conducting glue onto the signal line of a BNC cable. Subsequently, exposed conducting glue is carefully isolated again by applying a thick layer of isolating epoxy. Note that gluing of the hydrophobized sample is highly non-trivial due to the liquid repellency of the sample surface. Thereafter the BNC cable with the sample is immersed in saturated NaCl solution, the counter electrode (a mm thick copper wire) is brought in close proximity ($\approx$ 5mm) to the sample surface and its other end is connected to the shielding of the BNC cable. An AC voltage of variable frequency and amplitude (home built high voltage amplifier based on an APEX PA98) is applied across the sample.

Fig. G.2 shows a typical measured frequency response of a sample with radius $R = 3\mu$m, period $d = 15\mu$m, and hexagonal pattern obtained by applying several tens of volt, as compared to the ultrasound frequency response of the same sample

as measured in Chapter 6. The slight increase of the resonance frequency is probably due to a slight decrease of the hole radius due to the oxidization process (material expansion). The results demonstrates that electrically driven meniscus oscillation with an amplitude of the order several tens of nm can indeed be achieved. Moreover, the observed resonance frequency is truly remarkable. One would expect that the resonance occurs at half the frequency as compared to the case of pressure driven meniscus oscillations, since the force excerpted by the oscillating voltage is proportional to U^2, and

$$U^2 = U_0^2 \sin^2(\frac{\omega}{2}t) = \frac{1}{2} - \frac{1}{2}\cos(\omega t). \tag{G.12}$$

However, this is not the case. Meniscus oscillations of a frequency ω are excited efficiently by an AC voltage with the same frequency ω, and in contrast driving with half the frequency does not efficiently excite oscillations. This is indeed astonishing and I cannot explain these results quantitatively. Let me however point out two aspects that may be at the origin of this. (1) The positive and negative half cycle of the AC voltage are not equivalent, e.g. due to different ionic mobilities of the positive and negative charges. This would result in an asymmetry – similar to rectification – and in this way provide a contribution to the force with the same frequency as the driving. (2) The force on the meniscus is larger when it is bent downwards and smaller when it is bent upwards due to the different respective electric field strength. This results in a non-linearity in the equation of motion of a meniscus. In particular, following the simple model for the dynamics of a single meniscus as illustrated in subsection 2.3.1, we write the equation of motion of a cavity-meniscus system including electric driving as

$$m\ddot{\zeta} + 8\sigma\zeta = \frac{1}{2}\epsilon\frac{\pi R^2 U_0^2 \sin^2(\omega t)}{(d-\zeta)^2}, \tag{G.13}$$

where ζ is the meniscus deflection and $m = \rho R^3$, as before. Thus

$$m\ddot{\zeta}(d-\zeta)^2 + 8\sigma\zeta(d-\zeta)^2 = \frac{1}{2}\epsilon\pi R^2 U_0^2 \sin^2(\omega t). \tag{G.14}$$

The observed resonance behavior may be hidden in the solutions to such type of nonlinear differential equation.

G.3 Conclusions

We have demonstrated the possibility of electric driving of micromenisci, and shown that the resonance behavior is very similar to the equivalent system under ultrasound excitation. The system could enable ultrasound generation through a cavity-meniscus system. The observed resonance frequency suggests that nonlinear contributions in the equation of motion of the system may be important to model the system.

Appendix H

Superhydrophobic photonic crystals

The observed great sensitivity of the diffraction from a superhydrophobic optical grating on the deflection of the liquid-gas interfaces as discussed in Chapter 3 and 6, intrigues the question whether a photononic crystal (one-dimensional or two-dimensional) could be used in a similar way to serve readily as an integrated ultra sensitive ultrasound sensor, potentially coupled to an optical fiber. A photonic crystal is characterized by a band gap, a range of wavelength in which the device reflects incident light rather than transmitting it. The exact position of the band gap would depend on the deflection of the liquid-gas interfaces. Thus, a collective oscillation of the liquid-gas interfaces could be detected as an oscillatory change of the position of the band gap. In other words, one would tune the wavelength of a laser to the center of the steeply falling edge of the band gap, and detect the transmitted or reflected intensity (Fig. H.1). Without going into greater detail, we will present in this appendix first preliminary results that were obtained with such a system. We will restrict ourselves to describe in the following sections briefly the photonic crystal devices and the optical setup that was used to perform such experiments, and thereafter present first measurements of the photonic band gap of the system in the superhydrophobic as well as in the impregnated state. The appendix is conclude in Sec. H.2

H.1 Experiment

A schematic of the present device, which was modeled in [29] and characterized earlier in [46] is shown in Fig. H.2. The device consists of a ridge type waveguide with a $d = 212\,\mathrm{nm}$ thick Si_3N_4 guiding layer (refractive index $n_g = 2.01$), grown on top of a $l = 9\,\mu\mathrm{m}$ thick SiO_2 buffer layer (refractive index $n_c = 1.46$) on a silicon substrate. A shallow, $c = 2\,\mathrm{nm}$ high and $w = 2\,\mu\mathrm{m}$ wide ridge forming a single mode waveguide at $\lambda > 450\,\mathrm{nm}$, is etched into the Si_3N_4 layer using conventional photolithography and wet chemical etching. 401 grooves with a period $\Lambda = 190\,\mathrm{nm}$, groove width

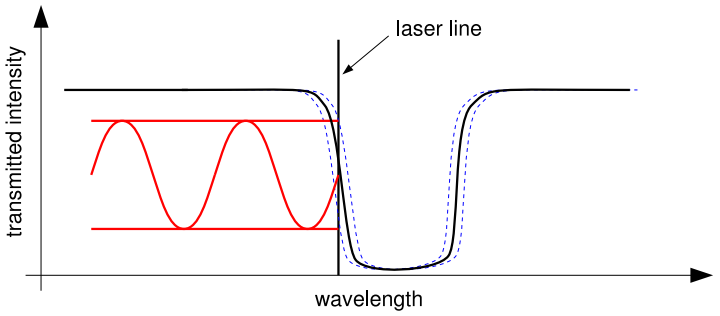

Figure H.1: **Principle of ultrasound detection using a photonic crystal.** A deflection of the liquid-gas interfaces shifts the position of the band gap (dashed blue lines). A laser is tuned to the center of the steeply falling edge of the band gap (vertical line). At this wavelength a shift of the bandgap results in a pronounced change of the transmitted intensity.

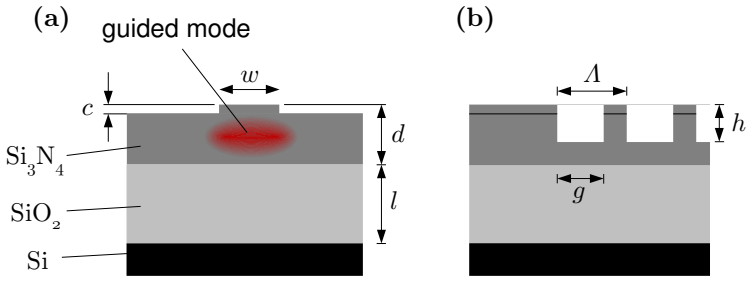

Figure H.2: **Photonic crystal waveguide grating. (a)** cross section **(b)** side view. A Si_3N_4 ridge type waveguide of thickness $d = 212$nm, width $w = 2\mu$m, and ridge height $c = 2$nm forming a single mode waveguide at $\lambda > 450$ nm, is fabricated on top of an $l = 9\mu$m thick SiO_2 buffer layer that is grown on silicon. The grating consists of 401 grooves with a period $\Lambda = 190$ nm, groove width $g = 0.6\Lambda$ and depth $h = 20$ nm. The length of the grooves is 80 μm.

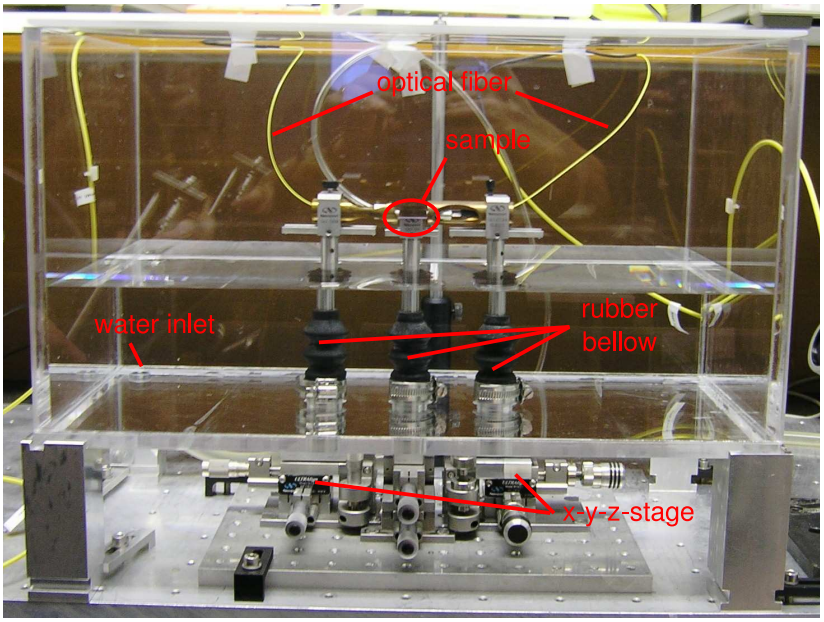

Figure H.3: **Setup for the characterization of superhydrophobic photonic crystals under water, under the influence of ultrasound.** The sample and optical fibers are mounted on high precision x-y-z-stages which are located underneath a transparent container that is sealed and flooded with liquid.

$g = 0.6\Lambda$ and depth $h = 20\,\mathrm{nm}$ form a one-dimensional photonic waveguide grating with a total length of $76.19\,\mu\mathrm{m}$. To ensure full overlap with the evanescent field tails in the slab region, the length of the grooves was chosen $80\,\mu\mathrm{m}$. The grooves were fabricated by direct e-beam writing and reactive ion etching. Subsequently the sample is hydrophobized through vapor deposition of a self assembled monolayer of an alkylsilane as described in appendix C. Light is coupled in and out from the waveguide using two optical fibers whose end faces are brought in close contact with the open ends of the waveguide ('butt-coupling') [1]. Fig. H.3 show our optical setup. The sample and optical fibers are mounted on high precision x-y-z-stages to allow for precise positioning of the fibers at the waveguide's end faces. The stages are located below a transparent container that can be flooded with liquid through a flexible tube connected to its bottom. After flooding the container, an ultrasound immersion transducer is placed above the sample in such a way that the sample is located in the focus of the transducer. The intensity of the transmitted light is measured over a wavelength range in the visible part of the spectrum using a tunable dye laser that is pumped with a 488nm Ar-ion laser.

Fig. H.4 shows measured wavelength scans before (green symbols) and after (red symbols) strong ultrasound excitation and after drying and immersing the sample again (blue symbols). It is seen that the sample is first in the superhydrophobic state, then a transition to the impregnated state is induced by the strong applied ultrasound field resulting in a shift of the photonic band gap towards larger wavelengths (red symbols), and after drying and immersing the device again, the superhydrophobic state is recovered and the position of the band gap shifts back (blue symbols). The recovery of the previous position of the band gap is not perfect, possibly due to contamination during the drying process or even partial destruction of the structure due to the strong ultrasound (e.g. pieces may have chipped off from the grating lamella as observed earlier with micron size superhydrophobic gratings after having cleaned them in an ultrasonic bath). The measurement demonstrates the successful realization of a superhydrophobic state on a photonic crystal. It further demonstrates the successful destruction of the superhydrophobic state through ultrasound and observation of the corresponding impregnated state. It remains to tune the laser wavelength to one of the edges of the band gap –the lower edge is expected to provide greater sensitivity, since in this case the electric field is predominantly located in the air gaps– and to measure ultrasound induced oscillations of the interfaces as an oscillatory variation of the transmitted intensity. We tried to observe such oscillations, however we were not successful. Observations were impeded primarily by a poor noise level of the optical measurement (or too low optical power), and further because the expected resonance frequency of the menisci is poorly known [2], which may simply

[1] Butt coupling is preferred over optical coupling through a microscope objective, since part of the setup will later be flooded with water, which in case of a lens resulted in a change of the focal length, making it necessary to readjust the optical alignment after flooding. In case of butt-coupling no realignment is needed

[2] the elongated character of the grooves leads to logarithmic corrections of the resonance frequency as compared to the well understood cylindrical holes investigated in Chapter 6 and 7, and moreover the large number of closely spaced grooves are expected to show strong hydrodynamic coupling that is –due to the close distance– beyond the scope of the theory presented in Sec. 2.3

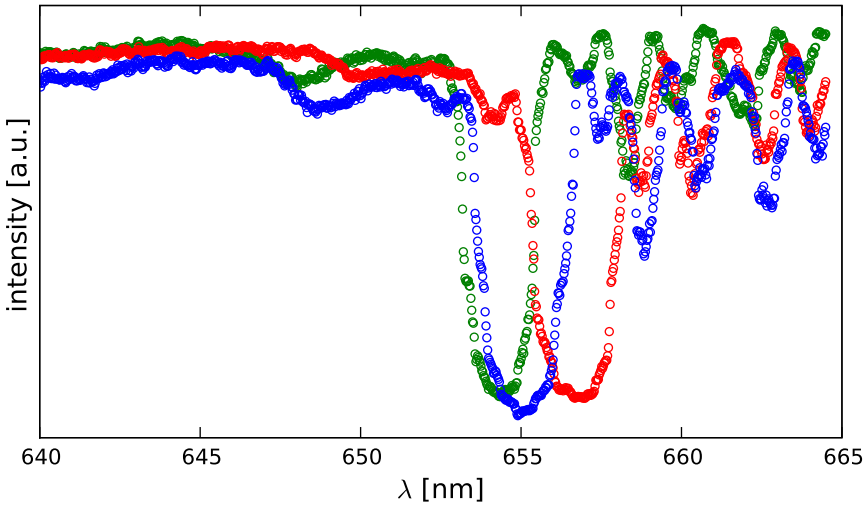

Figure H.4: **Ultrasound induced wetting transition.** The bandgap is determined before (green) and after (red) strong ultrasound excitation and after drying and re-immersing the sample (blue). The sample is first in the superhydrophobic state (green data; bandgap at shorter wavelength), undergoes an ultrasound induced transition to the impregnated state (red data; bandgap at larger wavelength) and is finally returned to the superhydrophobic state (blue data; bandgap at shorter wavelegth)

put the resonance frequency outside the frequency range of the ultrasound equipment available in experiment, and finally because the light is possibly concentrated in the center of the waveguide, such that only a tail of the electromagnetic field interacts with the liquid-gas interfaces. It was indeed the latter aspect that triggered the idea of the optical fiber based micro interferometer presented in Chapter 7, where the light interacts 'head on' with the liquid-gas interface.

H.2 Conclusions

We have demonstrated the possibility of creating a superhydrophobic photonic crystal that could serve as an ultrasound sensor – or vice versa, also as a photonic crystal with a tunable band gap (along the line of e.g. [63, 33]). To enable a successful detection of micromenisci oscillation, the design of a photonic crystal could be modified such that the overlap of the guided mode with the liquid-gas interfaces would be dramatically increased. Another approach could be to use a 2-dimensional photonic crystal consisting of cylindrical holes. Potentially all holes except one could be filled with a suitable solid material or encapsulated with a cover layer, and a photonic crystal microcavity could be formed. Such cavities can be routinely designed with a very large Q, and the device could be extremely sensitive to motions of a micromeniscus on the opening of one or more holes that are strongly coupled to the photonic crystal cavity.

Appendix I

Confocal detection of meniscus oscillations

It is well known that the diffraction pattern observed in the back focal plane of an optical tweezers provides sub-wavelength information about the position of an entrapped particle (e.g. [108, 53]). This poses the natural question whether the deflection of a micromeniscus could be determined in a similar way. In this appendix we demonstrate –without going into greater detail– the measurement of nanometer scale ultrasound induced micromeniscus oscillations through such a confocal detection scheme. We show that the practically achievable signal-to-noise ratio is comparable to that of a fiber optical micro interferometer as introduced in Chapter 7. We further show that the accuracy of the measurement is however primarily determined by drift: while in case of an optical tweezers the trapped particle remains close to the focus of the objective (and the diffraction pattern is used to determine the relative position of the bead with respect to the focus), in case of micromenisci formed at a superhydrophobic surface the object of interest remains at a fixed position in space. This makes it necessary to keep the absolute distance between the cavity-meniscus system and the objective fixed to a cm distance (the focal length of the objective) with nm accuracy. This is a formidable task, and for this reason the confocal detection cannot compete with the optical fiber based device presented in Chapter 7. However, the approach has unique advantages, e.g., an individual cavity-meniscus system that is part of a larger array could be addressed, and thereby the theory about hydrodynamic interaction and higher order modes of an array as presented in Sec. 2.3 could be investigated.

I.1 Experiment

Fig. I.1 shows our optical setup. An additional beam splitter is introduced in a bright field microscope between the objective and the projection lens. The parallel beam of a 488nm Ar-ion laser is coupled into the beam path over this beam splitter and is used to illuminate homogeneously the back aperture of the objective lens.

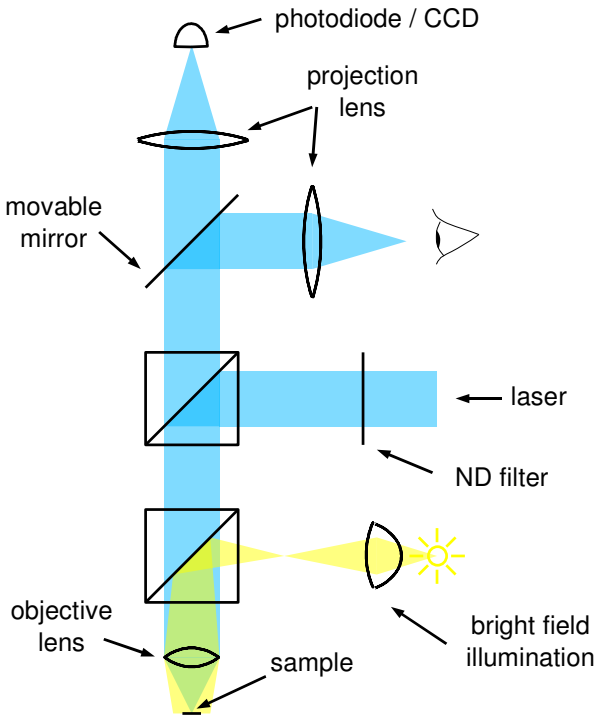

Figure I.1: **Optical setup for confocal detection of micromeniscus oscillations.** A bright field microscope is equipped with an additional beam splitter that is used to couple in parallel laser light. The laser light homogeneously illuminates the back aperture of the objective lens, resulting in a diffraction pattern in the vicinity of the focus.

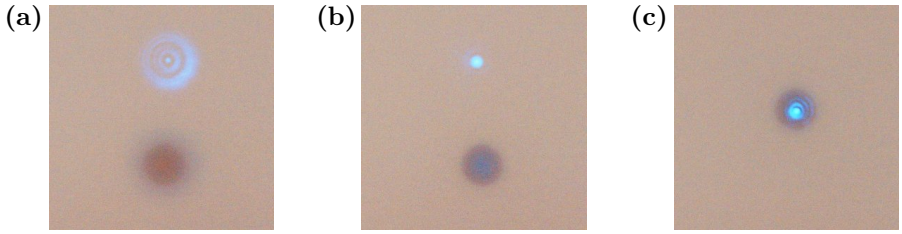

Figure I.2: **Diffraction pattern in the vicinity of the focus of a high N.A. lens.** **(a)** The laser beam is brought into the vicinity to the cylindrical cavity (dark circle). The sample is slightly defocused (the opening of the cavity appears blurred), such that the sample surface cuts a horizontal cross section through the laser diffraction pattern corresponding to $z \neq 0$. Several Airy type rings of comparable intensity are observed. **(b)** The laser beam is focused onto the sample surface (the opening of the cavity appears sharp). The laser diffraction pattern consists of an Airy disc (bright spot) and Airy rings of decreasing intensity (Airy rings are poorly captured by the ccd due to the device's limited dynamic range; the rings are easily seen by eye, due to the logarithmic intensity scale of the human eye). **(c)** The focus of the laser is brought onto the cavity-meniscus system.

The laser light converges to the focus where it generates a characteristic diffraction pattern. This light interacts with the cavity-meniscus system. The collected light is directed towards an eye piece for visual inspection and / or towards a second projection port. The second port is equipped either with a CCD camera or with a photodiode. To control the laser intensity, a series of neutral density filters can be inserted into the illuminating beam path before the microscope. A rectangular container $W \times D \times H \approx 20 \times 10 \times 5\,\mathrm{cm}$ is mounted on the microscope stage. The container is filled with water immersing the objective lens.

The sample consist of 9 cylindrical holes with radius $R = 3\,\mu$m and depth $H = 16\,\mu$m, arranged with a period $d = 300\mu$m on a 1×1mm array. The samples were etched into a silicon wafer and subsequently hydrophobized as described in Chapter 6. For this large period and small total number of cavity-meniscus systems hydrodynamic coupling is expected to be negligible.

The sample is immersed in water and placed in the vicinity of the focus of the objective lens. First the laser beam is strongly attenuated and the bright field mode of the optical microscope is used to locate a cavity. The sample is moved such that a cavity is located in the focus of the laser beam. Fig. I.2 shows snapshots of this procedure. The laser beam generates the typical diffraction pattern obtained when illuminating the back aperture of a well corrected high N.A. lens uniformly with parallel light. The bright spot in the center (Airy disk) is surrounded by rings of decreasing intensity (Airy rings). More generally the intensity in the vicinity of the

focus is given by [15] [12]

$$I(u,v) = \left(\frac{2}{u}\right)^2 [U_1^2(u,v) + U_2^2(u,v)] I_0, \tag{I.1}$$

where u and v are dimensionless optical coordinates

$$\begin{aligned} u =& \frac{2\pi}{\lambda}\left(\frac{a}{f}\right)^2 z, \\ v =& \frac{2\pi}{\lambda}\left(\frac{a}{f}\right) r. \end{aligned} \tag{I.2}$$

Here z and r are the coordinate in the direction of the optical axis and the radial coordinate, respectively, a and f are the aperture radius respectively the focal length of the lens and I_0 is the incident intensity. U_n are *Lommel functions* given by

$$U_n(u,v) = \sum_{s=0}^{\infty} (-1)^s \left(\frac{u}{v}\right)^{n+2s} J_{n+2s}(v), \tag{I.3}$$

and J_n are Bessel functions. On the optical axis, the latter reduces to

$$I(u,0) = \left(\frac{\sin(u/4)}{u/4}\right)^2 I_0, \tag{I.4}$$

which is the well known expression from which the depth discrimination of a confocal microscope is derived (e.g., [131]). Eq. (I.4) is plotted in Fig. I.3 for $a/f = 0.5$ (N.A.= 1). The period of the characteristic minima and maxima is determined by the numerical aperture and the wavelength of the light. The intensity is unity in the focus and the envelope of the maxima decreases with $1/z^2$ for large z.

In the experiments presented here, we are interested only in the wing of the central maximum. In particular, we adjust the position of the sample in z-direction such that the liquid-gas interface is located approximately at the center of the wing between the central maximum and the first minimum (red line) in Fig. I.3. In this case a small (few nm) deflection of the interface in z-direction will result in an approximately linear increase (or decrease) of the intensity that is incident on the interface, such that a sinusoidal oscillation of the interface position will result in a sinusoidal change of the reflected intensity.

I.2 Ultrasound induced oscillations

To excite the liquid-gas interface to nanometer scale oscillations, we immerse an ultrasound transducer into the liquid at few cm distance of the sample. To achieve a

[1] The intensity pattern in the vicinity of the focus of a high N.A. lens is indeed shown on the front cover of the latter book

[2] This treatment draws on the Fraunhofer approximation. For a more detailed treatment beyond the Fraunhofer approximation, giving right to the vector nature of light and taking into account the effect of the lens on the polarization state of the light, see e.g. [127].

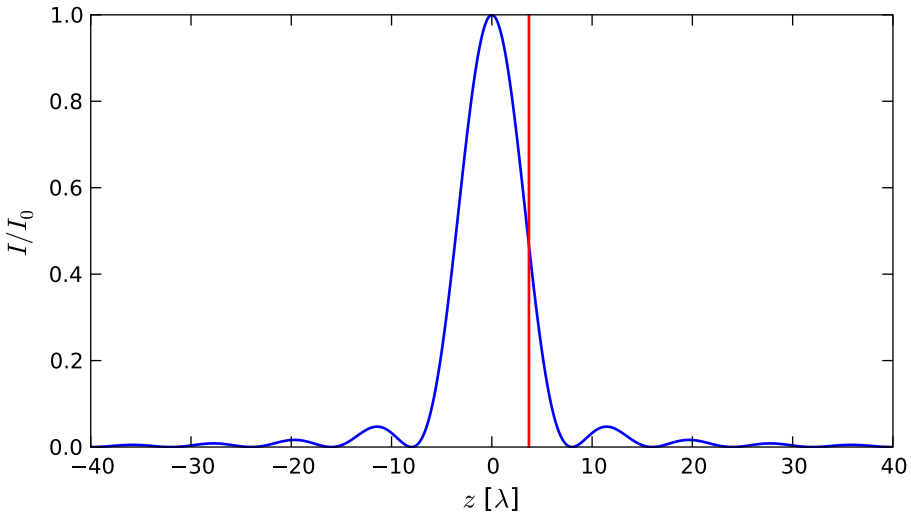

Figure I.3: **Intensity near the focus of a high N.A. lens on the optical axis.** The period of the characteristic minima and maxima is given by the numerical aperture and the wavelength of the light. The intensity is unity in the focus and the envelope of the maxima decreases as $1/z^2$ towards larger z. The red line marks the rest position of the liquid-gas interface on the wing of the central intensity peak for the detection of ultrasound induced meniscus oscillations.

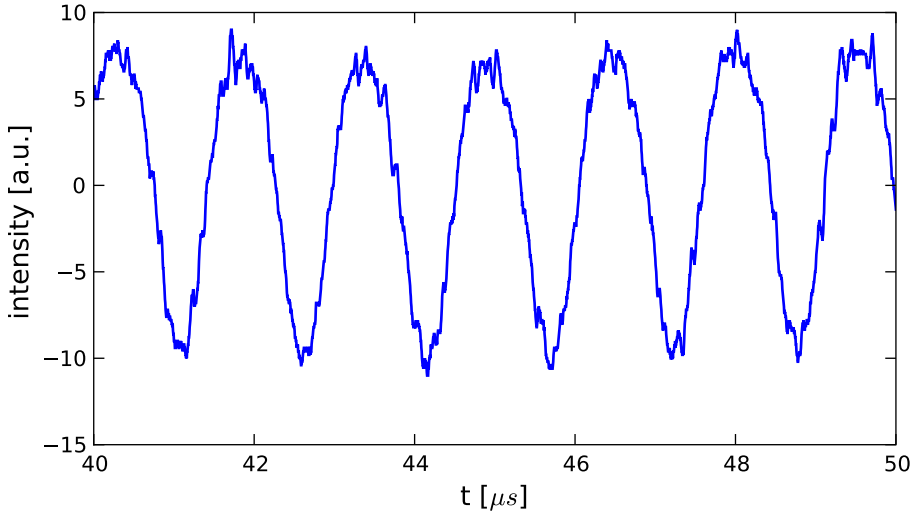

Figure I.4: **Current trace corresponding to meniscus oscillations.** The sinusoidal signal is slightly distorted (flattened maxima) indicating that the meniscus rest position is not aligned exactly on the center of the wing. In this case, the ultrasound driving frequency was 650kHz.

constant driving pressure over a large range of ultrasound frequencies we employ a piezoelectric hydrophone (GRAS10CH) as a transducer, and drive it with constant amplitude in a range were it provides a nearly flat frequency response.

To measure the change of the reflected intensity, we direct all collected light into the second projection port of the microscope and place a photodiode in the focus of the corresponding projection lens. We remove the attenuators from the illuminating laser beam, turn off the bright field illumination, and switch on the ultrasound. The rest position of the liquid-gas interface is brought onto the center of the wing of the central peak by driving the liquid-gas interface with a rather large amplitude and observing the shape of the oscillation signal while aligning the z-position of the sample (the interface is located at the center of the wing when the oscillations are sinusoidal and their amplitude is maximal; see also Chapter 7).

Fig. I.4 shows a typical timetrace of micromeniscus oscillations observed in this way. The signal-to-noise ratio of the raw data competes with that of meniscus oscillations detected through a fiber optical micro interferometer as introduced in Chapter 7. However, the working point of the displacement-to-intensity conversion (meniscus rest position) rapidly drifts away from the optimum at the wing of the central intensity peak to an arbitrary point in the diffraction pattern. E.g. the current trace shown here is one out of many traces with increasing frequency that make up a frequency sweep (for the determination of the frequency response of the system). This trace was

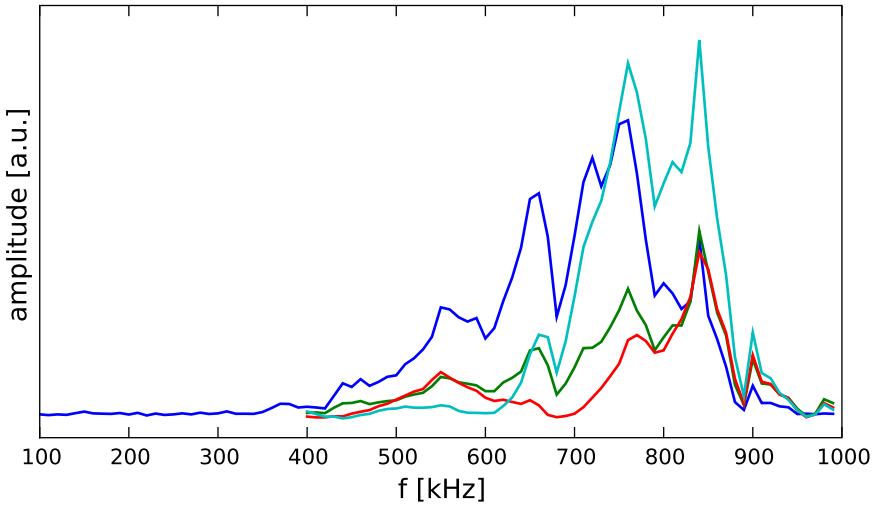

Figure I.5: **Frequency response of an individual cavity-meniscus system.** Individual frequency sweeps are shown with different colors. The data is modulated by strong periodic oscillations due to ultrasound standing waves.

acquired approximately after half of the sweep was completed. It is seen that already at this time the raw signal is slightly distorted (flattened maxima), indicating that the working point is no longer in the middle between the central maximum and the first minimum of the diffraction pattern. This drift makes the measurement of meniscus oscillations based on the diffraction pattern of an objective lens a formidable task.

I.3 Frequency response

Nevertheless, when the system is sufficiently equilibrated, and by reducing the number of data points in a frequency sweep, we successfully recorded the frequency response of the system. Fig. I.5 shows several measured frequency sweeps. The data indicates that the resonance frequency of the system is around 800kHz, in good agreement with the theoretical prediction $f = 805$kHz for a single cavity-meniscus system given in Tab. 6.1. The quality of the data is obscured by another effect that is difficult to avoid with the confocal detection scheme, namely ultrasound standing waves. The distance between the sample and objective lens is only slightly larger than the ultrasound wavelength. Therefore ultrasound wavetrains cannot be chosen short enough to allow for an undisturbed measurement during a single wavetrain, rather reflections from the objective lens arrive before the sample has finished its own transient response. These nearfield interactions depend strongly on the ultrasound wavelength. Waves

reflected from the objective, the sample, the container bottom and water surface may interfere constructively or destructively depending on the wavelength, resulting in strong periodic modulations on top of a frequency scan (see Fig. I.5). Nevertheless, having understood such effects, the present data can be considered as a confirmation of the theoretically predicted resonance frequency of a single cavity-meniscus system.

I.4 Conclusions

To conclude. We have demonstrated successfully the measurement of nanometer scale meniscus oscillations using an 'optical-tweezers-like' detection scheme. To this end we have studied the interaction of a micromeniscus with the intensity pattern of a high N.A. lens. The steep decrease of the illuminating intensity in vertical direction was used to convert the meniscus deflection into an intensity variation. By sweeping the ultrasound frequency we measured the frequency response of an individual cavity-meniscus system. The result confirmed the theoretical prediction for a single isolated cavity proposed in section 2.3 and Chapter 6.

Bibliography

[1] GNU General Public License, 2007. http://www.fsf.org/.

[2] A. Ahuja, J. A. Taylor, V. Lifton, A. A. Sidorenko, T. R. Salamon, E. J. Lobaton, P. Kolodner, and T. N. Krupenkin. Nanonails: A simple geometrical approach to electrically tunable superlyophobic surfaces. *Langmuir*, 24(1):9–14, 2008.

[3] E. Anderson, Z. Bai, C. Bischof, S.Blackford, J. Demmel, J. Dongarra, J. Du Croz, A. Greenbaum, S. Hammarling, A. McKenney, and D.Sorensen. *LAPACK User's Guide*. SIAM, Philadelphia, 3 edition, 1999. http://www.netlib.org/lapack/lug/.

[4] S. Ashkenazi, Y. Hou, T. Buma, and M. O'Donnell. Optoacoustic imaging using thin polymer étalon. *Appl. Phys. Lett.*, 86:134102, 2005.

[5] K. Autumn, Y.A. Liang, S.T. Hsieh, W. Zesch, W.A.I.P. Chan, T.W. Kenny, R. Fearing, and R.J. Full. Adhesive force of a single gecko foot-hair. *Nature*, 405(6787):681–685, 2000.

[6] C.D. Bain, E.B. Troughton, Y.T. Tao, J. Evall, G.M. Whitesides, and R.G. Nuzzo. Formation of monolayer films by the spontaneous assembly of organic thiols from solution onto gold. *J. Am. Chem. Soc.*, 111:321–335, 1989.

[7] G. Bakker. *Kapillarität und Oberflachen-Spannung.* Leipzig: Akademisch Verlags Gesellschaft, 1928.

[8] I. K. Baldry, J. Bland-Hawthorn, and J. G. Robertson. Volume phase holographic gratings: Polarization properties and diffraction efficiency. *Pub. Astron. Soc. Pac.*, 116:403, 2003.

[9] D. Bartolo, F. Bouamrirene, E. Verneuil, A. Buguin, P. Silberzan, and S. Moulinet. Bouncing or sticky droplets: Impalement transitions on superhydrophobic micropatterned surfaces. *Eur. Phys. Lett.*, 74:299, 2006.

[10] P. C. Beard, A. M. Hurrell, and T. N. Mills. Characterization of a polymer film optical fiber hydrophone for usein the range 1 to 20 mhz: A comparison with pvdf needle and membranehydrophones. *IEEE T. Ultrason. Ferr.*, 47(1):256–264, 2000.

[11] PC Beard and TN Mills. Extrinsic optical-fiber ultrasound sensor using a thin polymer film as a low-finesse Fabry-Perot interferometer. *Appl. Opt.*, 35:663–675, 1996.

[12] P. Bienstman. *Rigorous and efficient modelling of wavelength scale photonic components*. PhD thesis, University of Ghent, Belgium, 2001.

[13] J. Boehm. Kapillaritat und Saftsteigen. *Ber. Dtsch. Bot. Ges.*, 11:203–212, 1893.

[14] E. Bormashenko, Y. Bormashenko, T. Stein, G. Whyman, and E. Bormashenko. Why do pigeon feathers repel water? Hydrophobicity of pennae, Cassie–Baxter wetting hypothesis and Cassie–Wenzel capillarity-induced wetting transition. *J. Colloid Interface Sci.*, 311(1):212–216, 2007.

[15] Max Born and Emil Wolf. *Principles of Optics*. Cambridge University Press, 7 edition, 1999.

[16] N. Bremond, M. Arora, C.D. Ohl, and D. Lohse. Controlled Multibubble Surface Cavitation. *Phys. Rev. Lett.*, 96(22):224501, 2006.

[17] M. Brinkmann and R. Lipowsky. Wetting morphologies on substrates with striped surface domains. *J. Appl. Phys.*, 92:4296, 2002.

[18] P. Brunet, F. Lapierre, V. Thomy, Y. Coffinier, and R. Boukherroub. Extreme Resistance of Superhydrophobic Surfaces to Impalement: Reversible Electrowetting Related to the Impacting/Bouncing Drop Test. *Langmuir*, 2008. in press.

[19] JA Bucaro, HD Dardy, and EF Carome. Fiber-optic hydrophone. *J. Acoust. Soc. America*, 62:1302, 1977.

[20] A. B. D. Cassie and S. Baxter. Wettability of porous surfaces. *Trans. Faraday Soc.*, 40:546–551, 1944.

[21] R.B. Chapman and M.S. Plesset. Thermal effects in the free oscillation of bubbles. *J. Basic Eng. Trans. ASME Series D*, 93:373–376, 1971.

[22] XM Chen and A. Prosperetti. Thermal processes in the oscillations of gas bubbles in tubes. *J. Acoust. Soc. America*, 104:1389, 1998.

[23] T. Clausnitzer, T. Kämpfe, E.-B. Kley, A. Tünnermann, U. Peschel, A.V. Tishchenko, and O. Parriaux. An intelligible explanation of highly-efficient diffraction in deep dielectric rectangular transmission gratings. *Opt. Express*, 13:10448, 2005.

[24] T. Clausnitzer, T. Kämpfe, E.-B. Kley, A. Tünnermann, A.V. Tishchenko, and O. Parriaux. Highly-dispersive dielectric transmission gratings with 100% diffraction efficiency. *Opt. Express*, 16:5577, 2008.

[25] Tina Clausnitzer, Thomas Kämpfe, Frank Brückner, Roland Heinze, Ernst-Bernhard Kley, and Andreas Tünnermann. Reflection-reduced encapsulated transmission grating. *Opt. Lett.*, 33(17):1972–1974, 2008.

[26] Tina Clausnitzer, Jens Limpert, Karsten Zollner, Holger Zellmer, Hans-Joerg Fuchs, Ernst-Bernhard Kley, Andreas Tünnermann, Marco Jupe, and Detlev Ristau. Highly efficient transmission gratings in fused silica for chirped-pulse amplification systems. *Appl. Opt.*, 42:6934, 2003.

[27] David A. Content, Rene A. Boucarut, C. Bowers, Timothy J. Madison, Geraldine A. Wright, Don J. Lindler, L. K. Huang, Bernard P. Puc, Clive Standley, and Todd A. Norton. Development and testing of diffraction gratings for the space telescope imaging spectrograph. *Proc. SPIE*, 2807:267–278, 1996.

[28] C. Cottin-Bizonne, J.L. Barrat, L. Bocquet, and E. Charlaix. Low-friction flows of liquid at nanopatterned interfaces. *Nat. Mater.*, 2(4):237–240, 2003.

[29] J. Čtyrokỳ, S. Helfert, R. Pregla, P. Bienstman, R. Baets, R. De Ridder, R. Stoffer, G. Klaasse, J. PetráČek, P. Lalanne, et al. Bragg waveguide grating as a 1d photonic band gap structure: COST 268 modelling task. *Opt. Quant. Electron.*, 34:455–470, 2002.

[30] P.G. de Gennes, F. Brochard-Wyart, and D. Quéré. *Capillarity and Wetting Phenomena: Drops, Bubbles, Pearls, Waves*. Springer, Berlin, 2004.

[31] Pierre Simon de Laplace. *Mécanique céleste, Supplement to the tenth edition*. 1806.

[32] B.V. Derjaguin and N.V. Churaev. On the question of determining the concept of disjoining pressure and its role in the equilibrium and flow of thin films. *J. Colloid Interface Sci*, 66(3):389–398, 1978.

[33] Jiangbing Du, Yange Liu, Zhi Wang, Zhanyuan Liu, Bing Zou, Long Jin, Bo Liu, Guiyun Kai, and Xiaoyi Dong. Thermally tunable dual-core photonic bandgap fiber based on the infusion of a temperature-responsive liquid. *Opt. Express*, 16:4263–4269, 2008.

[34] G. van Rossum et al. Python programming language. http://www.python.org/.

[35] L. Gao and T.J. McCarthy. How wenzel and cassie were wrong. *Langmuir*, 23(7):3762–3765, 2007.

[36] X. GAO and LEI JIANG. Biophysics: Water-repellent legs of water striders. *Nature*, 432(7013):36–36, 2004.

[37] J. Genzer and K. Efimenko. Recent developments in superhydrophobic surfaces and their relevance to marine fouling: a review. *Biofouling*, 22(5):339–360, 2006.

[38] Emily A. Gibson, David M. Gaudiosi, Henry C. Kapteyn, Ralph Jimenez, Steve Kane, Rachel Huff, Charles Durfee, and Jeff Squier. Efficient reflection grisms for pulse compression and dispersion compensation of femtosecond pulses. *Opt. Lett.*, 31:3363, 2006.

[39] Elias N. Glytsis and Thomas K. Gaylord. Three-dimensional (vector) rigorous coupled-wave anlysis of anisotropic grating diffraction. *J. Opt. Soc. Am. A*, 7:1399, 1990.

[40] F. C. Goodrich. The Mathematical Theory of Capillarity. I. *Proc. Roy. Soc. A*, 260:481–489, 1961.

[41] Thomas B. Greenslade Jr. Wire diffraction gratings. *Am. J. Phys.*, 41:730, 1973.

[42] Thomas B. Greenslade Jr. Wire diffraction gratings. *The Physics Teacher*, 42(2):76–77, 2004.

[43] George M. Hale and Marvin R. Querry. Optical constants of water in the 200-nm to 200-micrometer wavelength region. *Appl. Opt.*, 12:555, 1973.

[44] S. Herminghaus. Roughness-induced wetting. *Eur. Phys. Lett.*, 52:165–170, 2000.

[45] Max Herzberger and Calvin D. Salzberg. Refractive indices of infrared optical materials and color correction of infrared lenses. *J. Opt. Soc. Am.*, 52(4):420–424, 1962.

[46] WCL Hopman, P. Pottier, D. Yudistira, J. van Lith, PV Lambeck, RM De La Rue, A. Driessen, H. Hoekstra, and RM de Ridder. Quasi-one-dimensional photonic crystal as a compact building-block for refractometric optical sensors. *IEEE J. Sel. Top. Quant.*, 11:11–16, 2005.

[47] S.W. Huang, S.L. Chen, T. Ling, A. Maxwell, M. O'Donnell, L.J. Guo, and S. Ashkenazi. Low-noise wideband ultrasound detection using polymer microring resonators. *Appl. Phys. Lett.*, 92:193509, 2008.

[48] K. Ichimura, S.K. Oh, and M. Nakagawa. Light-Driven Motion of Liquids on a Photoresponsive Surface. *Science*, 288:1624, 2000.

[49] M. Jin, X. Feng, J. Xi, J. Zhai, K. Cho, L. Feng, and L. Jiang. Super-Hydrophobic PDMS Surface with Ultra-Low Adhesive Force. *Macromol. rapid. Comm.*, 26:1805, 2005.

[50] J. F. Joanny and P. G. de Gennes. A model for contact angle hysteresis. *J. Chem. Phys.*, 81:552, 1984.

[51] D. D. Joseph and J. Wang. The dissipation approximation and viscous potential flow. *J. Fluid Mech.*, 505:365–377, 2004.

[52] C. Journet, S. Moulinet, C. Ybert, S.T. Purcell, and L. Bocquet. Contact angle measurements on superhydrophobic carbon nanotube forests: Effect of fluid pressure. *Eur. Phys. Lett.*, 71(1):104–109, 2005.

[53] S Keen, J Leach, G Gibson, and M J Padgett. Comparison of a high-speed camera and a quadrant detector for measuring displacements in optical tweezers. *J. Opt. A*, 9(8):S264–S266, 2007.

[54] T.N. Krupenkin, J.A. Taylor, T.M. Schneider, and S. Yang. From Rolling Ball to Complete Wetting: The Dynamic Tuning of Liquids on Nanostructured Surfaces. *Langmuir*, 20:3824–3827, 2004.

[55] T.N. Krupenkin, J.A. Taylor, E.N. Wang, P. Kolodner, M. Hodes, and T.R. Salamon. Reversible Wetting-Dewetting Transitions on Electrically Tunable Superhydrophobic Nanostructured Surfaces. *Langmuir*, 23:9128–9133, 2007.

[56] H. Kusumaatmaja, ML Blow, A. Dupuis, and JM Yeomans. The collapse transition on superhydrophobic surfaces. *Eur. Phys. Lett.*, 81:36003, 2008.

[57] A. Lafuma and D. Quere. Superhydrophobic states. *Nat. Mater.*, 2(7):457–460, 2003.

[58] I. Lahiri, LJ Pyrak-Nolte, DD Nolte, MR Melloch, RA Kruger, GD Bacher, and MB Klein. Laser-based ultrasound detection using photorefractive quantum wells. *Appl. Phys. Lett.*, 73:1041, 1998.

[59] L. Landau and B. Levich. *Acta Physicochim. USSR*, 17:42, 1942.

[60] L. D. Landau and E. M. Lifshitz. *Fluid mechanics*, volume 6 of *Course of theoretical physics*. Pergamon Press, Oxford, 1959.

[61] T. Leighton. *The acoustic bubble*. Academic Press, 1997.

[62] V. Leroy, M. Devaud, T. Hocquet, and J.C. Bacri. The bubble cloud as an N-degree of freedom harmonic oscillator. *Eur. Phys. J. E*, 17:189–198, 2005.

[63] J. Li, W. Huang, and Y. Han. Tunable photonic crystals by mixed liquids. *Colloids Surf., A*, 279:213–217, 2006.

[64] Lifeng Li. New formulation of the Fourier modal method for crossed surface-relief gratings. *J. Opt. Soc. Am. A*, 14(10):2758–2767, 1997.

[65] X.M. Li, D. Reinhoudt, and M. Crego-Calama. What do we need for a superhydrophobic surface? A review on the recent progress in the preparation of superhydrophobic surfaces. *Chem. Soc. Rev.*, 36(8):1350–1368, 2007.

[66] D. R. Lide. *CRC handbook of chemistry and physics*. CRC Press Boca Raton, FL, 1995.

[67] Shijie Liu, Jianyong Ma, Chaoyang Wei, Zicai Shen, Jianbin Huang, Yunxia Jin, Jianda Shao, and Zhengxiu Fan. Design of high-efficiency diffraction gratings based on total internal reflection for pulse compressor. *Opt. Commun.*, 273:290, 2007.

[68] R.A. Livingston and R.R. Krchnavek. Grazing angle planar diffraction grating for photonic wavelength demultiplexing. *Electronic Components and Technology Conference, 1996. Proceedings., 46th*, pages 958–962, 1996.

[69] K. Maeda, S. Yokoi, K. Kamada, and M. Kamimura. Foam stability and physicochemical properties of beer. *J. Am. Soc. Brew. Chem*, 49:14–18, 1991.

[70] John R. Marciante and Daniel H. Raguin. High-efficiency, high-dispersion diffraction gratings based on total internal reflection. *Opt. Lett.*, 29:542, 2004.

[71] A. Marmur. Wetting on Hydrophobic Rough Surfaces: To Be Heterogeneous or Not To Be? *Langmuir*, 19(20):8343–8348, 2003.

[72] T. M. Mayer, M. P. de Boer, N. D. Shinn, P. J. Clews, and T. A. Michalske. Chemical vapor deposition of fluoroalkylsilane monolayer films for adhesion control in microelectromechanical systems. *J. Vac. Sci. & Tech. B*, 18:2433–2439, 2000.

[73] D.L. Miller and W.L. Nyborg. Theoretical investigation of the response of gas-filled micropores and cavitation nuclei to ultrasound. *J. Acoust. Soc. America*, 73:1537, 1983.

[74] M. G. Moharam and T. K. Gaylord. Rigorous coupled-wave analysis of planar-grating diffraction. *J. Opt. Soc. Am.*, 71:811, 1981.

[75] M. G. Moharam and T. K. Gaylord. Diffraction analysis of dielectric surface-relief grating. *J. Opt. Soc. Am.*, 72:1385, 1982.

[76] M. G. Moharam and T. K. Gaylord. Rigorous coupled-wave analysis of metallic surface-relief gratings. *J. Opt. Soc. Am. A*, 3:1780, 1986.

[77] M. G. Moharam, Drew A. Pommet, Eric B. Grann, and T. K. Gaylord. Stable implementation of the rigorous coupled-wave analysis for surface-relief gratings: enhanced transmittance matrix approach. *J. Opt. Soc. Am. A*, 12:1077, 1995.

[78] C. Monat, P. Domachuk, and B. J. Eggleton. Integrated optofluidics: A new river of light. *Nat. Phot.*, 1:106 –114, 2007.

[79] T. Mori, K. Hasegawa, T. Hatano, H. Kasa, K. Kintaka, and J. Nishii. Surface-relief gratings with high spatial frequency fabricated using direct glass imprinting process. *Opt. Lett.*, 33:428–430, 2008.

[80] S. Moulinet and D. Bartolo. Life and death of a fakir droplet: Impalement transitions on superhydrophobic surfaces. *Eur. Phys. J. E*, 24(3):251–260, 2007.

[81] A. Nakajima, K. Hashimoto, and T. Watanabe. Recent studies on hydrophobic films. *Monatsh. Chem.*, 132:31, 2001.

[82] A. Nakajima, K. Hashimoto, T. Watanabe, K. Takai, G. Yamauchi, and A. Fujishima. Transparent superhydrophobic thin films with self-cleaning properties. *Langmuir*, 16(17):7044–7047, 2000.

[83] S. S. H. Naqvi, R. H. Krukar, and J. R. McNeil. Etch depth estimation of large-period silicon gratings with multivariate calibration of rigorously simulated diffraction profiles. *J. Opt. Soc. Am. A*, 11:2485, 1994.

[84] C. Neinhuis and W. Barthlott. Characterization and Distribution of Water-repellent, Self-cleaning Plant Surfaces. *Annals of Botany*, 79:667, 1997.

[85] J. Nishii, K. Kintaka, and T. Nakazawa. High-Efficiency Transmission Gratings Buried in a Fused-SiO2 Glass Plate. *Appl. Opt.*, 43(6):1327–1330, 2004.

[86] M. Nosonovsky. Multiscale roughness and stability of superhydrophobic biomimetic interfaces. *Langmuir*, 23(6):3157–3161, 2007.

[87] JF Oliver, C. Huh, and SG Mason. Resistance to spreading of liquids by sharp edges. *J. Colloid Interface Sci*, 59(3):568–581, 1977.

[88] T. Onda, S. Shibuichi, N. Satoh, and K. Tsujii. Super-Water-Repellent Fractal Surfaces. *Langmuir*, 12:2125–2127, 1996.

[89] O. Oralkan, AS Ergun, JA Johnson, M. Karaman, U. Demirci, K. Kaviani, TH Lee, and BT Khuri-Yakub. Capacitive micromachined ultrasonic transducers: next-generation arrays for acoustic imaging? *IEEE T. Ultrason. Ferr.*, 49:1596–1610, 2002.

[90] Edward D. Palik. *Handbook of optical constants of solids*. Academic Press, Orlando, 1985.

[91] A.R. Parker and C.R. Lawrence. Water capture by a desert beetle. *Nature*, pages 33–33, 2001.

[92] N.A. Patankar. On the modeling of hydrophobic contact angles on rough surfaces. *Langmuir*, 19(4):1249–1253, 2003.

[93] Song Peng and G. Michael Morris. Efficient implementation of rigorous coupled-wave analysis for surface-relief gratings. *J. Opt. Soc. Am. A*, 12:1087, 1995.

[94] R. Petit. *Electromagnetic theory of gratings*, volume 22 of *Topics in Current Physics*. Springer Verlag, Berlin, 1980.

[95] S.D. Poisson. *Nouvelle théorie de l'action capillaire*. Bachelier père et fils, 1831. `http://books.google.com/books?id=8N4EAAAAYAAJ&output=html`.

[96] A. Pozzato, S.D. Zilio, G. Fois, D. Vendramin, G. Mistura, M. Belotti, Y. Chen, and M. Natali. Superhydrophobic surfaces fabricated by nanoimprint lithography. *Microelec. Eng.*, 83(4-9):884–888, 2006.

[97] William H. Press, Brian P. Flannery, Saul A. Teukolsky, and William T. Vetterling. *Numerical Recipes in FORTRAN 77 – The Art of Scientific Computing.* Cambridge University Press, 2 edition, 1992.

[98] Demetri Psaltis, Stephen R. Quake, and Changhuei Yang. Developing optofluidic technology through the fusion of microfluidics and optics. *Nature*, 442:381–386, 2006.

[99] D. Quéré. Non-sticking drops. *Rep. Prog. Phys.*, 68(11):2495–2532, 2005.

[100] U. Rabe and W. Arnold. Acoustic microscopy by atomic force microscopy. *Applied Physics Letters*, 64:1493, 1994.

[101] Helmut Rathgen, 2007-2008. http://mrcwa.sourceforge.net/.

[102] Helmut Rathgen, Frieder Mugele, and Kazuyasu Sugiyama. Viscous dynamics of micromenisci. in preparation.

[103] Helmut Rathgen, Kazuyasu Sugiyama, Claus-Dieter Ohl, Detlef Lohse, and Frieder Mugele. Nanometer-resolved collective micromeniscus oscillations through optical diffraction. *Phys. Rev. Lett.*, 99:214501, 2007.

[104] J.W.S. Rayleigh and R.B. Lindsay. *The theory of sound. Vol. 1.* Macmillan, 1894. `http://www.archive.org/details/theoryofsoundvol000709mbp`.

[105] M. Reyssat, A. Pépin, F. Marty, Y. Chen, and D. Quéré. Bouncing transitions on microtextured materials. *Eur. Phys. Lett.*, 74:306–312, 2006.

[106] M. Reyssat, JM Yeomans, and D. Quéré. Impalement of fakir drops. *Eur. Phys. Lett.*, 81:26006, 2008.

[107] Stephane Robert, Alain Mure-Ravaud, and Dominique Lacour. Characterization of optical diffraction gratings by use of a neural method. *J. Opt. Soc. Am. A*, 19:24, 2002.

[108] A. Rohrbach and E.H.K. Stelzer. Trapping forces, force constants, and potential depths for dielectric spheres in the presence of spherical aberrations. *Appl. Opt.*, 41:2494–2507, 2002.

[109] M. Sbragaglia, A.M. Peters, C. Pirat, B.M. Borkent, R.G.H. Lammertink, M. Wessling, and D. Lohse. Spontaneous Breakdown of Superhydrophobicity. *Phys. Rev. Lett.*, 99:156001, 2007.

[110] M. Sbragaglia, A.M. Peters, C. Pirat, B.M. Borkent, R.G.H. Lammertink, M. Wessling, and D. Lohse. Spontaneous Breakdown of Superhydrophobicity. *Phys. Rev. Lett.*, 99(15):156001, 2007.

[111] M. Scheel, R. Seemann, M. Brinkmann, M. Di Michiel, A. Sheppard, B. Breidenbach, and S. Herminghaus. Morphological clues to wet granular pile stability. *Nat. Mater.*, 7:189–19, 2008.

[112] P. Schiffer. Bridge to sandpile stability. *Nat. Phys.*, 1:21–22, 2005.

[113] L.W. Schwartz and S. Garoff. Contact angle hysteresis on heterogeneous surfaces. *Langmuir*, 1(2):219–230, 1985.

[114] R. Seemann, M. Brinkmann, E.J. Kramer, F.F. Lange, and R. Lipowsky. Wetting morphologies at microstructured surfaces. *Proc. Nat. Acad. Sci. USA*, 102(6):1848–1852, 2005.

[115] Martin E. R. Shanahan. Meniscus shape and conact angle of a slightly deformed axisymmetric drop. *J. Phys. D: Appl. Phys.*, 22:1128–1135, 1989.

[116] J. H. Snoeijer, J. Ziegler, B. Andreotti, M. Fermigier, and J. Eggers. Thick films of viscous fluid coating a plate withdrawn from a liquid reservoir. *Phys. Rev. Lett.*, 100(24):244502, 2008.

[117] A.F. Spilhaus. Raindrop size, shape and falling speed. *J. Atm. Sci.*, 5(3):108–110, 1948.

[118] A. Steinberger, C. Cottin-Bizonne, P. Kleimann, and E. Charlaix. High friction on a bubble mattress. *Nat. Mater.*, 6:665, 2007.

[119] P. Swain and R. Lipowsky. Contact angles on structured surfaces: a new look at Cassie's and Wenzel's laws. *Langmuir*, 14:6772–6780, 1998.

[120] A. Taflove and S. C. Hagness. *Computational Electrodynamics: The Finite-Difference Time-Domain Method.* rtech House, Norwood, 2000.

[121] Geoffrey Taylor. The Instability of Liquid Surfaces when Accelerated in a Direction Perpendicular to their Planes. I. *Proc. Roy. Soc. London A*, 201:192–196, 1950.

[122] A. V. Tishchenko. Generalized source method: New possibilities for waveguide and grating problems. *Opt. Quantum Electron.*, 32:971–980, 2000.

[123] R. Truesdell, A. Mammoli, P. Vorobieff, F. van Swol, and C.J. Brinker. Drag Reduction on a Patterned Superhydrophobic Surface. *Phys. Rev. Lett.*, 97:44504, 2006.

[124] H. W. Turnbull. *James Gregory (1638-1675)*, pages 5–11. London, 1939.

[125] J. Turunen. *Diffraction theory of dielectric surface relief gratings.* Taylor & Francis, 1997.

[126] Anish Tuteja, Wonjae Choi, Minglin Ma, Joseph M. Mabry, Sarah A. Mazzella, Gregory C. Rutledge, Gareth H. McKinley, and Robert E. Cohen. Designing superoleophobic surfaces. *Science*, 318:1618–1622, 2007.

[127] Taco Dirk Visser. *Diffraction of electromagnetic waves and image formation in confocal microscopy.* PhD thesis, Universiteit van Amsterdam, 1992.

[128] Gibbs J. W. *Scientific Papers 1906.* New York: Dover, 1962. Dover reprint.

[129] R.N. Wenzel. Resistance of solid surfaces to wetting by water. *Ind. Eng. Chem.*, 28:988–994, 1936.

[130] T.D. Wheeler and A.D. Stroock. The transpiration of water at negative pressures in a synthetic tree. *Nature*, 455:208, 2008.

[131] T. Wilson. *Confocal Microscopy.* Academic Press, 1990.

[132] T. Young. An Essay on the Cohesion of Fluids. *Phil. Trans. R. Soc. London*, 95:65, 1805.

Summary and outlook

Summary

In this thesis optical diffraction was used to study the static and dynamic properties of microscopic liquid-gas interfaces that span between adjacent ridges of a superhydrophobic surface. An observed interference phenomenon at grazing incident angle led to the development of optical gratings with a large spectral bandwidth, and an observed sensitive response of the liquid-gas interfaces to ultrasound led to the development of a superhydrophobic fiber optical micro cavity that enables interferometric detection of the motion of a single microscopic meniscus.

In Chapter 3 angle resolved diffraction from superhydrophobic optical gratings was used to measure the shape of the microscopic liquid-gas interfaces with nanometer resolution, under an applied hydrostatic pressure, under ambient as well as water-vapor conditions. A transition from the superhydrophobic to the impregnated state was observed *in situ* on the microscopic level. It was shown that the macroscopic collapse is triggered by depinning of the microscopic contact lines at a threshold angle that is in close agreement with Young's macroscopic contact angle. The results confirmed experimentally that the assumption of a local contact angle, that forms the basis of several more recent contact angle models, is satisfied well below the micrometer scale. The experimental results are explained with a simple model that is based on the macroscopic laws of Laplace and Young, allowing the formulation of stability criteria for the design of optimal superhydrophobic and superoleophobic surfaces. Prospects of superhydrophobic surfaces for switchable and tunable diffractive optical elements were evaluated through numerical simulations. It was shown that a superhydrophobic optical grating fabricated from glass could provide an immersed grating with near 100% diffraction efficiency and a metallic grating with a larger grating period could provide a spectrally tunable grating with an on-off ratio close to one.

In Chapter 4 possible conformation of a drop on a superhydrophobic surface were considered. Competing definitions of a macroscopic apparent contact angle were reviewed and the role of metastable drop states and external forcing was illustrated. Recent experimental data was reviewed, that shows a deficiency of the Cassie-Baxter model to describe measured contact angles on connected surface patterns. The considerations underline the need for solving more recent 'local contact angle' models for drops on superhydrophobic surfaces, that appreciate the smallness of thermal

fluctuations and the consequent local validity of Young's condition and associated metastability of drop states. Further, they express the need for selecting from the set of allowed metastable states a suitable ensemble that provides a realistic and physical definition of a macroscopic apparent contact angle.

In Chapter 5 dielectric optical gratings were studied through numerical simulations, with focus on the achievable spectral bandwidth. Grating geometries were considered (i) in transmission, (ii) 'buried' grating between two glass bodies, (iii) TIR grating geometry. The effect of a high refractive index grating layer as well as slanted grating lamella was analyzed. It was shown that a suitable high refractive index grating layer dramatically improves the spectral bandwidth. Dielectric optical gratings with octave spanning -1dB bandwidth were devised, providing a larger spectral bandwidth than any grating known to date. Dielectric transmission gratings with 100% peak efficiency were devised by introducing a double layer grating. Slanted fused silica TIR gratings were studied. It was shown that these devices provide their largest efficiency not when operated in Littrow configuration but in a substantially different scattering geometry. Today, all grating designs are optimized for Littrow configuration. The observation recalls the theoretical foundation of the Littrow configuration and highlights that it is rigorously applicable only to symmetric grating profiles.

In Chapter 6, the collective dynamics of arrays of microscopic liquid-gas interfaces formed at the openings of cylindrical hydrophobic micro-cavities were studied through time resolved optical diffraction. Their resonance behavior was described in Chapter 8 with a model that solves the unsteady Stokes flow equations for a single cavity-meniscus system and accounts for hydrodynamic interaction through a monopole approximation. It was shown that the collective dynamics are governed by hydrodynamic interaction, that results in a pronounced decrease of the resonance frequency of an array of micromenisci as compared to a single micromeniscus.

The resonance behavior of a single cavity-meniscus system was studied experimentally in Chapter 7 through a hydrophobic optical micro-cavity fabricated on the end face of an optical fiber. The results confirmed quantitatively the unsteady Stokes flow model for a single cavity-meniscus system. By contrast, potential flow theory including dissipation integrals overestimated the heights of the resonance curves, i.e. underestimated dissipation, showing that viscous dissipation is dominated by vorticity generation inside the boundary layer. The experiments showed prospects for low noise ultrasound detection based on a single cavity-meniscus system on an optical fiber.

Outlook

It was the goal of this thesis to uncloak the information that is contained in the colorful light that is diffracted from a superhydrophobic surface. In retrospect, the amount of information that we found appears overwhelming. We found the static shape of the liquid-gas interfaces, found a confirmation of the locality of the contact angle, an explanation for the superhydrophobic-to-impregnated transition, design criteria for most stable superhydrophobic surfaces, prospects for efficient immersed gratings as

well as tunable optical gratings and other diffractive optical elements, large bandwidth dielectric gratings, collective microscopic ultrasonic oscillations of the liquid-gas interfaces, and a low noise ultrasound sensor based on a fiber-optical superhydrophobic micro-cavity.

The diffraction experient presented in Chapter 3 will allow in the future to investigate further properties of superhydrophobic surfaces in microscopic detail. For example, the mechanism of stability and collapse for reentrant surface profiles suggested in Chapter 3 may be probed. Further, the behavior of the microscopic liquid-gas interfaces under the influence of other external forces, such as electric forces, as encountered e.g. in electrowetting experiments with superhydrophobic surfaces, may be investigated. The prospects of superhydrophobic surfaces as highly efficient and tunable optical gratings may find a way into new technological applications of superhydrophobic surfaces.

The possibility of having dielectric optical gratings with a large spectral bandwidth (through introduction of a high refractive index grating layer, or through slanted lamella) as suggested in Chapter 5, will in the future enable large bandwidth dielectric gratings for many wavelength ranges, and based on many other suitable high index materials. Large bandwidth dielectric gratings will improve the performance of many modern optical applications, including lasers, astronomic telescopes and spectrographs. From a general perspective, they have the potential to replace current metallic grating technology. Certain is, that several of the gratings devised in Chapter 5, will be realized in practice and used for the generation of the shortest high power femtosecond laserpulses (chirped pulse amplification scheme). Through their large spectral bandwidth and simultaneous high dispersion, the gratings will enable pulse durations that have not previously been possible at high power. Thereby they will provide new insight into the ultrafast phenomena associated with the interaction of light and matter. Also certain is, that the suggested concepts (high refractive index material and slanted grating layers) are only the top of the iceberg. Today, virtually all dielectric gratings are based on rectangular grooves fabricated in fused silica. The results of Chapter 5 recall that the number of possible grating designs is countless, both with regard to material combinations and profile geometry. This is a largely unexplored territory. Today numerical tools and computer power are available that allow to evaluate rapidly possible grating designs. It is expected that many more new grating designs will be found, that will offer peak performance with respect to other key parameters, such as flatness of the spectral characteristics, polarization independence, etc..

With regard to a detailed understanding of superhydrophobic surfaces, Chapter 4 has pointed out that current models are far from being complete. It is the hope that full solutions of local contact angle models for drops on superhydrophobic surfaces will be found in the near future, through analytic treatments, or through numerical simulations.

The Chapters 6-8 provide an exhaustive experimental and theoretical treatment of the ultrasound induced dynamics of single and multiple cavity-meniscus systems. The work enables the future use of microscopic liquid-gas interfaces for low noise ultrasound detection, and it provides a detailed theory that can be used to predict

the performance of such a device. In the future practical aspects will be adressed, such as packaging of the device and long term stability, as well as other possible liquids such as mercury, that will improve the finesse of the optical cavity. It will be evaluated whether capacitive detection of the meniscus deflection is possible, and whether an electric excitation of the menisci can as well be used for ultrasound generation.

Samenvatting

Superhydrophobe oppervlakken: vanaf mechanica van vloeistoffen tot optica

In dit proefschrift word optische breking toegepasst voor het bestuderen van de statische en dynamische egenschappen van microscopische vloeistof-gas grensvlakken, die aan de textuur van superhydrophobe oppervlakken sitten. En interferentie fenomeen, dat bij en vlak invall van de licht wordt waargenomen, leidt tot het ontwikkeling van optische roosters med en groote spektrale breede. De gevoelige reactie van de vloeistof-gas grensvlakken tegen ultrasone klang leidt tot het ontwikkeling van superhydrophobe optische micro-cavities op glasvezels, die en interferometrische opsporing van de beweging van en enkele microscopische meniscus maaken mogelijk.

In hoofdstuk 3 wordt hoek opgelosste optische breking gebruikt om de form van de microscopische vloeistof-gas grensvlakken med nanometer precisie te meten, under en hydrostatische druk, under gewoone condities en under vloeistof-stoom condities. En overgang van de superhydrophobe tot de impregerte toestand wordt op de microscopische niveau waargenomen. Het is gelaten zien dat de macroscopische collaps van de depinning van de miscroscopische contact lijnen aangestoten is, bij en hoek die dicht med de macroscopische Young hoek overeenkomt. De resultaate bevestigen experimenteel dat de aanneming van en lokaale contact hoek, die ook vormt de basis voor enige contact hoek modelen, is wel goed gekeurt op de microscopische schaal. De experimentele resultaten worden med en enekele model verklaart, dat is gebasert op de macroscopische wetten van Laplace en Young. Dat makt dat formuleren van stabiliteits kriterien mogelijk, die teogepasst kunnen worden voor het design van optimaale superhydrophobe en superoleophobe oppervlakken. De mogelijkheid van het toepassen van superhydrophobe oppervlakken voor schakelbare brekende optische elementen wordt door numerische berekningen underzoekt. Het was laten zien dat en superhydrophobe optische rooster als en begraven optische rooster med bijna 100% efficiëncie kan toegepasst worden en en metallische rooster med en groote periode is en spctral schakelbrae rooster med en on-off proportie dichtbij een.

In hoofdstuk 4 de vorm van druppels op superhydrophobe oppervlakken wordt geonderzoekt. Concurrerende definities van en macroscopische contact heok worden besproken en de rol van metastabiele druppel vormtjes en extrene krachten wordt illustreert. Nieuwe experiementeele gegevens worden besproken die laaten zien dat

de Cassie-Baxter model niet toegepasst is om de contact hoek van verbondene oppervlakken monsters te berekenen. De discussie wijzt aan dat het belangrijk is locale contact hoek modelen voor druppel op superhydrophobe oppervlakken optelossen. Deze modelen waardeeren de kleine omvang van thermische schommelingen en de voortvloeiende locale geldigheid van Youngs voorwaarde en de metastabieliteit van druppels toestanden. Zij drukken ook uit dat het belangrijk is uit de verzameling van mogelijke metastabiele druppels toestanden en geschikt ensemble uit te zoeken, dat een realistische definitie van en macroscopische contact hoek geeft.

In hoofdstuk 2.58 worden dielectrische optische roosters door numerieke simulaties geonderzoekt, med nadruk op de mogelijke spectrale breede. Roosters worden geonderzoekt (i) in transmissie, (ii) 'begraven' rooster ussen twee glas stuckjes, (iii) rooster baserend op totale reflectie. De effect van en laag med hoge brekingsindex en ook scheefe lamellen worden geanalyseerd. Het wordt laten zien dat en geschikte laag med en hoge brekingsindex de spectrale breede stark vergroot. Dielectrische optische roosters worden voorgestellt, die en -1dB spectrale breede hebben, die bijna een octav overspannt. Dielectrische transmisssie roosters worden voorgestellt die 100% peak efficiencie hebben. Deze worden mogelijk door en twee laag rooster. Scheefe fused silica roosters worden geonderzoekt. Het was laten zien, dat deze roosters de hoogste efficiencie niet in de Littrow configuratie hebben, mar in en andere stark verschillenen configuratie. Vandag worden bijna alle roosters voor de Littrow configuratie geoptimaliseerd. Deze observatie herinnert aan de theoretische grondlag van de Littrow configuratie en onderstrekt dat die slechts voor symmetrische rooster profilen toepasselijk is.

In hoofdstuk 6 wordt de collectiefe dynamica van arrays van microscopische vloeistofgas grensvlakken aan cilindrische hydrophobe micro-cavities door tijd opgelosste optische brekning geonderzoekt. Het resonantie gedrag wordt in hoofdstuk 8 med en model verklaard dat de onvaste Stokes vergelijking vor een enkele cavity-meniscus system losst en hydrodynamische interactie door en monopole benadering beschrijft. Het was laten zien dat de collectiefe dynamica van hydrodynamische interactie bestemmt is, die in een verlaging van de resonantie frequentie resulteert.

De resonantie bedraging van en ekele cavity-meniscus system wordt in hoofdstuk 7 experimenteel onderzoekt med hulp van en hydrophobe optische micro-cavity die op de end van en optische vezel vervaardigd wordt. De resultaaten bevestigen kwantitatief de onvaste Stokes stroom model voor en enkele cavity-meniscus system. Niet zo potentielle stroom theorie, die de dissipatie door zogenaamd dissipatie integrals beschrieft, en de hoogte van de resonantie curven overschatzt. Dat wijzt op, dat viscose dissipatie door vorticitie generatie in de dun laag van vleostof dichtbij de oppervlak wordt domineert. De experimenten verspreken en toepassing van enkele cavity-meniscus systemen op optische vezels als gevoelige ultrasone detectoren.

List of publications

This thesis is based on the following publications.

Chapter 3

Helmut Rathgen and Frieder Mugele, *Microscopic properties of the superhydrophobic state*, submitted.

Chapter 5

Helmut Rathgen and H. L. Offerhaus, *Large bandwidth, highly efficient optical gratings through high index materials*, submitted.

Chapter 6

Helmut Rathgen, Kazuyasu Sugiyama, Claus-Dieter Ohl, Detlef Lohse, and Frieder Mugele, *Nanometer-resolved collective micromeniscus oscillations through optical diffraction*, Phys. Rev. Lett., 99, 214501 (2007)

Helmut Rathgen, Kazuyasu Sugiyama, and Frieder Mugele, *Viscous dynamics of oscillating micromenisci*, in preparation

Chapter 7

Helmut Rathgen, Kazuyasu Sugiyama, Frans Segerink, and Frieder Mugele, *Hearing with a bubble*, submitted

Helmut Rathgen, Kazuyasu Sugiyama, and Frieder Mugele, *Optics with Superhydrophobic Surfaces - a New Class of Switches and Sensors*, Optical Society of America, Frontiers in Optics proceedings, *post deadline paper* A1 (2007)

Helmut Rathgen. *Ultrasound detection using a gas-liquid interface*, Patent application no. PCT/EP2008/000455

Other publications contributed during the PhD

K. M. van Delft, J. C. T. Eijkel, D. Mijatovic, T. S. Druzhinina, H. Rathgen, N. R. Tas, A. van den Berg, and F. Mugele, *Micromachined Fabry-Pérot interferometer with embedded nanochannels for nanoscale fluid dynamics*, Nano Lett., 7, 345 (2007)

Roald M. Tiggelaar, Fernando Benito-López, Dorothee C. Hermesa, Helmut Rathgen, Richard J. M. Egberink, Frieder Mugele, David N. Reinhoudt, A. van den Berg, Albert and Willem Verboom and Han J. G. E. Gardeniers, *Fabrication, mechanical testing and application of high-pressure glass microreactor chips*, Chem. Eng. J., 131, 163 (2007)

Other publications

Helmut Rathgen, Mikhail I. Katsnelson, Olle Eriksson, and Gertrud Zwicknagl, *Polar magneto-optical Kerr effect for low-symmetric ferromagnets*, Phys. Rev. B, 72, 014451 (2005)

Helmut Rathgen and M. I. Katsnelson, *Symmetry Assumptions, Kramers–Kronig Transformation and Analytical Continuation in Ab Initio Calculations of Optical Conductivities*, Phys. Scripta, T109, 170 (2004)

Media coverage

Een veelkleurig oor. Feature in the Dutch newspaper *NRC HANDELSBLAD*, 01. 12. 2007, p.38

Ultrasone Microfoon. Feature in the Belgium newspaper *De Standaard*, 06. 12. 2007, p.29

Publicly released software

mrcwa – Multilayer Rigorous Coupled Wave Analysis, a fast flexible optical grating solver. released under the GPLv3, http://mrcwa.sourceforge.net/

curriculum vitæ

Helmut Rathgen
born January 12, 1978 in Hamburg, Germany
german, unmarried, no children

2004 – today	PhD student at the University of Twente, The Netherlands, with Prof. Frieder Mugele, Physics of Complex Fluids, *Superhydrophobic surfaces: from Fluid Mechanics to Optics.*
2003	Diploma in physics at the TU Braunschweig, Germany, grade: 1.0 *mit Auszeichnung*, Diploma thesis at the Institute for Mathematical Physics, *Microscopic Theory of Magneto–Optical Effects in Ultra–Thin Multilayers.*
2001 – 2003	Student in physics at the University of Uppsala, Sweden
2001	Intermediate Diploma in physics, grade: 1.0
1999 – 2001	Student in physics at the TU Braunschweig, Germany
1998 – 1999	Student in architecture at the TU Braunschweig, Germany
1997	Abitur at the Gymnasium Lüchow, Germany, grade: 1.6

Scholarships and Awards

2008	NanoNed Innovation award (5000 €)
2000 – 2003	Scholarship of the Studienstiftung der Deutschen Wirtschaft
2001 – 2002	Scholarship of the DAAD
2001	Diploma Award of the Braunschweiger Hochschulbund (1000 €)

Acknowledgments

The work presented in this thesis is the result of four years of collaboration, where the most important one has been with my supervisor Frieder Mugele. As you know, Frieder, I have very much enjoyed working with you, though approaches and opinions have been different at times. You have given me a great freedom that allowed me to pursue this work. Our long and winding discussions on the writing and re-writing of manuscripts and modifications of talks have been very educational, and I hope that I have acquired some of your clear way of presenting scientific material. Thank you for taking that time! You have been an encouraging and supporting supervisor.

I wish to thank Detlef Lohse for a fruitful collaboration, including valuable discussions, his engagement in the writing of paper [3], access to his computer cluster, on which part of the computations for paper [1] and [2] where performed, and technical support from his group.

I wish to thank all members of my Committee, Elisabeth Charlaix, Federico Toschi, Matthias Wessling, Dirk van den Ende, and Herman Offerhaus.

It has been a privilege to collaborate with Kazuyasu Sugiyama, whose theoretical work has been invaluable. Thank you, Kaz, for your outstanding theoretical work. Thank you for presenting this work at the ICMF in Dresden. Your interest in this work has meant a lot to me.
ありがとうございます.

I am grateful to Claus-Dieter Ohl, whose unhesitant support for this work has played a key role. It has been a pleasure to work with you on the ultrasound business.

I wish to thank Dirk van den Ende, who has had at any time an open ear for discussing technical details, as well as entirely speculative scientific ideas. Your rigorous approach has been exemplary to me.

I am grateful to Herman Offerhaus for a great collaboration in the last two years. Your enthusiasm for bubble based ultrasound detection as well as large bandwidth optical gratings has been very encouraging.

I wish to thank Wico Hopman for a wonderful collaboration on superhydrophobic photonic crystals. It was a pleasure to work with you, Wico, and your expertiese in photonic crystals has been invaluable in our controlled flooding of the IOMS labs.

Fruitful discussions with Andrea Prosperetti are acknowledged. Special thanks goes to Mauro Sbragaglia, who has triggered this work by asking: “Is it possible to measure when these microscopic liquid-gas interfaces collapse?”. Thank you, Benji, for many fruitful discussions and enthusiastic support.

I thank my colleagues from the PCF group for their enthousiasm and their help, and for creating this pleasant working environment. Thanks go to our secretary Annelies.

This work has been possible only due to the skillful support of many knowledgeable colleagues. I wish to thank Frans Segerink and Jeroen Korterik for fiber FIBing and their expertise in electronics. Who else would come up with a SPICE simulated PD-transimpedance amp design within five minutes, and would know about power MOSFET based OpAmp's that are suitable for low-noise all-silicon high voltage radio frequency amplifiers? I wish to thank Anton Hollink for a great and incredibly fast support with lasers and fiber optics in the IOMS group.

I wish to thank Nicolas Bremond for lending me samples, and for great evenings that he shared with me. Thank you, Nico, for your hospitality in Paris. Thanks go to Hao, Gor, Christophe Pirat, Johan Bomer, and Martine Cantuel for sample fabrication. I would like to thank Jan Eijkel from the BIOS group for his support. Thanks go to Valeria, Marlies, Rory and Jeroen for support with ultrasound equipment. I thank Gilbert and Leon for excellent computer support.

A very special thought goes to Caroline. Your support and patience during the past months of writing has really made this booklet possible.

I would like to thank my office mates Sissi and Burak. Bedankt! Teşekkür! Also, gracie, Roberto! It has been really a pleasure to share the office with you. Thank you, Burak, for excellent travels, great weekend activities, deep discussions at Paddy's and numerous dinners at your place. I whish to thank Gor, who completed the team of late night workers. I don't know how to say thank you in Armenian - probably it is equally appropriate to say: kenazet! Thanks for your company in Austria. Thanks go to Dileep for, amongst others, wonderful chicken curries. I wish to thank Hao for introducing me to the fine art of Chinese tee. Thank you, Florent, for excellent dinners and wine purchases. Thanks go to Jane, Shiva, Eko, Adrian and Arun. I wish to thanks my colleagues Tamara, Manu and Benjamin, who first explored Enschede with me. I would like to thank Diana, who has been very encouraging, Nicki, and Renske.

I wish to thank my flat mate Enrico. It has been a great pleasure to share the flat with you. Thank you for many great weekend trips, wonderful vacation in Sicily, countless evening filling dinners, and much more. Thanks go to Sam and Sam for many fruitful discussions and generous support with fluid samples. Thank you Bandito, Stephan, Gab and Yas. Thanks go to Julian, Daniel and Edip, whose support with packing and moving has been crucial.

I am really grateful to all of you, that you shared the time in Enschede with me.